TU/e EINDHOVEN UNIVERSITY OF TECHNOLOGY

Inter-particle biomolecular reactivity

Citation for published version (APA):
Scheepers, M. R-M. W. (2020). *Inter-particle biomolecular reactivity: how aggregation rates and selectivity are influenced by charge, surface crowders and multivalent interactions*. [Phd Thesis 1 (Research TU/e / Graduation TU/e), Applied Physics and Science Education]. Technische Universiteit Eindhoven.

Document status and date:
Published: 12/06/2020

Document Version:
Publisher's PDF, also known as Version of Record (includes final page, issue and volume numbers)

Please check the document version of this publication:

• A submitted manuscript is the version of the article upon submission and before peer-review. There can be important differences between the submitted version and the official published version of record. People interested in the research are advised to contact the author for the final version of the publication, or visit the DOI to the publisher's website.
• The final author version and the galley proof are versions of the publication after peer review.
• The final published version features the final layout of the paper including the volume, issue and page numbers.

Link to publication

General rights
Copyright and moral rights for the publications made accessible in the public portal are retained by the authors and/or other copyright owners and it is a condition of accessing publications that users recognise and abide by the legal requirements associated with these rights.

• Users may download and print one copy of any publication from the public portal for the purpose of private study or research.
• You may not further distribute the material or use it for any profit-making activity or commercial gain
• You may freely distribute the URL identifying the publication in the public portal.

If the publication is distributed under the terms of Article 25fa of the Dutch Copyright Act, indicated by the "Taverne" license above, please follow below link for the End User Agreement:

www.tue.nl/taverne

Take down policy
If you believe that this document breaches copyright please contact us at:

openaccess@tue.nl

providing details and we will investigate your claim.

Download date: 05. Oct. 2023

Inter-Particle Biomolecular Reactivity

How aggregation rates and selectivity are influenced by charge, surface crowders and multivalent interactions

PROEFSCHRIFT

ter verkrijging van de graad van doctor aan de Technische Universiteit Eindhoven,
op gezag van de Rector Magnificus prof. dr. ir. F.P.T. Baaijens,
voor een commissie aangewezen door het College van Promoties,
in het openbaar te verdedigen op 12 juni 2020 om 16:00 uur

door

Max Rose-Marie Wilhelmus Scheepers

geboren te Heerlen

Dit proefschrift is goedgekeurd door de promotoren en de samenstelling van de promotiecommissie is als volgt:

voorzitter:	prof. dr. ir. G.M.W. Kroesen
1e promotor:	prof. dr. ir. M.W.J. Prins
copromotor:	dr. ir. L.J. van IJzendoorn
leden:	prof. dr. ir. G. Papastavrou (Universität Bayreuth)
	prof. dr. ir. J. Huskens (Universiteit Twente)
	prof. dr. ir. R. Tuinier
	prof. dr. ir. P.P.A.M. van der Schoot (reserve lid)

Het onderzoek of ontwerp dat in dit proefschrift wordt beschreven is uitgevoerd in overeenstemming met de TU/e Gedragscode Wetenschapsbeoefening

In science we resemble children collecting a few pebbles at the beach of knowledge,
while the wide ocean of the unknown unfolds itself in front of us
- Sir Isaac Newton

Inter-particle biomolecular reactivity: How aggregation rates and selectivity are influenced by charge, surface crowders and multivalent interactions
Eindhoven University of Technology, 2020

Copyright © 2020, M.R.W. Scheepers
Cover design by R. Lubken, L. van Smeden, A. Buskermolen and M.R.W. Scheepers

A catalogue record is available from the Eindhoven University of Technology Library
ISBN: 978-90-386-5051-7

Printed by Gildeprint Drukkerijen, Enschede, The Netherlands.

Abstract

Specific and nonspecific interactions between biofunctionalized colloidal particles determine the efficiency and selectivity in applications like particle-based biosensing, targeted drug delivery and directed colloidal assembly. In this thesis, we investigate by experiments and simulations how particle aggregation is influenced by specific and nonspecific interactions, and how this reactivity can be tuned using charge, surface crowders and multivalent interactions.

We developed two experimental methods that allow quantification of the rate of aggregation between colloidal particles. In Chapter 2, an ensemble-based optomagnetic cluster (OMC) experiment is described, in which aggregation is accelerated using magnetic fields and the rate of aggregation is measured by optical scattering. In Chapter 3, a single-dimer aggregation (SDA) experiment is described, in which single particle dimers are magnetically formed and video microscopy is used to detect dimer aggregation and dissociation. The OMC experiment shows that the nonspecific aggregation rate decreases strongly with increasing particle surface charge, whereas no significant effect was observed as a function of antibody density on the particle surface. A comparison of the OMC and SDA data reveals a significant heterogeneity of nonspecific surface reactivity of the particles.

In Chapter 4, we quantify how specific multivalent interactions cause aggregation, and demontrate that the aggregation rate can be tuned by introducing crowding molecules on the particle surface. Moreover, in Chapter 5 we show that the aggregation process becomes more selective when the affinity of the binders on the particle surface is decreased. Finally, Chapter 6 reports measurements with human blood plasma which indicate that the aggregation-inducing corona proteins are mainly located in the hard corona. Chapter 7 summarizes the findings of the thesis, discusses the impact for applications, and lists directions for further research.

List of abbreviations

Abbreviation	Meaning
AFM	Atomic Force Microscopy
bp	base pairs
BPM	Biosensing based on Particle Mobility
BSA	Bovine Serum Albumin
cTnI	Cardiac Troponin I
CV	Coefficient of Variation
DLS	Dynamic Light Scattering
HSA	Human Serum Albumin
IgG	Immunoglobulin G
mAb	monoclonal Antibody
MW	Molecular Weight
nt	nucleotides
OEG	Oligo Ethylene Glycol
OMC	Optomagnetic Cluster experiment
PBS	Phosphate Buffered Saline
PD	Photodetector
PEG	Poly-Ethylene Glycol
PSA	Prostate Specific Antigen
SDA	Single-Dimer Aggregation experiment
SEM	Scanning Electron Microscopy
SI	Supporting Information
TEM	Transmission Electron Microscopy
TIRM	Total Internal Reflection Microscopy

Contents

Chapter 1

Introduction

This thesis describes a study on the inter-particle biomolecular reactivity of biofunctionalized microparticles. In this introductory chapter, the main application areas of these particles are summarized. The physico-chemical parameters that determine the particle surface reactivity will be discussed as well as a brief historical overview of the experimental methods that have been used to quantify surface-surface interaction. Finally the aim and outline of the thesis are discussed.

1.1 Colloids and applications

Colloidal solutions are metastable systems containing particles with a size between the nanoscale and the microscale. The particles are made of various materials e.g. magnetic iron oxides[1-5], silica[6], polymers[7], gold[8,9], silver[10] and combinations thereof[11]. Colloids are used in many applications because of their large surface-to-volume ratio, their versatile mechanical and optical properties, and because they allow a wide range of functionalization strategies. Fig. 1.1a shows SEM images of two examples of microparticles used in this thesis: silica and polystyrene superparamagnetic particles.

Particle surface functionalizations relevant for biomedical applications will be addressed in this thesis. For example, particles can be functionalized to serve as carriers or to be used as labels in diagnostic assays[8,12]. In agglutination assays or cluster assays the presence of the target molecule induces particle aggregation, see Fig. 1.1b. The amount of particle clustering is measured using turbidimetry[13], nephelometry[14], dynamic light scattering (DLS)[15] or using an optomagnetic readout[16,17]. A more recent technique with single particle resolution is biosensing based on particle mobility (BPM) where the motion freedom of a tethered particle decreases upon binding of a target molecule[18,19], see Fig. 1.1c. By analyzing the

motion of many tethered particles over time, the concentration of the target molecule can be monitored.

Colloids are also used in nanomedicine as contrast agents in magnetic resonance imaging[1,20] or as carriers for drug delivery[1-3,21,22]. In targeted drug delivery, the particles encapsulate a drug and should only bind to diseased cells, without affecting healthy cells[21], see Fig. 1.1d. For this purpose the particles are functionalized with ligands that bind either specifically to the receptors that are unique to the diseased cells, or selectively to a certain density of receptors that are overexpressed on the diseased cells[23,24].

In biophysical research, colloidal particles function as optical or magnetic tweezers for studies on proteins[25] and DNA[26]. Self-assembly[27] and directed-assembly[27,28] of colloidal solutions find applications in for example 3D photonic crystals[29-31].

1.2 Inter-particle aggregation

A major challenge in developing particle-based applications is to control colloidal stability and minimize particle aggregation. The aggregation is typically irreversible and can cause large variabilities in the applications. For example, particle aggregation is an important factor determining the efficiency of drug delivery processes[32] and aggregation can strongly affect the coefficient of variation and limit of detection of particle-based assays[17]. In these examples, particle aggregation is of a nonspecific origin, often caused by Van Der Waals interaction[33], electrostatic interaction[34], or hydrophobic interaction[35].

Maintaining particle stability and functionality is especially difficult in complex biological media like blood plasma[36]. Upon exposing a colloidal particle to blood plasma, each of the thousands of plasma proteins[37] start to interact with the particle surface. Over time, a dense layer of proteins can adhere to the particle surface, called the protein corona, which largely determines the fate and functionality of the particle. Initially the protein corona is dominated by the highly concentrated proteins. As a function of time, these proteins are exchanged for the lower concentrated but higher affinity proteins[38,39]. The final composition of the protein corona around a particle depends on plasma composition and on many particle characteristics, e.g. particle size[40,41], shape[42], material[43], charge[44] and coating[44,45]. The final protein corona is often described as consisting of a hard and a soft corona where the affinity of the proteins for the particle surface is the discriminating factor[46]. The hard corona is generally considered to consist of tightly bound proteins that do not readily desorb, whereas

the soft corona contains the weakly bound proteins that are in a constant dynamic equilibrium with the bulk.

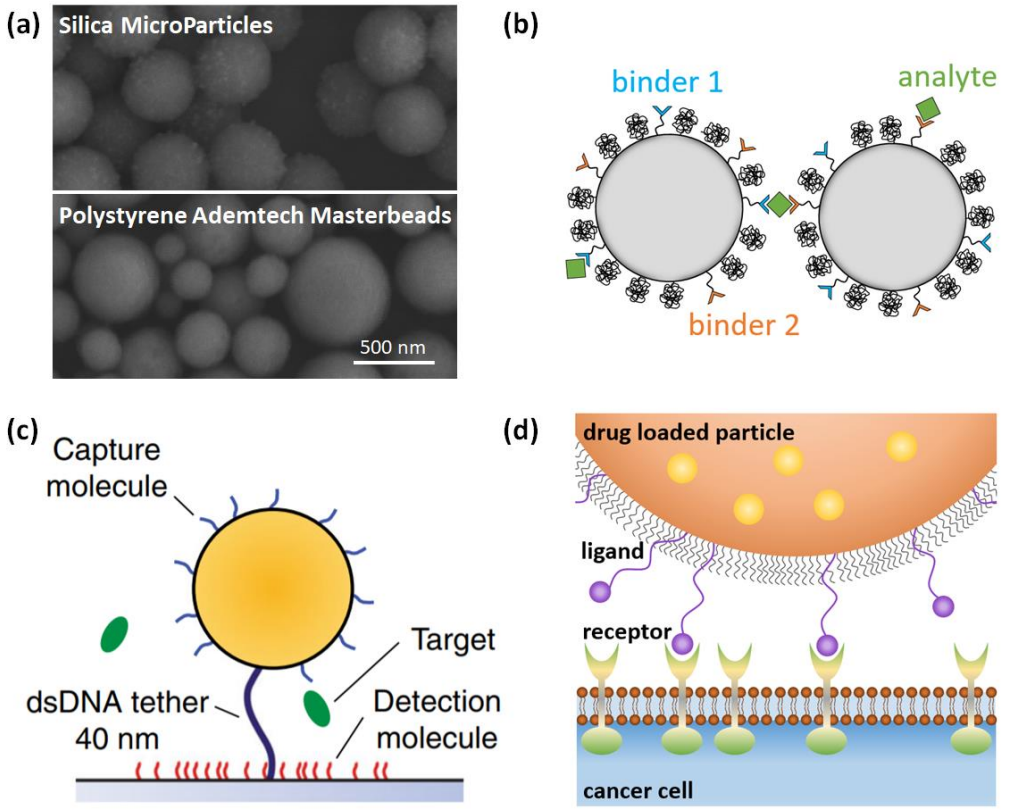

Fig. 1.1 Colloids and applications. (a) SEM images of Silica MicroParticles and Polystyrene Ademtech Masterbeads. Both particles have a mean diameter of 500 nm, but the Ademtech Masterbeads have a broad size dispersion. **(b)** Cluster assay in which the presence of a target molecule, called analyte, induces particle aggregation via the binder molecules on the particles. **(c)** Biosensing based on particle mobility (BPM) in which the mobility of a tethered particle decreases upon binding with a capture molecule to the detection molecule via the target molecule. **(d)** Targeted drug delivery in which a drug loaded particle, which is functionalized with ligands, binds selectively to diseased cells, for example a cancer cell.

To prevent nonspecific particle aggregation, the particle surface is often functionalized with charged molecules, e.g. carboxylic acids, ionic surfactants or DNA. The surface charge on the particles induces electrostatic repulsion[47,48] on inter-particle distances smaller than the Debye length[49]. Another way of stabilizing colloidal solutions is by coating the particles with passive surface crowders, e.g. oligo-ethylene glycol (OEG) and poly-ethylene glycol (PEG)[50]. These molecules form a mushroom- or brush-shaped layer on the particle surface, depending on their

surface density. In complex media, the surface crowders are able to decrease the fouling of proteins on the particle surface and thereby decrease particle aggregation and increase pharmacokinetics[51,52].

In contrary to the undesired nonspecific particle aggregation, many applications employ specific interactions between particles to facilitate for example detection[8,12] and directed assembly[27,28]. Specific biomolecular interaction between particles is obtained by coating a ligand-receptor pair on the particles, e.g. antibody-antigen[53], aptamer-protein[54], DNA hybridization[55] and streptavidin-biotin bonds[56]. In case the interaction is strong enough, stable particle-dimers can be formed by a single biomolecular bond. However, for weak interactions multiple parallel bonds are necessary to form a stable particle dimer.

The ratio between specific and nonspecific particle aggregation determines the specificity in an assay. In this thesis, nonspecific and (multivalent) specific particle aggregation are investigated on particles functionalized with multiple specific biomolecular binders.

1.3 Quantifying particle surface reactivity

The interactions between (particle) surfaces have been investigated by various experimental methods. The surface force apparatus[57,58] developed by Israelachvili and Tabor in the early seventies allows quantification of interaction forces at angstrom resolution, but is limited to molecularly smooth surfaces in air or in vacuum. In the late eighties and early nineties, colloidal probe AFM[59,60], total internal reflection microscopy[61] (TIRM) and optical tweezers[62] were developed. Colloidal probe AFM has been used to measure force-distance curves in liquids between a single micrometer sized colloidal probe and a surface or a second particle[63], while the interactions between two particles have also been measured with optical tweezers[64]. Both methods allow quantification of inter-particle forces between individual biofunctionalized particles, but require difficult and complicated experimental setups and yield low statistics. Using TIRM[65-67], the energy landscape between functionalized surfaces has been explored with high statistics, but is limited to particle-surface interactions.

Particles with interacting surfaces can ultimately form aggregates or clusters in a colloidal solution. Already in the mid-1950s, cluster assays were developed by Singer and Plotz[68] and are used to quantify biomarker concentrations[13,14,16,68,69]. Particles capture biomarkers from solution onto their functionalized surface and subsequent particle collisions lead to the formation of dimers and larger clusters, depending on

the biomarker concentration. Cluster assays based on the thermal diffusion of particles are slow and can therefore operate only with relatively unstable colloidal systems, i.e. particles with a high chemical reactivity. Baudry et al.[16] demonstrated that the assay time can be significantly reduced using superparamagnetic particles in combination with external magnetic fields. Particles become magnetized in the external field and self-organize into chains by attractive magnetic dipole interactions, which accelerates cluster formation. Ranzoni et al.[70] used this optomagnetic cluster experiment to measure picomolar concentrations of prostate specific antigen (PSA) directly in blood plasma. This method can be used to study inter-particle aggregation induced by magnetic confinement in stable colloidal solutions, for any surface functionalization and with high statistics. In this thesis the optomagnetic cluster experiment is used as the method to quantify particle surface reactivity.

1.3.1 Superparamagnetic particles

In this thesis superparamagnetic particles are used to study the inter-particle biomolecular surface reactivity. Fig. 1.1a shows a SEM image of the silica and polystyrene superparamagnetic particles that are used in this research. Both particles have a mean diameter of 500 nm, however, the polystyrene Ademtech Masterbeads have larger size distribution (coefficient of variation 25%) compared to the Silica MicroParticles (coefficient of variation < 5%).

Superparamagnetic particles typically consist of many ferro- or ferri-magnetic nanocrystals, randomly dispersed in the polymer or silica matrix. Each nanocrystal is single-domain. When the magnetic anisotropy energy of a nanocrystal is much larger than the thermal energy ($KV \gg k_B T$)[71], the magnetic moment of the nanocrystal is aligned with the easy axis of magnetic anisotropy. However, in superparamagnetic particles the nanocrystals are very small and the thermal energy exceeds the anisotropy energy ($k_B T \gg KV$). Moreover, the easy axes of the nanocrystals are randomly aligned within the particle. Therefore, a superparamagnetic particle at room temperature does not have a net magnetic moment in the absence of an external magnetic field. When an external magnetic field is applied so that the magnetic energy exceeds the thermal energy, $mB > k_B T$, the magnetic moments of the nanocrystals tend to align with the magnetic field, whereby the particle acquires a nonzero net magnetic moment. For a superparamagnetic particle that consists of a large ensemble of nanocrystals, the magnetic moment of the particle increases with the magnetic field according to the Langevin function.

In a system with several superparamagnetic particles, the application of an external magnetic field introduces a nonzero magnetic moment for each particle in the direction of the external magnetic field. Particles mutually experience magnetic

dipole-dipole interactions, causing particles to align in strings along the magnetic field lines. In this thesis the dipole-dipole interactions between superparamagnetic particles are employed in two ways to study particle surface reactivity: An ensemble method in which particle clustering is measured by light scattering (optomagnetic OMC experiment) and a single-dimer aggregation method based on microscopy (SDA experiment).

1.3.2 The optomagnetic cluster (OMC) experiment

The ensemble method to study inter-particle biomolecular reactivity, developed in this thesis, is the optomagnetic cluster (OMC) experiment, see Fig. 1.2a. The method briefly works as follows. A square cuvette filled with a dispersion of superparamagnetic particles is placed in the centre of a quadrupole electromagnet. A laser is focussed in the cuvette and the light scattered by the particles is measured with a photodetector at an angle of 90 degrees w.r.t. the incoming laser beam. By applying an external magnetic field, particles are attracted to each other, which accelerates the biomolecular aggregation process. By rotating the magnetic field in the horizontal plane, single particles and dimers rotate with the magnetic field. As the scattering cross-section of dimers depends on their orientation, and the scattering cross-section of a monomer is independent of its orientation, an oscillating scattering signal is a measure for the concentration of dimers in solution. A four-step magnetic actuation protocol is used to quantify the aggregation rate. The scattering cross-section of dimers is different from trimers and larger clusters[72]; however, it is not easy to disentangle data for a mixture of multimers, so the OMC method is limited to measuring the aggregation of dimers, i.e. the actuation times are kept short in order to prevent the formation of larger clusters.

Using the OMC experiment, the aggregation rate of an ensemble of particles can be measured within a few minutes, yielding high statistics. The method allows the measurement of superparamagnetic particles with different particle surface functionalizations.

1.3.3 The single-dimer aggregation (SDA) experiment

The single-dimer aggregation (SDA) experiment combines magnetic confinement and single particle resolution and allows observation of the differences in particle surface reactivity between individual dimers. Fig. 1.2b conceptually depicts the SDA experiment. Individual primary particles are bound to a substrate. In the presence of a tilted out-of-plane magnetic field, a secondary particle is magnetically trapped on the primary particle. By rotating the magnetic field around the vertical axis, the secondary particle moves over the surface of the primary particle, effectively probing

to biomolecular aggregation. Using video microscopy the multiple aggregation and dissociation events of multiple single dimers can be followed in time. The orientation of the dimer in the aggregated state gives information about the local surface reactivity of the primary particle.

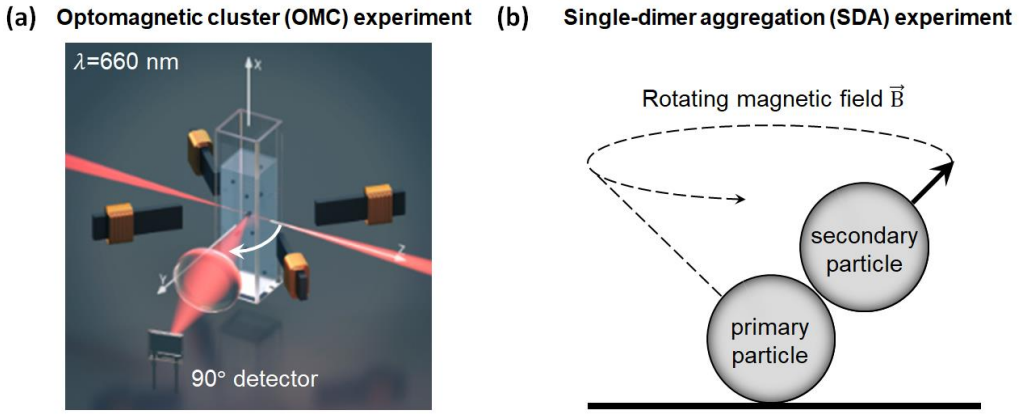

Fig. 1.2 Quantifying particle aggregation. (a) Optomagnetic cluster (OMC) experiment which allows quantification of ensemble dimer-formation rates**. (b)** Single-dimer aggregation (SDA) experiment which is used to study the heterogeneity among particle surface reactivity.

1.4 Research goal and outline of the thesis

The aim of this research is to quantify inter-particle biomolecular reactivity and investigate how aggregation and selectivity depend on the physico-chemical properties of the particle surface. More specifically, the influence of charge, surface crowders and multivalent interactions on particle aggregation rates have been investigated using experiments and simulations. The long term aim is to further our understanding of inter-particle interactions and to be able to design the particle surface to optimize their functionality in the desired application.

In **chapter 2** the optomagnetic cluster (OMC) experiment is described with which particle aggregation rates can be measured on an ensemble of particles. A four-step magnetic actuation protocol was developed to quantify an aggregation rate, and the influence of the magnetic field settings are studied. The effect of particle surface charge is investigated on the nonspecific aggregation of carboxylic acid coated particles, by varying pH and ionic strength of the buffer.

Chapter 3 introduces a single-dimer aggregation (SDA) experiment in which individual aggregation and dissociation events of single-dimers of particles are tracked over time with bright field optical microscopy. Using home-made image

analysis software, heterogeneities in particle surface reactivity were observed for particles functionalized with antibodies and PEG. It is shown that the aggregation rate only slightly depends on the antibody-to-PEG ratio. Experimental data of the SDA experiment and OMC experiment on identical particles are compared with simulations, which confirms the heterogeneity in the particle surface reactivity.

In **chapter 4** the surface reactivity of particles coated with specific binders is studied by quantifying the multivalent particle aggregation rate using the OMC experiment. The main goals of this chapter are to investigate the specific particle aggregation rate as a function of the specific binder density and study the influence of passive surface crowders on the aggregation rate. For this purpose a DNA based model system and an antibody sandwich system were used, in which aggregation was induced using a specific bridging molecule, an oligonucleotide or a protein. The particle surface reactivity was tuned by varying the binder surface density and by varying the molecular weight of the surface crowder.

In **chapter 5** a DNA-based model system is used to study particle surface reactivity for low affinity DNA interactions. Experimental proof is provided that multivalent weak interactions enhance selectivity in inter-particle binding. Using a stochastic binding simulation the affinity of the DNA interaction is quantified.

In **chapter 6** inter-particle aggregation rates are quantified in a complex matrix to assess the potential of particles to be used in diagnostic applications. The effect of particle functionalization on the surface reactivity is measured in different dilutions of blood plasma, showing that PEGylated particles are most stable. Furthermore, by pre-depleting the plasma samples with functionalized particles, it is demonstrated that the aggregation-inducing corona proteins are specific for the particle surface coating.

Finally, **chapter 7** summarizes the conclusions and presents an outlook.

References

[1] Sun, C.; Lee, J. S. H.; Zhang, M. Magnetic nanoparticles in MR imaging and drug delivery. *Adv. Drug. Del. Rev*. **2008**, 60, 1252-1265

[2] Indira, T. K.; Lakshmi, P. K. Magnetic nanoparticles - A review. *Int. J. of Pharm. Sci. and Nanotech* **2010**, 3 (3), 1035-1042

[3] Pankhurst, Q. A.; Connoly, J.; Jones, S. K.; Dobson, J. Applications of magnetic nanoparticles in biomedicine. *J. Phys. D: Appl. Phys*. **2003**, R167-R181

[4] Gupta, A. K.; Gupta, M. Synthesis and surface engineering of iron oxide nanoparticles for biomedical applications. *Biomaterials* **2005**, 26, 3995-4021

[5] Mosayebi, J.; Kiyasatfar, M.; Laurent, S. Synthesis, functionalization and design of magnetic nanoparticles for theranostic applications. *Adv. Health. Mater.* **2017**, 1700306

[6] Li, Z.; Barnes, J. C.; Bosoy, A.; Stoddart, J. F.; Zink, J. I. Mesoporous silica nanoparticles in biomedical applications. *Chem. Soc. Rev*. **2012**, 41, 2590-2605

[7] Rao, J. P.; Geckeler, K. E. Polymer nanoparticles: preparation techniques and size-control parameters. *Prog. in Poly. Sci.* **2011**, 36, 887-913

[8] Zeng, S.; Yong, K. T.; Roy, I.; Dinh, X. Q.; Yu, X.; Luan, F. A review on functionalized gold nanoparticles for biosensing applications. *Plasmonics* **2011**, 6, 491-506

[9] Daniel, M. C.; Astruc, D. Gold nanoparticles: Assembly, supramolecular chemistry, quantum-size-related properties, and applications towards biology, catalysis and nanotechnology. *Chem. Rev.* **2004**, 104, 293-346

[10] Prabhu, S.; Poulose, E. K. Silver nanoparticles: mechanism of antimicrobial action, synthesis, medical applications, and toxicity effects. *Int. Nano Letters* **2012**, 2, 32

[11] Mahmoudi, M.; Sant, S.; Wang, B.; Laurent, S.; Sen, T. Superparamagnetic iron oxide nanoparticles (SPIONs): Development, surface modification and applications in chemotherapy. *Adv. Drug Del. Rev.* **2011**, 63, 24-46

[12] Howes, P.D.; Chandrawati, R.; Stevens, M.M. Colloidal nanoparticles as advanced biological sensors. *Science*, **2014**, 346, 6205

[13] Visser, E.W.A.; van IJzendoorn, L.J.; Prins, M.W.J. Particle motion analysis reveals nanoscale bond characteristics and enhances dynamic range for biosensing. *ACS Nano* **2016**, 10, 3, 3093-3101

[14] Visser, E.W.A.; Yan, J.; van IJzendoorn, L.J.; Prins, M.W.J. Continuous biomarker monitoring by particle mobility sensing with single molecule resolution. *Nat. Comm.* **2018**, 2541

[15] Cohen, R.J.; Benedek, G.B. Immunoassay by light scattering spectroscopy. *Immunochemistry*, **1975**, 12, 4, 349-351

[16] Virella, G.; Waller, M.; Fudenberg, H. Nephelometric method for determination of rheumatoid factor. *J. Immunol. Methods*, **1978**, 22, 3, 247-251

[17] Fischer, K.; Schmidt, M. Pitfalls and novel applications of particle sizing by dynamic light scattering. *Biomaterials* **2016**, 98, 79-91

[18] Baudry, J.; Rouzeau, C.; Goubault, C.; Robic, C.; Cohen-Tannoudji, L.; Koenig, A.; Bertrand, E.; Bibette, J. Acceleration of the recognition rate between grafted ligands and receptors with magnetic forces. *PNAS*, **2006**, 103, 44, 16076-16078

[19] Ranzoni, A.; Schleipen, J.J.H.B.; van IJzendoorn, L.J.; Prins, M.W.J. Frequency-selective rotation of two-particle nanoactuators for rapid and sensitive detection of biomolecules. *Nano Lett.*, **2010**, 11, 5, 2017-2022

[20] Vuong, Q.L.; Gillis, P.; Roch, A.; Gossuin, Y. Magnetic resonance relaxation induced by superparamagnetic particles as contrast agents in magnetic resonance imaging: a theoretical review. *WIREs Nanomed. Nanobiotechnol.* **2017**, 9, 1468

[21] Müller, R. H.; Mäder, K.; Gohla, S. Solid lipid nanoparticles for controlled drug delivery - a review of the state of the art. *Europ. J. Pharma. and Biopharma.* **2000**, 50, 161-177

[22] Mohanraj, V. J.; Chen, Y. Nanoparticles - A review. *Trop. J. Pharm. Res.* **2006**, 5 (1) 561-573

[23] Linja, M.J.; Savinainen, K.J.; Saramäki, O.R.; Tammela, T.L.J.; Vessella, R.L.; Visakorpi, T. Amplification and overexpression of androgen receptor gene in hormone-refractory prostate cancer. *Cancer Research* **2001**, 61, 3550-3555

[24] Di Renzo, F.; Olivero, M.; Katsaros, D.; Crepaldi, T.; Gaglia, P.; Zola, P.; Sismondi, P.; Comoglio, P.M. Overexpression of the MET/HGF receptor in ovarian cancer. *Int. J. Canc.* **1994**, 58, 658-662

[25] van Reenen, A.; Gutiérrez-Mejía, F.; van IJzendoorn, L.J.; Prins, M.W.J. Torsion profiling of proteins using magnetic particles. *Biophys. J.* **2013**, 104, 5, 1073-1080

[26] Lipfert, J.; Kerssemakers, J.W.J.; Jager, T.; Dekker, N.H. Magnetic torque tweezers: measuring torsional stiffness in DNA and RecA-DNA filaments. *Nature Meth.* **2010**, 7, 977-980

[27] Min, Y.; Akbulut, M.; Kristiansen, K.; Golan, Y.; Iraelachvili, J. The role of interparticle and external forces in nanoparticle assembly. *Nat. Mater.* **2008**, 7, 527-538

[28] Shenhar, R.; Norsten, T.B.; Rotello, V.M. Polymer mediated nanoparticle assembly: Structural control and applications. *Adv. Mater.* **2005**, 17, 6, 657-669

[29] Inan, H.; Poyraz, M.; Inci, F.; Lifson, M.A.; Baday, M.; Cunningham, B.T.; Demirci, U. Photonic crystals: emerging biosensors and their promise for point-of-care applications, *Chem. Soc. Rev.* **2017**, 46, 366-388

[30] Subramanian, G.; Manoharan, V.N.; Thorne, J.D.; Pine, D.J. Ordered macroporous materials by colloidal assembly: A possible route to photonic bandgap materials. *Adv. Mater.* **1999**, 11, 15, 1261-1265

[31] Xia, Y.; Gates, B.; Park, S.H. Fabrication of three-dimensional photonic crystals for use in the spectral region from ultraviolet to near-infrared, *J. Light. Technol.* **1999**, 17, 11, 1956-1962

[32] Suk, J. S.; Xu, Q.; Kim, N.; Hanes, J.; Ensign, L. M. PEGylation as a strategy for improving nano-particle based drug and gene delivery. *Adv. Drug Del. Rev.* **2016**, 99, 28-51

[33] Hamaker, H.C. The Londen - van der Waals attraction between spherical particles. *Physica IV* **1937**, 10, 1058-1072

[34] Shipway, A.N.; Lahav, M.; Gabai, R.; Wilner, I. Investigations into electrostatically induced aggregation of Au nanoparticles. *Langmuir* **2000**, 16, 23, 8789-8795

[35] Zangi, R.; Berne, B.J. Aggregation and dispersion of small hydrophobic particles in aqueous electrolyte solutions. *J. Phys. Chem. B* **2006**, 110, 45, 22736-22741

[36] Dobrovolskaia, M.A.; Patri, A.K.; Zheng, J.; Clogston, J.D.; Ayub, N.; Aggarwal, P.; Neun, B.W.; Hall, J.B.; McNeil, S.E. Interaction of colloidal gold nanoparticles with human blood: effects on particle size and analysis of plasma protein binding profiles. *Nanomed. Nanotechnol.* **2009**, 5, 2, 106-117

[37] Schwenk, J.M.; Omenn, G.S.; Sun, Z.; Cambell, D.S.; Baker, M.S.; Overall, C.M.; Aebersold, R.; Moritz, R.L.; Deutsch, E.W. The human plasma proteome draft of 2017: Building on the human plasma PeptideAtlas from mass spectrometry and complementary assays. *J. Proteome. Res.* **2017**, 16, 4299-4310

[38] Dell'Orco, D.; Lundqvist, M.; Oslakovic, C.; Cedervall, T.; Linse, S. Modeling the time evolution of the nanoparticle protein corona in a body fluid. *PLoS ONE* **2010**, 5, 6, e10949

[39] Sahneh, F.D.; Scoglio, C.; Riviere, J. Dynamics of nanoparticle-protein corona complex formation: Analytical results from population balance equations. *PLoS ONE* **2013**, 8, 5, e64690

[40] Tenzer, S.; Docter, D.; Rosfa, S.; Wlodarski, A.; Kuharev, J.; Rekik, A.; Knauer, S.K.; Bantz, C.; Nawroth, T.; Bier, C.; Sirirattanapan, J.; Mann, W.; Treuel, L.; Zellner, R.; Maskos, M.; Schild, H.;

Stauber, R.H. Nanoparticle size is a critical physicochemical determinant of the human blood plasma corona: a comprehensive quantitative proteomic analysis. *ACS Nano* **2011**, 5, 9, 7155-7167

[41] Foroozandeh, P.; Aziz, A.A. Merging worlds of nanomaterials and biological environment: factors governing protein corona formation on nanoparticles and its biological consequences. *Nanoscale Res. Lett.* **2015**, 10, 221

[42] García-Álvares, R.; Hadjidemetriou, M.; Sánchez-Iglesias, A.; Liz-Marzán, L.M.; Kostarelos, K. In vivo formation of protein corona on gold nanoparticles. The effect of their size and shape. *Nanoscale* **2017**, 10, 1039

[43] Lundqvist, M.; Stigler, J.; Elia, G.; Lynch, I.; Cedervall, T.; Dawsen, K.A. Nanoparticle size and surface properties determine the protein corona with possible implications for biological impacts. *PNAS* **2008**, 105, 38, 14265-14270

[44] Sakulkhu, U.; Mahmoudi, M.; Maurizi, L.; Salaklang, J.; Hofmann, H. Protein corona composition of superparamagnetic iron oxide nanoparticles with various physico-chemical properties and coatings. *Sci. Rep.* **2014**, 4, 5020

[45] Johnston, B.D.; Kreyling, W.G.; Pfeiffer, C.; Schäffer, M.; Sarioglu, H.; Ristig, S.; Hirn, S.; Haberl, N.; Thalhammer, S.; Hauck, S.M.; Semmler-Behnke, M.; Epple, M.; Hühn, J.; Del Pino, P.; Parak, W.J. Colloidal stability and surface chemistry are key factors for the composition of the protein corona of inorganic gold nanoparticles. *Adv. Funct. Mater.* **2017**, 27, 1701956

[46] Pederzoli, F.; Tosi, G.; Vandelli, M.A.; Belletti, D.; Forni, F.; Ruozi, B. Protein corona and nanoparticles: how can we investigate on? *WIREs Nanomed Nanobiotechnol.* **2017**, 9, 1467

[47] Paik, U.; Hackley, V.A.; Choi, S.; Yung, Y. The effect of electrostatic repulsive forces on the stability of $BaTiO_3$ particles suspended in non-aqueous media. *Coll. Surf. A* **1998**, 135, 1-3, 77-88

[48] Schneider, C.; Hanisch, M.; Wedel, B.; Jusufi, A.; Ballauff, M. Experimental study of electrostatically stabilized colloidal particles: colloidal stability and charge reversal. *J. Coll. Int. Sci.* **2011**, 358, 1, 62-67

[49] Tadmor, R.; Hernández-Zapata, E.; Chen, N.; Pincus, P.; Israelachvili, J.N. Debye length and double layer forces in polyelectrolyte solutions. *Macromolecules* **2002**, 35, 6, 2380-2388

[50] Blaszykowski, C.; Sheikh, S.; Thompson, M. A survey of state-of-the-art surface chemistries to minimize fouling from human and animal biofluids. *Biomater. Sci.* **2015**, 3, 1335-1370

[51] Gbadamosi, J.K.; Hunter, A.C.; Moghimi, S.M. PEGylation of microspheres generates a heterogeneous population of particles with differential surface characteristics and biological performance. *FEBS Lett.* **2002**, 532, 338-344

[52] Perry, J.L.; Reuter, K.G.; Kaj, M.P.; Herlihy, K.P.; Jones, S.W.; Luft, J.C.; Napier, M.; Bear, J.E.; DeSimone, J.M. PEGylated PRINT particles: The impact of PEG density on protein binding, macrophage association, biodistribution and pharmacokinetics. *Nano Lett.* **2012**, 12, 5304-5310

[53] Braden, B.C.; Poljak, R.J. Structural features of the reactions between antibodies and protein antigens. *J. FASEB* **1995**, 9, 9-16

[54] Gelinas, A.D.; Davies, D.R.; Janjic, N. Embracing proteins: structural themes in aptamer-protein complexes. *COSB* **2016**, 36, 122-132

[55] Strunz, T.; Oroszlan, K.; Schäfer, R.; Güntherodt, H. Dynamic force spectroscopy of single DNA molecules. *PNAS* **1999**, 96, 11277-11282

[56] Shu, W.; Laue, E.D.; Seshia, A.A. Investigation of biotin-streptavidin binding interactions using microcantilever sensors. *Biosens. Bioelectron.* **2007**, 22, 9-10, 2003-2009

[57] Israelachvili, J.N.; Tabor, D. The measurement of van der Waals dispersion forces in the range 1.5 to 130 nm. *Proc. Roy. Soc. London Series A* **1972**, 331(1584), 19-38

[58] Israelachvili, J.N.; Tabor, D. Van der Waals forces: theory and experiment. *Prog. Surf. Mem. Sci.* **1973**, 7(1), 1-55

[59] Ducker, W.A.; Senden, T.J.; Pashley, R.M. Direct measurement of colloidal forces using an atomic force microscope. *Nature* **1991**, 353, 6341, 239-241

[60] Butt, H.J. Measuring electrostatic, van der Waals and hydration forces in electrolyte solutions with an atomic force microscope. *Biophys. J.* **1991**, 60, 6, 1438-1444

[61] Prieve, D.C. Measurement of colloidal forces with TIRM. *Adv. Coll. Int. Sci.* **1999**, 82, 1-3, 93-125

[62] Ashkin, A.; Dziedzic, J.M.; Bjorkholm, J.E.; Chu, S. Observation of a single-beam gradient force optical trap for dielectric particles. *Opt. Lett.* **1986**, 11, 5, 288-290

[63] Helfricht, N.; Mark, A.; Drowling-Carter, L.; Zambelli, T.; Papastavrou, G. Extending the limits of direct force measurements: colloidal probes from sub-micron particles. *Nanoscale* **2017**, 9, 9491

[64] Schein, P.; Kang, P.; O'Dell, D.; Erickson, D. Nanophotonic force microscopy: Characterizing particle-surface interactions using near field photonics. *Nano Lett.* **2015**, 15, 1414-1420

[65] van Ommering, K.; Koets, M.; Paesen, R.; van IJzendoorn, L.; Prins, M. Bond characterization by detection and manipulation of particle mobility in an optical evanescent field biosensor. *J. Phys. D: Appl. Phys.* **2010**, 43, 385501

[66] Wang, Z.; He, C.; Gong, X.; Wang, J.; Ngai, T. Measuring the surface-surface interactions induced by serum proteins in a physiological environment. *Langmuir*, **2016**, 32, 12129-12136

[67] Biancaniello, P.L.; Crocker, J.C. Line optical tweezers instrument for measuring nanoscale interactions and kinetics. *Rev. Sci. Instrum.*, **2006**, 77, 113702

[68] Singer, J.M.; Plotz, C.M. The latex fixation test. *Am. J. Med.*, **1956**, 21, 888-892

[69] Oppenheimer, S.; Odencrantz, J. A quantitative assay for measuring cell agglutination: Agglutination of sea urchin embryo and mouse teratoma cells by concanavalin A. *Exp. Cell. Res.*, **1972**, 73, 2, 475-480

[70] Ranzoni, A.; Sabatte, G.; van IJzendoorn, L.J.; Prins, M.W.J. One-step homogeneous magnetic nanoparticle immunoassay for biomarker detection directly in blood plasma. *ACS Nano*, **2012**, 6, 4, 3134-3141

[71] Moerland, C.P.; van IJzendoorn, L.J.; Prins, M.W.J. Rotating magnetic particles for lab-on-chip applications - a comprehensive review. *Lab on a chip* **2019**, 19, 919-933.

[72] van Vliembergen, R.W.L.; van IJzendoorn, L.J.; Prins, M.W.J. Nanoscale interparticle distance within dimers in solution measured by light scattering. *Langmuir*, **2018**, 34, 1, 179-186

Chapter 2

Rate of dimer formation in stable colloidal solutions quantified using an attractive interparticle force

We describe an optomagnetic cluster experiment to understand and control the interactions between particles over a wide range of timescales. Aggregation is studied by magnetically attracting particles into dimers, and by quantifying the number of dimers that become chemically bound within a certain time interval. An optomagnetic readout based on light scattering of rotating clusters is used to measure dimer formation rates. Magnetic field settings, i.e. field rotation frequency, field amplitude and on- and off-times, have been optimized to independently measure both the magnetically induced dimers and the chemically bound dimers. The chemical aggregation rate is quantified in solutions with different pH and ionic strength. The measured rates are extrapolated to effective dimer formation rates in absence of force, showing that aggregation rates can be quantified over several orders of magnitude including conditions of very low chemical reactivity.

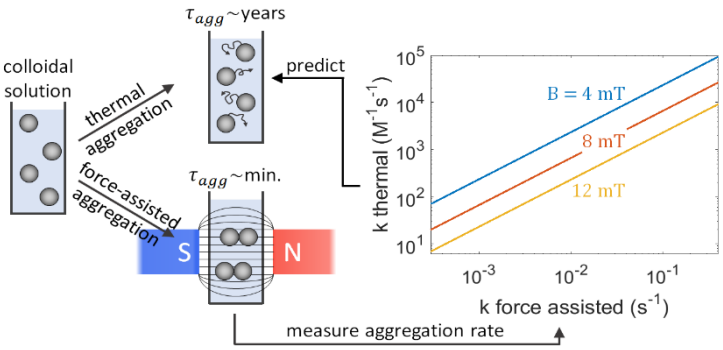

This chapter has been published as: Scheepers, M.R.W.; Romijn, A.R.; van IJzendoorn, L.J.; Prins, M.W.J. Rate of dimer formation in stable colloidal solutions quantified using an attractive interparticle force. *Langmuir*, **2019**, 35, 32, 10533-10541

2.1 Introduction

Colloidal solutions are metastable systems containing particles with a size between the nanoscale and microscale. The particles are made of numerous materials and are found in many applications because of their large surface-to-volume ratio, their versatile mechanical and optical properties, and because they allow a wide range of functionalization strategies. Colloids are used in biomedical applications, e.g. as carriers for drug delivery[1,2], as contrast agents in magnetic resonance imaging[1,3] and as labels to facilitate diagnostic assays[4]. In biophysical research, colloidal particles function as optical or magnetic tweezers for studies on proteins[5] and DNA[6]. Self-assembly[7] and directed-assembly[7,8] of colloidal solutions find applications in for example 3D photonic crystals[9-11]. In these applications inter-particle interactions play an important role. Biomedical applications are hampered by corona-induced particle aggregation[12], causing low efficiencies in drug delivery[1,13] and low sensitivity and limit-of-detection in biosensing[14]. The optical properties of photonic crystals depend on the 2D and 3D particle arrangements, which are determined by the interparticle forces[7,10]. Thus it is crucial to understand and control the interactions between particles, on short as well as long timescales.

In this work we focus on investigating the early stages of particle aggregation, when dimers are formed in a solution that still dominantly consists of monomers. The dimer formation process is important for example in diagnostic agglutination assays. Agglutination assays, also known as aggregation or cluster assays, are used quantify biomolecular concentrations via particle aggregation[15-18]. Clusters of particles are formed in dependence of (bio)chemical reactivity between the particles, and the aggregation is typically measured by turbidimetry[17], nephelometry[18], or dynamic light scattering (DLS)[19]. As colloidal solutions exist both in equilibrium and far-from-equilibrium, the timescale at which aggregation occurs can vary from microseconds or less, up to many years. Advances in the synthesis of antifouling coatings are leading to colloidal particles that are stable also in complex solutions[12].

Cluster assays based on the thermal diffusion of particles are slow and can therefore operate only with relatively unstable colloidal systems, i.e. particles with a high chemical reactivity. Baudry et al.[20] demonstrated that the assay time can be significantly reduced using superparamagnetic particles in combination with external magnetic fields. Particles become magnetized in the external field and self-organize into chains by attractive magnetic dipole interactions, which accelerates cluster formation.

Here we study how attractive magnetic forces can be used to quantify the early stages of aggregation, in colloidal systems with a relatively low chemical reactivity.

We use the optomagnetic cluster (OMC) experiment of Ranzoni et al.[14] to measure the amount of dimers in solution. In this method, a rotating magnetic field is applied that rotates clusters of particles, causing an oscillating optical signal due to their orientation dependent scattering cross-section. Single particles, due to their spherical shape, do not contribute to the oscillating scattering intensity, making this optomagnetic method suited to detect low concentrations of dimers against a background of monomers. We describe in this chapter how time-dependent data in the OMC experiment can be used to quantify dimer formation rates in colloidal systems with low chemical reactivity. The experimental approach is corroborated by calculations, showing how experimental parameters can be tuned to obtain control of the aggregation kinetics. Subsequently nonspecific particle aggregation rates are measured in varying electrostatic conditions (pH and ionic strength). Finally, the measured rates are extrapolated to aggregation rates without applied attractive forces, in order to determine the chemical aggregation rates of colloidal solutions with low reactivity.

2.2 Materials and methods

2.2.1 Materials

Carboxylated superparamagnetic Masterbeads were purchased from Ademtech (nominal size 0.5 μm, hydrodynamic diameter from DLS is 528 nm with coefficient of variation 25%). Buffer components: phosphate buffered saline (PBS) tablets, citric acid anhydrous, sodium citrate dihidrate, potassium chloride, Pluronic F-127 and Protein LoBind Eppendorf tubes were all obtained from Sigma Aldrich. Borosilicate glass 3.3 cuvettes with square cross-section, inner dimensions of 1.00±0.05 mm, outer dimensions of 1.23±0.05 mm and a length of 20±1 mm were obtained from Hilgenberg.

2.2.2 pH buffer preparation

Buffers with different pH values were prepared using two citrate salts: citric acid anhydrous (HOC(COOH)(CH_2-COOH)) and sodium citrate dihidrate (HOC(COONa)(CH_2-COONa)·$2H_2O$). The buffer strength was kept at 10 mM in all experiments of this chapter, and the molar ratio of the two salts determined the pH of the buffer. In several experiments potassium chloride (KCl) was added to increase the salt concentration of the buffer solution without affecting the pH. After adding all salts to deionized water, the pH of the buffer was measured with a WTW Inolab pH 720 pH probe (precision of 0.1). The exact composition of the used buffers can be found in Table S2.1 in the Supporting Information.

2.2.3 Zeta potential measurement

The average surface charge of the particles was quantified by measuring the zeta potential of the particles with a Malvern Zetasizer Nano ZS. Particle were diluted to 0.1 mg/mL, and triplicate measurements were performed using either citric acid buffers of varying pH (10 mM citric acid buffer, ionic strength 150 mM) or using deionized water to disperse the particles. At the high salt concentrations, the operating voltage of the zetasizer was limited to max. 10 V in order to prevent electrolysis at the electrodes, which decreases the signal-to-noise ratio in the measurements. The uncertainty in the zeta potential measurement is relatively large because of the low absolute value of the zeta potential of the measured particles ($\Delta\zeta \approx 2\text{mV}$).

2.2.4 Experimental setup

The OMC experiment is schematically depicted in Fig. S2.2 of the Supporting Information. In the middle of the setup a square glass cuvette containing a particle solution is located. Around the cuvette four electromagnets are positioned in a cross arrangement. With this quadrupole setup in-plane rotating magnetic fields are created by flowing a sinusoidal current through each of the four coils with a phase lag of 90° between neighboring coils, using a homemade LabVIEW program. A 660 nm laser (Single Mode Hitachi HL6545MG laser, Thorlabs) is focused into a square glass cuvette containing the particle solution by a positive lens (AC254-150-A-ML f=150.0 mm lens, Thorlabs). The light scattered by the rotating particles (monomers, dimers, trimers, etc.) is collected at an angle of 90° with respect to the laser beam. A positive lens (AC254-075-A-ML f=75.0 mm lens, Thorlabs) focusses the scattered light onto a photodetector (PDA36A-EC Si amplified detector, Thorlabs) which is read out by the same LabVIEW program. MATLAB analysis software has been developed to further analyze the scattering signals.

2.2.5 Mie scattering simulation

Mie scattering simulations were performed on two- and three-particle clusters, using the MSTM v. 3.2 code developed by Mackowsky[21]. The simulations were performed using a monochromatic 660 nm light source with s-polarization, as used in the experiments. The particles were simulated as smooth spheres with a diameter that is normally distributed around an average of 500 nm, with a coefficient of variation (CV) equal to 25%. The distance between the particles was kept at 10 nm. The refractive index of the particles was calculated according to equation 1 from Vliembergen et al.[22] giving a value of 1.7±0.1.

2.3 The optomagnetic cluster experiment (OMC)

Fig. 2.1a sketches the process of dimer formation without and with an attractive interparticle force. In both cases the clustering of particles is a multistep process, containing a transport step that leads to an encounter complex, and subsequently a chemical aggregation step in which a chemical bond is formed between the particles[23]. In this chapter we study the formation of nonspecific bonds, i.e. interparticle bonds due to general physicochemical interactions such as van der Waals interactions or hydrophobic interactions between particle surfaces (so not bonds due to selective biomolecular interactions). We assume that the particles are homogeneously reactive and therefore neglect rotational alignment[13,24,25].

For stable colloidal systems without attractive interparticle forces, the thermal aggregation rate k_{agg}^{th} is much smaller than the separation rate k_{sep}^{th}. The effective rate of dimer formation $k_{agg}^{th,eff}$ can be written in terms of the encounter, separation and aggregation rates:

$$k_{agg}^{th,eff} = \frac{k_{enc}^{th} \cdot k_{agg}^{th}}{k_{sep}^{th} + k_{agg}^{th}} \cong \frac{k_{enc}^{th} \cdot k_{agg}^{th}}{k_{sep}^{th}} \qquad \text{for} \quad k_{agg}^{th} \ll k_{sep}^{th} \tag{2.1}$$

The process of thermal dimer formation can take months or longer for stable colloidal solutions. To bring the aggregation process into timescales that are more suited for measurements, we propose to apply an attractive interparticle force, in the form of a dipolar magnetic force resulting from magnetic particles and an applied magnetic field. The magnetic dipole-dipole interaction accelerates the primary encounter step k_{enc}^{mag} to make it no longer diffusion limited[26]. Additionally it prevents the separation of magnetic dimers, that is, $k_{sep}^{mag} = 0$. In this way we will demonstrate that the OMC experiment can be used to quantify the rate of chemical dimer formation in the presence of an external magnetic field, that is, parameter k_{agg}^{mag}.

To quantify the number of dimers formed over time, we use the optomagnetic readout principle developed by Ranzoni et al.[14] that allows to measure dimer concentrations in the picomolar range. Briefly, a laser is focused inside a cuvette containing a solution of superparamagnetic particles, which is situated in the center of a quadrupole electromagnet (Fig. 2.1b). The scattered light is collected by a photodiode at an angle of 90° w.r.t. the incoming laser beam. To distinguish clusters from single particles, an in-plane rotating magnetic field is applied. The scattered light of a rotating single particle is constant as a function of time, whereas the scattered light from a rotating cluster yields an oscillating signal as a function of time due to its asymmetry. Fig. S2.3a shows the measured photodiode signal as a function of time. When the magnetic field is off, a baseline signal is measured due to scattering

of both single particles and clusters. When the rotating field is turned on, an oscillating signal is measured on top of the baseline. As each rotating cluster contributes to the amplitude of the oscillating signal, this amplitude represents a measure of the cluster concentration. To extract the amplitude of the oscillation, the Fourier spectrum of each pulse train is analyzed (Fig. S2.3b). The peak in the Fourier spectrum at twice the field rotation frequency (A2f) is used as a measure of the cluster concentration. Fig. S2.3c shows a calibration measurement in which a stock solution of Ademtech particles was titrated into several dilutions and the |A2f| peak was measured. The stock solution consists almost completely of single particles, with only a few dimers being present as verified by microscopy, see Fig. S2.3d (one dimer per 12-15 monomers). The linear relation between dimer concentration and mean 2f amplitude proves that the dimer concentration can sensitively be quantified with the OMC experiment, without the interference of magnetic cluster formation, due to the application of sufficiently long field-free time intervals.

In order to quantify particle aggregation rates, we developed a four step protocol shown in Fig. 2.1c. During the first step, the initial cluster concentration is measured using a pulsed rotating magnetic field with a short on-time (t_{on}=0.2s) and a long off-time (t_{off}=10s). The long off-time is used to allow cluster formation relaxation during the measurement and avoid build-up of magnetic clusters. During the second step a rotating field is turned on continuously. This causes the particles to form magnetic clusters that rotate with the field and causes the |A2f| signal to increase linearly in time. This step aims to create magnetic clusters and keep the particles in close proximity for a certain interaction time. During this interaction time a fraction of the magnetic clusters will form a nonspecific non-covalent chemical bond and thus become a chemical cluster. During the third step, the magnetic field is turned off. This functions as a waiting time, so that all free particles can diffuse and redistribute homogeneously throughout the solution. Finally, in step four, the resulting chemical cluster concentration is measured, using the same protocol as described for step one.

During the actuation time t_{act}, more and more magnetic dimers are formed. This means that the interaction time is not the same for all magnetic dimers and that the average interaction time of dimers is smaller than t_{act}. The fact that the number of magnetic dimers increases linearly over time during the actuation phase (see Fig. 2.1c) makes that the average interaction time of magnetic dimers is equal to $\frac{1}{2}t_{act}$.

During the interaction time the particles in a dimer are in close proximity, i.e. a nanometer scale surface-to-surface distance, which enhances the possibility to form a nonspecific chemical bond. Of all magnetic dimers formed ($N_{mag,tot}$), a fraction reacts to become a chemical dimer. The number of chemical dimers ΔN_{chem} is quantified

after the waiting time t_{wait}. Finally the aggregation rate k_{agg}^{mag} is calculated by equation 2.2.

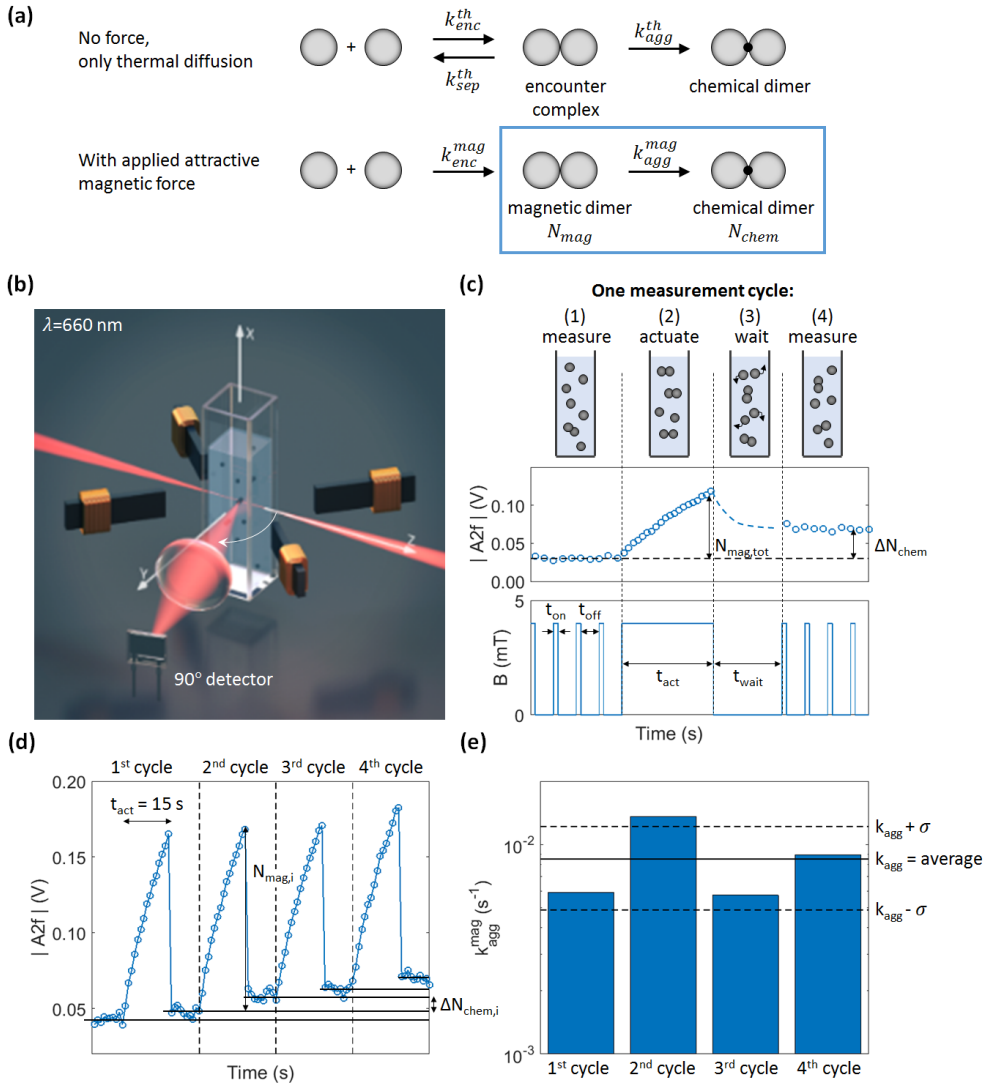

Fig. 2.1 Rate of dimer formation quantified in an optomagnetic cluster experiment. (a) Reaction scheme for particle dimer formation in the absence and presence of an attractive interparticle force. **(b)** Sketch of the experimental setup showing a cuvette filled with a particle solution situated in the centre of a quadrupole electromagnet. A laser (λ=660nm) is focused inside the cuvette and the light scattered by the particles is collected at a 90° angle w.r.t. the incoming laser beam. **(c)** Complete measurement protocol: 1. Initial dimer concentration is measured with short magnetic pulses. 2. Rotating magnetic field is turned on during an actuation time t_{act} to induce the formation of magnetic dimers that can react to become a chemical dimer. 3. Waiting time to let the particle solution redistribute homogeneously. 4. Final chemical dimer concentration is measured. **(d)** Multistep measurement showing an increase in the amount of chemical dimers after each measurement cycle. **(e)** Magnetic aggregation rate for each measurement cycle,

determined by equation 2.2. Mean and standard deviation of the magnetic aggregation rate are indicated by the horizontal lines.

$$k_{agg}^{mag} = \frac{\Delta N_{chem}/N_{mag,tot}}{\frac{1}{2}t_{act}} \tag{2.2}$$

To increase statistics, multiple actuation cycles are applied (see Fig. 2.1d). The aggregation rate is quantified for every cycle and the average and standard deviation are calculated (see Fig. 2.1e).

2.4 Tuning experimental settings

In step one and four of the OMC experiment (Fig. 2.1c), measurement pulses are used to quantify the number of chemical dimers in the solution ΔN_{chem}. For an accurate quantification, the pulse should not induce additional magnetic or chemical dimers. For this purpose several experimental parameters have been optimized: field on-time and off-time, field amplitude, field frequency and particle concentration.

The influence of the field on-time on the measured number of dimers was investigated by performing fifty measurement pulses for a varying field on-time and a constant intermittent off-time of 10s. Fig. 2.2a shows the measured |A2f| signal normalized to the |A2f| of the first measurement pulse. For on-times of 1s or more the |A2f| signal significantly increases with the number of measurement pulses, whereas for an on-time of 0.2s the measured value does not increase as a function of time. The fluctuations in the measured |A2f| are caused by dimers diffusing in and out of the focus volume of the laser, changing the local dimer concentration. For the chosen experimental settings ($B = 4$mT, $f = 5$Hz and $[particle] = 1.0$pM) the on-time should be 0.2s to prevent the formation of additional dimers during an individual measurement pulse.

In the previous experiment the off-time was chosen to be long enough to avoid any influence on the measurement, however decreasing the off-time can also lead to magnetic aggregation because particles may not have enough time to redisperse in between measurement pulses. Fig. 2.2b shows the normalized |A2f| signal for measurement pulses with an on-time of 0.2s and a varying off-time. For off-times longer than 5s the chemical dimers can be measured without inducing additional magnetic dimers.

Increasing the magnetic field amplitude accelerates the kinetics of magnetic dimer formation by quadratically increasing the attractive dipole-dipole force (Fig. S2.4a). The field rotation frequency does not have a significant influence on the measured |A2f|, as long as the frequency is below the break down frequency for dimers[14]

$f_{bd} \approx 7$ Hz at $B = 4$mT (Fig. S2.4b). In the remainder of this chapter the following experimental parameters are used for the measurement pulses: $t_{on} = 0.2$s, $t_{off} = 10$s, $B = 4$mT, $f = 5$Hz and $[particle] = 1$pM.

During step two of the OMC experiment the magnetic field is turned on continuously during the actuation time t_{act}. Initially, the sample contains mainly monomers and a few chemical dimers, as has been observed by microscopy (1 dimer per 12-15 monomers). During actuation the number of dimers increases and eventually also larger clusters (trimers, tetramers, etc.) are formed. Fig. 2.2c shows the scaled |A2f| signal for actuation pulses of 90s for several magnetic field amplitudes. Initially, the signal increases with time indicating magnetic cluster formation. However, at some point the signal starts to level off, has a maximum, and eventually starts to decrease. For increasing magnetic field amplitude the kinetics of magnetic dimer formation speeds up, indicated by the maximum shifting to shorter times. Fig. 2.2d shows the dependence of the |A2f| for several particle concentrations during the actuation pulse. Higher particle concentrations do not only increase the total number of dimers that can be created, but they also accelerate the formation of magnetic dimers. The field rotation frequency has only minor influence on the dimer formation kinetics (Fig. S2.4c).

Fig. 2.2e shows the evolution of the normalized |A2f| signal as a function of time for an actuation time of 90 seconds. The scattered light is measured simultaneously at an angle of 16° and 90° w.r.t. the incoming laser. The scattering intensity at 90° reaches a maximum first while the scattering intensity at 16° still increases. This seems to indicate a higher sensitivity for larger clusters at a scattering angle of 16°.

To interpret the experimental results of Fig. 2.2e and to get an upper limit of the percentage of two-particle clusters over time, we performed simulations as reported in Fig. 2.2f. The simulations are based on two aspects, namely the cluster growth dynamics and the scattering cross-sections of the clusters. For each cluster size ($i =$ dimer, trimer, tetramer, etc.) the number of clusters is calculated as a function of time $N_i(t)$ and also the corresponding complex $2f$ scattering cross-section at the detector angle α, $2f_{i,\alpha}$. The total complex $2f$ signal is the product of the number of clusters multiplied by the complex scattering cross-section summed over all cluster sizes. The |A2f| signal is the absolute value of this complex number:

$$|A2f|_{90} = \left|N_d \cdot 2f_{d,90} + N_{tr} \cdot 2f_{tr,90} + N_{te} \cdot 2f_{te,90} + \cdots\right| \tag{2.3}$$

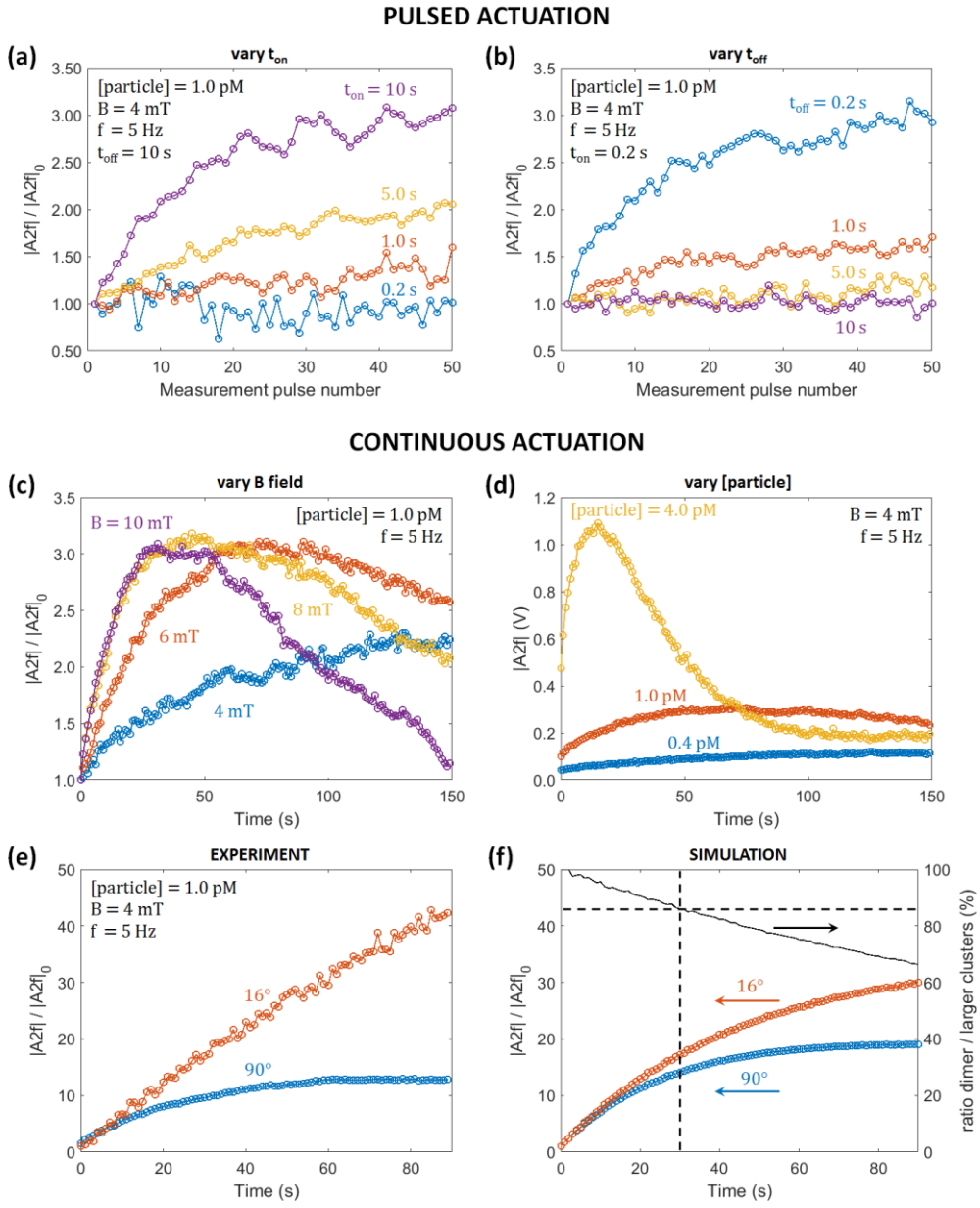

Fig. 2.2 Study of experimental parameters. Amplitude of the 2f Fourier peak of 50 measurement pulses scaled to the first measurement, showing that **(a)** on-times longer than 0.2s lead to magnetic dimer formation over time and **(b)** off-times shorter than 5s also cause magnetic dimer formation. **(c)** Scaled |A2f| signal for a 150s actuation pulse for different magnetic field amplitudes, showing faster particle aggregation kinetics for higher field amplitudes. **(d)** Scaled |A2f| signal for a 150s actuation pulse for different particle concentrations, showing an increasing absolute number of clusters and faster aggregation kinetics for higher particle concentrations. **(e)** Measured scaled |A2f| signal for a continuous actuation pulse of 90s measured at the 16° and 90° detector angle. **(f)** Estimated upper limit of the scaled |A2f| signal for the 16° and 90° detector angle with the corresponding percentage of clusters that is a dimer. The 16° and 90° Fourier amplitudes show similar trends as the measured curves of Fig. 2.2e, but they do not serve the

purpose to reproduce the measured curves. The dashed line indicates the maximum actuation time that is used.

The cluster growth dynamics is modelled using the Smoluchowski population balance equations describing the reaction of two monomers (m) becoming a dimer (d), a monomer and a dimer becoming a trimer (tr), and so on[27]. For tetramers (te) for example, there are two production terms and two loss terms when cluster sizes up to hexamers (h) are included, see equations 2.4-2.7. For each cluster size the population balance equations yield a differential equation for the rate of cluster formation, as shown for tetramers in equation 2.8. Here k_{ij} is the j^{th} formation rate of an i-particle cluster and N_i is the number of i-particle clusters. By numerically solving the system of coupled differential equations up to and including hexamers, the cluster distribution was calculated as a function of time. Note that the initial cluster distribution and all of the reaction rates need to be predefined. The initial cluster distribution was estimated from microscopy images of the stock solution, but is difficult to accurately determine. The dimer reaction rate k_d is calculated from the initial slope of the actuation curve, and an upper limit for the reaction rates k_{ij} (> dimer) follows from k_d and the number of particles in the reacting clusters (described in full detail in section S2.5 of the Supporting Information).

$$m + tr \rightarrow te \quad (rate\ k_{te1}) \tag{2.4}$$

$$d + d \rightarrow te \quad (rate\ k_{te2}) \tag{2.5}$$

$$te + m \rightarrow p \quad (rate\ k_{p1}) \tag{2.6}$$

$$te + d \rightarrow h \quad (rate\ k_{h1}) \tag{2.7}$$

$$\frac{dN_{te}(t)}{dt} = k_{te1}N_m(t)N_{tr}(t) + k_{te2}N_d(t)N_d(t) - k_{p1}N_m(t)N_{te}(t) - k_{\mathrm{h1}}N_d(t)N_{te}(t) \tag{2.8}$$

In order to find the complex scattering cross-section of the clusters, Mie scattering simulations have been performed[14]. The scattering intensity of clusters with various numbers of particles, particle sizes, interparticle distances and orientations, has been calculated at the detector angles of 16° and 90°. The oscillating scattering signal of a dimer, trimer and tetramer are shown in the Supporting Information (Fig. S2.6). The calculations show that due to the size dispersion of the particles (CV ~25%) the characteristic peaks of dimers, trimers and tetramers are broadened. Taking the Fourier transform of the simulated scattering signals yields the complex scattering cross-section for dimers, trimers and tetramers. Fig. S2.5b shows that the amplitude of

the complex scattering cross-sections of larger clusters increases more for detection at 16° than for detection at 90°. Also the phases of the complex scattering cross-sections are different. This explains why the total scattering signal (Fig. 2.2e) increases sub-linearly for both 16° and 90°, and why the sub-linearity is stronger for the 90° signal. A description of the scattering simulations and the comparison with the measurements is given in Section S2.6 of the Supporting Information.

Using the complex scattering cross-sections obtained from the Mie scattering simulations and the calculated evolution of the cluster distribution as a function of time, the normalized |A2f| signal can be estimated as a function of time for both detector angles, shown in Fig. 2.2f. The calculated time dependence of the |A2f| signals shows similar shape and trends as the measured |A2f| signals, although this calculation depends on many input parameters like particle size distribution, refractive index, detector angle, and so forth. The simulated signal shows faster kinetics than the measured signal, especially the 16° signal, which could be caused by overestimating the reaction rates for larger clusters. A full Brownian dynamics simulation of the magnetic clustering process could be a next step, but this lies outside of the scope of the present chapter. Using the simulation data we can estimate the percentage of clusters that is a dimer at each point in time, see Fig. 2.2f. This shows that for actuation times of less than 30s, at least 85% of clusters is a dimer. This result justifies the procedure to derive the rate constant of dimer formation from the measurement as described in equation 2.2.

With the above found experimental settings the total experiment time is 5-15 minutes dependent on the amount of actuation cycles that is performed. As such, gravitational effects can be neglected in the OMC experiment. A full calculation of the typical time scale of sedimentation is given in Section S2.7 of the Supporting Information.

2.5 Particle aggregation as a function of pH and ionic strength

In order to test the validity of the OMC experiment for determining rate constants, we measured the influence of electrostatic interactions on the dimer formation rate k_{agg}^{mag}. The electrostatic interaction between particles was varied in two ways: firstly by changing the surface charge of the particles via the pH of the solution, and secondly by changing the Debye length via the ionic strength of the solution, see Fig. 2.3.

To control the particle surface charge density, the pH of the citrate buffer was varied between 4 and 7 (see Materials and methods section). Carboxyl functionalized

superparamagnetic Ademtech Masterbeads were used with a nominal diameter of 500 nm. The effect of pH on particle surface charge was quantified by zeta potential measurements shown in Fig. 2.3a (right y-axis). Increasing the pH from pH 4 towards pH 7 leads to a more-negative zeta potential, as a higher fraction of carboxyl groups is deprotonated. The absolute value of the zeta potential decreases at low pH which implies that the isoelectric point of the particles is approached. The aggregation rate of the Ademtech Masterbeads was measured in each of these solutions. The left y-axis in Fig. 2.3a shows the aggregation rate (averaged over four cycles) as a function of the pH of the citric acid solution. A clear decrease in the aggregation rate of more than an order of magnitude was measured for increasing pH (more negative zeta potentials). This demonstrates that electrostatic charge is an important factor for particle aggregation kinetics and shows the ability to quantify the aggregation kinetics with the OMC experiment.

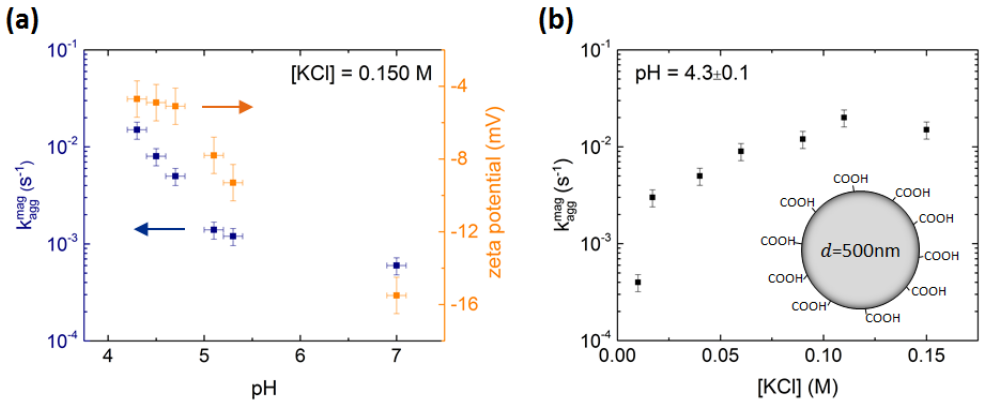

Fig. 2.3 Magnetic aggregation rate of COOH functionalized particles with 500nm diameter, as a function of pH and ionic strength. (a) Measured dimer formation rate as a function of the pH of the citrate buffer with a [KCl] of 0.150 M. Right y-axis shows zeta potential measurements. **(b)** Measured aggregation rate as a function of the [KCl] in the citric acid buffer of pH 4.3.

The influence of ionic strength on the particle aggregation rate was measured by varying the amount of KCl added to a citrate buffer at pH 4.3. Fig. 2.3b shows that the aggregation rate increases by more than an order of magnitude with increasing ionic strength, underlining the importance of electrostatic interactions for the aggregation rate. In summary, the measured trends of the particle aggregation rate as a function of zeta potential and ionic strength are consistent and provide proof of concept for the aggregation experiment. A quantitative interpretation of the data will be addressed in the next section.

2.6 Translation to aggregation rates in absence of magnetic attraction

Fig. 2.4a sketches the potential energy landscape of a dimer as a function of the interparticle distance x, in the presence of an attractive interparticle force. At large interparticle distances ($x \gg d$) the magnetic dipole-dipole attraction is very weak and the potential energy is close to zero (not included in the graph). For somewhat shorter interparticle distance ($x > d$) the particles attract each other, which causes the formation of magnetic dimers. Once a magnetic dimer is formed, the two particles are in close proximity and a chemical bond can be formed. In order for the particles to chemically react, the energy barrier U_b needs to be overcome. The presence of the attractive interparticle force lowers the energy barrier compared to the situation of particles free in solution. The aggregation rate that is measured with the optomagnetic cluster experiment, k_{agg}^{mag}, describes the average rate at which a magnetic dimer crosses the energy barrier to become a chemical dimer, for a certain magnetic field amplitude.

The energy barrier U_b depends on magnetic field strength, but is dominated by steric, electrostatic and van der Waals interactions. A complete calculation of the potential energy landscape is outside of the scope of this chapter. Here, we assume that the magnetic interaction gives a weak reduction of the energy barrier, so that the rate of dimer formation k_{agg}^{mag} equals the thermal aggregation rate k_{agg}^{th} with a field-dependent correction factor $\alpha(B)$ (with $\alpha(B) < 1$). Using equation 2.1 the thermal dimer formation rate for particles free in solution ($k_{agg}^{th,eff}$) can now be expressed as:

$$k_{agg}^{th,eff} = \frac{k_{enc}^{th} \cdot k_{agg}^{th}}{k_{sep}^{th}} = \frac{k_{enc}^{th} \cdot \alpha(B) \cdot k_{agg}^{mag}(B)}{k_{sep}^{th}} \tag{2.9}$$

If k_{agg}^{mag} is measured in the OMC experiment as a function of the applied magnetic field, then extrapolation to zero field (where $\alpha(B) = 1$) provides a convenient way to estimate k_{agg}^{th}, as will be shown later. This leaves us with the need to estimate the thermal encounter rate k_{enc}^{th} and the thermal separation rate k_{sep}^{th}.

In absence of an attractive interparticle force, particles are free in solution and move solely due to Brownian motion. The average encounter rate k_{enc}^{th} of particles of radius R in a solution with viscosity η can be calculated using the diffusion limited rate equation[28].

$$k_{enc}^{th} = \frac{4k_BT}{3\eta} \tag{2.10}$$

The thermal encounter rate for particles with a diameter of 500 nm (as used in our experiments) in an aqueous solution with $\eta = 1\,\mathrm{mPa \cdot s}$ is $5.5 \cdot 10^{-18}\,\mathrm{m^3 s^{-1}}$, or $3 \cdot 10^{9}\,\mathrm{M^{-1} s^{-1}}$.

The separation rate k_{sep}^{th} describes the typical rate at which two particles in an encounter complex diffuse away from each other. In order to find an estimate for k_{sep}^{th} an interparticle distance needs to be defined at which an encounter complex will be considered as two separate particles (Fig. 2.1a). At this separation distance the encounter complex can no longer become a chemical dimer. We define the separation distance as the interparticle distance at which the potential energy is less than $k_B T$. The energy landscape for the particles used here is unknown, and will vary for different particles, coatings and solvents. However, Biancaniello et al.[29] and Wang et al.[30] succeeded in measuring the potential energy landscape of two particles inside an optical trap and of a particle near a surface, respectively. Both energy landscapes tail off at an interparticle distance of about 40 nm. The separation rate can now be calculated as the typical time in which a particle diffuses $\Delta x = 40$ nm.

$$k_{sep}^{th} = \frac{k_B T}{\pi \eta R (\Delta x)^2} \tag{2.11}$$

This gives a typical time of 300 µs and thus k_{sep}^{th} is estimated to be $3 \cdot 10^{3}\ \mathrm{s^{-1}}$.

In order to experimentally determine the effect of the magnetic field on the aggregation rate, we measured the aggregation rate of streptavidin coated Ademtech Masterbeads in PBS at different field amplitudes (Fig. 2.4b). The data show a dependence that appears linear on lin-log axes. The fitted magnetic field correction factor $\alpha(B)$ is given by the following expression:

$$\alpha(B) = \exp[-(3.0 \pm 0.8) \cdot 10^{2} \cdot B] \tag{2.12}$$

Combining k_{enc}^{th}, k_{sep}^{th} and $\alpha(B)$ gives an expression for $k_{agg}^{th,eff}$, the effective dimer formation rate of particles free in solution, as a function of k_{agg}^{mag}, the aggregation rate measured with the optomagnetic cluster experiment. The resulting relationship is shown in Fig. 2.4c. For example, a measured $k_{agg}^{mag} = 2 \cdot 10^{-2}\ \mathrm{s^{-1}}$ in the OMC experiment using a magnetic field of 4 mT corresponds to a thermal aggregation rate $k_{agg}^{th,eff} \sim 2 \cdot 10^{4}\ \mathrm{M^{-1} s^{-1}}$. This means that a solution with a particle concentration of 1 pM thermally shows significant aggregation on a timescale of $5 \cdot 10^{7}$ s ~ 2 years. The shelf life of these particle is indeed about a few years, after which severe aggregation is observed. In comparison, in case the particles would immediately aggregate upon a single collision (hit-and-stick behaviour), then the characteristic aggregation time would be drastically shorter, namely about 5 minutes. This example clearly

demonstrates that the OMC experiment is able to quantify aggregation rates in stable colloidal solutions with very low reactivities.

The range of rates that can be measured with the OMC experiment has an upper limit, which is determined by the maximum fraction of magnetic dimers that can react to a chemical dimer during the shortest possible actuation pulse. If all magnetic dimers become a chemical dimer during a mean interaction time of 2 s, it would correspond to $k_{agg,max}^{mag} = 5 \cdot 10^{-1}\,\mathrm{s}^{-1}$. The lowest measurable rate is determined by the standard deviation of the fraction of chemically converted magnetic dimers, and the longest possible actuation pulse. Estimating this fraction to be about 0.02 after an interaction time of 30 s, leads to $k_{agg,min}^{mag} = 5 \cdot 10^{-4}\,\mathrm{s}^{-1}$. Fig. 2.4c shows the corresponding range in $k_{agg}^{th,eff}$ that can be measured. By varying the magnetic field amplitude, aggregation can even be accelerated, extending the measurable range of dimer formation rates from about 10^1 to $10^5\ \mathrm{M}^{-1}\mathrm{s}^{-1}$.

2.7 Conclusion

We described an experiment that allows to quantify the dimer formation rate of submicrometer magnetic particles with low surface reactivity. Dimer concentrations are measured using an optomagnetic detection principle and attractive magnetic forces are used to accelerate chemical aggregation by bringing particles in close proximity. The aggregation rate is determined from the fraction of dimers that chemically aggregates during a certain interaction time.

The magnetic field settings to quantify aggregation rates were extensively studied and tested. The nonspecific aggregation rate of carboxylated 500 nm particles was measured for varying pH and ionic strength of the aqueous buffer. The aggregation rate increases over 2 orders of magnitude when decreasing the absolute zeta potential of the particles (by decreasing the pH of the buffer solution), or when increasing the ionic strength of the solution, in both cases caused by a reduction of the inter-particle electrostatic repulsion.

Aggregation rates measured with the OMC experiment are significantly faster than the aggregation rate of identical particles in absence of a magnetic field. The aggregation rates measured in presence of attractive magnetic forces were extrapolated to chemical aggregation rates in the absence of force, taking into account the thermal encounter and separation rates due to Brownian motion. The rates measured with the OMC experiment translate to thermal dimer formation rates $k_{agg}^{th,eff}$ in the range of $10^1 - 10^5\ \mathrm{M}^{-1}\mathrm{s}^{-1}$. Thus the described methodology makes a range of very low aggregation rates experimentally accessible, for fundamental

studies on colloidal stability as well as optimizations with respect to surface chemistries and performance in complex matrices.

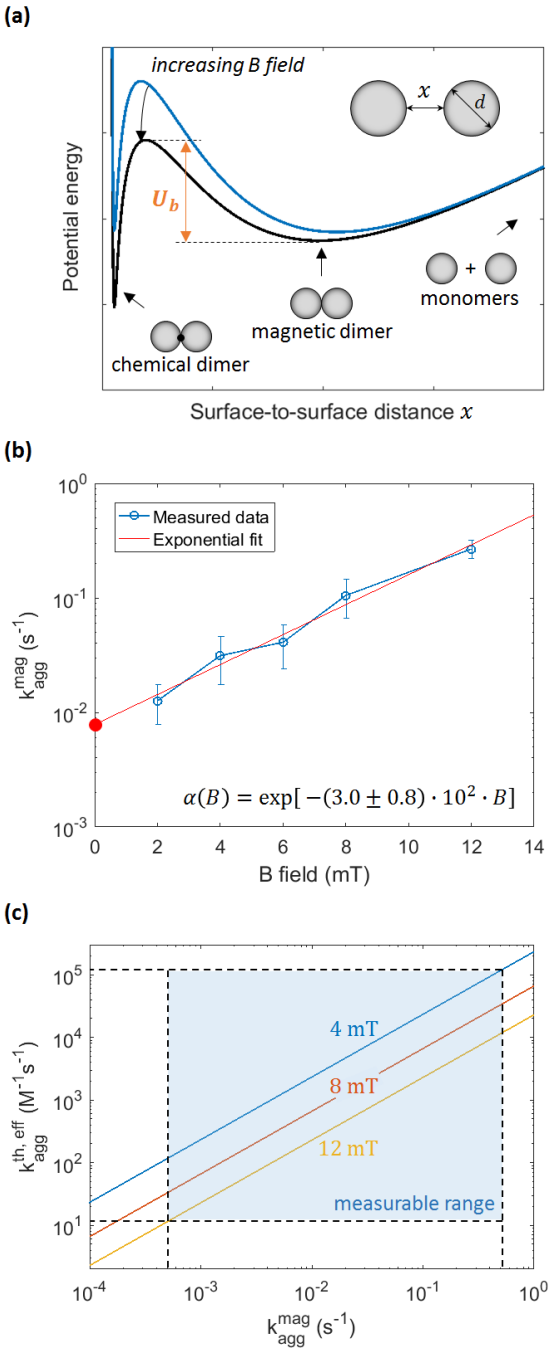

Fig. 2.4 Interpretation of k_{agg} measured with OMC experiment. (a) Schematic representation of the effect of the magnetic dipole-dipole interactions on the potential energy landscape known from DLVO

theory. **(b)** Dependence of the aggregation rate on the magnetic field amplitude. Extrapolating the exponential fit to zero field gives the aggregation rate in absence of the magnetic field. **(c)** Effective thermal dimer formation rate as a function of the measured aggregation in the OMC experiment.

2.8 Supporting Information

S2.1 Citric acid buffer composition

The pH of the buffer solutions is varied by changing the molar ratio between the two buffering citrate salts: citric acid anhydrous and sodium citrate dihydrate. Table S2.1 shows the weight over volume percentages of both salts corresponding a certain pH. Typically the measured pH after buffer preparation shows a deviation from the predicted pH of less than 0.1 pH units.

Table S2.1 Citric acid buffer composition. Molar ratio between citric acid and sodium citrate determines the pH of the resulting solution. Deviation between predicted and measured pH is typically less than 0.1 pH units.

pH	Citric acid, anhydrous (%w/v)	Sodium citrate, dihydrate (%w/v)
4.0	0.1199	0.1105
4.3	0.1056	0.1324
4.5	0.0955	0.1478
4.8	0.0803	0.1712
5.0	0.0703	0.1864
6.0	0.0242	0.2570
7.0	0.0034	0.2888
8.0	0.0004	0.2935

S2.2 Experimental setup of optomagnetic cluster experiment

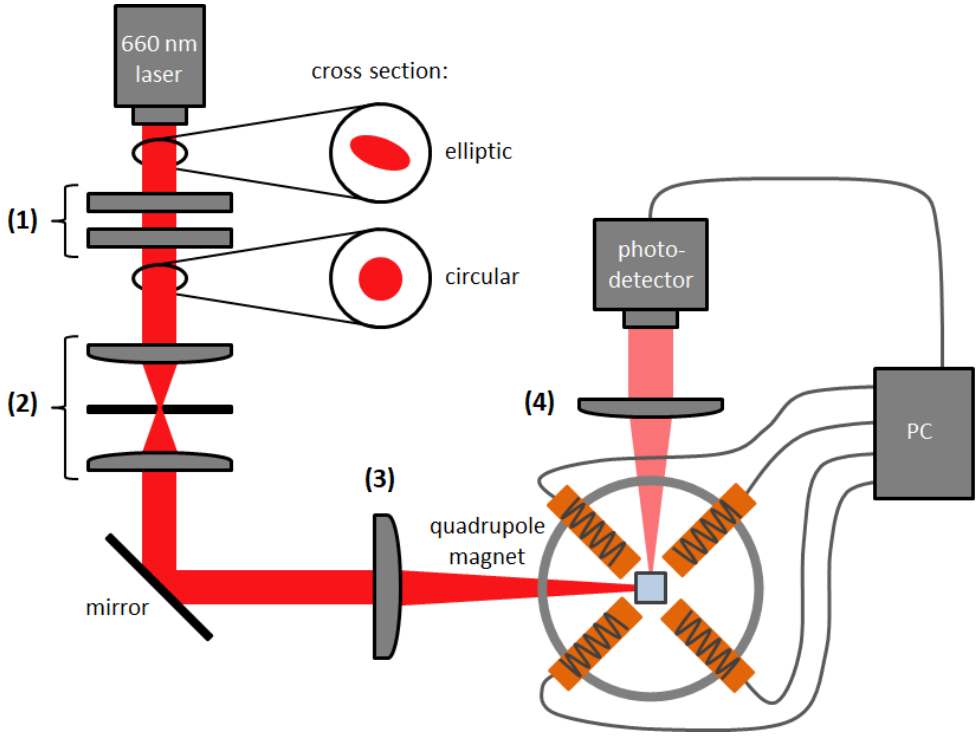

Fig. S2.2 Experimental setup. A 660 nm laser is focused into a glass cuvette which is situated in a quadrupole electromagnet setup which is able to create an in-plane rotating magnetic field. The light scattered by the particles is collected by a positive lens and a photodetector located at a 90° angle w.r.t. the incoming laser beam. Before the laser beam enters the cuvette it passes several optical elements: The laser has an elliptic spot which is modified to a circular spot by the use of two cylindrical lenses (1). To get a collimated bundle, the laser is focused onto a pinhole by a positive lens and collimated by another lens at the other side of the pinhole (2). A positive lens is used to focus the light in the center of the cuvette (3). The light scattered by the particles is collected, at a 90° angle w.r.t. the incoming laser beam, using a photodetector. In front of the photodetector a positive lens is placed to increase the angle over which the scattering signal is collected (4). A PC controls the current through the electromagnets and acquires the data from the photodetector.

S2.3 Optomagnetic cluster readout

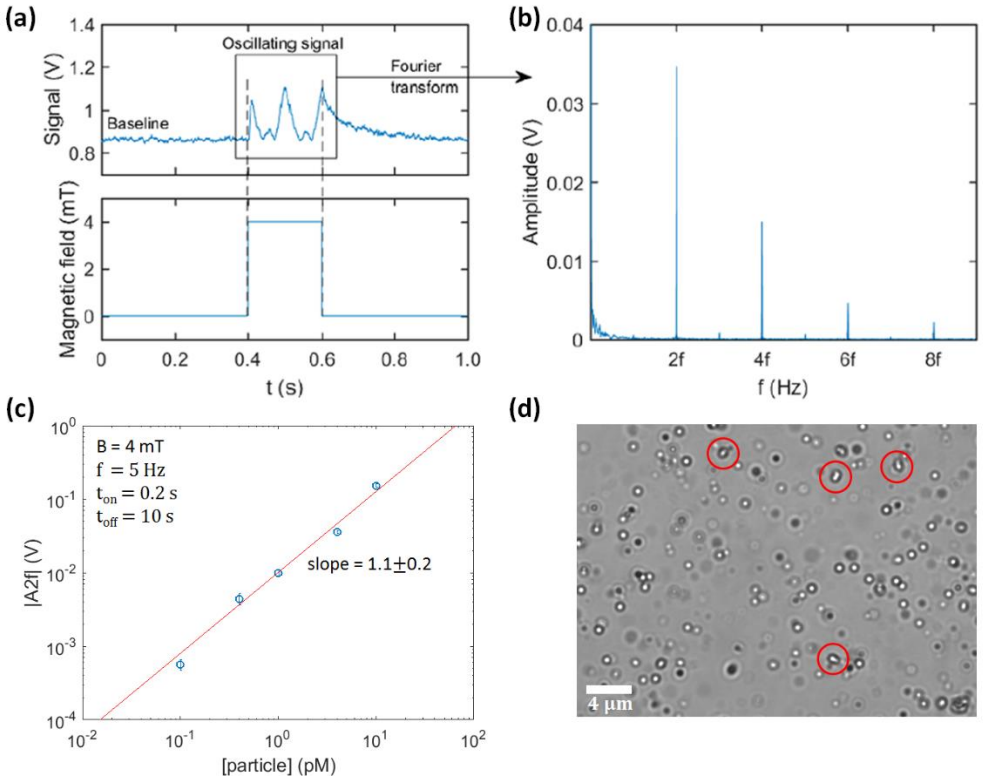

Fig. S2.3 Optomagnetic cluster readout. (a) Measured photodiode signal at a scattering angle of 90°, as a function of time. In the absence of a rotating magnetic field a baseline scattering signal is measured. In the presence of a rotating magnetic field an oscillating scattering signal is measured. **(b)** Fourier spectrum of the oscillating signal of Fig. S2.3a showing peaks at multiples of twice the field rotation frequency. The peak at the 2f frequency, |A2f|, is used as a measure of the cluster concentration. **(c)** Calibration curve showing the average |A2f| signal of 50 measurement pulses as a function of the particle concentration. Since there is a constant fraction of the particle stock solution already in dimer form, the dimer concentration scales with the particle concentration. The fit has a slope of 1.1±0.2 indicating a linear dependence of the measured signal on the dimer concentration. **(d)** Microscopy image of the stock solution of the Ademtech Masterbeads COOH of 500nm diameter, showing a small fraction of dimers. Some examples of dimers are indicated by the red circles.

S2.4 Tuning experimental settings

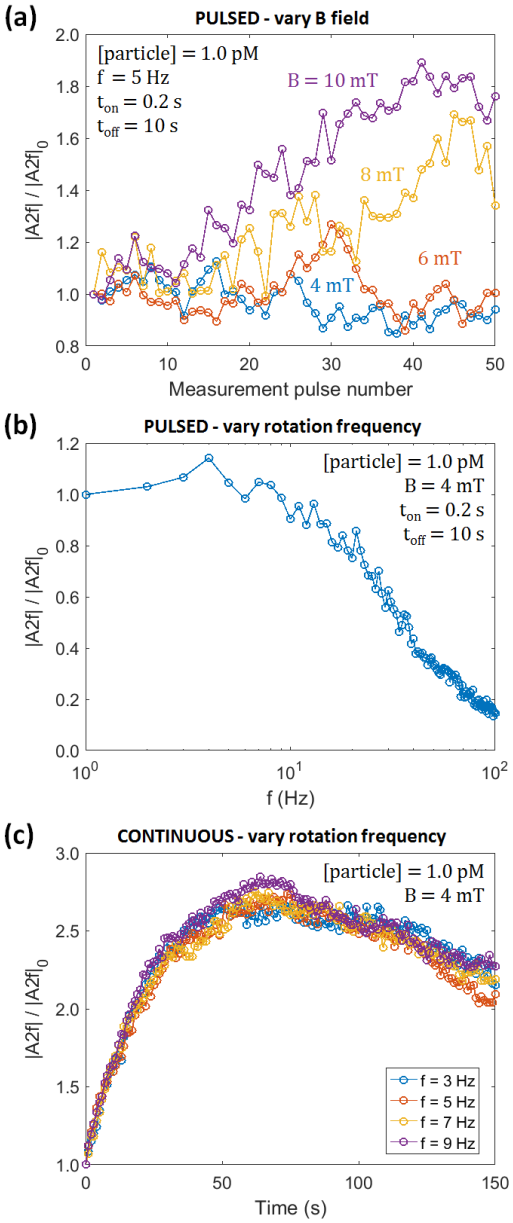

Fig. S2.4 Tuning experimental settings. (a) Normalized |A2f| signal of fifty measurement pulses for varying magnetic field amplitude. For fields larger than 6 mT unwanted magnetic or chemical clusters are formed during the measurement procedure. **(b)** Frequency sweep showing the normalized |A2f| signal as a function of the field rotation frequency. For low frequencies the signal is constant, but for frequencies exceeding the breakdown frequency of $f_{bd} \approx 7\ Hz$ the signal starts to decrease. The frequency $f = 5\ Hz$ is below the breakdown frequency. **(c)** Normalized |A2f| signal during a continuous actuation pulse of 150 s for varying field rotation frequencies around the breakdown frequency. The |A2f| signal does not depend significantly on the rotation frequency in the measured range.

S2.5 Calculated clustering process

Fig. S2.5a shows the measured |A2f| signal over time for the 16° and 90° detector. This signal shows a non-linear increase and subsequently even a decrease. The time until the maximum signal is measured is longer for the 16° detector compared to the 90° detector. This suggests that the detection at 16° is more sensitive to the scattering of larger clusters. From the Mie scattering simulations the complex scattering cross-sections are known. In Fig. S2.5b we show the relative absolute scattering cross-sections of trimers and tetramers w.r.t. dimers.

The distribution of clusters (dimers, trimers, etc.) over time is calculated using the rate equations shown in equation S2.1-S2.9. Although we can only calculate the contributions to the scattering signal of clusters up to tetramers (as the Mie scattering simulation for pentamers costs weeks of calculation), clusters up to hexamers are taken into account to make sure that the loss terms for the monomers, dimers, trimers and tetramers are taken into account.

The dimer reaction rate k_d is calculated from the initial slope of the actuation curve shown in Fig. S2.5a, since initially mainly dimers are formed. This slope, in units of V/s, can be converted to a rate in [dimers]/s using the calibration curve shown in Fig. S2.3c. The higher order reaction rates should be higher because at large inter-cluster-distance ($x \gg d$) the attractive dipole force is larger. An upper limit of the higher order reaction rates is subsequently estimated by multiplying the dimer reaction rate by the product of the number of particles of each reacting cluster. For example, the reaction rate k_{p2} equals $6k_d$.

$$m + m \rightarrow d\ (k_d) \tag{S2.1}$$

$$m + d \rightarrow tr\ (k_{tr}) \tag{S2.2}$$

$$m + tr \rightarrow te\ (k_{te1}) \tag{S2.3}$$

$$d + d \rightarrow te\ (k_{te2}) \tag{S2.4}$$

$$m + te \rightarrow p\ (k_{p1}) \tag{S2.5}$$

$$d + tr \rightarrow p\ (k_{p2}) \tag{S2.6}$$

$$m + p \rightarrow \mathrm{h}\ (k_{\mathrm{h}1}) \tag{S2.7}$$

$$d + te \rightarrow \mathrm{h}\ (k_{\mathrm{h}2}) \tag{S2.8}$$

$$tr + tr \rightarrow \mathrm{h}\ (k_{\mathrm{h}3}) \tag{S2.9}$$

The six coupled differential equations S2.10-S2.15 follow from the nine cluster reactions S2.1- S2.9. This set of equations is numerically solved, giving the cluster distribution as a function of time. Using the distribution of dimers, trimers and tetramers and their corresponding calculated complex 2f components, the scattering signal can be calculated as a function of time, see Fig. S2.5c.

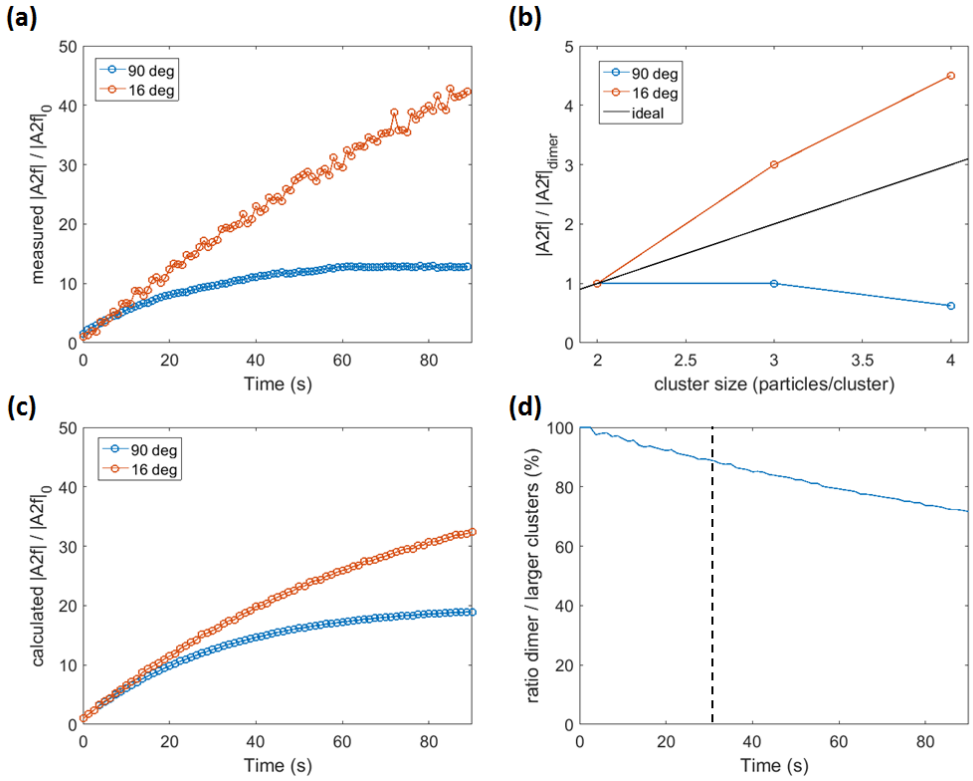

Fig. S2.5 Measured and calculated actuation pulse. (a) Measured normalized |A2f| signal during an actuation pulse. **(b)** Relative scattering cross-sections for dimers, trimers and tetramers obtained from Mie scattering simulations. **(c)** Calculated relative scattering cross-section, showing agreement with the measurement of Fig. S2.4a. **(d)** Calculated percentage of clusters that is a dimer throughout the actuation pulse.

$$\frac{dN_m(t)}{dt} = -2k_d N_m(t)N_m(t) - k_{tr}N_m(t)N_d(t) - k_{te1}N_m(t)N_{tr}(t) - k_{p1}N_m(t)N_{te}(t) - k_{h1}N_m(t)N_p(t) \quad \text{(S2.10)}$$

$$\frac{dN_d(t)}{dt} = +k_d N_m(t)N_m(t) - k_{tr}N_m(t)N_d(t) - 2k_{te2}N_d(t)N_d(t) - N_d(t)N_{tr}(t) - k_{h2}N_d(t)N_{te}(t) \quad \text{(S2.11)}$$

$$\frac{dN_{tr}(t)}{dt} = +k_{tr}N_m(t)N_d(t) - k_{te1}N_m(t)N_{tr}(t) - k_{p2}N_d(t)N_{tr}(t) - 2k_{\mathrm{h3}}N_{tr}(t)N_{tr}(t) \quad \text{(S2.12)}$$

$$\frac{dN_{te}(t)}{dt} = +k_{te1}N_m(t)N_{tr}(t) - k_{te2}N_d(t)N_d(t) - k_{p1}N_m(t)N_{te}(t) - k_{\mathrm{h2}}N_d(t)N_{te}(t) \quad \text{(S2.13)}$$

$$\frac{dN_p(t)}{dt} = +k_{p1}N_m(t)N_{te}(t) + k_{p2}N_d(t)N_{tr}(t) - k_{\mathrm{h1}}N_m(t)N_p(t) \quad \text{(S2.14)}$$

$$\frac{dN_{\mathrm{h}}(t)}{dt} = +k_{\mathrm{h1}}N_m(t)N_p(t) + k_{\mathrm{h2}}N_d(t)N_{te}(t) + k_{\mathrm{h3}}N_{tr}(t)N_{tr}(t) \quad \text{(S2.15)}$$

From the calculated distribution of clusters over time, the fraction of clusters that is a dimer can be calculated. Fig. S2.5d shows that over time the clusters grow, and that for typical actuation times of 10-30s at least 85% of the signal originates from dimers.

S2.6 Scattering signal shape

The shape of the measured scattering signal at a 90° detector angle during a 150s actuation pulse (Fig. S2.6a-b) is compared with the shape of the theoretical scattering signal for dimers, trimers and tetramers, obtained from Mie scattering calculations (Fig. S2.6c-e). The simulated signal is plotted with and without including the size dispersion. The size distribution causes characteristics of the signal to vanish. Both the measured and theoretical signal show two large and two smaller peaks per full rotation of the clusters. The relative height of the smaller peak increases slightly over time, however, due to size dispersion of the particles the characteristics of the dimer, trimer and tetramers signals cannot be identified in the measured signal.

The signals measured with the 16° detector show the appearance of a shoulder on the side of the peak in the scattering signal over time. This shoulder is a characteristic that is only found in the theoretical signals for the trimer and tetramers. Since the shoulder starts to grow between 40-80s it seems that the contribution of dimers to the scattering signal is dominant, at least until 40s.

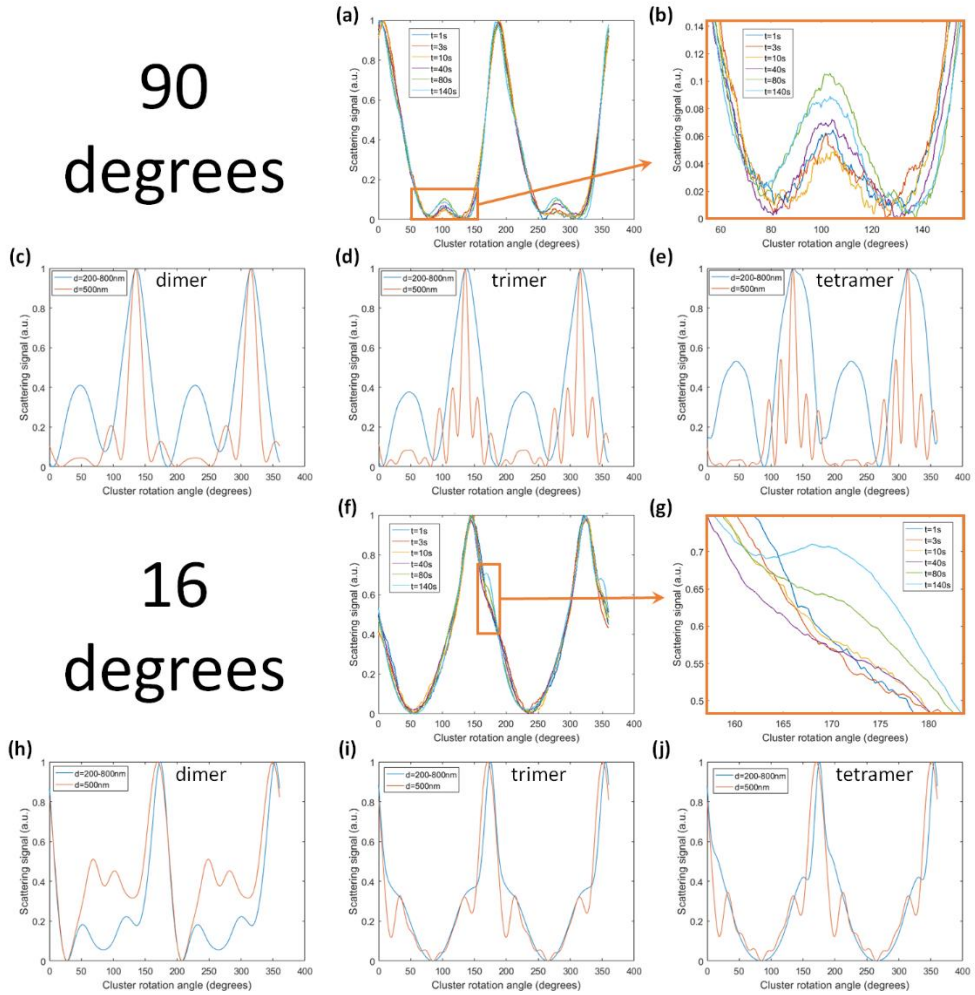

Fig. S2.6 Measured and theoretical signal shapes. (a) Normalized measured scattering signal as a function of the rotation angle of the cluster. **(b)** Zoom in showing the growth of the smaller peak of the scattering signal. Only after 40s the peak starts to increase significantly. **(c)-(e)** Simulated scattering signals for a dimer, a trimer and a tetramer. The signals are simulated for perfectly monodisperse particles and for a normally distributed size between 200 and 800 nm, with an average diameter of 500 nm. **(f)-(j)** same graphs for the 16° detector.

S2.7 Sedimentation during the OMC measurement

In the OMC experiment light scattering on the particles inside the focus volume of the laser is measured. However, the magnetic actuation is performed not only on the particles inside the focus volume, but the complete volume of the cuvette that is located in between the four electromagnets. The height of the electromagnets is 5 mm, creating a homogeneous magnetic field over at least a distance of 3 mm, see Fig. S2.7. For each large or small particle that will sediment out of the focus volume will a new

large of small particle will sediment into the focus volume. Until particles start to enter the focus volume that were not always within the homogeneous magnetic field volume. In other words, the time it takes the large particles to sediment over a distance of 1.5 mm determines after which measurement time sedimentation starts to play a role. The sedimentation velocity for the largest particles in the distribution, estimated radius of 400 nm, is calculated with equation S2.16:

$$v_{sediment} = \frac{2}{9}\frac{(\rho_p - \rho_f)}{\eta} g R^2 = 3.49 \cdot 10^2 \text{ nm/s} \quad \text{(S2.16)}$$

Where

$\rho_p = 2.0 \cdot 10^3 \text{ kg/m}^3$

$\rho_f = 1.0 \cdot 10^3 \text{ kg/m}^3$

$\eta = 1 \cdot 10^{-3} \text{ kg/m} \cdot \text{s}$

$g = 9.81 \text{ m/s}^2$

$R = 400 \cdot 10^{-9} \text{ m}$ (Largest particles in the distribution)

The typical time it takes these large particles to sediment over a distance of 1.5 mm is calculated with equation S2.17:

$$t_{sediment} = \frac{\Delta h}{v_{sediment}} = 1.19 \text{ hour} \quad \text{(S2.17)}$$

Where

$\Delta h = 1.5 \cdot 10^6 \text{ nm}$

$v_{sediment} = 3.49 \cdot 10^2 \text{ nm/s}$

This calculation shows that only after 1.19 hour sedimentation should start to play a role. The typical time of an experiment is 5-15 minutes so sedimentation will not play a role in the OMC experiment.

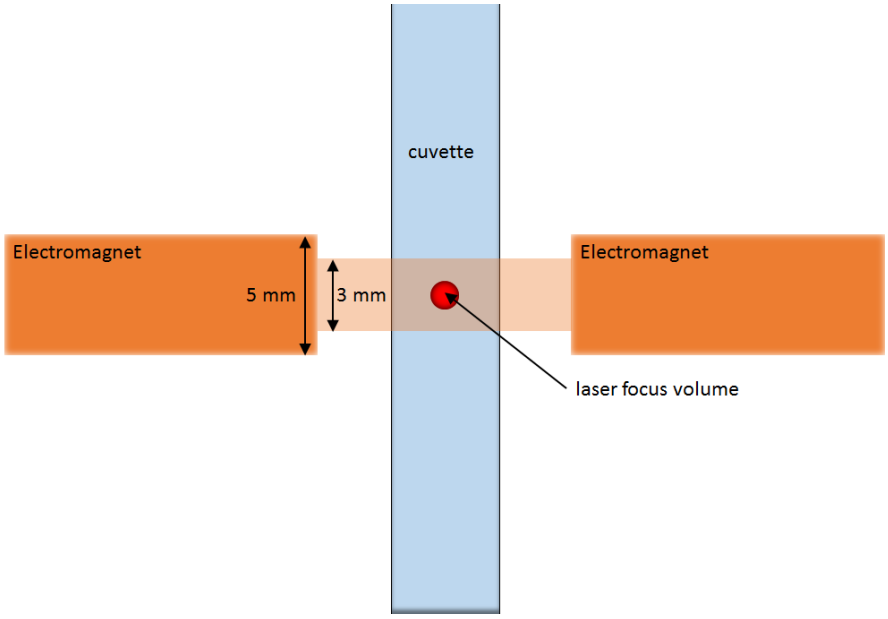

Fig. S2.7 Sedimentation. Schematic section of the experimental setup. The height of the electromagnets is 5 mm, creating a homogeneous magnetic field over a height of at least 3 mm. The distance that particles need to sediment from above the homogeneous field into the laser focus volume is about 1.5 mm.

References

[1] Sun, C.; Lee, J. S. H.; Zhang, M. Magnetic nanoparticles in MR imaging and drug delivery. *Adv. Drug. Del. Rev.* **2008**, 60, 1252-1265

[2] Indira, T. K.; Lakshmi, P. K. Magnetic nanoparticles - A review. *Int. J. of Pharm. Sci. and Nanotech* **2010**, 3 (3), 1035-1042

[3] Vuong, Q.L.; Gillis, P.; Roch, A.; Gossuin, Y. Magnetic resonance relaxation induced by superparamagnetic particles as contrast agents in magnetic resonance imaging: a theoretical review. *WIREs Nanomed. Nanobiotechnol.* **2017**, 9, 1468

[4] Howes, P.D.; Chandrawati, R.; Stevens, M.M. Colloidal nanoparticles as advanced biological sensors. *Science*, **2014**, 346, 6205

[5] van Reenen, A.; Gutiérrez-Mejía, F.; van IJzendoorn, L.J.; Prins, M.W.J. Torsion profiling of proteins using magnetic particles. *Biophys. J.* **2013**, 104, 5, 1073-1080

[6] Lipfert, J.; Kerssemakers, J.W.J.; Jager, T.; Dekker, N.H. Magnetic torque tweezers: measuring torsional stiffness in DNA and RecA-DNA filaments. *Nature Meth.* **2010**, 7, 977-980

[7] Min, Y.; Akbulut, M.; Kristiansen, K.; Golan, Y.; Iraelachvili, J. The role of interparticle and external forces in nanoparticle assembly. *Nat. Mater.* **2008**, 7, 527-538

[8] Shenhar, R.; Norsten, T.B.; Rotello, V.M. Polymer mediated nanoparticle assembly: Structural control and applications. *Adv. Mater.* **2005**, 17, 6, 657-669

[9] Inan, H.; Poyraz, M.; Inci, F.; Lifson, M.A.; Baday, M.; Cunningham, B.T.; Demirci, U. Photonic crystals: emerging biosensors and their promise for point-of-care applications, *Chem. Soc. Rev.* **2017**, 46, 366-388

[10] Subramanian, G.; Manoharan, V.N.; Thorne, J.D.; Pine, D.J. Ordered macroporous materials by colloidal assembly: A possible route to photonic bandgap materials. *Adv. Mater.* **1999**, 11, 15, 1261-1265

[11] Xia, Y.; Gates, B.; Park, S.H. Fabrication of three-dimensional photonic crystals for use in the spectral region from ultraviolet to near-infrared, *J. Light. Technol.* **1999**, 17, 11, 1956-1962

[12] Müller, J.; Bauer, K.N.; Prozeller, D.; Simon, J.; Mailänder, V.; Wurm, F.R.; Winzen, S.; Landfester, K. Coating nanoparticles with tunable surfactants facilitates control over the protein corona. *Biomaterials* **2017**, 115, 1-8

[13] Suk, J. S.; Xu, Q.; Kim, N.; Hanes, J.; Ensign, L. M. PEGylation as a strategy for improving nano-particle based drug and gene delivery. *Adv. Drug Del. Rev.* **2016**, 99, 28-51

[14] Ranzoni, A.; Schleipen, J. J. H. B.; van IJzendoorn, L. J.; Prins, M. W. J. Frequency-selective rotation of two-particle nanoactuators for rapid and sensitive detection of biomolecules. *Nano Lett.* **2011**, 11, 5, 2017-2022

[15] Singer, J.M.; Plotz, C.M. The latex fixation test. *Am. J. Med.*, **1956**, 21, 888-892

[16] Oppenheimer, S.; Odencrantz, J. A quantitative assay for measuring cell agglutination: Agglutination of sea urchin embryo and mouse teratoma cells by concanavalin A. *Exp. Cell. Res.*, **1972**, 73, 2, 475-480

[17] Cohen, R.J.; Benedek, G.B. Immunoassay by light scattering spectroscopy. *Immunochemistry*, **1975**, 12, 4, 349-351

[18] Virella, G.; Waller, M.; Fudenberg, H. Nephelometric method for determination of rheumatoid factor. *J. Immunol. Methods*, **1978**, 22, 3, 247-251

[19] Fischer, K.; Schmidt, M. Pitfalls and novel applications of particle sizing by dynamic light scattering. *Biomaterials* **2016**, 98, 79-91

[20] Baudry, J.; Rouzeau, C.; Goubault, C.; Robic, C.; Cohen-Tannoudji, L.; Koenig, A.; Bertrand, E.; Bibette, J. Acceleration of the recognition rate between grafted ligands and receptors with magnetic forces. *PNAS*, **2006**, 103, 44, 16076-16078

[21] Mackowski, D. A general superposition solution for electromagnetic scattering by multiple spherical domains of optically active media. *J. Quant. Spectrosc. Ra.*, **2014**, 133, 264-270

[22] van Vliembergen, R.W.L.; van IJzendoorn, L.J.; Prins, M.W.J. Distance within colloidal dimers probed by rotation-induced oscillations of scattered light. *Optics Express*, **2016**, 24, 2

[23] van Reenen, A.; de Jong, A.M.; Prins, M.W.J. Accelerated particle-based target capture the role of volume transport and near surface alignment. *J. Phys. Chem. B*, **2013**, 117, 1210-1218

[24] Delcanale, P.; Miret-Ontiveros, B.; Arista-Romero, M.; Pujals, S.; Albertazzi, L. Nanoscale mapping functional sites on nanoparticles by points accumulation for imaging in nanoscale topography (PAINT). *ACS Nano*, **2018**, 12, 7629-7637

[25] Jayaraman, A. Polymer grafted nanoparticles: Effect of chemical and physical heterogeneity in polymer grafts on particle assembly and dispersion. *Polymer Physics*, **2013**, 51 524-534

[26] Reynolds, C.P.; Klop, K.E.; Lavergne, F.A.; Morrow, S.M. Deterministic aggregation kinetics of superparamagnetic colloidal particles. *J. Chem. Phys.*, **2015**, 143, 214903

[27] Smoluchowski, M. Drei vorträge über diffusion Brownische molekularbewegung und koagulation von kolloidteilchen. *Physik. Zeitschrift*, **1916**, 2, 1, 530-594

[28] Nekrasov, V.M.; Polshchitsin, A.A.; Yurkin, M.A.; Yakovleva, G.E.; Meltsev, V.P.; Chernyshev, A.V. Brownian aggregation rate of colloidal particles with several active sites. *J. Chem. Phys.*, **2014**, 141, 064309

[29] Biancaniello, P.L.; Crocker, J.C. Line optical tweezers instrument for measuring nanoscale interactions and kinetics. *Rev. Sci. Instrum.*, **2006**, 77, 113702

[30] Wang, Z.; He, C.; Gong, X.; Wang, J.; Ngai, T. Measuring the surface-surface interactions induced by serum proteins in a physiological environment. *Langmuir*, **2016**, 32, 12129-12136

Chapter 3

Single-dimer formation rate reveals heterogeneous particle surface reactivity

Biofunctionalized micro- and nanoparticles are important for a wide range of applications, but methodologies to measure, modulate, and model interactions between individual particles are scarce. Here, we describe a technique to measure the aggregation rate of two particles to a single dimer, by recording the trajectory that a particle follows on the surface of another particle as a function of time. The trajectory and the inter-particle potential are controlled by a magnetic field. Particles were studied with and without conjugated antibodies in a wide range of pH conditions. The data shows that the aggregation process strongly depends on the particle surface charge density and hardly on the antibody surface coverage. Furthermore, microscopy videos of single particle dimers reveal the presence of reactive patches and thus heterogeneity in the particle surface reactivity. The aggregation rates measured with the single-dimer experiment are compared to data from an ensemble aggregation experiment. Quantitative agreement is obtained using a model that includes the influence of surface heterogeneity on particle aggregation. This single-dimer experiment clarifies how heterogeneities in particle reactivity play a role in colloidal stabilitv.

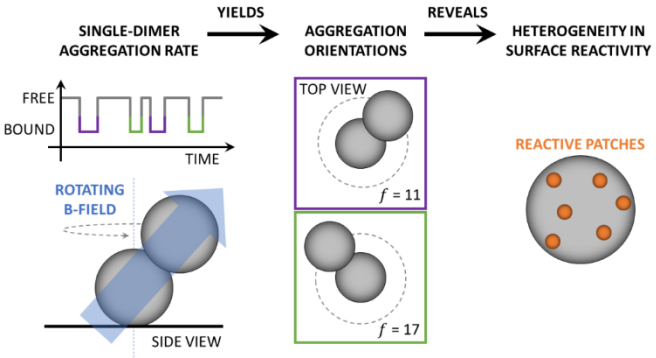

This chapter has been published as: Scheepers, M.R.W.; van IJzendoorn, L.J.; Prins, M.W.J. Single dimer formation rate reveals heterogeneous particle surface reactivity. *Langmuir*, **2019**, 35, 44, 14272-14281

3.1 Introduction

Micro- and nanoparticles are widely used for biomedical applications such as drug delivery[1-5], magnetic resonance imaging[1], biosensing[6,7], and cancer therapy[8]. The particles are made of various materials e.g. magnetic iron oxides[1-3,9,10], silica[11], polymers[12], gold[6,13], silver[14] and combinations thereof[15]. Furthermore the particles are coated and biofunctionalized in order to give them the desired biomedical properties.

A major challenge in developing biomedical applications is to control colloidal stability and minimize particle aggregation. The aggregation is typically irreversible and can cause large variabilities in the measurements. For example, particle aggregation is an important factor determining the efficiency of drug delivery processes[16] and aggregation can strongly affect the coefficient of variation and limit of detection of particle-based assays[17].

The stability of colloidal suspensions can be measured by optical methods such as dynamic light scattering (DLS) and turbidity[18-20]. In previous work, we developed an ensemble method to quantify particle aggregation rates in solution, named the optomagnetic cluster experiment (OMC)[21]. In the OMC experiment, clusters of particles are formed and the average rate of dimer formation of an ensemble of particles is quantified by analysis of the optical Mie scattering signal. Smaller amounts of material can be analyzed using flow cytometry[22] or microscopic imaging[23]. However, these methods do not reveal heterogeneities of surface reactivity of individual particles.

Single particles can be studied with techniques such as atomic force microscopy (AFM), total internal reflection microscopy (TIRM) and particle tweezers, e.g. optical[24], acoustic[25] or magnetic tweezers[26]. In colloidal AFM[27] a single particle is attached to the apex of the cantilever and is pushed onto another surface to probe the interaction potential. AFM can be used to probe particle-particle interactions[28,29], but most literature has studied particle-substrate interactions[30]. In TIRM, the height of a particle above a surface is monitored while the particle is attracted using gravitational, optical[31] or magnetic forces[32]. In particle tweezers, particles can be trapped and manipulated using applied fields. With all of these methods one can measure the repulsive parts of particle-substrate and particle-particle potentials. However, these methods were not developed to quantify the kinetics of an inter-particle aggregation process, which requires repeated probing of the stochastic association process and extraction of the rate of aggregation from time-dependent statistical data.

Here we describe a measurement technique wherein repeated association and dissociation events are observed on single dimers of particles, so that their individual aggregation rate can be quantified. The particles are magnetic and brought into each other's proximity by magnetic dipole-dipole forces. The attractive magnetic force brings the surfaces of the particles very close to each other, to a distance of several nanometers. This close proximity gives a high effective attempt frequency, so that aggregation kinetics can be studied even when particles have strong repulsive interactions and a high energy barrier for association.

The single-dimer aggregation (SDA) experiment is sketched in Fig. 3.1a. A first particle is immobilized on a substrate and a second particle is attracted onto the first one by magnetic dipole-dipole forces. The dipole forces result from an applied magnetic field that magnetizes the particles. To be able to determine if the dimer is aggregated or not, a precessing magnetic field is used, see Fig. 3.1a. When the dimer is not aggregated, the secondary particle can follow the precessing motion of the magnetic field, being visible in video microscopy as a circular trajectory of the second particle. When the dimer is aggregated, the second particle is bound to the first particle and does not perform a circular motion. Transient events between bound and unbound states are determined by analyzing time series of microscopy images, revealing the kinetics of the particle aggregation process. In the experiment multiple particle dimers are simultaneously imaged over time (Fig. 3.1b,c), transitions are determined between aggregated and non-aggregated states (Fig. 3.1d,e) and from the statistics the aggregation rate is determined (Fig. 3.1f).

In this study we investigate particles with a diameter of 0.5 μm and 1.0 μm, and the dependence is measured of the aggregation rate on charge conditions (zeta potential) and biomolecular coating conditions (antibody surface density). The data shows a dominant role of the particle surface charge on aggregation rate and indicates that immobilized antibodies only weakly influence the aggregation rate. Using a model that includes heterogeneity in the particle surface reactivity, we will demonstrate quantitative agreement between the aggregation rate obtained with the single-dimer experiment and with an ensemble-based method[21].

3.2 Materials and methods

3.2.1 Materials

Carboxylated superparamagnetic Masterbeads (nominal size 0.5 μm, hydrodynamic diameter from DLS is 528 nm with coefficient of variation 25%) were purchased from Ademtech and carboxylated MyOne C1 Dynabeads (nominal size 1.0

μm, hydrodynamic diameter from DLS is 1050 nm with coefficient of variation 2%) were purchased from ThermoFischer. Monoclonal mouse IgG against cardiac troponin I was supplied by Hytest. Buffer components: phosphate buffered saline (PBS) tablets, citric acid anhydrous, sodium citrate dihidrate, potassium chloride, Pluronic F-127, 2-(N-morpholino)ethanesulfonic acid (MES) were obtained from Sigma Aldrich. Also 1-ethyl-3-(dimethylaminopropyl)carbodiimide hydrochloride (EDC), N-hydroxysulfosuccinimide (sulfo-NHS), bovine serum albumin (BSA, >98% pure) and Protein LoBind Eppendorf tubes were obtained from Sigma Aldrich. Amine-terminated polyethylene glycol (PEG) with a molecular weight of 5kDa (Blockmaster CE510) was purchased from JSR Microsciences. Glass substrates of size 26x22 mm^2 and thickness 0.16-0.19 mm were obtained from Menzel Gläser.

3.2.2 Particle functionalization

Magnetic particles (Ademtech Masterbeads, 528 nm) were functionalized through an EDC-NHS reaction with different surface coverages of monoclonal mouse IgG against cardiac troponin I (c-TnI) and blocked with the amine-terminated PEG (5kDa). All steps were performed at room temperature.

The stock particles (50 mg/mL) were first magnetically washed four times with a 50 mM MES solution of pH 6.2 containing 60 mg/mL Pluronic F-127 in order to wash away the storage buffer. Between each washing step the particles were shortly vortexed to redisperse them. The final concentration after the washing procedure was 20 mg/mL. The particle solution was then sonicated two times ten seconds to undo possible particle aggregation that occurred during storage or during washing steps.

Subsequently the carboxyl groups on the particles were activated by incubating the particles in a solution of 10 mg/mL EDC and 10 mg/mL NHS for 30 minutes on a roller bench. These solutions were prepared within 5 minutes before using them, to minimize hydrolysis of the compounds prior to the activation step. After the activation step the particle solutions were magnetically washed twice with MES buffer, redispersed by vortexing and sonicated two times during ten seconds.

Monoclonal mouse antibodies against c-TnI were incubated with the particles during 2 hours on the roller bench, to covalently attach the antibodies via their primary amines. Hereafter, a solution of amine-terminated 5kDa PEG was added to the particle solution at an end concentration of 0.8 μM, in order to saturate the remaining active carboxyl groups on the surface of the particles. The mixture was incubated overnight on the roller bench.

Finally, the particle solution was magnetically washed three times and sonicated, after which the solution was stored at an end concentration of 10 mg/mL at 6°C.

3.2.3 *Surface functionalization*

In order to immobilize the primary particles on a glass substrate, the glass was first rinsed consecutively with acetone, isopropanol and methanol in a sonic bath for 10 minutes each. After each rinsing step the substrate was dried with a nitrogen gun. During the first incubation step goat-anti-mouse IgG was physisorbed onto the glass substrate during 60 minutes (200 nM in PBS). In the second incubation step the remaining uncovered surface area was blocked with a 10 mg/mL BSA in PBS solution during 15 minutes. Then, in the third step the primary particles were incubated at a 500 fM particle concentration to bind to the functionalized substrate during 60 minutes. The polyclonal goat-anti-mouse IgG on the substrate binds to the monoclonal mouse-anti-cTnI antibodies on the particles. During the last incubation step 500 nM polyclonal mouse IgG solution was incubated during 60 minutes to block the remaining goat-anti-mouse IgG on the surface. This prevents secondary particles, which may also contain mouse IgG, to bind to the substrate. For experimental details on the surface functionalization, see Section S3.1 of the Supporting Information.

3.2.4 *Quantification of antibody coverage on the particles*

The coverage of antibodies on the particles after functionalization was quantified by a supernatant assay with a commercial Easy-Titer Mouse IgG assay kit (Thermo Scientific catalogue number 23300). In these experiments protein LoBind tubes were used. From the antibody concentration in the supernatant, the antibody coverage was calculated. This calculation gave an average number of immobilized antibodies per particle, without information about the orientation or functionality of the antibodies. The error in the antibody coverage is determined from the standard deviation of three measurements.

3.2.5 *Zeta potential measurements*

The average surface charge of the particles was quantified by measuring the zeta-potential of the particles with a Malvern Zetasizer Nano ZS. Particles were diluted to 0.1 mg/mL and triplicate measurements were performed either in PBS buffer (10 mM phosphate buffer, pH 7.4, ionic strength 150 mM) or in citric acid buffer of different pH's (10 mM citric acid buffer, ionic strength 150 mM). The error in the determination of the pH of the buffer solutions is about 0.1. At these high salt concentrations, the operating voltage was limited to max. 10 V in order to prevent electrolysis at the electrodes, which decreases the signal-to-noise ratio in the measurements. The uncertainty in the zeta potential measurement is relatively large due to the low absolute value of the zeta potential of the measured particles ($\Delta\zeta \approx 2\mathrm{mV}$).

3.2.6 *Experimental setup with magnetic field and microscopic imaging*

The single-dimer aggregation experiment is conceptually depicted in Fig. 3.1. The experimental setup is schematically shown in Fig. S3.2a and a photographic image is shown in Fig. S3.2b. To create out-of-plane rotating magnetic fields, five electromagnets are located around the sample. Four electromagnets are placed around the sample, creating a magnetic field in the plane of the sample, and one electromagnet below the sample creates an out-of-plane field component. The current flowing through the coils of the electromagnets is generated by a voltage source that is driven with Matlab. The sample is placed in a PEEK (polyether ether ketone) sample holder which is located in the middle of the electromagnets. The sample is illuminated by a Leica fiber optic light source coming from the side, which is directed onto the sample by a silver right-angle prism mirror.

The sample is imaged with bright field microscopy by a Leica DM6000B microscope with a 63x water immersion objective and a 2x internal magnification. Recordings are made with an Andor Neo sCMOS camera; standard recording settings are: 30 ms exposure time, 5 Hz frame rate and 3000 frames (10 minutes). For these experiments a home-made flow cell is used in which all the incubation steps are performed, see Fig. S3.2c. The flow cell consists of a cleaned glass slide with a sticker made of optical grade plastic attached to it, containing an open channel for liquid flow. The in- and outlet are made of flexible silicone tubing sealed with UV curable gel. A Harvard apparatus 11plus syringe pump is used to pull the liquid through the flow cell.

3.2.7 *Analysis software*

Recordings of the single-dimer aggregation experiment were analyzed with a homemade Matlab script. The script consist of three steps: (i) detecting and tracking primary particles, (ii) detecting when a secondary particle gets magnetically trapped on a primary particle and (iii) detecting binding and unbinding of the rotating dimer.

Primary particles in solution appear as high intensity spots on a lower intensity background (Fig. 3.1b). The locations of individual particles were determined by calculating the center of intensity of the high intensity spots. The locations of particles in subsequent frames were correlated to obtain the trajectory of an individual particle. A drift correction was performed based on the average motion of the primary particles during the recording.

At some point during the recording a freely diffusing secondary particle can become trapped on one of the primary particles. Because these particles are only 528 nm in diameter, when two of them get trapped they appear as a single elongated

diffraction limited spot (Fig. 3.1c). The center position of the diffraction limited spot changes upon a trapping event, making it possible to detect trapping by thresholding the change in position of a primary particle (Fig. S3.3a). If a third particle is trapped on the dimer, this system was not tracked any further.

As soon as a secondary particle is trapped on the primary particle, the experiment starts for this dimer. The secondary particle makes a circular motion path on the primary particle. This is observed as a rotation of the elongated diffraction limited spot. The orientation of the long axis of the diffraction limited spot was tracked over time and by thresholding on the rotation speed, binding and unbinding was detected as a decrease or increase in the rotation speed, respectively (Fig. S3.3b).

3.3 The single-dimer aggregation experiment (SDA)

We have developed an experimental technique which allows to study the kinetics of particle aggregation on single dimers. The principle of the experiment is shown in Fig. 3.1. Single superparamagnetic particles are immobilized on a glass substrate in a multivalent fashion, i.e. these particles are not able to rotate freely in any direction. These immobilized particles will be referred to as the primary particles. Subsequently, due to an applied magnetic field (B=6mT), individual particles, called secondary particles, are magnetically trapped on the primary particles and form a dimer (Fig. 3.1a). The particles are now held together by a magnetic dipole-dipole force in the direction of the magnetic field. The magnetic force is high enough to keep the secondary particles magnetically trapped throughout the whole experiment (~10 min). On the other hand, the magnetic force is much weaker than the forces that underlie a chemically aggregated state of the dimer. The orientation of the magnetic field is chosen to be tilted with respect to the horizontal plane of the substrate. This ensures that the secondary particles do not touch the substrate (~100 nm distance between the secondary particles and the substrate) and allows for application of a rotating field for detection purposes.

To be able to detect if a dimer is in a non-aggregated (free) of in an aggregated (bound) state, the orientation of the applied magnetic field is continuously rotated around the vertical axis, so that the field performs a precession motion trajectory, see Fig. 3.1a. In a free state, the secondary particle follows the magnetic field orientation and therefore makes a circular motion path on top of the primary particle. In a bound state, the secondary particle is immobilized and cannot follow the rotation of the magnetic field. By determining the state of the dimer as a function of time, association events as well as dissociation events can be identified. The time-to-aggregation is

defined as the time that the dimer spends in the free state. From statics of the time-to-aggregation, the aggregation rate can be calculated.

In the experiment, multiple single dimers are simultaneously imaged with bright field microscopy. Fig. 3.1b shows a quarter of a full field of view with individual primary particles. Several microscope images of a single-dimer aggregation experiment are shown in Fig. 3.1c. The first row of images shows the trapping of a secondary particle onto the primary particle. The two 500 nm particles in the dimer cannot individually be optically resolved, thus the dimer appears as a single elongated diffraction limited spot in the microscope. The second row shows how a freely rotating dimer switches to a bound state. Supplementary Video S1 shows the full recording of this dimer. The microscopy recordings are analyzed with a homemade Matlab script (described in Materials and Methods Section).

Fig. 3.1d shows the cumulative number of rotations of a single dimer over time. In the free state, the secondary particle rotates along with the magnetic field ($\omega/2\pi = 0.5$ Hz) and makes complete rotations. In the bound state, the secondary particle cannot make a complete field rotation; it shows a weak wiggling motion indicating that it is bound but not fully immobilized. Fig. 3.1e shows a full time trace of a single dimer, distinguishing the bound state and the free state based on the rotated angle between two consecutive frames. The orange line shows the state of the dimer as detected by the analysis software. Multiple aggregation events are observed for the same dimer with different times-to-aggregation. The wiggling motion in the bound state is also observed in this plot. The upward spikes in the signal are due to the transient passage of particles in solution through the microscopic field of view, which perturbs the image analysis of the dimer. The range of measurable times-to-aggregation is limited on the low side by the field rotation frequency and the angular resolution. On the high side, the times-to-aggregation are limited by the total duration of the experiment (for more detail see Section S3.4 of the Supporting Information).

Times-to-aggregation of all the dimers in the field of view can be presented in a survival plot, see Fig. 3.1f. When plotted on linear-logarithmic x-y scales, then the observation of a straight line implies that the process can be described by a single aggregation rate k_{agg}. The data is fitted to obtain the average k_{agg} and the uncertainty in k_{agg}.

The single-dimer aggregation experiment allows studies of the aggregation behavior for many types of magnetic particles, surface chemistries, surface charge, buffer conditions and magnetic field conditions. In the following paragraph, we firstly describe the influence of the particle surface charge density on the aggregation

rate by varying the pH of the solution, and secondly we investigate the influence of the surface coating of the particles by varying the antibody coverage on the secondary particle. Thereafter, we will discuss heterogeneity observed in the aggregation process.

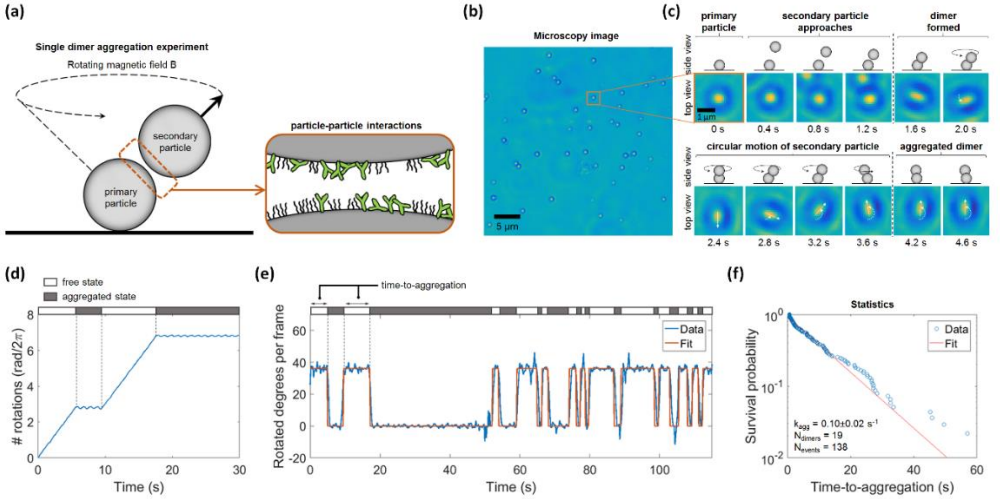

Fig. 3.1 Single-dimer aggregation (SDA) experiment. (a) Experimental concept: Single particles are immobilized on a glass substrate, called primary particles. In the presence of a rotating (precessing) magnetic field a secondary particle is trapped on the primary particle by magnetic dipole-dipole interactions. The secondary particle follows the rotating field, making a circular motion path on top of the primary particle. Upon particle aggregation, the secondary particle becomes immobilized and stops following the rotating magnetic field. **(b)** Microscopy image of a quarter of a full field of view of primary particles. **(c)** Microscope images showing how a single secondary particle is trapped onto a primary particle (upper row) and how a circulating secondary particle stops circulating upon aggregation (lower row). The full recording is given in Supplementary Video S1. **(d)** Cumulative number of rotations for a single dimer. In the free state the dimer follows the field. In the aggregated state the dimer shows a wiggling behavior, because the secondary particle still has a limited freedom of motion. **(e)** Time trace of the rotation speed of a single dimer, showing 12 aggregation and dissociation events, including a fit of the data by the analysis software. The small spikes in the time trace originate from particles in solution that diffuse into the imaged region, thereby perturbing the image analysis. **(f)** Survival plot of the times-to-aggregation of 19 single dimers in a field of view. Data is fitted as: $\frac{N(t)}{N(0)} = \exp(-k_{agg}t)$. The fit to the data gives $k_{agg} = 0.10 \pm 0.02\ \mathrm{s}^{-1}$.

3.4 Aggregation rate depends on particle surface charge

The most important factor for stabilizing colloids in buffer solutions is the particle surface charge density, which is often expressed in terms of the zeta potential. Generally, by increasing the surface charge, the absolute value of the zeta potential increases, whereby the aggregation rate decreases[33,34]. Using the single-dimer aggregation experiment we investigated and quantified the aggregation rate as a function of zeta potential by varying the pH in several citric acid buffers.

Two different types of particles were used: 0.5 μm Ademtech particles coated with monoclonal antibodies (~10% antibody surface coverage) against cardiac troponin I (cTnI) and blocked with a 5kDa PEG (for details about the particle coating and immobilization, see the Materials and methods Section), or uncoated MyOne carboxylic acid particles with a diameter of 1.0 μm. The carboxylic acid particles have a high surface charge density at high zeta potentials. The pH dependence of the zeta potential of both types of particles was measured and is shown in Fig. 3.2a. The carboxylic particles indeed show a three times larger absolute value of zeta potential than the antibody coated particles. Using these two types of particles, two dimer systems are compared on their aggregation properties: an equal-particle system with dimers consisting of two antibody coated 0.5 μm particles, and dimers consisting of two different particles (Fig. 3.2b). The 0.5μm-0.5μm dimers were studied at 6 mT magnetic field and the 0.5μm-1.0μm dimers at 4 mT magnetic field, in order to keep the magnetic dipole-dipole forces the same in the two dimer systems.

Fig. 3.2c shows the aggregation data of the two dimer systems. The equal-particle dimer system aggregated immediately (i.e. within about a second) for pH≤5.1, and shows a finite aggregation rate of about 0.2 s^{-1} for pH≥6.1. Already at pH 6.1 a fraction of the dimers shows immediate aggregation upon dimer formation, indicating that conditions are at the edge of the measurable rate window. The aggregation rate shown in Fig. 3.2c is determined from the dimer subpopulation showing non-zero times-to-aggregation. Between pH 5.1 and 6.1 a transition takes place where all or a few particles show immediate aggregation upon dimer formation. This pH range where the dimer aggregation behavior strongly changes is indicated in Fig. 3.2c by the green area.

For the different-particle dimer system, a binary behavior is observed: for pH≤4.6 aggregation occurs immediately upon dimer formation, and for pH≥4.8 no aggregation at all occurs during the time of an experiment (Supplementary Video S2 and S3 show an example of immediate aggregation and no aggregation, respectively). Apparently, the aggregation rate strongly depends on the surface charge of the particles. When changing the pH of the buffer from 4.6 to 4.8, the zeta potential of the 0.5 μm particles do not change significantly, but the zeta potential of the 1.0 μm particles changes by about 6 mV. This leads to a very large change in the aggregation rate of at least four orders of magnitude, i.e. the rate traverses the complete range of measurable rate constants (Fig. 3.2c). The pH range where the dimer aggregation behavior strongly changes is indicated in blue. This data clearly demonstrates that particle aggregation in buffer solutions is strongly dependent on electrostatic interactions.

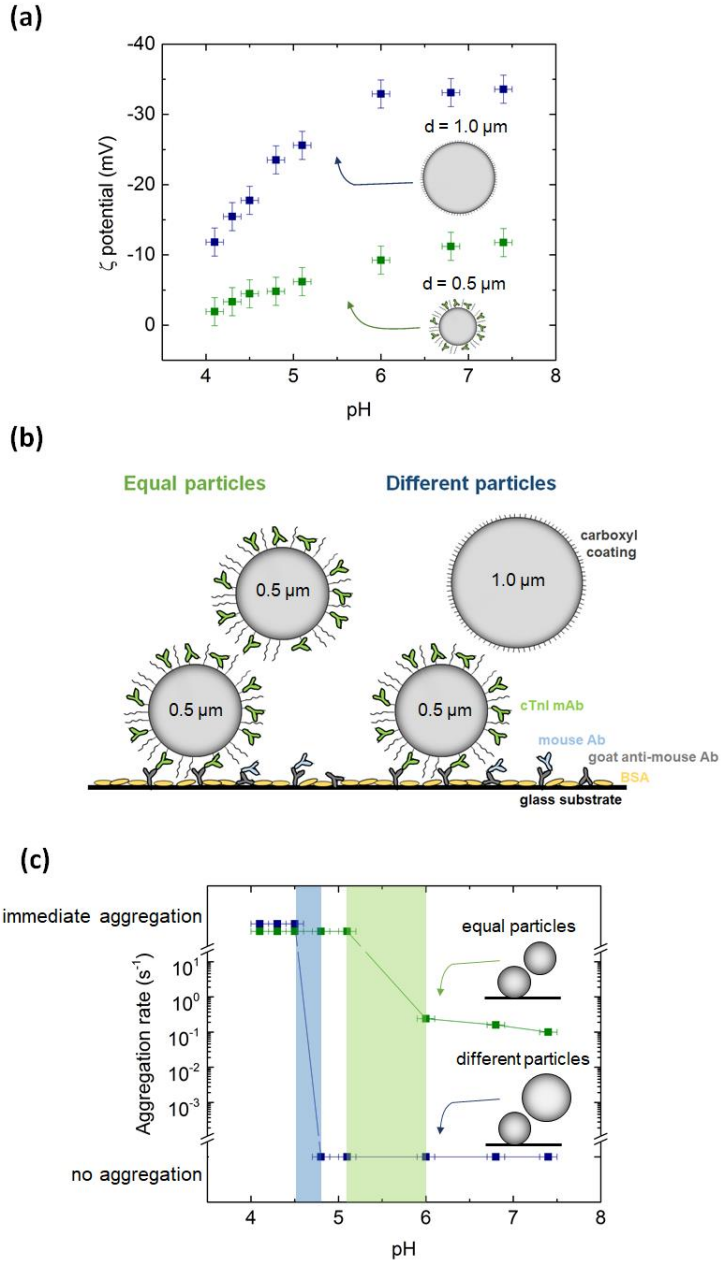

Fig. 3.2 Single-dimer aggregation experiment as a function of surface charge. (a) The zeta potential of the 0.5 µm and the 1.0 µm particles measured as a function of pH of the citric acid buffer (ionic strength 150 mM). **(b)** Schematic representation of the two dimer systems: The equal-particle dimer system consists of two antibody coated 0.5 µm particles, and the different-particle dimer system consists of both an antibody coated 0.5 µm particle and a carboxylated 1.0 µm particle. **(c)** Measured aggregation rate for both dimer systems at different pH of the citric acid buffer (ionic strength 150 mM).

3.5 Aggregation rate for antibody coated particles

The antibody coverage on the 0.5 μm particles was varied in order to study the influence of the surface coating on the aggregation rate. The particles were functionalized via EDC-NHS with different concentrations of monoclonal antibodies against cTnI and subsequently blocked with a 5kDa PEG. Fig. 3.3a shows the measured antibody coverage as determined with the supernatant assay described in the Section Materials and Methods. The graph shows that functionalizing the particles with a higher antibody concentration leads to a higher antibody coverage, until saturation occurs at a coverage of about 10^4 antibodies per particle, which we define as 100% antibody coverage. This corresponds to an average surface area of 100 nm^2 per antibody, assuming a smooth spherical surface of the particle. The green circles indicate the antibody concentrations that were used for the subsequent experiments: no antibodies, ~10%, and ~100% antibody coverage.

The zeta potential of the particles, measured in PBS at pH 7.4, decreased due to the functionalization process and shows no significant difference for the three antibody coverages given the uncertainty intervals, see Fig. 3.3b. This is an important observation, because it allows us to study the influence of the antibody coverage on the aggregation rate, independent of the surface charge density on the particles.

The experiment as a function of antibody coating was performed with particles of equal size (0.5 μm). The primary particles were coated with a ~10% coverage of antibodies and blocked with PEG in all experiments. The secondary particles had either no antibodies, ~10% antibody coverage, or ~100% antibody coverage. Fig. 3.3c shows the measured aggregation rate for each experiment (survival plots of time-to-aggregation are shown in Section S3.5 of the Supporting Information). The measured values for no and 10% antibody coverage are equal within the error bars, and the aggregation rate for 100% antibody coverage is slightly higher. It should be noted that Fig. 3.3c has a linear y-scale whereas Fig. 3.2c has a logarithmic y-scale. Therefore, the differences in the aggregation rate for different Ab coverages (cf. Fig. 3.3c) are extremely small compared to the differences in aggregation rate as a function of pH (cf. Fig. 3.2c). Clearly, the aggregation rate depends only very weakly on the antibody coverage. The very weak dependence on surface coating has also been observed for other molecular systems (details are added to Section S3.6 of the Supporting Information).

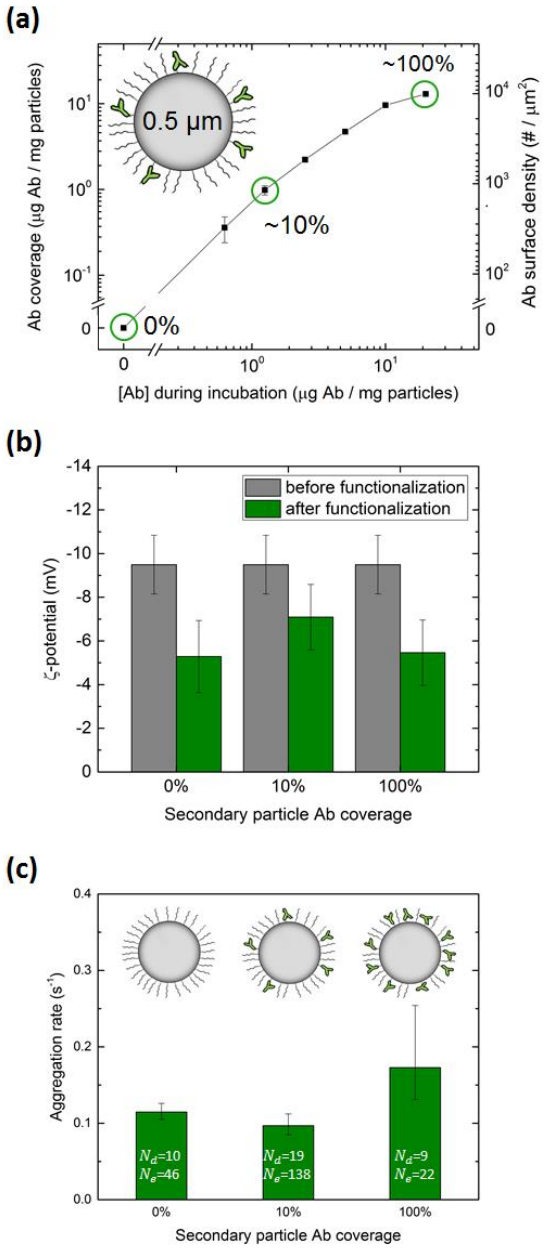

Fig. 3.3 Single-dimer aggregation experiment using two 0.5 µm particles, as a function of antibody coverage on the secondary particles. (a) Antibody coverage on the secondary particle as a function of antibody concentration during particle functionalization. The right y-axis shows the calculated antibody surface density. **(b)** Zeta potential of the secondary particles before and after functionalization with antibodies and PEG. Measurements were performed in PBS at pH 7.4. **(c)** Aggregation rate measured with the single-dimer experiment for three surface coverages of the secondary particle: zero Ab coverage, ~10% Ab coverage, and ~100% Ab coverage. The number of dimers N_d and the number of measured events N_e are shown for each Ab coverage. The data show that the aggregation rate hardly depends on the antibody surface coverage.

It is interesting to discuss the results of the single-dimer aggregation (SDA) experiments with respect to earlier protein aggregation studies. The latter studies have shown that monoclonal antibodies at high concentrations ([mAb] > 60 mg/mL) suffer from significant protein aggregation[35-37]. In the SDA experiment, a high coverage of mAb's on the particles leads to a high local mAb concentration at the interface between two magnetically confined particles. The local antibody concentration in the interaction volume between two particles in a dimer can be calculated using the antibody surface coverage and by estimating the interaction volume as a cylinder centered around the contact point of the particles having a length of 10 nm. For particles with a mAb coverage of ~10% the local mAb concentration is already about 100 mg/mL. Therefore, the observed particle aggregation might be caused by aggregation of mAb's.

In the described SDA experiments, the primary particle has a 10% antibody surface coverage, which implies that there are always antibodies present at the contact point of the primary and secondary particle. This might explain why we observe only small differences in the aggregation rate when varying the antibody density on the secondary particle. In the SDA experiment of this chapter, the primary particles were multivalently immobilized via antibodies on the primary particle; therefore the antibody coverage on the primary particles could not be reduced. In follow-up work, it will be interesting to develop novel primary particle immobilization strategies that will allow scaling of the antibody surface density on the primary particle.

3.6 Inter-dimer and intra-dimer heterogeneities

An experimental method that resolves single particles and single dimers allows to investigate inter-dimer and intra-dimer variations in the aggregation rate. We have studied to what extent such differences can be observed in our single-dimer aggregation experiment. Since the experiments have limited aggregation event statistics per individual dimer, only large inter-dimer differences in the aggregation rates can be resolved. Large differences are seen only in certain conditions, such as in the pH 5.1 equal-particle experiment of Fig. 3.2c, where some dimers are immediately bound and other dimers show repeated aggregation and disaggregation.

Intra-dimer heterogeneities have also been observed. Fig. 3.4 shows an example of a time trace of a dimer (10% Ab coverage, pH = 7.4, ionic strength 150 mM), where nine aggregation events have been related to their corresponding dimer angle, as indicated in the colored squares on the right. The data shows that aggregation events occur at preferential dimer angles: the secondary particle binds at well-defined

positions on the primary particle. In this case the large majority of aggregation events occurs at the dimer angle indicated in purple and the other angles occur rarely. This is a direct observation of preferential binding locations on the primary particle and heterogeneity of particle reactivity, resulting from the single-dimer resolution of the experiment.

This feature of the single-dimer experiment can be used to study the presence of reactive patches on a particle surface by its influence on particle aggregation. Reactive patches can arise for example by unfolding of proteins on the particle surface[38-41] or incomplete particle functionalization, causing certain locations on the particle to be more or less reactive. By systematically comparing the distribution of dimer aggregation orientations in different molecular systems, hypotheses on patchiness of particle reactivity can be tested.

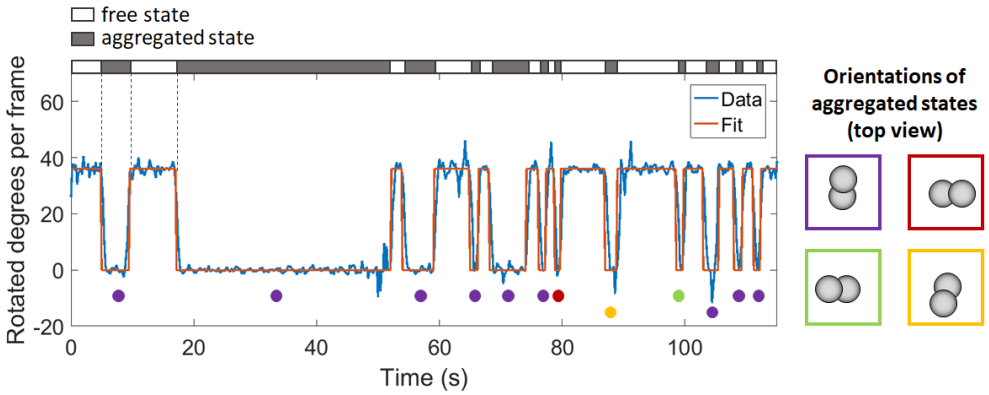

Fig. 3.4 Heterogeneous binding orientations. A measured time trace of single-dimer (dis)aggregation. Colored dots at each binding event indicate the orientation of the dimer, showing that the primary particle has preferential aggregation locations on its surface.

3.7 Simulations of heterogeneous particle surface reactivity

To interpret the measured aggregation rates, a model and simulation code have been developed to study the effect of heterogeneity in particle surface reactivity on measured aggregation rates. The simulation has been developed for both the single-dimer aggregation experiment (SDA) and the previously described ensemble optomagnetic cluster experiment (OMC)[21]. This allows us to quantitatively compare the aggregation rates obtained by two experimental methods on the same particle system.

To introduce heterogeneity on the particle surface, N reactive patches are randomly placed on each particle, see Fig. 3.5a. These reactive patches are simulated

as small spherical caps on the particle surface, where the reactivity of the particle is equal to $k = k_{patch}$. The surface area of the particle that is not covered by a sticky patch has a reactivity $k = 0$. This black-and-white approach might not be completely correct since it is known that nonspecific interactions span a wide range of association rates[26], however it is used as a first approximation. The radius of the spherical cap is chosen to be $R_{patch} = 2.5$ nm, a typical interaction size for a protein. Note however that the outcome of the simulation hardly depends on the size of the patch. From the number of reactive patches on a particle, its reactive surface coverage η_{rs} is defined as the fraction of the surface that is covered by reactive patches, see equation 3.1.

$$\eta_{rs} = \frac{1}{2}N\left(1 - \sqrt{1-\left(\frac{R_{patch}}{R_{particle}}\right)^2}\right) \cong \frac{N}{4}\left(\frac{R_{patch}}{R_{particle}}\right)^2 \quad \text{for} \quad R_{patch} \ll R_{particle} \tag{3.1}$$

In the SDA simulation one of the particles is fixed in a certain random orientation, mimicking the immobilized primary particle. A second particle approaches the primary particle in a random orientation at an angle of 45° with respect to the vertical axis, mimicking the trapped secondary particle. The secondary particle is now moved in a circular fashion over the surface of the primary particle. The rotation frequency is chosen equal to the experimentally used field rotation frequency $f = 0.5$ Hz. The particles interact with each other only at the surface area close to the point of contact between the particles. An interaction volume is defined as shown in Fig. 3.5a. This interaction volume creates an interaction area on both particles of a spherical cap centered around the contact point. The interaction distance, the width of the interaction volume, is chosen to be equal to 10 nm, as it is unlikely that bond formation occurs at longer distances.

In each simulation step ($\Delta t = 10^{-2}$ s) the program checks on both particles if there is overlap between reactive patches on the particle and its interaction area. When both particles have at least one reactive patch in their interaction area, then there is a possibility for aggregation, see Fig. 3.5a. The probability for aggregation during a single time step is given by equation 3.2.

$$P_{agg,SDA} = \Delta t \cdot k_{patch} \tag{3.2}$$

Using random numbers the program checks if aggregation occurs. If so, the time-to-aggregation is determined and otherwise the secondary particle is moved further for a new time step. The effective aggregation rate is obtained from the simulation by a survival plot of multiple times-to-aggregation originating from multiple single dimers.

Fig. 3.5b shows the contact configurations of the two particles. In the SDA experiment, the secondary particle moves over the surface of the primary particle. Here we distinguish two limiting cases: rolling and shoving. A shoving secondary particle slides over the primary particle and exposes only a single contact area. A rolling secondary particle rolls over the primary particle and thereby exposes its equatorial area, indicated in orange in Fig. 3.5b. In the OMC experiment, dimers rotate as a whole, so only single contact areas of the particles are exposed.

The dimer formation rate for the OMC experiment was modelled as follows. During the magnetic actuation pulse, a magnetic dimer i contains two particles each with N patches, brought together in a random orientation. Throughout the remaining time of the actuation pulse, $t_{int,i}$, the particles interact in the same orientation. In case there is overlap on both particles between a reactive patch and its interaction area, aggregation occurs with a probability given by equation 3.3.

$$P_{agg,OMC} = k_{patch} \cdot t_{int,i} \tag{3.3}$$

The aggregation rate k_{agg}^{OMC} in the simulation is determined in the same way as experimentally (equation 2.2).

Fig. 3.5c shows the effective aggregation rates obtained from the simulations as a function of the reactive surface coverage η_{rs}, for $k_{patch} = 1\ \mathrm{s}^{-1}$. As expected, high reactive surface coverages lead to high aggregation rates. For the SDA simulation, coverages over a few percent give an aggregation rate equal to the patch aggregation rate. For the OMC simulation, the aggregation rate levels off at $10^{-1}\ \mathrm{s}^{-1}$ because the aggregation rate is limited by the inverse of the mean interaction time ($< t_{int} >^{-1} = 0.1\ \mathrm{s}^{-1}$)[21].

The simulations of the SDA experiment show that the aggregation rates depend on the motion configuration. At low reactive surface coverages, the shoving particles give a higher aggregation rate than rolling particles. This difference is caused by a reactivity bias. Dimers that do not show aggregation events during the experiment, because one of the particles has no reactive patch in the exposed surface area, do not contribute to measurement statistics in the survival plot. This means that the deduced aggregation rates are biased toward reactive dimers, which is more pronounced for shoving particles because these have a higher chance to lack a reactive patch in the exposed contact area.

We can now compare experimental results with results from the simulations. Aggregation rates have been measured on the 0.5 μm particles with a 10% Ab coverage, in both the SDA and OMC experiments. The found aggregation rates, including their uncertainty intervals, are presented in Fig. 3.5c by the green and

orange horizontal bars. The experimental and simulated rates are in agreement for $k_{patch} = 1\ s^{-1}$, a reactive surface coverage of 0.04-0.07% (corresponding to 40-70 patches per particle) and when the secondary particle makes a shoving motion in the SDA experiment. Simulations performed with different patch aggregation rates show that agreement is achieved in a narrow range of patch aggregation rates: $k_{patch} = 1.0 \pm 0.3\ s^{-1}$. A shoving motion of the secondary particle indicates that the mechanical torque due to its anisotropy[42] is larger than the torque exerted due to shoving-induced friction; this is an interesting mechanistic result that merits further study.

In conclusion, the simulations described in this section allow a comparison between aggregation rates measured with the SDA and OMC experiments. Due to the presence of reactive patches on the particles (see Fig. 3.4), the motion configuration and exposed surface areas of the particles (see Fig. 3.5b) appear to have a large influence on the measured aggregation rates. Further studies should focus on unravelling the precise nature of the patches and their reactivity.

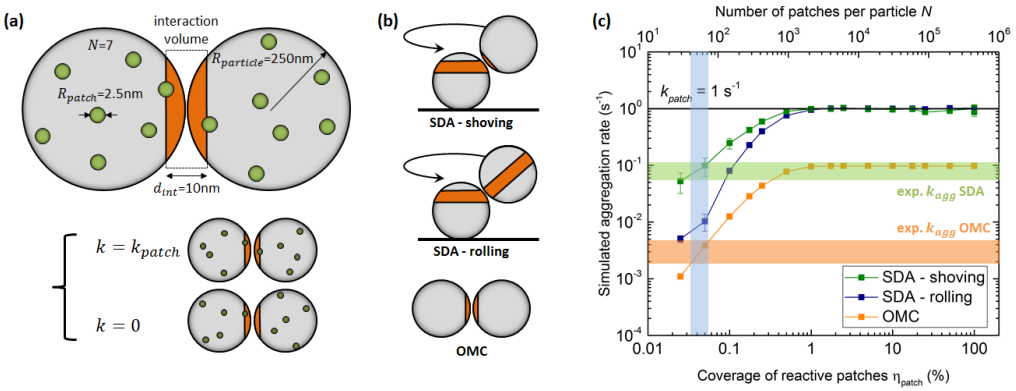

Fig. 3.5 Simulation of aggregation in case of heterogeneous surface reactivity. (a) Heterogeneity in surface reactivity is simulated as N reactive patches on a non-reactive particle. An interaction volume is defined by two spherical caps centered around the contact point between particles. Aggregation can only occur when the interaction area on both particles contains at least one reactive patch. **(b)** The total probed interaction area on both particles depends on the experiment type and the motion of the secondary particle. For the SDA experiment a rolling secondary particle probes more area on the secondary particle compared to the shoving case. In the OMC experiment only the two initial spherical interaction areas have interaction. **(c)** Simulated aggregation rate as a function of the coverage of reactive patches on the particles, with $R_{patch} = 2.5$ nm, $R_{particle} = 250$ nm, and $k_{patch} = 1\ s^{-1}$. Experimental results for the system of particles with 10% Ab coverage are indicated by the horizontal bars.

3.8 Conclusion

In this chapter we described a new experimental method to investigate particle aggregation on single particle dimers. Nonspecific aggregation has been studied

between particles with and without conjugated antibodies, in a wide range of pH conditions. The data shows that the aggregation rate strongly depends on the particle surface charge density, with variations over more than four orders of magnitude when changing the pH of the solution. Varying antibody type and surface coverage resulted in only a factor 1.5 change in the aggregation rate.

Video microscopy of aggregation and disaggregation events of individual dimers revealed discrete areas with high reactivity, i.e. strong heterogeneity in surface reactivity of the particles. Apparently reactive patches are present on the surface of the particles. Simulations on the aggregation of heterogeneously reactive particles resulted in quantitative agreement between the experimental data of the single-dimer aggregation experiment and an ensemble-based method to quantify particle aggregation[21]. The simulations show that the motion configurations and exposed particle surface areas are important due to the patchy nature of the particle surface reactivity. Interesting follow-up studies will be to investigate the (bio)chemical characteristics and amount of patches on different particles, and to investigate possible differences in how specific and nonspecific interactions influence aggregation rates.

The single-dimer aggregation experiment can be used for studying superparamagnetic particles of many material types and with different biochemical coatings. The size range of the particles is limited on the lower side by the resolution of the optical microscope, and on the upper side by the drag of the secondary particle. The drag can be reduced by decreasing the rotation frequency of the field, but that also reduces the time resolution of the experiment and limits the maximum observable aggregation rate.

In conclusion, the described single-dimer aggregation experiment gives the unique ability to reveal the influence of particle surface heterogeneities on inter-particle aggregation. The developed methodology and model description will be valuable for further scientific studies as well as optimizations of the functional properties of colloids.

3.9 Supporting Information

S3.1 Substrate functionalization

To verify the immobilization strategy of primary particles on the substrate, two experiments were performed. In the first experiment the number of immobilized primary particles on the substrate was counted for different concentrations of the goat-anti-mouse IgG on the substrate. Fig. S3.1a shows a curve with saturation at a concentration of 200 nM. Given the Ab concentration during incubation with the substrate, the amount of antibodies on the particles, and the curvature of the particle, it can be calculated that around 10^2 molecular bonds are formed between a single particle and the substrate.

In the second experiment, the substrate was functionalized and particles were immobilized as described above. Thereafter, the substrate was blocked with different concentrations of polyclonal mouse IgG, after which a second incubation step with primary particles was done. Fig. S3.1b shows that the goat-anti-mouse IgG was blocked by incubation with 100 nM mouse IgG, demonstrating that the particles were indeed bound to goat-anti-mouse IgG molecules on the substrate.

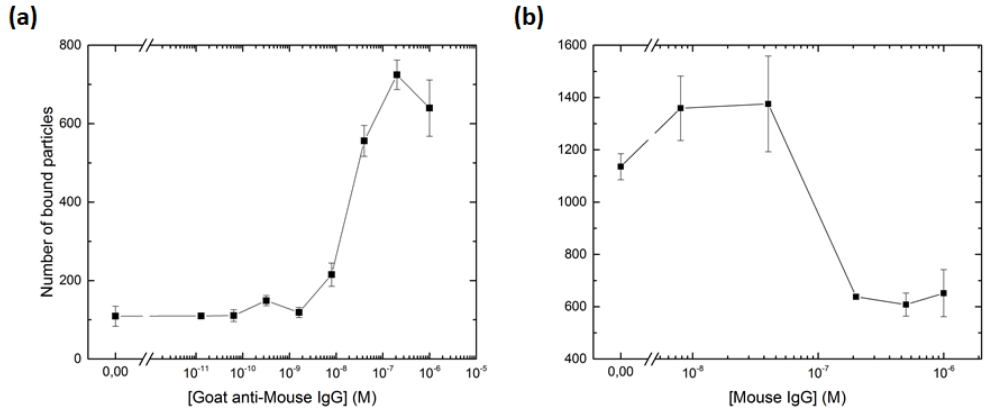

Fig. S3.1 Control experiments on surface functionalization. (a) Graph showing the amount of functionalized particles that binds to the functionalized surface as a function of the concentration of antibodies during incubation. **(b)** Graph showing how blocking the antibodies on the surface leads to a decreases in the number of bound particles.

S3.2 Experimental setup and flow system

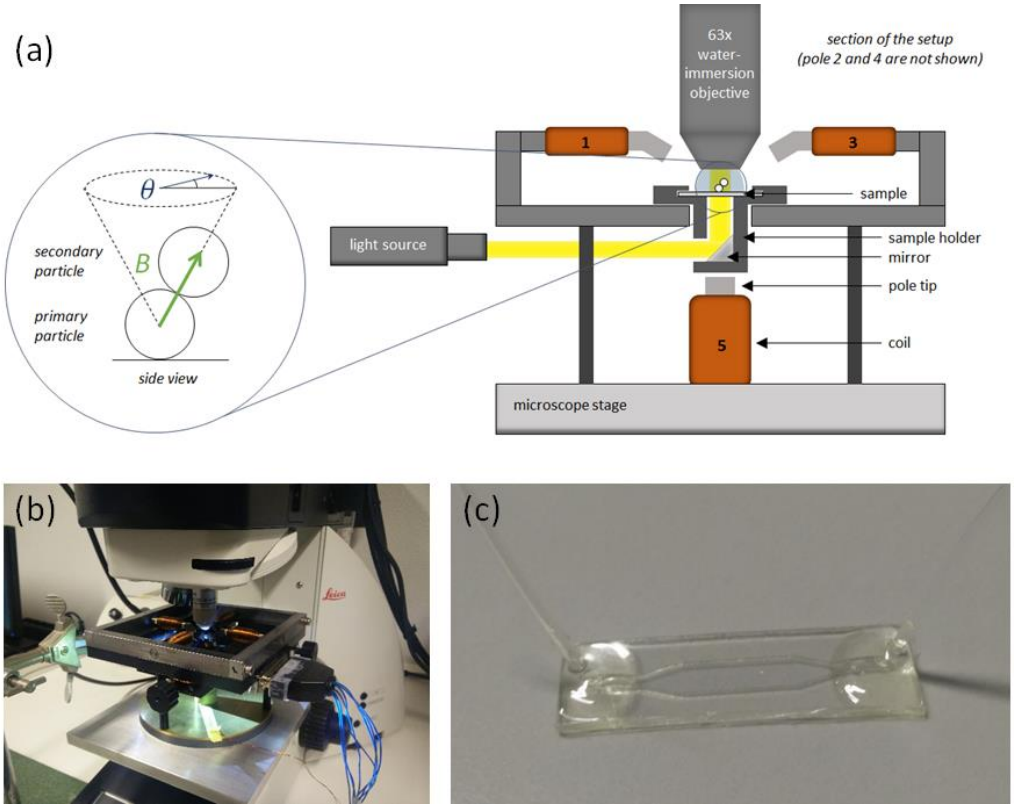

Fig. S3.2 Experimental setup. (a) Schematic representation of the experimental setup consisting of a five-pole electromagnet, a light source coming from the side, a 63x water immersion objective and a camera. **(b)** Picture of the experimental setup. **(c)** Picture of the home-made flow cell.

S3.3 *Analysis software*

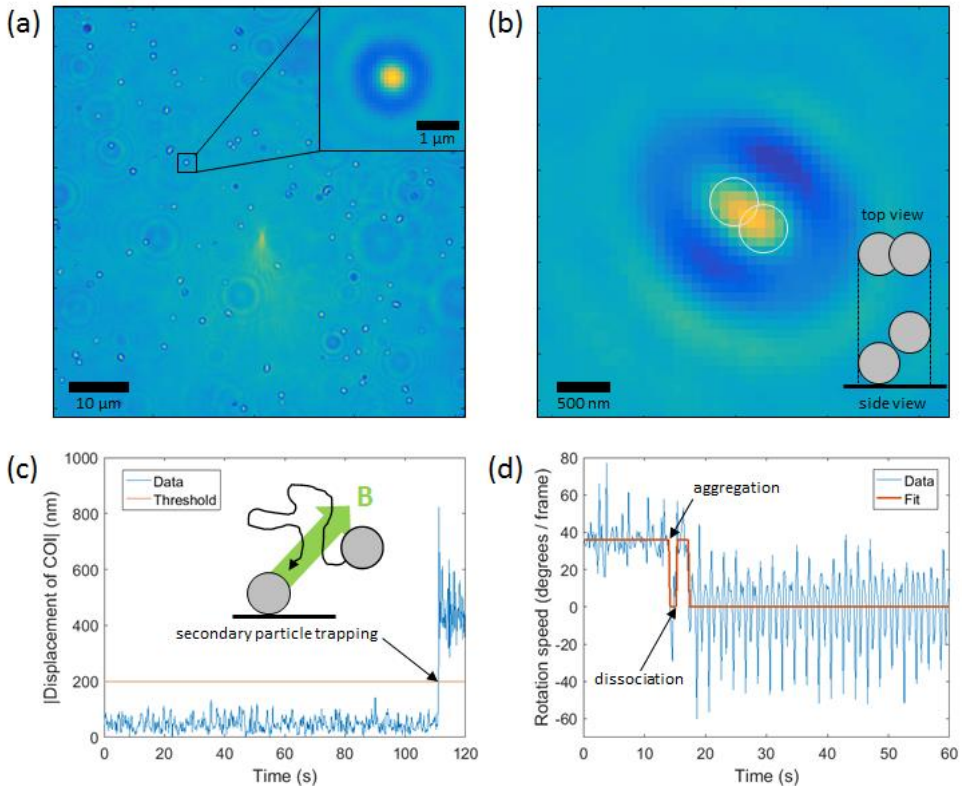

Fig. S3.3 Raw data analysis software. (a) Typical microscope image showing a full field of view filled with primary particles. Zoom shows a single primary particle. **(b)** Zoomed microscope image of a single secondary particle trapped on a single primary particle in a tilted out-of-plane magnetic field. The two particles cannot be optically distinguished, instead an elongated diffraction limited spot is observed. **(c)** Displacement of the center of intensity (COI) over time showing a stepwise increase upon secondary particle trapping. This is detected using a threshold. **(d)** Rotation speed of a single dimer over time, including a fit. Rotation speed is rather constant (5 fps / 0.5 Hz = 36 °/frame), until aggregation occurs, because then the rotation speed drops to zero. After dissociation the rotastion speed goes up again. In the bound state, periodic fluctuations in the rotation speed are due to the non-zero remaining wiggling motion of the dimer.

S3.4 *Statistics of the time-to-aggregation*

The available observation time per dimer is limited by the time between the moment the secondary particle gets trapped, which is random, and the moment when an additional particle gets trapped on that same dimer, resulting in the formation of a trimer and the end of the dimer experiment. It is possible to optimize the number of aggregation events per dimer by varying the particle concentration in solution, but it is a trade-off. At low secondary particle concentration in solution only few secondary particles are trapped on primary particles; at high secondary particle concentration, a dimer experiment has a short duration due to faster formation of a trimer.

The range of times-to-aggregation that can be measured with the single-dimer aggregation experiment is limited by several experimental constraints. The rotation angle per frame (field rotation frequency/frame rate) needs to be large enough to detect with the software. It is possible to increase the framerate, however, increasing the field rotation frequency is not preferred because the particle should be able to follow the field rotation in the free state. Therefore the shortest measureable time-to-aggregation (~0.4 s) is determined by the maximum field rotation frequency. The longest time-to-aggregation depends again on the time between the secondary particle gets trapped, which is random, and the time that another secondary particle gets trapped on that same dimer (< 10 min).

S3.5 Varying Ab coverage: histograms of time-to-aggregation

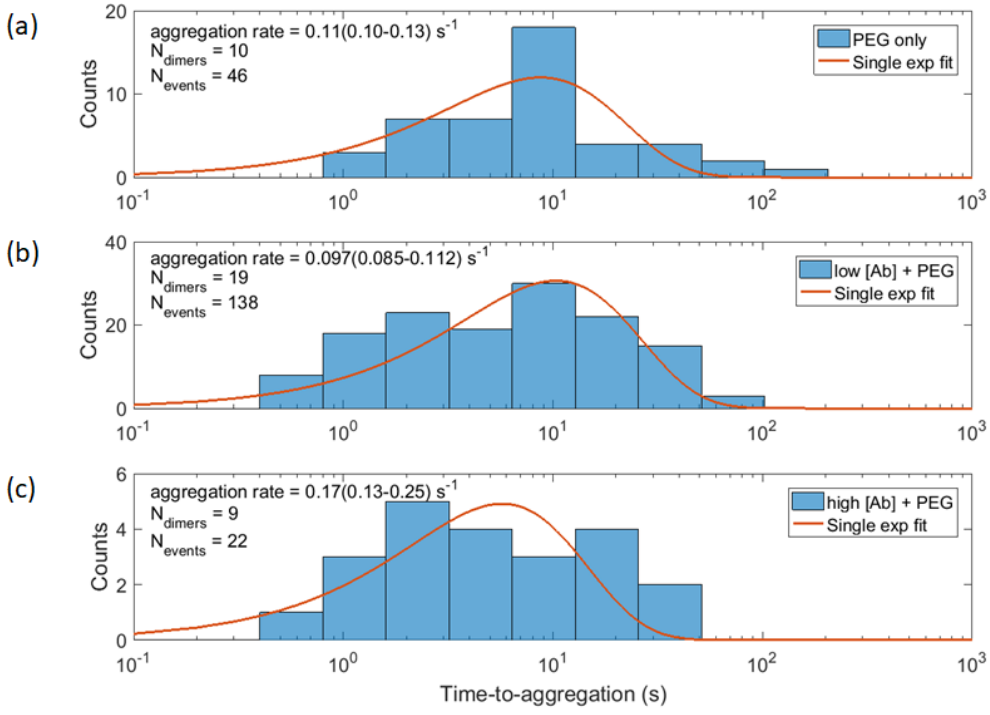

Fig. S3.5 Varying antibody coverage. Histograms of the time-to-aggregation including the extracted rate constant from the single exponential fit for secondary particles with **(a)** PEG only, **(b)** low [Ab] + PEG and **(c)** high [Ab] + PEG.

S3.6 Aggregation rate as a function of particle surface chemistry

To investigate the influence of the surface chemistry of the particles on the aggregation process three experiments are performed with different particle coatings: Firstly, a primary particle coated with a-cTnI Ab1 + 5kPEG and secondary particle coated with a-cTnI Ab1 + 5kPEG + 5% BSA physisorption (Fig. S3.6a). Secondly, a primary particle coated with a-cTnI Ab1 + 5kPEG and bare secondary particle with carboxyl groups (Fig. S3.6b). Thirdly, a primary particle coated with a-cTnI Ab2 + 5kPEG and secondary particle coated with a-cTnI Ab2 + 5kPEG (Fig. S3.6c). The variations in the obtained aggregation rate are small. The error in the aggregation rate is the fit error. However, the real error in the measurement also depends on the amount of statistics.

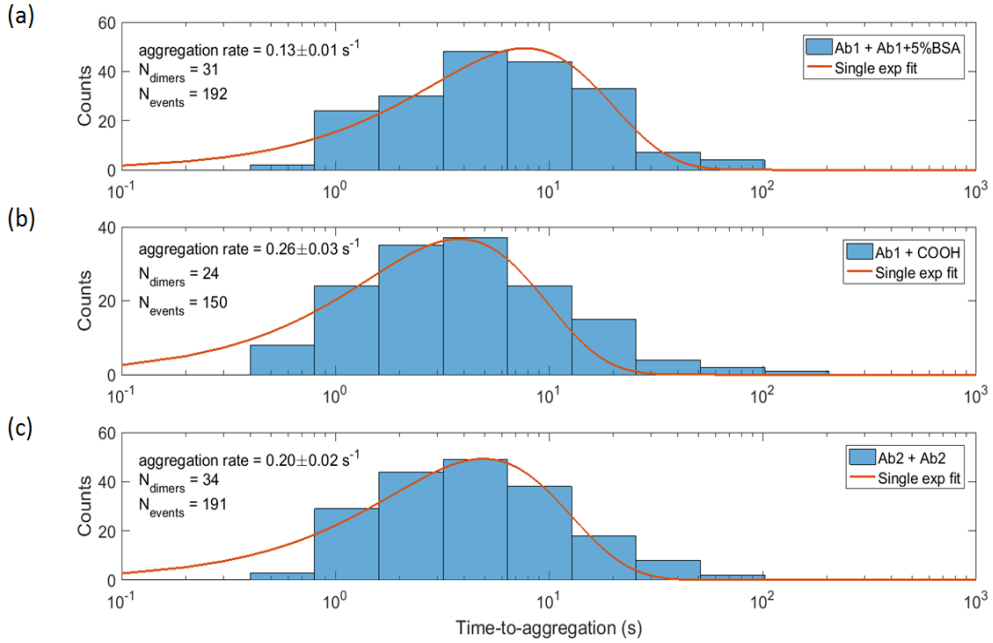

Fig. S3.6 Varying surface chemistry. Histograms of the time-to-aggregation measured with the single-dimer aggregation experiment for 500 nm particles with different surface chemistries: **(a)** Primary particle coated with a-cTnI Ab1 + 5kPEG and secondary particle coated with a-cTnI Ab1 + 5kPEG + 5% BSA physisorption. **(b)** Primary particle coated with a-cTnI Ab1 + 5kPEG and bare secondary particle with carboxyl groups. **(c)** Primary particle coated with a-cTnI Ab2 + 5kPEG and secondary particle coated with a-cTnI Ab2 + 5kPEG.

References

[1] Sun, C.; Lee, J. S. H.; Zhang, M. Magnetic nanoparticles in MR imaging and drug delivery. *Adv. Drug. Del. Rev.* **2008**, 60, 1252-1265

[2] Indira, T. K.; Lakshmi, P. K. Magnetic nanoparticles - A review. *Int. J. of Pharm. Sci. and Nanotech* **2010**, 3 (3), 1035-1042

[3] Pankhurst, Q. A.; Connoly, J.; Jones, S. K.; Dobson, J. Applications of magnetic nanoparticles in biomedicine. *J. Phys. D: Appl. Phys.* **2003**, R167-R181

[4] Müller, R. H.; Mäder, K.; Gohla, S. Solid lipid nanoparticles for controlled drug delivery - a review of the state of the art. *Europ. J. Pharma. and Biopharma.* **2000**, 50, 161-177

[5] Mohanraj, V. J.; Chen, Y. Nanoparticles - A review. *Trop. J. Pharm. Res.* **2006**, 5 (1) 561-573

[6] Zeng, S.; Yong, K. T.; Roy, I.; Dinh, X. Q.; Yu, X.; Luan, F. A review on functionalized gold nanoparticles for biosensing applications. *Plasmonics* **2011**, 6, 491-506

[7] Howes, P. D.; Chandrawatti, R.; Stevens, M. M. Colloidal nanoparticles as advanced biological sensors. *Science* **2014**, 346 (6205)

[8] Wicki, A.; Witzigmann, D.; Balasubramanian, V.; Huwyler, J. Nanomedicine in cancer therapy: Challenges, opportunities, and clinical applications. *J. of Contr. Release* **2015**, 200, 138-157

[9] Gupta, A. K.; Gupta, M. Synthesis and surface engineering of iron oxide nanoparticles for biomedical applications. *Biomaterials* **2005**, 26, 3995-4021

[10] Mosayebi, J.; Kiyasatfar, M.; Laurent, S. Synthesis, functionalization and design of magnetic nanoparticles for theranostic applications. *Adv. Health. Mater.* **2017**, 1700306

[11] Li, Z.; Barnes, J. C.; Bosoy, A.; Stoddart, J. F.; Zink, J. I. Mesoporous silica nanoparticles in biomedical applications. *Chem. Soc. Rev.* **2012**, 41, 2590-2605

[12] Rao, J. P.; Geckeler, K. E. Polymer nanoparticles: preparation techniques and size-control parameters. *Prog. in Poly. Sci.* **2011**, 36, 887-913

[13] Daniel, M. C.; Astruc, D. Gold nanoparticles: Assembly, supramolecular chemistry, quantum-size-related properties, and applications towards biology, catalysis and nanotechnology. *Chem. Rev.* **2004**, 104, 293-346

[14] Prabhu, S.; Poulose, E. K. Silver nanoparticles: mechanism of antimicrobial action, synthesis, medical applications, and toxicity effects. *Int. Nano Letters* **2012**, 2 (32)

[15] Mahmoudi, M.; Sant, S.; Wang, B.; Laurent, S.; Sen, T. Superparamagnetic iron oxide nanoparticles (SPIONs): Development, surface modification and applications in chemotherapy. *Adv. Drug Del. Rev.* **2011**, 63, 24-46

[16] Suk, J. S.; Xu, Q.; Kim, N.; Hanes, J.; Ensign, L. M. PEGylation as a strategy for improving nano-particle based drug and gene delivery. *Adv. Drug Del. Rev.* **2016**, 99, 28-51

[17] Ranzoni, A.; Schleipen, J. J. H. B.; van IJzendoorn, L. J.; Prins, M. W. J. Frequency-selective rotation of two-particle nanoactuators for rapid and sensitive detection of biomolecules. *Nano Lett.* **2011**, 11, 2017-2022

[18] Chen, K. L.; Mylon, S. E.; Elimelech, M. Aggregation kinetics of alginate-coated hematite nanoparticles in monovalent and divalent electrolytes. *Environ. Sci. Technol.* **2006**, 40, 1516-1523

[19] French, R. A.; Jacobson A. R.; Kim, B.; Isley, S. L.; Penn, R. L.; Baveye, P. C. Influence of ionic strength, pH, and cation valence on aggregation kinetics of titanium dioxide nanoparticles. *Environ. Sci. Technol.* **2009**, 43, 1354-1359

[20] Liu, J.; Legros, S.; Ma, G.; Veinot, J. G. C.; von der Kammer, F.; Hofmann, T. Influence of surface functionalization and particles size on the aggregation kinetics of engineered nanoparticles. *Chemosphere* **2012**, 87, 918-924

[21] Scheepers, M.R.W.; Romijn, A.R.; van IJzendoorn, L.J.; Prins, M.W.J. Rate of dimer formation in stable colloidal solutions quantified using an attractive interparticle force. *Langmuir*, **2019**, accepted for publication

[22] Van Der Pol, E.; Coumans, F.A.W.; Grootemaat, A.E.; Gardiner, C.; Sargent, I.L.; Harrison, P.; Sturk, A.; Van Leeuwen, T.G.; Nieuwland, R. Particle size distribution of exosomes and microvesicles determined by transmission electron microscopy, flow cytometry, nanoparticle tracking analysis, and resistive pulse sensing. *J. Thromb. Haemost.* **2014**, 12, 1182-1192

[23] Daynès, A.; Temurok, N.; Gineys, J.; Cauet, G.; Nerin, P.; Baudry, J.; Bibette, J. Fast magnetic field-enhanced linear colloidal agglutination immunoassay. *Anal. Chem.* **2015**, 87, 7583-7587

[24] Grier, D.G. Optical tweezers in colloid and interface science. *Curr. Opin. Colloid interface Sci.* **1997**, 2, 264-270

[25] Courtney, C.R.P.; Demore, C.E.M.; Wu, H.; Grinenko, A.; Wilcox, P.D.; Cochran, S.; Drinkwater, B.W. Independent trapping and manipulation of microparticles using dexterous acoustic tweezers. *Appl. Phys. Lett.* **2014**, 104 154103

[26] Kemper, M.; Spridon, D.; van IJzendoorn, L.J.; Prins, M.W.J. Interactions between protein coated particles and polymer surfaces studied with the rotating particles probe. *Langmuir*, **2012**, 28, 8149-8155

[27] Ducker, W. A.; Senden, T. J.; Pashley, R.M. Direct measurement of forces using an atomic force microscope. *Nature* **1991**, 353, 239-241

[28] Götzinger, M.; Peukert, W. Dispersive forces of particle-surface interactions: Direct AFM measurement and modeling. *Powder Technology* **2003**, 130, 102-109

[29] Helfricht, N.; Mark, A.; Drowling-Carter, L.; Zambelli, T.; Papastavrou, G. Extending the limits of direct force measurements: colloidal probes from sub-micron particles. *Nanoscale* **2017**, 9, 9491

[30] Freitas, A. M.; Sharma, M. M. Detachment of particles from surfaces: An AFM study. *Coll. Int. Sci.* **2001**, 233, 73-82

[31] Schein, P.; Kang, P.; O'Dell, D.; Erickson, D. Nanophotonic force microscopy: Characterizing particle-surface interactions using near field photonics. *Nano Lett.* **2015**, 15, 1414-1420

[32] van Ommering, K.; Koets, M.; Paesen, R.; van IJzendoorn, L.; Prins, M. Bond characterization by detection and manipulation of particle mobility in an optical evanescent field biosensor. *J. Phys. D: Appl. Phys.* **2010**, 43, 385501

[33] Bouyer, F.; Robben, A.; Yu, W.L.; Borkovec, M. Aggregation of colloidal particles in the presence of oppositely charged polyelectrolytes: Effect pf surface charge heterogeneities. *Langmuir* **2001**, 17, 5225-5231

[34] Freitas, C.; Müller, R.H. Effect of light and temperature on zeta potential and physical stability in solid lipid nanoparticle dispersions. *Int. J. of Pharmaceutics* **1998**, 168, 221-229

[35] Nicoud, L.; Jagielski, J.; Pfister, D.; Lazzari, S.; Massant, J.; Lattuada, M.; Morbidelli, M. Kinetics of monoclonal antibody aggregation from dilute toward concentrated conditions. *J. Phys. Chem. B*. **2016**, 120, 3267-3280

[36] Vázquez-Rey, M.; Lang, D.A. Aggregates in monoclonal antibody manufacturing processes. *Biotechnology and Bioengineering* **2011**, 108, 7, 1494-1508

[37] Shire, S.J.; Shahrokh, Z.; Liu, J. Challenges in the development of high protein concentration formulations. *J. Pharm. Sci.* **2004**, 93, 6, 1390-1402

[38] Buijs, J.; Hlady, V. Adsorption kinetics, conformation and mobility of the growth hormone and lysozyme on solid surfaces studied with TIRF. *J. Colloid Interface Sci.* **1997**, 190, 171-181

[39] Kim, J.; Somorjai, G.A. Molecular packing of lysozyme, fibrinogen and bovine serum albumin on hydrophilic and hydrophobic surfaces studied by infrared visible sum frequency generation and fluorescence microscopy. *J. Am. Chem. Soc.* **2003**, 125, 3150-3158

[40] Norde, W.; Favier, J.P. Structure of adsorbed proteins and desorbed proteins. *Colloids and surfaces* **1992**, 64, 87-93

[41] Cheng, Y.Y.; Chang, H.C.; Hoops, G.; Su, M.C. Stabilization of yeast cytochrome c covalently immobilized on fused silica surfaces. *J. Am. Chem. Soc.* **2004**, 126, 10828-10829

[42] Moerland, C.P.; van IJzendoorn, L.J.; Prins, M.W.J. Rotating magnetic particles for lab-on-chip applications - A comprehensive review. *Lab Chip*, **2019**, 19,919-933

Chapter 4

Inter-particle biomolecular reactivity tuned by surface crowders

The rate at which colloidal particles can form biomolecular bonds controls the kinetics of applications such as particle-based biosensing, targeted drug delivery and directed colloidal assembly. Here we study how the reactivity of the particle surface depends on its molecular composition, quantified by the inter-particle rate of aggregation in an optomagnetic cluster experiment. Particles were functionalized with DNA or with proteins for specific binding, and with polyethylene glycol as a passive surface crowder. The data show that the inter-particle binding kinetics are dominated by specific interactions, which surprisingly can be tuned by the passive crowder molecules, for both the DNA and the protein system. The experimental results are interpreted using model simulations, which show that the crowder-induced decrease of the particle surface reactivity can be described as a reduced reactivity of the specific binder molecules on the particle surface.

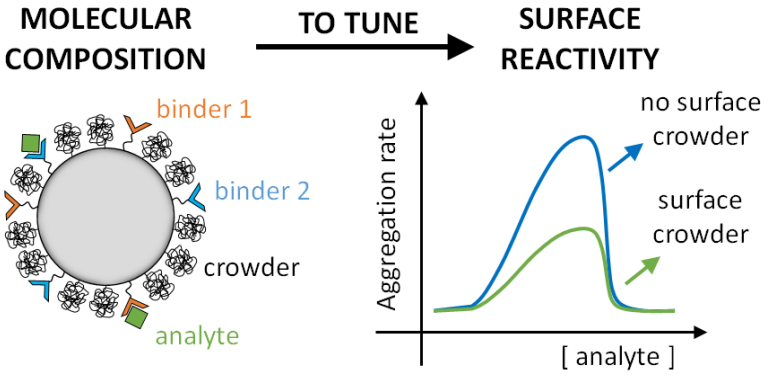

This chapter is in preparation as a manuscript: Scheepers, M.R.W.; Haenen, S.R.R.; Coers, J.M.; van IJzendoorn, L.J.; Prins, M.W.J. Inter-particle biomolecular reactivity tuned by surface crowders.

4.1 Introduction

The behaviour of biofunctionalized colloidal particles in complex biological systems is determined by both specific and non-specific interactions, each conferred to the particle by different molecular means. Specific binding functionality is conferred to the particles by coupling macromolecules with specific binding affinities to the particle surface, such as antibodies[1,2], oligonucleotides[3,4], or aptamers[5,6]. Non-specific interactions can be controlled by providing e.g. charges[7] or hydrophilic polymers[8,9] on the particle surface, in order to stabilize the particles and achieve low biofouling properties.

The specific and nonspecific binding properties of biofunctionalized particles can be studied in biochemical assays as well as in biophysical experiments. An example of a biophysical experiment is colloidal probe atomic force microscopy (AFM), to measure force-distance curves in liquids between a single micrometer sized colloidal probe and a surface or a second particle[10]. The potential energy landscape of functionalized particles above a substrate can be explored using total internal reflection microscopy (TIRM)[11-13], and the interactions between two functionalized particles can be studied using optical tweezers[14]. However, these methods cannot quantify the biomolecular reactivity of colloidal particles.

In this paper we quantify the biomolecular reactivity of functionalized colloidal particles in an optomagnetic cluster (OMC) experiment[15]. The OMC experiment was originally developed for rapid and sensitive biomarker quantification by measuring the equilibrium aggregation state of a colloidal solution[1]. Ranzoni et al. showed subpicomolar detection of prostate specific antigen (PSA) in buffer and in blood plasma. Recently, we demonstrated that the OMC experiment allows quantification of the non-specific kinetic rate of dimer formation k_{agg} within an ensemble of biofunctionalized particles[15]. The parameter k_{agg} represents the rate at which biochemical inter-particle aggregation occurs, for particles that are in a well-defined state of proximity. In the OMC experiment, the proximal state is created and controlled by an attractive magnetic inter-particle force. The aggregation rate k_{agg} is a measure of the particle surface reactivity and represents the particle equivalent of the molecular association rate k_{on}.

The aggregation rate of colloidal particles has contributions from specific and nonspecific interactions, which are often studied independently. For example, passive hydrophilic molecules are applied in order to form a crowded layer that generates steric repulsion between particles[8,9]. In this study, we hypothesized that the steric repulsion by hydrophilic surface crowders might affect not only nonspecific interactions between particles, but may also have an effect on specific inter-particle

interactions. For this purpose, particles were provided with a coating consisting of specific binders (antibodies or DNA oligonucleotides) and passive polyethylene glycol (PEG) molecules of different molecular weights. The dependence of the particle surface reactivity on the density of specific binders was studied in a sandwich-type aggregation assay, where aggregation is induced using a specific bridging molecule (a protein or an oligonucleotide) called the analyte, see Fig. 4.1. The data show that the specific aggregation rate is reduced, for all analyte concentrations, by the presence of PEG molecules on the particle surface, as schematically shown in Fig. 4.1c. Simulations are performed to interpret the data in terms of the underlying molecular parameters. The paper concludes with an outlook on reactivity modulations that may be achieved by further surface engineering.

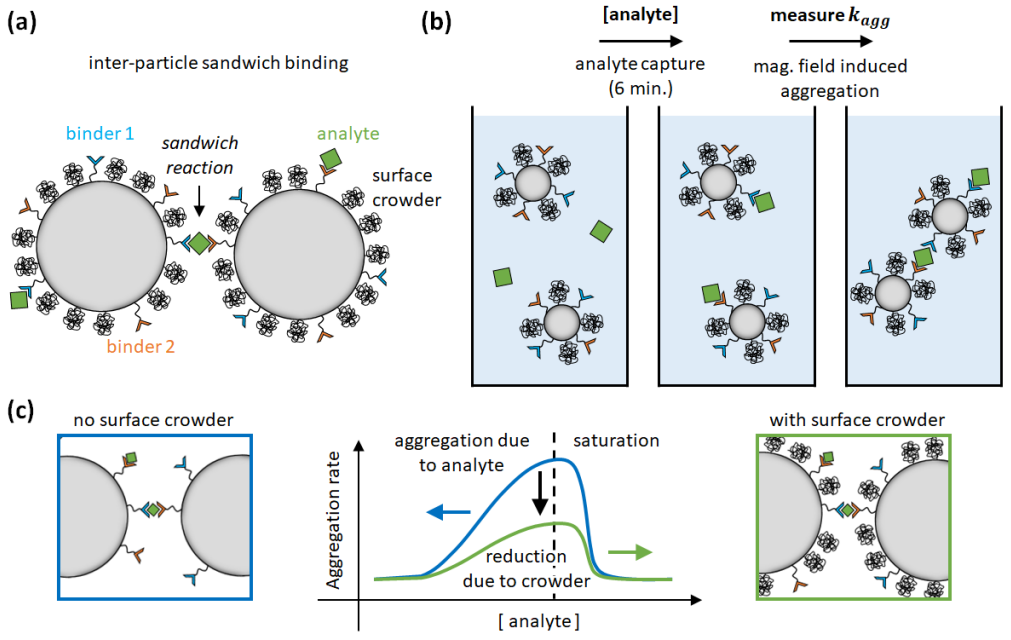

Fig. 4.1 Study of inter-particle biomolecular reactivity as a function of surface-crowding PEG molecules. (a) Particle dimers are formed in a sandwich-type aggregation assay, with specific binder molecules on the particle surface (binder 1 and binder 2) and specific bridging molecules called analyte. The particle is also functionalized with PEG crowders, to investigate the influence of the PEG molecules on the specific particle aggregation process. **(b)** The assay consists of an analyte capture phase of 6 min, and subsequently an aggregation rate measurement using optomagnetic detection15. **(c)** The aggregation rate is measured as a function of analyte concentration. The experiments show that PEG molecules on the particle surface reduce the specific aggregation rate.

4.2 Materials and methods

4.2.1 Materials

Carboxylated superparamagnetic Masterbeads were purchased from Ademtech SA (diameter 528 nm, coefficient of variation 25%). Streptavidin coated superparamagnetic silica particles were obtained from MircoParticles GmbH (diameter 511 nm, coefficient of variation <5%). Biotinylated DNA docking strands and DNA analyte strands were purchased from Integrated DNA Technology Inc. (IDT). For a complete list of the used DNA sequences, see Supporting Information section S4.2. Prostate specific antigen (PSA) was purchased from Abcam plc. and a matching pair of monoclonal mouse IgGs against PSA (α-PSA10 and α-PSA66) were supplied by Fujirebio Europe N.V. Amine-terminated polyethylene glycol (PEG) and biotin-terminated PEG with molecular weights of 5, 10, 20, 30 and 40 kDa were purchased from Creative PEGworks. Phosphate buffered saline (PBS) tablets, Pluronic F-127, 2-(N-morpholino)ethanesulfonic acid (MES), 1-ethyl-3-(dimethylaminopropyl)carbodiimide hydrochloride (EDC), tris(hydroxymethyl)aminomethane (tris), N-hydroxysulfosuccinimide (sulfo-NHS), bovine serum albumin (BSA, >98% pure), biotin-Atto655 and DNA LoBind and Protein LoBind Eppendorf tubes were obtained from Sigma Aldrich Inc. Borosilicate glass 3.3 cuvettes with inner dimensions of 1.00±0.05 mm x 1.00±0.05 mm and outer dimensions of 1.23±0.05 mm x 1.23±0.05 mm, and a length of 20±1 mm were obtained from Hilgenberg GmbH and used in the optomagnetic cluster experiment.

4.2.2 Particle functionalization for DNA model system

Streptavidin coated silica MicroParticles were functionalized with biotinylated DNA docking and DNA filler strands and biotinylated PEG (10, 20, 30 or 40 kDa) by sequential incubation steps. First, 15 µL of the particle stock solution (10 mg/mL) was mixed with 285 µL of DNA docking strand solution in PBS, and incubated for 60 minutes in an incubator shaker (1200 rpm, room temperature). Subsequently 2 µL of a large excess of DNA filler strands is added to saturate the particle surface with DNA, and incubated for 60 minutes in an incubator shaker (1200 rpm, room temperature). The amount of functional docking DNA during the first incubation step was varied throughout the experiments.

For measuring the effect of PEG on the aggregation rate, first DNA docking strand were coated on the particle, and the docking-DNA-to-particle-ratio was kept equal to 5,000. After the first incubation step, the particle solution was magnetically washed to remove unbound DNA docking strands. The particles were redispersed in a 1 mM biotin-PEG solution of a certain molecular weight and incubated for 60 minutes in an

incubator shaker (1200 rpm, room temperature) to saturate the remaining streptavidin groups with biotin-PEG.

After the second incubation step, the particle solution was magnetically washed again to remove the unbound PEG. The particles were redispersed in a 10 mg/mL BSA in PBS solution to suppress nonspecific aggregation of the particles. The particle solution was then incubated in a sonic bath for 10 minutes and the solution was sonicated (10x 0.5s) to reduce the number of clusters in the solution.

4.2.3 Quantification of the DNA docking strand coverage

To quantify the number of DNA docking strands on the streptavidin coated Microparticles an indirect fluorescence supernatant assay is performed. First, the biotin capacity of the particles is quantified by binding increasing amounts of biotin-atto655 on the particles, during 60 minutes in an incubator shaker (1200 rpm, room temperature). The lowest b-atto655 concentration at which there is still b-atto655 left over in the supernatant after incubation is quantified using a Fluoroskan Ascent FL (λ_{ex} = 646 nm, λ_{em} = 679 nm, spectral width 5 nm). The b-atto655 capacity per particle is equal to $N_{b-atto655}$ = (4.3±0.5)·10^4.

Next, increasing amounts of biotinylated DNA are added to the particles and incubated during 60 minutes in an incubator shaker (1200 rpm, room temperature). After this incubation step, the particle solution is magnetically washed to remove unbound DNA strands. Subsequently, b-atto655 is added in a concentration that is slightly above the b-atto655 capacity of the particles. Again an incubation step is performed during 60 minutes in an incubator shaker (1200 rpm, room temperature). Particles that are not fully coated with DNA strands will bind some of the b-atto655 in the solution, the fully coated particles will not bind b-atto655. After the incubation the particle solutions are magnetically washed and the fluorescence of the supernatant is measured. The amount of b-atto655 in the supernatant for a certain DNA concentration, $I_{s.n.}([DNA])$, is related to the number of DNA on the particle, N_{DNA}, according to equation 4.1.

$$N_{DNA} = \frac{I_0 - I_{s.n.}([DNA])}{I_0 - I_{s.n.}([DNA]=0)} \cdot N_{b-atto655} \tag{4.1}$$

Here I_0 is the fluorescence intensity of the b-atto655 solution that is added in the second incubation step, and $I_{s.n.}([DNA] = 0)$ is the fluorescence intensity of the supernatant when adding non-functionalized streptavidin Microparticles. For more details of the supernatant assay, see Supporting Information section S4.3.

4.2.4 Particle functionalization for the antibody sandwich system

Carboxylic acid coated Ademtech Masterbeads were functionalized through an EDC-NHS reaction with a matching pair of monoclonal PSA antibodies that target a different epitope on the PSA antigen. The particle surface area in between the antibodies area was coated with an amine-terminated PEG (10, 20, 30 or 40 kDa) and the remaining surface area was blocked with tris. All steps were performed at room temperature.

First, 4 µL of particle stock solution (50 mg/mL) was mixed with 196 µL a 100 mM MES solution (pH 5.0), 50 µL EDC in MES solution (10 mg/mL) and 50 µL NHS in MES solution (10 mg/mL). The particles were incubated for 30 minutes on a roller bench to activate the carboxyl groups on the particle surface.

After the activation step the particles were magnetically washed twice and redispersed in 200 µL MES solution. Subsequently the particle solution was sonicated (10x 0.5s) to undo the particle clustering that occurred during the magnetic washing steps. Then, 100 µL of antibody solution was added to the particles and incubated for 30 minutes on a roller bench, to covalently attach the antibodies to the particles. The antibody concentration was varied in one of the experiments. However, if not specified in the text, the antibody-to-particle ratio during incubation was kept equal to 1500.

After the antibody coating step 50 μL of amine-terminated PEG solution (1 mM) was added to the particle solution and incubated for 180 minutes on a roller bench. To block the remaining active carboxyl groups, 100 µL of tris buffer is added (150 mM NaCl, 50 mM tris, pH 7.6) and incubated overnight on a roller bench. Finally, the particle solution is magnetically washed twice and the particle are redispersed in a 10 mg/mL BSA in PBS solution to suppress nonspecific particle aggregation. Finally, the particle solution was sonicated (10x 0.5s) to undo the particle clustering that occurred during the functionalization process.

4.3 Specific particle aggregation quantified for DNA and protein systems

The specific particle aggregation rate is first investigated for the DNA system and the protein system without passive surface crowders. The inter-particle aggregation rate is quantified using the OMC experiment. This methodology is summarized in section S4.1 of the Supporting Information.

In the DNA model system, see Fig. 4.2a, streptavidin coated Microparticles were functionalized with biotinylated DNA docking strands and DNA filler strands. The docking DNA consists of a 20 bp dsDNA with a 15 nt ssDNA overhang. The filler strands are similar to the docking strands, but do not have the 15 nt ssDNA overhang. The maximum docking strand density per particle was quantified using an indirect supernatant assay, giving $\sigma_{dock,max}$ = (2.0±0.4)·10^4 μm^{-2}. By varying the concentration of docking DNA and filler DNA strands, the docking strand coverage was controlled (functionalization protocol is described in Materials and methods section). A complete description of the DNA strands and the supernatant assay is given in sections S4.2 and S4.3 of the Supporting Information, respectively.

The DNA analyte is symmetric, with a central 20 bp dsDNA fragment and on both ends a 15 nt ssDNA overhang that can bind to the docking DNA on the particles, in this way forming a specific molecular bridge between two particles. The 15-bp complementarity ensures that this bond is stable throughout the complete experiment (~10 min). The DNA coated particles were incubated with a controlled concentration of analyte DNA for six minutes. After five minutes of incubation, the OMC actuation protocol was started, such that during the last minute of the incubation the first measurement phase was executed. Subsequently the actuation phase, waiting phase and second measurement phase were performed. The aggregation rate k_{agg} was then determined using equation S4.1.

Fig. 4.2b shows the measured aggregation rate as a function of the analyte concentration scaled to the particle concentration, for four different docking strand coverages on the particles. Without analyte, the observed aggregation rate is much lower than the rates observed in the presence of analyte, demonstrating the high molecular control of the system. For analyte-to-particle-ratios below 10^3, the aggregation rate increases with analyte concentration by two effects: Having more analytes per particle increases the probability that an analyte molecule is present in the interaction area of a dimer, allowing for specific aggregation of the two particles. For even more analytes per particle, all dimers have analytes in their interaction area and an increase in the number of analytes in the interaction area further increases the particle reactivity. For analyte-to-particle-ratios around 10^3, the aggregation rate reaches a maximum value. At this point the system is in its most reactive state, which implies that half of the docking strands is covered with an analyte strand. For analyte-to-particle-ratios higher than 10^3, the aggregation rate decreases because the docking strands on the particle surface become saturated with analyte strands. Note that the actual number of analytes per particle may be lower than the indicated analyte-to-particle ratio, due to the short incubation time of six minutes.

The docking strand surface density was also varied in this experiment. The total number of DNA strands on the particles was kept constant by saturating the surface with filler strands, in order to keep the electrostatic repulsion constant. For each non-zero analyte concentration, the particles with a higher docking strand coverage aggregate faster. For a docking strand surface density $\sigma_{dock} \leq 5.1 \cdot 10^2$ μm^{-2}, the aggregation rate is measurable for the complete analyte concentration range. For a binder density of $\sigma_{dock} = 2.0 \cdot 10^4$ μm^{-2} and analyte-to-particle-ratios above $4 \cdot 10^2$, the aggregation rate is equal to the experimental limit of 0.1 s^{-1}. Under these conditions, the particle surface is so reactive that all magnetic dimers chemically aggregate during the interaction time in the experiment.

In the antibody sandwich system, see Fig. 4.2c, carboxylic acid coated Ademtech Masterbeads were functionalized with a matching pair of anti-PSA antibodies (α-PSA10 and α-PSA66) via EDC-NHS chemistry (complete functionalization protocol is described in Materials and methods section). Note that each particle contains both types of antibodies. In the presence of PSA, the particles can specifically aggregate by sandwiching a PSA molecule between an α-PSA10 antibody on one particle and an α-PSA66 antibody on the other particle, or vice versa. The particle surface reactivity was varied by varying the antibody concentration during the particle functionalization and the incubation with the PSA analyte. Fig. 4.2d shows the measured aggregation rate as a function of the PSA concentration scaled to the particle concentration, for three different antibody concentrations. The PSA incubation time was six minutes.

The measured aggregation rate of the antibody coated particles shows a similar analyte concentration dependence as the DNA sandwich system. For increasing PSA concentrations the aggregation rate initially increases w.r.t. the nonspecific aggregation rate. For PSA-to-particle-ratios between 10^3 and 10^4, the aggregation rate reaches its maximum value and for the highest antibody concentration reaches the experimental limit. For PSA-to-particle-ratios higher than 10^4, the aggregation rate decreases due to saturation of the antibodies on the particle surface. A control experiment was performed in which the aggregation rate was measured for particles functionalized with only a single type of antibody. Fig. S4.4 shows that the aggregation rate of the control does not depend on PSA concentration, thus confirming that the PSA induced binding is only possible for a matching antibody pair.

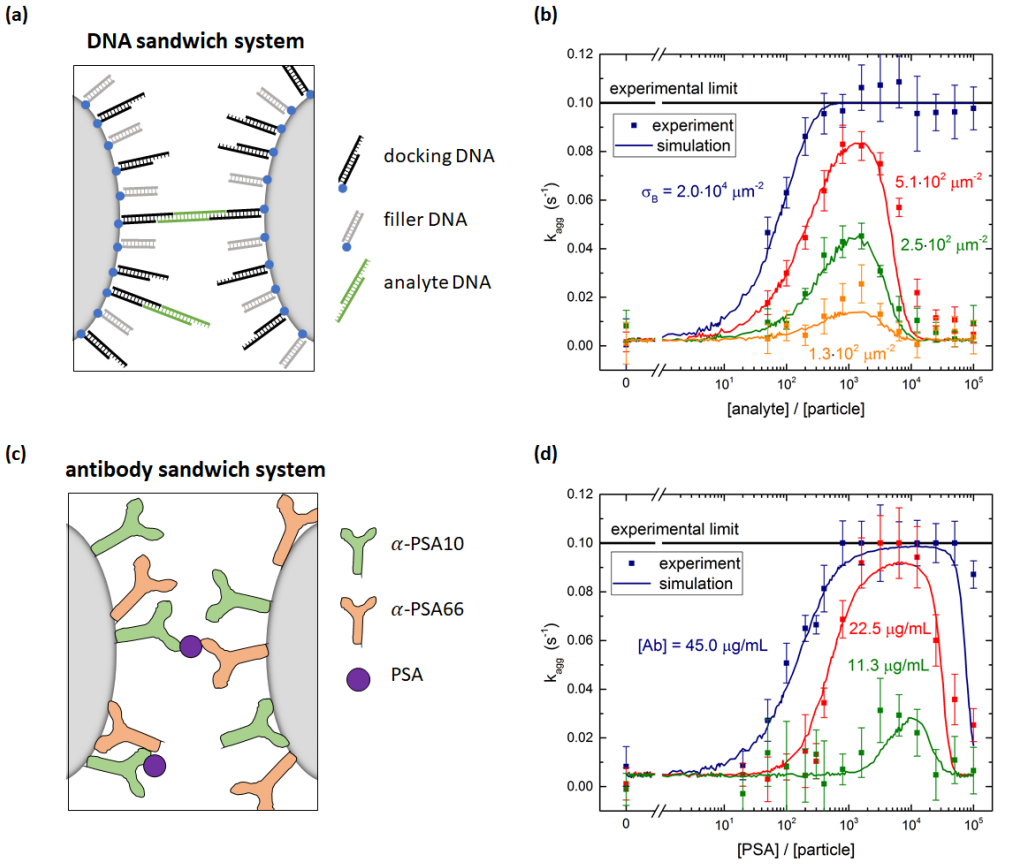

Fig. 4.2 Specific particle aggregation rates measured with the optomagnetic experiment. (a) DNA sandwich system consisting of streptavidin coated particles functionalized with biotinylated DNA docking and filler strands. Specific binding is induced by a symmetric DNA analyte molecule. **(b)** Measured aggregation rate as a function of the DNA analyte concentration for particles with different densities of DNA docking strands. The lines through the data points represent simulation results. The input parameters of these simulations can be found in Supporting Information Section S4.6. **(c)** Antibody sandwich system consisting of carboxylic acid coated particles functionalized with a matching pair of PSA antibodies. The PSA molecules form specific molecular bridges between the particles. **(d)** Measured aggregation rate as a function of the PSA concentration for particles functionalized with different concentrations of PSA antibodies. The lines through the data points represent simulation results. The input parameters of these simulations can be found in Supporting Information Section S4.6.

The particle aggregation process is not only determined by the surface reactivity of the particles, but also by the particle encountering process. Previous measurements performed by Ranzoni et al.[8] on a comparable antibody sandwich system showed that the equilibrium particle cluster concentration as a function of PSA concentration is sensitive in the range of 0.2-200 PSA per particle. The aggregation rate measurements described here show a PSA dependence in the range of 300-3000 PSA per particle. The difference in PSA dynamic range is caused by the different particle

encountering processes. Ranzoni et al. used multiple short magnetic field pulses, whereby magnetic dimers were brought in close proximity many times for a short interaction time. Each time a different interaction area on the particle was probed, such that even particles with a single PSA molecule are at some point in the correct orientation for binding. For a PSA concentration that is much larger than the particle concentration, all particles can aggregate and the equilibrium state is always the fully clustered state. In the experiments of this paper, we measure the aggregation rate by bringing dimers in close proximity only once for a longer interaction time. For [PSA] ≈ [particle], most magnetic dimers will not have their binding sites aligned, and therefore the aggregation rate cannot be distinguished from the nonspecific interaction. For [PSA] ≫ [particle], all magnetic dimers can aggregate if the antibody surface density is sufficiently high.

4.4 Simulating specific particle aggregation

To interpret the measured aggregation rates, a stochastic binding simulation was developed which mimics the specific aggregation process in the OMC experiment. Briefly, during an actuation time t_{act} magnetic dimers are formed at a constant rate (as shown in Section S4.1 of the Supporting Information). Each dimer has a probability to chemically aggregate which depends on several parameters that are included in the simulation: the binder and analyte density on the particle surface, the intrinsic molecular analyte-binder binding rate, and the interaction time of the magnetic dimer. For all magnetic dimers it is checked if chemical aggregation occurs, after which the average aggregation rate of the ensemble of particles is calculated according to equation S4.1. The resulting aggregation rates are then compared to the experimental results.

In the simulation, particles are modelled as spheres with radius R and a binder surface density σ_B (either DNA docking strands or antibodies) where the number of binders per particle follows a Poisson distribution. For a given analyte concentration $[A]$ and a given binder areal surface density σ_B, the rate at which analytes from the solution bind to the binders on the particle surface during the incubation time is described by equation 4.2.

$$\frac{d\sigma_{AB}}{dt} = k_{on}[A]\sigma_B \tag{4.2}$$

Here, σ_{AB} represents the particle surface density of bound analytes. k_{on} is the association rate between analyte and binder, for a binder on a particle surface and analyte in solution. Using equation 4.2 we can numerically calculate the analyte

surface density after the incubation time t_{inc} as a function of the analyte concentration in solution.

During the actuation time, magnetic dimers are created at a constant encounter rate k_{enc}, neglecting monomer depletion and the formation of larger clusters (as justified in section S4.1 and reference 15). For two particles that are magnetically attracted to become a dimer, we define an interparticle distance Δx with a cylindrical interaction volume defined as schematically shown in Fig. 4.3a. The length of the cylindrical volume is limited by the specific bond length of the interaction, L_{bond}. For the DNA model system this is taken as the length of the hybridized docking-analyte-docking DNA complex (~31 nm), whereas for the antibody system it is taken as the length of the antibody-antigen-antibody sandwich (~35 nm).

The interaction volume defines an interaction area at the particle surfaces in which the analytes on one particle can form bonds with the binders on the other particle, and vice versa. The specific particle aggregation rate depends on the surface reactivity of the particles and can be expressed in terms of the analyte areal density σ_{AB} (analyte A bound to binder B) and the free binder areal density σ_B. The rate of formation of chemical bonds between two interacting surfaces is described by k_{chem}, expressed in unit $\mu m^2 s^{-1}$. This describes the rate of bond formation between one particle with unit binder density and another particle with unit analyte density, averaged over all possible configurations of the binders and analytes in the interaction area on the particles. The rate k_{chem} depends on the molecular interaction and the distance between the interacting surfaces. For two particles, the interacting surfaces are curved and the interaction distance is a function of the position in the interaction area.

The density of bonds that is formed between analytes on particle 1 and binders on particle 2 and vice versa during the interaction time t_{int} is numerically calculated using equation 4.3.

$$\frac{d\sigma_{bond}}{dt} = k_{chem}\sigma_{AB}\sigma_B \tag{4.3}$$

The absolute number of bonds between the particles in the dimer is calculated by multiplying the bond density by the interaction area, see equation 4.4.

$$N_{bonds} = \sigma_{bond}A_{int} \tag{4.4}$$

In case $N_{bonds} \geq 1$, the dimer is marked as a chemical dimer. In addition to the specific aggregation a constant non-specific aggregation rate $k_{chem,ns}$ is included in the simulation. Similar to the experiment, the ensemble average aggregation rate k_{agg} is calculated, see equation S4.1.

A parameter scan has been performed to investigate the effect of several input parameters on the simulated particle aggregation rate k_{agg}. In each scan all other parameters were kept constant at the default value shown in Table S4.4. Fig. 4.3b-d show the simulated aggregation rates as a function of the analyte-to-particle concentration ratio. The simulated curves resemble the trends observed in the measurements: for low analyte concentration the aggregation rate increases with analyte concentration, for intermediate analyte concentration the aggregation rate reaches a maximum value and for high analyte concentration the aggregation rate decreases. The position of the maximum represents the situation where 50% of the binders is covered by an analyte.

Fig. 4.3b shows the simulated aggregation rate for different analyte association rates k_{on}. For increasing k_{on}, the analyte coverage on the particle is higher at the same analyte concentration, shifting the curves to lower analyte concentrations. In the limit of an infinite association rate, the analyte coverage equals the analyte-to-particle concentration ratio until the surface is saturated with analytes. Fig. S4.4a shows that for increasing binder density σ_B the aggregation rate increases and the position of the maximum shifts to higher analyte concentrations.

The simulated particle aggregation rate k_{agg} depends strongly on the intrinsic molecular aggregation rate k_{chem}, see Fig. 4.3c. For increasing k_{chem}, bond formation occurs faster which makes the particle surface more reactive, and thus the aggregation rate increases. The x-position of the maximum of the curve depends only on σ_B, t_{inc} and k_{on} and does not change with k_{chem}. However, the height of the maximum does increase with k_{chem}. Fig. 4.3d shows that increasing the interparticle distance Δx leads to a decrease in the particle aggregation rate which can be attributed to a decrease in the interaction area and the accompanying decrease in the absolute number of interacting analytes and binders.

The parameter scan for the experimental settings, magnetic dimer formation rate k_{enc} (Fig. S4.5b) and the actuation time t_{act} (Fig. S4.5c) are relatively modest and are explained in more detail in section S4.5 of the Supporting Information. Adding a nonspecific aggregation rate to the simulation, $k_{chem,ns}$ = 0.1 s^{-1}, leads to a non-zero background aggregation, see Fig. S4.5d.

The experimentally measured aggregation rates of Fig. 4.2b and 4.2d are accompanied by simulated aggregation rate curves. Apart from σ_B and the parameters relevant for the molecular system such as L_{bond} and $k_{chem,ns}$, all other input parameters are kept constant in the simulation. Particle radius R, incubation time t_{inc} and actuation time t_{act} are known in the experiment and the interparticle distance is estimated to be equal to the bond length minus the thickness of the two

coatings on the particles (Δx~19 nm). A complete list of the values of the input parameters for these simulations is given in Section S4.6 of the Supporting Information.

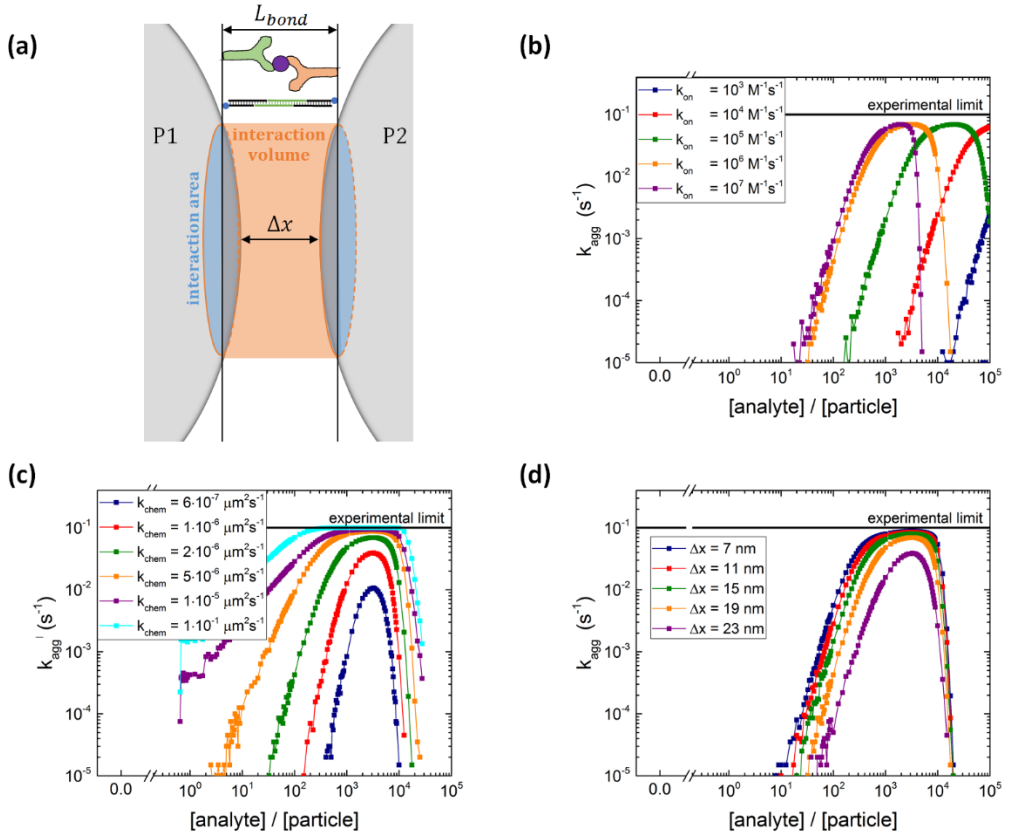

Fig. 4.3 Particle aggregation simulations with different input parameters k_{on}, k_{chem}, Δx. (a) Definition of interaction volume where the interaction areas on the two particles can form chemical bonds. The size of the interaction area depends on the maximum bond length (L_{bond}~35 nm for antibody sandwich system and L_{bond}~27 nm for DNA system) and on the interparticle distance Δx. **(b)** Simulated aggregation rate as a function of the analyte-to-particle ratio, for different analyte association rate constants k_{on} (k_{chem}= 2·10-6 µm2s-1 and Δx = 19 nm). Increasing the association rate leads to a shift of the curve to lower analyte concentrations. **(c)** Parameter scan of the chemical aggregation rate k_{chem} (k_{on} = 106 M-1s-1 and Δx = 19 nm). For higher k_{chem}, the aggregation rate increases. **(d)** Parameter scan of the interparticle distance Δx (k_{on} = 106 M-1s-1 and k_{chem}= 2·10-6 µm2s-1). A larger interparticle distance leads to a smaller interaction area and thus lower aggregation rates.

The simulated aggregation rate curves for the DNA model system in Fig. 4.2b closely resemble the experimental data. From this simulation two unknown parameters are obtained: the analyte association rate k_{on} = 1.5·10^6 $M^{-1}s^{-1}$ and the intrinsic chemical aggregation rate k_{chem} = 5.0·10^{-4} $\mu m^2 s^{-1}$. The association rate

obtained here, is similar in magnitude to the association rate measured for similar sized DNA oligonucleotides bound on the surface of a graphene field-effect transistor[16]. For the highest possible DNA docking strand density on the particle, the analyte association rate seems to be lower. Fig. S4.7 shows the measured aggregation rate for σ_{dock} = 2.0·10^4 μm^{-2} accompanied by simulations using k_{on} = 1.5·10^6 M^{-1}s^{-1} and k_{on} = 1.0·10^5 M^{-1}s^{-1}. The data and simulation agree best for the lower association rate. At this high DNA docking strand density, association of the negatively charged DNA analyte from the solution may be hindered by the negative charge on the particle.

The simulations of the antibody sandwich system are shown in Fig. 4.2d. The data give k_{on} = 1.9·10^5 M^{-1}s^{-1} and k_{chem} = 9.5·10^{-6} μm^{2}s^{-1}. The association and the intrinsic chemical binding rate for the PSA antibody system are lower compared to the DNA model system. Apparently, DNA hybridization is faster than antibody-antigen binding, which is probably due to multiple orientations in which DNA oligos can start hybridizing, while the reaction between an antibody and an antigen is orientationally much more restricted.

4.5 Tuning specific aggregation rate using passive surface crowders

In this section we investigate if it is possible to tune the specific reactivity of microparticles by incorporating PEG molecules on the particle surface. For the DNA model system the particles were coated with a lower density of biotinylated DNA docking strands and the remainder of the surface was saturated with biotin-PEG, see Fig. 4.4a. The DNA docking strand density was quantified to be σ_{dock} = (5.6±0.5)·10^3 μm^{-2}, so 28% of the docking strand capacity, leaving room for immobilization of PEG molecules.

Fig. 4.4b shows the measured aggregation rate as a function of the analyte-to-particle ratio, for DNA particles coated with 10, 20, 30 or 40 kDa PEG or without PEG. The 10 and 20 kDa PEG curves are very similar to the measurement without PEG, only the 10 and 20 kDa curves are shifted to slightly higher analyte concentrations. Such a horizontal shift of the curve has been observed in the parameter scan of the simulation for a decreasing association rate k_{on}. Consequently, one might hypothesize that the presence of the PEG close to the docking strands may hinder the association of analytes on the docking strands.

The nonspecific interaction is higher for the 10 and 20 kDa PEG coated particles compared to the 0, 30 and 40 kDa PEG coated particles, possibly caused by nonspecific PEG-DNA interaction[17]. The Flory radius of a 10 kDa PEG molecule ($2R_F$ = 18 nm) is similar to the length of the docking strands (L_{dock} ≈ 16 nm) on the

particle, which makes interaction between the PEG on one particle and the DNA on the other particle possible. For the 20 kDa PEG ($2R_F$ = 28 nm), the 30 kDa PEG ($2R_F$ = 36 nm) and the 40 kDa PEG ($2R_F$ = 42 nm), the Flory radius significantly exceeds the length of the docking strand, such that steric repulsion between the PEG molecules may prevent nonspecific aggregation. However, for the 20 kDa PEG the nonspecific aggregation rate is still high. The confinement of the particles due to the attractive magnetic dipole-dipole force may deform the steric barrier and still allow for nonspecific interactions between the particles in a dimer.

The specific aggregation rate significantly decreases for the 30 and 40 kDa PEG, see Fig. 4.4b. By adding the PEG molecules to the particle surface, steric hindrance occurs and the aggregation rate between the particles decreases due to a decreased particle surface reactivity. To interpret the effect of the PEG molecules on particle surface reactivity, the molecular rate of bond formation k_{chem} was varied in the simulation. In the simulations, the k_{on} and k_{chem} values that were obtained in the previous section are used as the basis for the low MW data. The non-specific aggregation rate is obtained from the measurements of Fig. 4.4b and the association rate is chosen to be k_{on} = $1.5{\cdot}10^5$ $M^{-1}s^{-1}$ to match with the experimental data. Table S4.8 shows an overview of the used simulation parameters. The experimental data of the low molecular weight PEG (≤ 20 kDa) and high molecular weight PEG (≥ 30 kDa) is matched with the simulations, see Fig. 4.4c. The green and blue bands show the error margin of the experimental data and the green and blue lines are simulated aggregation rate curves. The simulated curve for the high MW data is obtained from the low MW simulation by only changing the molecular rate of bond formation from k_{chem} = $5.0{\cdot}10^{-4}$ $\mu m^{-2}s^{-1}$ to k_{chem} = $6.5{\cdot}10^{-7}$ $\mu m^{-2}s^{-1}$. This indicates that the effect of the PEG coating on the particle can be described as an effective decrease of the intrinsic molecular binding rate between the DNA molecules, by almost three orders of magnitude.

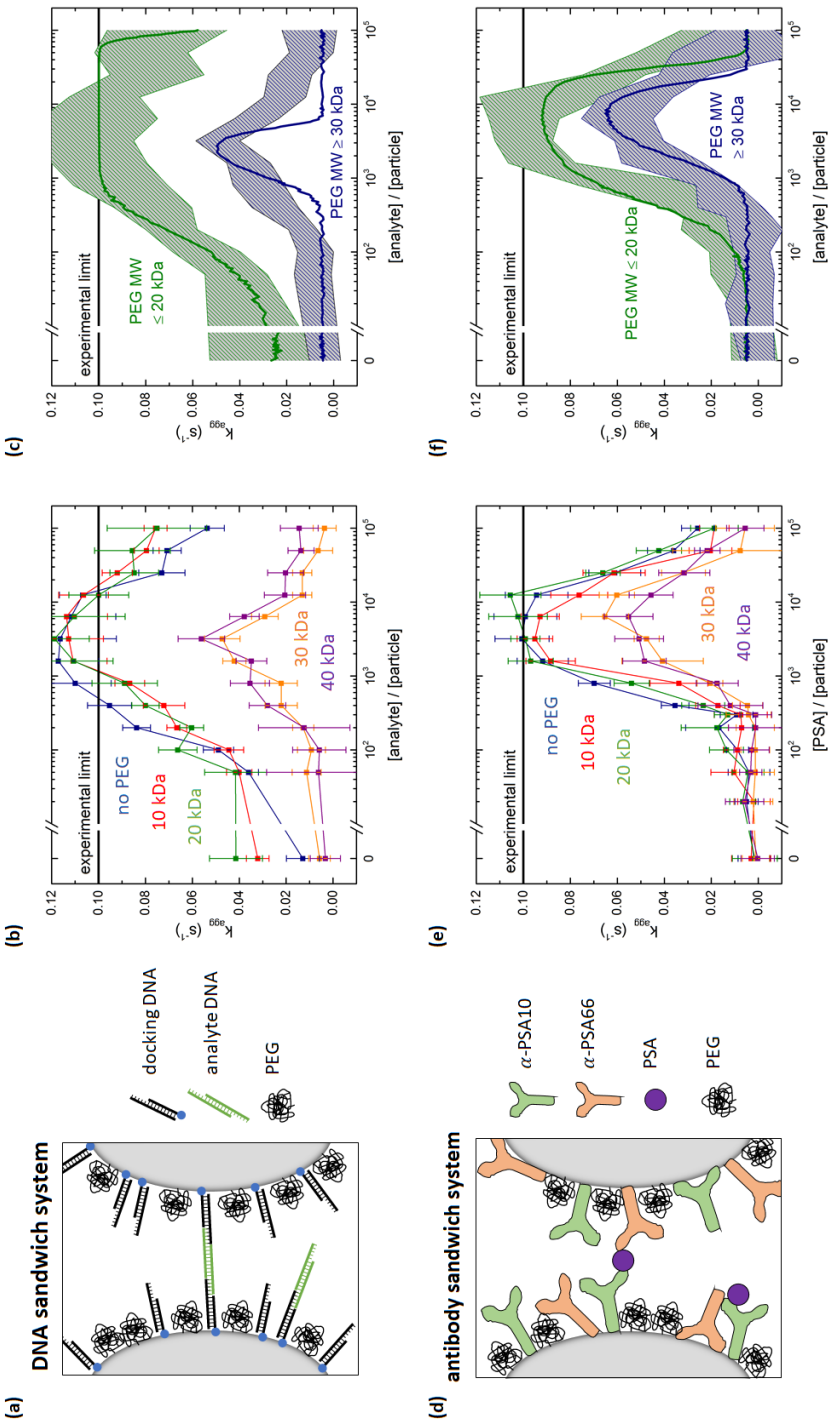

Fig. 4.4 **Tuning particle surface reactivity using PEG surface crowders. (a)** DNA sandwich system including a PEG coating. **(b)** Measured aggregation rate for the DNA sandwich system for particles coated with biotinylated docking strands and biotin-PEG of different molecular weights. For PEG MW ≥ 30 kDa,

the aggregation rates clearly decrease. **(c)** Experimental data plotted in two bands. A low MW PEG band (≤ 20 kDa) and a high MW PEG band (≥ 30 kDa). The curves represent simulations using input parameters shown in Table S4.8. **(d)** Antibody sandwich system including a PEG coating. **(e)** Measured aggregation rate for the antibody sandwich system, for particles coated with a matching pair of PSA antibodies and amine-PEG of different molecular weights. For PEG MW ≥ 30 kDa the aggregation rates clearly decrease. **(f)** Experimental data plotted in two bands. A low MW PEG band (≤ 20 kDa) and a high MW PEG band (≥ 30 kDa). The curves represent simulations using input parameters shown in Table S4.8.

For the antibody sandwich system, the antibody concentration during functionalization was kept constant at 11.25 μg/mL. The simulations of the previous section showed that for this antibody concentration the antibody density is σ_{Ab} = $3.8{\cdot}10^{3}$ μm^{-2}. This corresponds to 19-57% of the geometrically expected maximum surface coverage, for upright or side-on orientation respectively. The remainder of the surface was blocked with amine-PEG molecules. Fig. 4.4e shows the measured aggregation rate as a function of the PSA-to-particle ratio, for particles coated with 10, 20, 30 or 40 kDa PEG or without PEG. The nonspecific interaction is lower compared to the DNA model system and does not depend on the molecular weight of the PEG. The curves show a similar trend with PEG molecular weight as was observed for the DNA model system. PEG molecular weights ≥ 30 kDa cause a significant decrease in the aggregation rate. This observation is supported by the maximum bond length being similar in both systems: $L_{bond} \approx 31$ nm for the docking-analyte-docking complex and $L_{bond} \approx 35$ nm for the antibody sandwich.

Fig. 4.4f shows the experimental bands and the simulated curves for the low MW PEG (≤ 20 kDa) and the high MW PEG (≥ 30 kDa) for the antibody sandwich system. Again, by changing the molecular rate of bond formation k_{chem}, the simulation can be matched with the experimental data. The effective decrease in molecular binding rate for the antibody sandwich system is from k_{chem} = $9.5{\cdot}10^{-6}$ $\mu m^{-2}s^{-1}$ to k_{chem} = $1.4{\cdot}10^{-6}$ $\mu m^{-2}s^{-1}$, which is a significantly lower decrease than for the DNA model system. This might be explained by a significantly lower PEG density is on the DNA coated particles compared to the antibody coated particles, originating from the different coupling chemistries. To test this hypothesis, the effect of PEG density on the reduction in particle reactivity should be studied more thoroughly.

4.6 Conclusion

We described aggregation rate measurements on biofunctionalized microparticles, for a DNA sandwich system and an antibody sandwich system, using an optomagnetic cluster experiment. Particles were coated with specific binders, either DNA docking strands or a matching pair of antibodies. The kinetics of particle

aggregation was measured in the presence of analyte molecules, from which the particle surface reactivity was quantified.

Subsequently, we studied the influence of crowder molecules on the specific interactions between particles. Particles were coated with a mixed surface functionalization of specific binder molecules and PEG as a passive surface crowder. The aggregation rates were measured for a wide range of analyte concentrations and several different molecular weights of the PEG molecules. For high MW PEG ($\geq$ 30 kDa), the specific aggregation rate significantly decreases with respect to the low MW PEG ($\leq$ 20 kDa), indicating that the crowder molecules tune the particle surface reactivity. Aggregation rate simulations were compared with the experimental results, showing that the decrease in particle surface reactivity by the high MW PEG molecules can be modelled as an effective decrease in the molecular rate of bond formation.

To our knowledge, this is the first study that quantifies the effect of passive surface crowders on the reactivity of biofunctionalized particles. The results reveal a novel way to tune the specific reactivity, namely by adding passive surface crowder molecules on the surface, which gives a new dimension for the control of properties of colloidal particles for biological applications.

4.7 Supporting Information

S4.1 Optomagnetic cluster (OMC) experiment

In this paper specific particle aggregation rates will be measured using the OMC experiment described in a previous paper[21]. Fig. S4.1a sketches the optomagnetic cluster (OMC) experiment. A square glass cuvette filled with a solution of particles is situated in the centre of a quadrupole electromagnet setup, which can produce a rotating magnetic field in the y,z plane. A 660 nm laser is focussed insight the cuvette and the light scattered by the particles is measured by a photodetector at an angle of 90° w.r.t. to the incoming laser beam. In the presence of a rotating magnetic field, with a rotation frequency below the breakdown frequency, the dimers in the solution will rotate along with magnetic field.

Fig. S4.1c shows the oscillating scattering signal for both types of superparamagnetic particles used in this paper: polystyrene Ademtech Masterbeads (d = 528 nm, CV ≈ 25%) and silica Microparticles (d = 511 nm, CV < 5%). The differences in the scattering signals of Ademtech and Microparticle dimers are caused by differences in refractive index, size and size dispersion. For example, the oscillating scattering signal of the Microparticles contains more peaks compared to the Ademtech signal, although the particle size is very similar. However, due to the large size dispersion of the Ademtech particles the measured scattering signal is the average of many dimers consisting of particles with different sizes, whereby detailed features of the scattering signal are lost. Note that even in case the size dispersion of Ademtech and Microparticles are equal, it is unlikely that the scattering signals are completely similar due to the different refractive indices of the particles ($n_{Ademtech}$ = 1.83±0.08, $n_{Microparticles}$ = 1.59±0.04).

The amplitude of the oscillating scattering signal is a measure of the amount of dimers that are present in the solution. Therefore, the Fourier transform of the scattering signals of Fig. S4.1c is shown in Fig. S4.1d. Several peaks are observed at frequencies that are multiples of two times the field rotation frequency f_{rot} = 5 Hz. The peak at the frequency equal to four times the field rotation frequency, |A4f|, is used as a measure of the dimer concentration. Fig. S4.1e shows a calibration measurement of the |A4f| as a function of the concentration of a particle stock solution. In these stock solutions a certain fraction of the particles is in dimer form (1 in 12 for Ademtech, 1 in 9 for Microparticles) which leads to a measurable |A4f| peak. By diluting the stock solution several times, the dimer concentration is varied and the |A4f| is measured. The slopes of the fitted curves in the loglog plot being about equal to 1 indicate a linear relation between |A4f| and dimer concentration for both particle types. Fig. S4.1f shows a single actuation cycle that is used to quantify

the aggregation rate for both particle types. Both panels show a constant |A4f| throughout the measurement phases and a rather linearly increasing |A4f| during the actuation phase.

To quantify the aggregation rate a four-step actuation protocol is followed, as can be seen in Fig. S4.1b. Initially the number of already present chemical dimers is measured using magnetic pulses with a short on-time, t_{on} = 0.4 s, and a long off time, t_{off} = 10 s. During the subsequent actuation phase, the rotating magnetic field is turned on continuously during a time t_{act} = 20 s to induce additional magnetic dimers, causing the |A4f| signal to increase approximately linearly over time (this is true for both types of particles, see Fig. S4.1f). Since each magnetic dimer is formed at a different point in time, each magnetic dimer has a different interaction time in which it has the possibility to form a chemical bond. The mean interaction time of all dimers, for a constant magnetic dimer formation rate, equals half the actuation time. After the actuation phase, the field is turned off during a waiting time t_{wait} = 80 s to let the non-aggregated particles redisperse in solution. Ultimately, the number of chemical dimers is measured again and compared to the initial number of dimers. The increase in the number of chemical dimers, ΔN_{chem}, depends on how reactive the particles are. To calculate the aggregation rate k_{agg}^{mag}, the fraction of magnetic dimers that becomes a chemical dimer during the actuation phase, $\Delta N_{chem}/N_{mag,tot}$, is divided by the mean interaction time of all magnetic dimers.

$$k_{agg} = \frac{\Delta N_{chem} \,/\, N_{mag,tot}}{\frac{1}{2} t_{act}} \tag{S4.1}$$

In case of very reactive particles, it is possible that all magnetic dimers form a chemical bond during the interaction time. For a 20 s actuation time the maximum experimentally measurable aggregation rate is limited to $k_{agg,max}^{mag}$ = 0.1 s^{-1}.

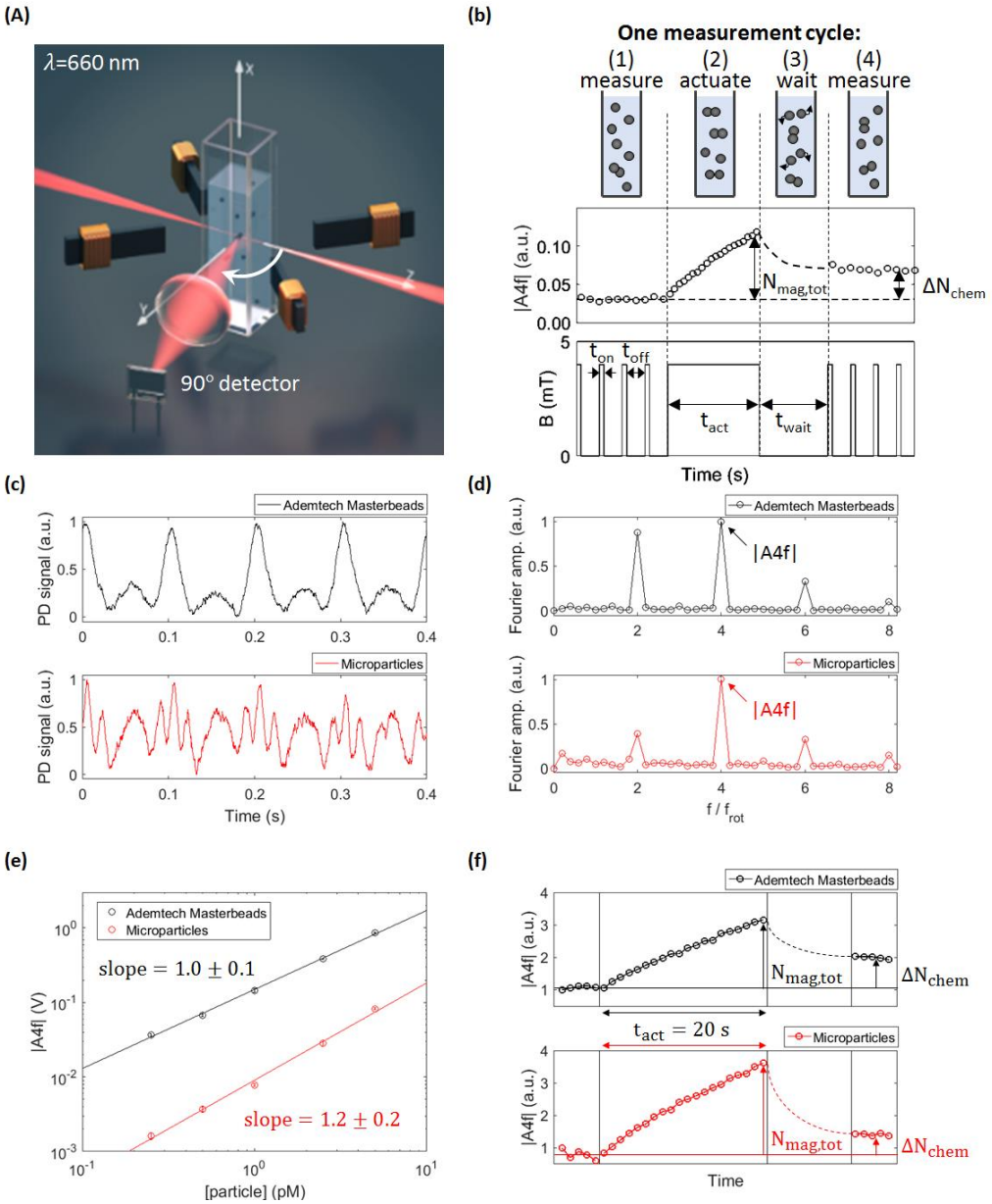

Fig. S4.1 Optomagnetic cluster experiment. (a) Optomagnetic dimer quantification: A 660 nm laser is focussed inside a cuvette filled with a particle solution. The scattering of the particles is measured at an angle of 90° w.r.t. the incoming laser beam. Four electromagnets are placed around the cuvette to apply a rotating magnetic field. Particle dimers are rotated, which leads to an oscillating scattering signal. The amplitude of the oscillating signal is used as measure of the dimer concentration. **(b)** Four-step actuation protocol to quantify the aggregation rate. First, the initial number of chemical dimers in the solution is measured using short magnetic field pulses. Then the field is turned on continuously to induce additional magnetic dimers, during an actuation time t_{act}. The field is subsequently turned off for a waiting time t_{wait} to let the unbound particles redistribute in the solution. Finally, the new number of chemical dimers is

measured. Using equation S4.1 the aggregation rate can be determined. **(c)** Oscillating scattering signal of both types of superparamagnetic particles, Ademtech Masterbeads and Microparticles, measured by a photodetector at an angle of 90° w.r.t. the incoming laser beam in the presence of a rotating magnetic field, f_{rot} = 5 Hz. **(d)** Fourier transform of the oscillating scattering signals of Fig. S4.1c, showing peaks at multiples of two times the field rotation frequency. **(e)** Calibration measurement of |A4f| as a function of particle concentration of a stock solution (containing a constant number of dimers), indicating that the |A4f| scales linearly with dimer concentration. **(f)** Single actuation cycle to measure the aggregation rate with the OMC experiment, for both particle types.

S4.2 List of used DNA strands

In this paper three different DNA constructs are used: A functional docking strand, a DNA filler strand and an analyte strand. These double stranded DNA constructs are built up from the five single stranded DNA sequences shown in Table S4.2. The DNA docking strand is obtained by annealing the base strand B with the docking strand D. The DNA filler strand is obtained by annealing the base strand B with the filler strand F. The analyte construct is obtained by annealing the analyte strand 1 with the analyte strand 2.

Table S4.2 Single stranded DNA sequences for DNA model system. Overview of the single stranded DNA sequences from which the DNA docking strand (B+D), the DNA filler strand (B+F) and the DNA analyte strand (A1+A2) are made of.

Code:	Name:	Sequence:
B	base strand	biotin-5′-CCT CCC AGC CCA TCC TAA CC-3′
F	filler strand	3′-GGA GGG TCG GGT AGG ATT GG-5′
D	docking strand	3′-GGA GGG TCG GGT AGG ATT GG AAG CAG CAG AAC AAA-5′
A1	analyte strand 1	5′-TTC GTC GTC TTG TTT CCA CCC TTC CCG CCC CTC CC-3′
A2	analyte strand 2	5′-TTC GTC GTC TTG TTT GGG AGG GGC GGG AAG GGT GG-3′

S4.3 Supernatant assay for DNA docking strand density quantification

To determine the maximum DNA coverage of the streptavidin coated Microparticles for short biotinylated DNA strands, an indirect fluorescence supernatant assay is performed. Fig. S4.3a shows in blue a calibration curve of the fluorescence intensity corresponding to concentration of biotin-atto655. The capacity of the Microparticles for b-atto655 is measured by incubating different b-atto655 concentrations with a constant particle concentration. After 60 minutes of incubation in an incubator shaker (1200 rpm, room temperature), the fluorescence of the supernatant is measured (green line in Fig. S4.3a). The b-atto655 capacity per particle is obtained from the point in the graph where the fluorescence intensity of the

supernatant starts increasing, $N_{b-atto655}$ = (4.3±0.5)·10⁴. The measured capacity is slightly lower than the geometrical capacity that can be expected based on the size of the particle (d = 511 nm), the size of a streptavidin (sphere, d ~ 5 nm) and the number of functional biotin binding pockets per streptavidin (~2.5 out of 4), see Fig. S4.3a.

In the indirect supernatant assay the particles are first functionalized with different amounts of biotinylated DNA strands for 60 minutes in an incubator shaker (1200 rpm, room temperature). Subsequently particles are magnetically washed and another incubation step is performed with a b-atto655 concentration that is slightly higher than the b-atto655 capacity. From the fluorescence intensity of the supernatant, the DNA coverage can be calculated using equation 4.1. Fig. S4.3b shows that when increasing the DNA concentration the DNA coverage also increases, until a plateau is reached at $N_{dock,max}$ = (1.6±0.3)·10⁴. The corresponding maximum docking strand coverage is $\sigma_{dock,max}$ = (2.0±0.4)·10⁴ µm⁻². The DNA capacity is about a factor three lower than the b-atto655 capacity, which can most likely be explained by the negative charge on the DNA backbone.

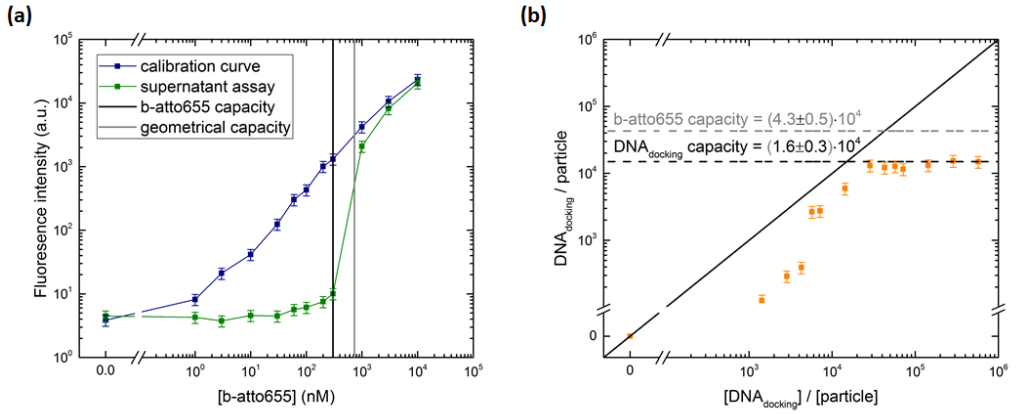

Fig. S4.3 Supernatant assay for DNA docking strand quantification. (a) Calibration curve (blue) of the fluorescence intensity as a function of the biotin-atto655 concentration. Supernatant assay (green) after b-atto655 incubation with streptavidin coated Microparticles to obtain the capacity of the particles for b-atto655. **(b)** DNA coverage per particle as a function of the DNA concentration during incubation, measured with an indirect fluorescence supernatant assay.

S4.4 Antibody sandwich system: control experiment

To investigate whether the aggregation in the antibody sandwich system is specific and originating from the antibody sandwich, a control experiment is performed. Two batches of particles are functionalized: One batch coated with only αPSA10 antibodies and one batch coated with only αPSA66 antibodies. Fig. S4.4

shows the aggregation rate that is measured with the OMC experiment, using either a mixture of both particles (blue data points) or only particles coated with αPSA10 (green data points). For the mixture of particles a clear increase in the aggregation rate is observed as a function of the [PSA] to [particle] ratio. For the control experiment with only αPSA10 coated particles no response is observed for increasing [PSA] to [particle] ratio.

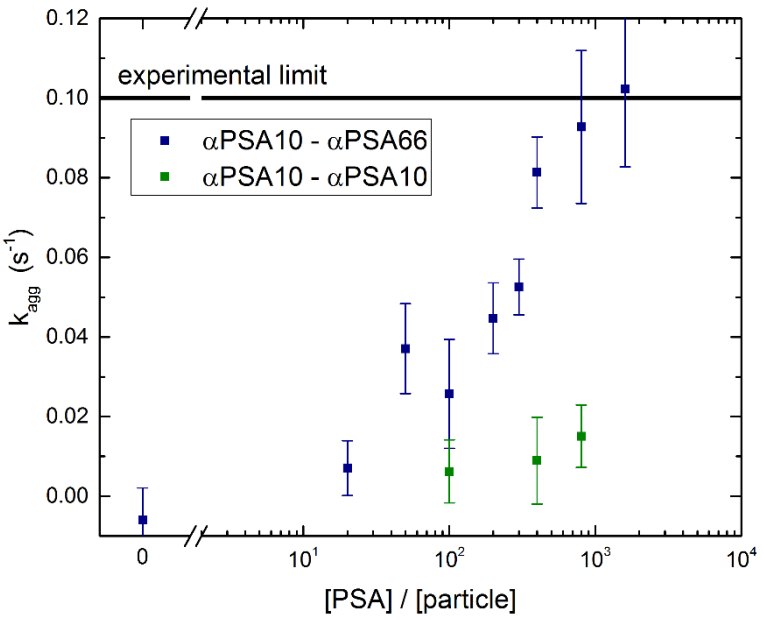

Fig. S4.4 Control experiment for antibody sandwich system. Aggregation rate is measured for a mixture of particles coated with αPSA10 and particles coated with αPSA66 (blue) and a control experiment where only particles are used with αPSA10 (green).

S4.5 Simulation parameter scan

A parameter scan of the input parameters of the aggregation simulation has been performed to investigate the effect of each parameter on the simulated aggregation rate. Table S4.5 shows the default input values of the simulation during the parameter scan. While one parameter is scanned, the other parameters are constant and equal to the default values. Some parameters are not scanned: particle radius R, maximum bond length L_{bond} and incubation time t_{inc}.

Table S4.5 Default values input parameters of simulation. Overview of the default values of the input parameters that are used in the parameter scan of the aggregation rate simulations.

default input values parameter scan			
parameter	**symbol**	**value**	**unit**
particle radius	R	0.25	μm
maximum bond length	L_{bond}	0.027	μm
interparticle distance	Δx	0.019	μm
incubation time	t_{inc}	360	s
analyte association rate	k_{on}	10^6	$M^{-1}s^{-1}$
actuation time	t_{act}	20	s
magnetic dimer formation rate	k_{enc}^{mag}	10^3	s^{-1}
chemical aggregation rate	k_{chem}	$2 \cdot 10^{-6}$	$\mu m^2 s^{-1}$
nonspecific chemical aggregation rate	$k_{chem,ns}$	0	s^{-1}
binder surface density	σ_B	$5.1 \cdot 10^3$	μm^{-2}

Fig. S4.5a shows the parameter scan for the binder surface density σ_B. For increasing binder density the aggregation rate curve shifts upward to higher rates, as more binders leads to more options to form bonds between the particles. Fig. S4.5b shows the parameter scan for the magnetic encounter rate k_{enc}^{mag}. The aggregation process does not depend on the encounter rate, but for higher encounter rates, the statistics increases and thus the fluctuations decrease. Fig. S4.5c shows the parameter scan for the actuation time t_{act}. For increasing actuation times the probability that a dimer aggregates is larger. This leads to a higher aggregation rate. However, for very reactive dimers, i.e. when the typical time-to-aggregation is smaller than the mean interaction time, the aggregation rate is underestimated. This underestimation is greater for the longer actuation times compared to the shorter actuation times. Therefore the curves intersect around their peak values. Fig. S4.5d shows the parameter scan for the nonspecific aggregation rate. For nonzero nonspecific aggregation rate a baseline of the simulated aggregation rate is observed. For increasing nonspecific aggregation rates, this baseline level shifts upwards to higher aggregation rates.

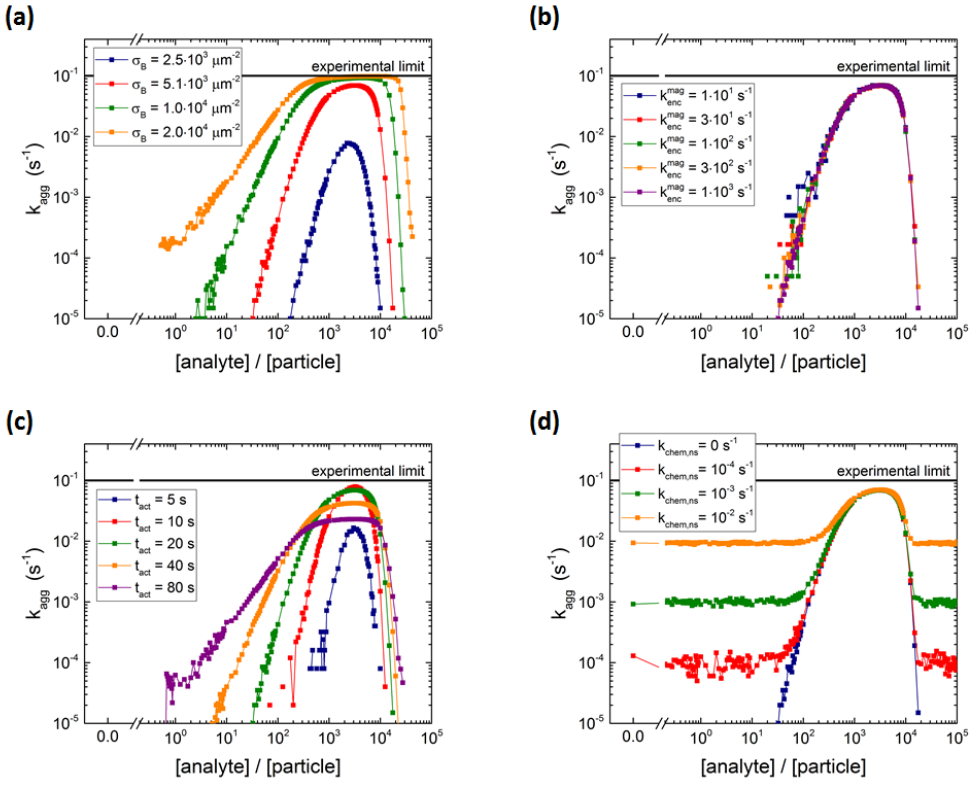

Fig. S4.5 Parameter scan of aggregation simulation. (a) Simulated aggregation rate as a function of the analyte-to-particle ratio for the parameter scan of the binder surface density σ_B. Increasing binder density leads to increasing aggregation rate for every analyte concentration, i.e. the curve shifts upwards. **(b)** Parameter scan of the magnetic dimer formation rate k_{enc}^{mag}. Changing the rate at which magnetic dimers are formed does not change the aggregation process, though it determines the statistical fluctuations in the simulation. **(c)** Parameter scan of the actuation time. For increasing actuation time, the mean interaction time will increase, and therefore the aggregation rate will increase. However, the maximum measurable aggregation rate decreases for increasing actuation time, which leads to a lower peak of the curve for increasing actuation times. **(d)** Parameter scan of the nonspecific chemical aggregation rate $k_{chem,ns}$. For increasing nonspecific aggregation rate the background aggregation level increases.

S4.6 Input parameter for simulation of varying binder density

The input parameters used for the simulated curves shown in Fig. 4.2b and 4.2d are shown in Table S4.6. The particle radius R, the incubation time t_{inc}, the actuation time t_{act} and the magnetic encounter rate k_{enc}^{mag} have equal values for the DNA model system and the antibody sandwich system. The bond length L_{bond}, interparticle distance Δx, the association rate k_{on}, the specific chemical aggregation rate k_{chem} and the nonspecific chemical aggregation rate $k_{chem,ns}$ are different for the two experimental systems, but they are constant throughout the simulations. The binder

density on the particle surface σ_B is varied experimentally and therefore also varied in the simulations.

Table S4.6 Simulation input parameters. Overview of the parameters that are used in the simulation to match to the experimental results of Fig. 4.1d and Fig. 4.1f.

DNA model system			Antibody sandwich system		
parameter	**value**	**unit**	**parameter**	**value**	**unit**
R	0.25	µm	R	0.25	µm
L_{bond}	0.031	µm	L_{bond}	0.035	µm
Δx	0.019	µm	Δx	0.019	µm
t_{inc}	360	s	t_{inc}	360	s
k_{on}	$1.5 \cdot 10^6$	$M^{-1}s^{-1}$	k_{on}	$1.9 \cdot 10^5$	$M^{-1}s^{-1}$
t_{act}	20	s	t_{act}	20	s
k_{enc}^{mag}	10^2	s^{-1}	k_{enc}^{mag}	10^2	s^{-1}
k_{chem}	$5.0 \cdot 10^{-4}$	$\mu m^2 s^{-1}$	k_{chem}	$9.5 \cdot 10^{-6}$	$\mu m^2 s^{-1}$
$k_{chem,ns}$	0.005	s^{-1}	$k_{chem,ns}$	0.005	s^{-1}
σ_B	$1.3 \cdot 10^2$ $2.5 \cdot 10^2$ $5.1 \cdot 10^2$ $2.0 \cdot 10^4$	μm^{-2}	σ_B	$7.6 \cdot 10^3$ $(45.0 \frac{\mu g}{mL})$ $3.8 \cdot 10^3$ $\left(22.5 \frac{\mu g}{mL}\right)$ $1.0 \cdot 10^3$ $\left(11.3 \frac{\mu g}{mL}\right)$	μm^{-2}

S4.7 Association rate dependence for high docking strand coverage

Fig. S4.7 shows the experimental data for high docking strand coverage σ_{dock} = $2.0 \cdot 10^4$ µm^{-2}. The data is accompanied with two simulations using the input parameters of Table S4.6 and an association rate of either k_{on} = $1.5 \cdot 10^6$ M^{-1}s^{-1} and k_{on} = $1.0 \cdot 10^5$ M^{-1}s^{-1}. The experimental data agrees best with the association rate k_{on} = $1.0 \cdot 10^5$ M^{-1}s^{-1}, whereas the for the lower docking strand coverages in Fig. 4.2b the data agrees best with k_{on} = $1.5 \cdot 10^6$ M^{-1}s^{-1}. The lower association rate at higher docking strand

density might be explained by the fact that there is much more DNA bound at the surface of the particles which has a repulsive electrostatic effect.

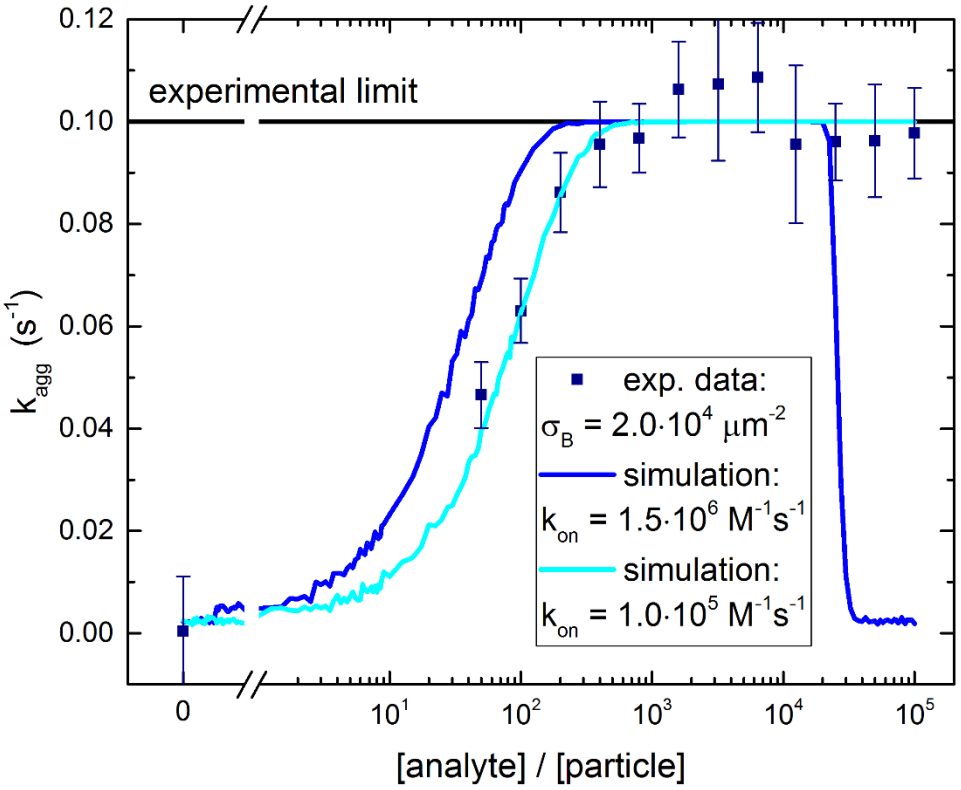

Fig. S4.7 Lower association rate for high docking strand density Measured aggregation rate for the DNA model system with a DNA docking strand density σ_{dock} = 2.0·10⁴ µm⁻². The experimental data is accompanied with two simulated curves having analyte association rate k_{on} = 1.5·10⁶ M⁻¹s⁻¹ and k_{on} = 1.0·10⁵ M⁻¹s⁻¹.

S4.8 Input parameter for simulation of varying PEG molecular weight

The input parameters used for the simulated curves shown in Fig. 4.4c and 4.4f are shown in Table S4.8. The particle radius R, the incubation time t_{inc}, the actuation time t_{act} and the magnetic encounter rate k_{enc}^{mag} have equal values for the DNA model system and the antibody sandwich system. The bond length L_{bond}, interparticle distance Δx, the association rate k_{on} and the nonspecific chemical aggregation rate $k_{chem,ns}$ are different for the two experimental systems. The specific molecular binding rate k_{chem} is varied in the simulation to reproduce the experimental results in the presence of a PEG coating.

Table S4.8 Simulation input parameters. Overview of the parameters that are used in the simulation to match to the experimental results of Fig. 4.4c and Fig. 4.4f.

DNA model system			Antibody sandwich system		
parameter	**value**	**unit**	**parameter**	**value**	**unit**
R	0.25	µm	R	0.25	µm
L_{bond}	0.031	µm	L_{bond}	0.035	µm
Δx	0.019	µm	Δx	0.019	µm
t_{inc}	360	s	t_{inc}	360	s
k_{on}	$1.5 \cdot 10^5$	$M^{-1}s^{-1}$	k_{on}	$1.9 \cdot 10^5$	$M^{-1}s^{-1}$
t_{act}	20	s	t_{act}	20	S
k_{enc}^{mag}	10^2	s^{-1}	k_{enc}^{mag}	10^2	s^{-1}
k_{chem}	**low MW PEG** $5.0 \cdot 10^{-4}$ **high MW PEG** $6.5 \cdot 10^{-7}$	$\mu m^2 s^{-1}$	k_{chem}	**low MW PEG** $9.5 \cdot 10^{-6}$ **high MW PEG** $1.4 \cdot 10^{-6}$	$\mu m^2 s^{-1}$
$k_{chem,ns}$	**low MW PEG** 0.03 **high MW PEG** 0.005	s^{-1}	$k_{chem,ns}$	**low MW PEG** 0.005 **high MW PEG** 0.005	s^{-1}
σ_B	$5.6 \cdot 10^3$	μm^{-2}	σ_B	$3.8 \cdot 10^3$	μm^{-2}

References

[1] Ranzoni, A.; Sabatte, G.; van IJzendoorn, L.J.; Prins, M.W.J. One-step homogeneous magnetic nanoparticle immunoassay for biomarker detection directly in blood plasma. *ACS Nano*, **2012**, 6, 4, 3134-3141

[2] Davies, D.R.; Cohen, G.H. Interactions of protein antigens with antibodies. *PNAS* **1996**, 93, 7-12

[3] Bonham, A.J.; Braun, G.; Pavel, I.; Moskovits, M.; Reich, N.O. Detection of sequence-specific protein-DNA interactions via surface enhanced resonance Raman scattering. *J. Am. Chem. Soc.* **2007**, 129, 47, 14572-14573

[4] Wang. M.D.; Yin, H.; Landick, R.; Gelles, J.; Block, S.M. Stretching DNA with optical tweezers. *Biophys. J.* **1997**, 72, 3, 1335-1346

[5] Jing, M.; Bowser, M.T. Methods for measuring aptamer-protein equilibria: A review. *Anal. Chim. Acta* **2011**, 686, 9-18

[6] Srinivas, R.L.; Chapin, S.C.; Doyle, P.S. Aptamer-functionalizes microgel particles for protein detection. *Anal. Chem.* **2011**, 83, 23, 9138-9145

[7] Müller, J.; Bauer, K.N.; Prozeller, D.; Simon, J.; Mailänder, V.; Wurm, F.R.; Winzen, S.; Landfester, K. Coating nanoparticles with tunable surfactants facilitates control over the protein corona. *Biomaterials* **2017**, 115, 1-8

[8] Gillich, T.; Acikgöz, C.; Isa, L.; Schlüter, A.D.; Spencer, N.D.; Textor, M. PEG-stabilized core-shell nanoparticles: Impact of linear versus dendritic polymer shell architecture on colloidal properties and the reversibility of temperature induced aggregation. *ACS Nano* **2013**, 7, 1, 316-329

[9] Sorret, L.L.; Monticello, C.R.; DeWinter, M.A.; Schwartz, D.K.; Randolph, T.W. Steric repulsion forces contributed by PEGylation of interleukin-1 receptor antagonist reduce gelation and aggregation at the silicon oil-water interface. *J. Pharm. Sci.* **2019**, 108, 162-172

[10] Helfricht, N.; Mark, A.; Drowling-Carter, L.; Zambelli, T.; Papastavrou, G. Extending the limits of direct force measurements: colloidal probes from sub-micron particles. *Nanoscale* **2017**, 9, 9491

[11] Schein, P.; Kang, P.; O'Dell, D.; Erickson, D. Nanophotonic force microscopy: Characterizing particle-surface interactions using near field photonics. *Nano Lett.* **2015**, 15, 1414-1420

[12] van Ommering, K.; Koets, M.; Paesen, R.; van IJzendoorn, L.; Prins, M. Bond characterization by detection and manipulation of particle mobility in an optical evanescent field biosensor. *J. Phys. D: Appl. Phys.* **2010**, 43, 385501

[13] Wang, Z.; He, C.; Gong, X.; Wang, J.; Ngai, T. Measuring the surface-surface interactions induced by serum proteins in a physiological environment. *Langmuir*, **2016**, 32, 12129-12136

[14] Biancaniello, P.L.; Crocker, J.C. Line optical tweezers instrument for measuring nanoscale interactions and kinetics. *Rev. Sci. Instrum.*, **2006**, 77, 113702

[15] Scheepers, M.R.W.; Romijn, A.R.; van IJzendoorn, L.J.; Prins, M.W.J. Rate of dimer formation in stable colloidal solutions quantified using an attractive interparticle force. *Langmuir*, **2019**, 35, 10533-10541

[16] Xu, S.; Zhan, J.; Man, B.; Jiang, S.; Yue, W.; Gao, S.; Guo, C.; Liu, H.; Li, Z.; Wang, J.; Zhou, Y. Real-time reliable determination of binding kinetics of DNA hybridization using a multi-channel graphene biosensor. *Nat. Comm.*, **2017**, 8, 14902

[17] Knowles, D.B.; LaCroix, A.S.; Deines, N.F.; Shkel, I.; Thomas Record Jr., M. Separation of preferential interaction and excluded volume effects on DNA duplex and hairpin stability. *PNAS* **2011**, 108, 31, 12699-12704

Chapter 5

Multivalent weak interactions enhance selectivity of inter-particle binding – experimental proof

Targeted drug delivery critically depends on the binding selectivity of cargo transporting colloidal particles. Extensive theoretical work has shown that two factors are necessary to achieve high selectivity for a threshold receptor density: multivalency and weak interactions. Here, we study multivalent and weak interactions between DNA-coated particles, as a mimic of ligand-receptor interactions between particles and cells. Using an optomagnetic cluster experiment, particle aggregation rates are measured as a function of ligand and receptor densities. The data show that the binding becomes more selective for shorter DNA ligand-receptor pairs, proving that multivalent weak interactions lead to enhanced selectivity in inter-particle binding. Simulations confirm the experimental findings and show the role of ligand-receptor dissociation in the selectivity of inter-particle binding.

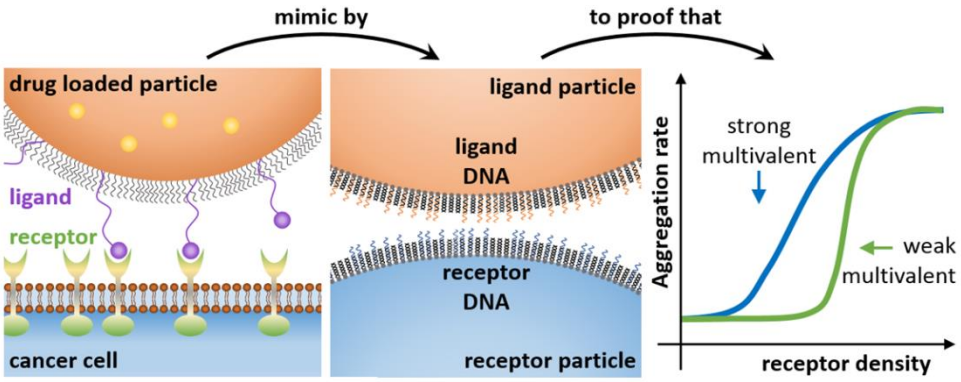

This chapter is in preparation as a manuscript: Scheepers, M.R.W.; van IJzendoorn, L.J.; Prins, M.W.J. Multivalent weak interactions enhance selectivity of inter-particle binding – experimental proof.

5.1 Introduction

Large efforts in nanomedicine focus on developing methods to target nanoparticles to highly specific cell types in order to improve diagnosis and treatment[1-3]. The targeting relies on identifying membrane receptor signatures that are unique to the targeted cell. However, in many diseases the receptors are not unique for diseased cells, but the receptors are expressed at higher levels compared to healthy cells.[4,5] Therefore, the drug delivery particles should exhibit receptor-density specificity, i.e. the particles should bind as selectively as possible to cells with a receptor density above a certain threshold density, see Fig. 5.1a.

The group of Frenkel in Cambridge has done extensive theoretical work on the topic of receptor-density specificity. They have developed a statistical mechanical model that describes the interaction between ligand-coated guest particles and a receptor-coated host substrate.[6] The model yields the fraction of bound guest particles θ in the equilibrium state as a function of the receptor density. The selectivity of the guest-host binding is quantified by a selectivity parameter α, which is smaller than one if the binding has a sublinear dependence on receptor density, and larger than one if the dependence is faster than linear (superselectivity). The work of Frenkel and other groups predict that a high receptor-density specificity can be achieved by using particles that interact in a multivalent fashion with a cell membrane.[6-10] Interestingly, the selectivity is higher when the equilibrium association constant K_a of an individual ligand-receptor pair is lower.[6,11,12] Many weak bonds are more selective than a single strong bond.

Several experimental studies have proven parts of Frenkel's theoretical work. Mani et al. showed that antibody conjugated micrometre sized particles bind faster to antigen coated surfaces for higher antibody densities[13], proving that the binding kinetics increases with multivalency. Albertazzi et al. showed superselectivity in self assembling of a supramolecular BTA polymer by introducing a multivalent binder[14]. Dubacheva et al. showed superselective binding for a model system of multivalent hyaluronic acid polymers binding to a functionalized surface.[15] However, a comprehensive experimental study is lacking on how weak multivalent interactions yield enhanced selectivity.

Here, we mimic the particle-cell interaction by a particle-particle interaction, see Fig. 5.1b. Colloidal particles are suspended in solution, where half of the particles are coated with ligands at a surface density σ_L, called the ligand particles (L), and the other half of the particles are coated with receptors at a surface density σ_R, called the receptor particles (R). We use a DNA model system in which ligand DNA and receptor DNA consist of single-stranded overhangs, exposed from 20 bp double

stranded DNA fragments. When two particles (R = 250 nm) are in close proximity, multiple ligand-receptor bonds can be formed, depending on the binder densities. By changing the length of the single stranded overhangs, i.e. changing the number of complementary bases, the strength of the individual ligand-receptor bonds can be tuned.

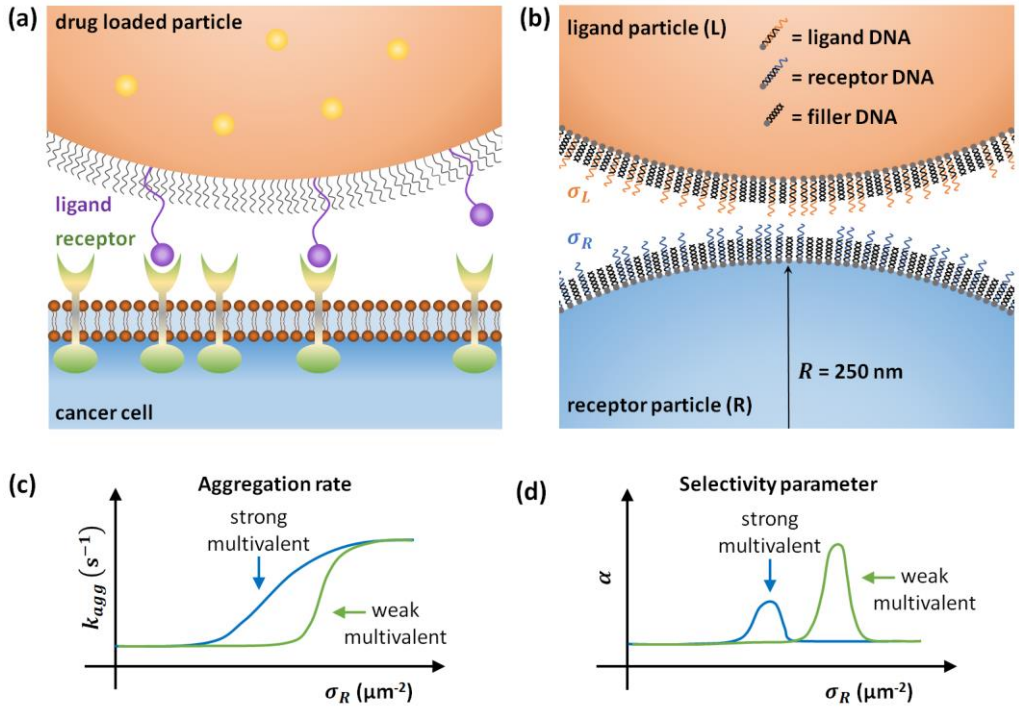

Fig. 5.1 Particle-particle interaction mimics cell-particle interactions. (a) Multivalent binding of a ligand coated particle to receptors on a cell membrane. **(b)** Ligand particles are coated with short DNA constructs with a single-stranded overhang, called ligand DNA. Receptor particles are coated with short DNA constructs with a complementary single-stranded overhang, called receptor DNA. The overhang complementarity determines the strength of the ligand-receptor interaction. Filler dsDNA strands, without single-stranded overhang, are inserted to maintain a constant surface charge density. **(c)** The aggregation rate is measured as a function of the receptor density, for a constant ligand density. Weaker interactions, with fewer complementary nucleotides in the single-stranded overhang of the receptor strand, cause a higher selectivity of inter-particle binding. **(d)** The selectivity parameter α is calculated from the dependence of aggregation rate on receptor density. Weak multivalent interactions yield enhanced selectivity compared to strong multivalent interactions.

To quantify the binding between the ligand and receptor particles, we measure the inter-particle aggregation rate k_{agg} using a previously developed optomagnetic cluster (OMC) experiment.[16] The parameter k_{agg} represents the rate at which biochemical inter-particle aggregation occurs, for particles that are in a well-defined state of proximity. Briefly, a dispersion of superparamagnetic particles is exposed to

an external magnetic field. The attractive inter-particle magnetic force brings particles in a well-defined proximal state and accelerates the formation of inter-particle ligand-receptor bonds. The number of biochemically bound dimers is recorded as a function of time, which allows quantification of the inter-particle aggregation rate k_{agg}. A complete description of the OMC experiment is given in Section S5.1 of the Supporting Information.

In this paper, we experimentally study how the kinetics of particle-particle binding scales with the density of ligands, density of receptors, and their interaction strengths. The selectivity parameter is quantified for complementary DNA lengths ranging from 15 bp to as few as 5 bp, i.e. from strong to very weak interactions. Additionally a simulation model is presented which elucidates that enhanced selectivity can be obtained by only increasing the dissociation rate of the ligand-receptor pairs. The paper concludes with a discussion about how the obtained results can be interpreted for applications in targeted drug delivery.

5.2 Materials and methods

5.2.1 Materials

Streptavidin coated superparamagnetic Ademtech Masterbeads were purchased from Ademtech (diameter 528 nm, coefficient of variation 25%). Biotinylated DNA strands were purchased from IDT (for a complete list of the used DNA sequences, see Supporting Information section S2). Phosphate buffered saline (PBS) tablets, bovine serum albumin (BSA, >98% pure), biotin-Atto655 and Protein LoBind Eppendorf tubes were obtained from Sigma Aldrich. Borosilicate glass 3.3 cuvettes with inner dimensions of 1.00±0.05 mm x 1.00±0.05 mm and outer dimensions of 1.23±0.05 mm x 1.23±0.05 mm, and a length of 20±1 mm were obtained from Hilgenberg GmbH.

5.2.2 Particle functionalization

Streptavidin coated Ademtech Masterbeads were functionalized with biotinylated ligand or receptor DNA strands and filler DNA strands by sequential incubation steps. First, 15 µL of the particle stock solution (10 mg/mL) was mixed with 285 µL of ligand DNA or receptor DNA solution in PBS, and incubated for 60 minutes in an incubator shaker (1200 rpm, room temperature). Subsequently 2 µL of a large excess of filler DNA was added to saturate the remaining streptavidin groups with DNA, and incubated for 60 minutes in an incubator shaker (1200 rpm, room temperature). The amount of functional ligand DNA or receptor DNA strands on the particle was varied throughout the experiments. After the second incubation step, the particle solution was magnetically washed to remove the unbound DNA strands. The

particles were redispersed in a 10 mg/mL BSA in PBS solution to suppress nonspecific aggregation of the particles. The particle solution was then incubated in a sonic bath for 10 minutes and the solution was sonicated (10x 0.5s) to reduce the number of background clusters in the solution.

5.2.3 Supernatant assay for DNA docking strand coverage quantification

To quantify the number of DNA strands on the streptavidin coated Ademtech Masterbeads an indirect fluorescence supernatant assay was performed. First, the biotin capacity of the particles was quantified by binding increasing amounts of biotin-atto655 (b-atto655) on the particles, during 60 minutes in an incubator shaker (1200 rpm, room temperature). The lowest b-atto655 concentration at which there is still b-atto655 left over in the supernatant after incubation was quantified using a Thermo Fischer Fluoroskan Ascent FL (λ_{ex} = 646 nm, λ_{em} = 679 nm, spectral width 5 nm), see Fig. S3a. The b-atto655 capacity per particle was equal to $N_{b-atto655}$ = (7.3±0.6)·10⁴.

Next, increasing amounts of ligand or receptor biotinylated DNA were added to the particles and incubated during 60 minutes in an incubator shaker (1200 rpm, room temperature). After this incubation step, the particle solution was magnetically washed to remove unbound DNA strands. Subsequently, b-atto655 was added in a concentration that was slightly above the b-atto655 capacity of the particles followed by an incubation step of 60 minutes in an incubator shaker (1200 rpm, room temperature). Particles that were not fully coated with DNA strands bind some of the b-atto655 in the solution, while the fully coated particles do not bind any b-atto655 anymore. After the incubation the particle solutions were magnetically washed and the fluorescence of the supernatant was measured. The amount of b-atto655 in the supernatant for a certain DNA concentration, $I_{s.n.}([DNA])$, is related to the number of DNA on the particle, N_{DNA}, according to equation 5.1.

$$N_{DNA} = \frac{I_0 - I_{s.n.}([DNA])}{I_0 - I_{s.n.}([DNA]=0)} \cdot N_{b-atto655} \tag{5.1}$$

Here I_0 is the fluorescence intensity of the b-atto655 solution that is added in the second incubation step, and $I_{s.n.}([DNA] = 0)$ is the fluorescence intensity of the supernatant when adding non-functionalized streptavidin Ademtech Masterbeads. For more details of the supernatant assay, see Supporting Information section S5.3.

5.3 Aggregation rate as a function of receptor and ligand density

We investigate how the binding between a ligand conjugated particle and a receptor coated cell surface depends on the ligand and receptor density. For this purpose the particle-cell interaction is mimicked by a particle-particle interaction using the DNA model system of Fig. 5.1b. Streptavidin coated Ademtech Masterbeads were functionalized with three different biotinylated DNA constructs: Ligand DNA, receptor DNA and filler DNA. Ligand DNA strands consist of a 20 bp double-stranded DNA spacer with a 15 nt single-stranded overhang. Receptor DNA strands also consist of a 20 bp double-stranded spacer, but they have a single stranded overhang that varies from 5 up to 15 nt. The filler DNA consists only of the 20 bp double-stranded spacer and is used to saturate the particle with DNA, such that the surface charge of the particle remains constant throughout the experiments.

The streptavidin coated particles were sequentially incubated for one hour. First with a certain concentration of either ligand or receptor DNA to obtain a certain ligand or receptor coverage, and subsequently with an excess of filler DNA to saturate the particle surface (complete description of functionalization process is given in the Materials and methods section). To quantify the number of functional DNA strands that bind to the particles during the one hour incubation, a supernatant assay was performed (the supernatant assay is described in detail in Section S5.3 of the Supporting Information). Fig. S5.3b shows the dependence of the bound DNA surface density as a function of the incubated DNA surface density, calculated by dividing DNA concentration by particle concentration. The measured curve follows a linear relation until a plateau is reached. The DNA surface density of this plateau represents the DNA capacity of the particle: $\sigma_{DNA,max}$ = (2.2±0.5)·10^4 μm^{-2}. The obtained relation between incubated DNA coverage and bound DNA coverage is used in the remainder of this paper, such that the ligand density σ_L or receptor density σ_R always represent bound surface densities.

To quantify the binding between ligand particles and receptor particles, they were mixed in a 1:1 ratio and the aggregation rate was measured using the optomagnetic cluster experiment.[16] Fig. 5.2a shows the measured aggregation rate as a function of the receptor density for the 15 complementary basepair system. The data point at zero receptor density quantifies the nonspecific interaction between the DNA coated particles: $k_{agg,ns}$ = (5±2)·10^{-3} s^{-1}. For non-zero receptor densities, the measured aggregation rate is significantly higher than the nonspecific aggregation rate, and increases with increasing receptor density. Over a range of more than two orders of magnitude increase in the receptor density, the aggregation rate increases by only one order of magnitude. This binding process is sublinear, with a weak dependence on receptor surface density and therefore a low selectivity parameter, as can be seen

from the low slope. Higher ligand densities lead to higher aggregation rates, as more ligands can bind with the receptors on the other particle.

For receptor densities $\sigma_R > 10^3$ μm^{-2}, a plateau is reached at an aggregation rate slightly above k_{agg} = 0.05 s^{-1}. This is the highest aggregation rate that can be measured for this system using the OMC experiment. Only 50% of the magnetic dimers that are formed during the actuation time consist of a ligand particle and a receptor particle, allowing for specific binding. The other 50% of the magnetic dimers consists of either two ligand particles or two receptor particles, having only nonspecific interactions. Fig. S5.4 shows that their nonspecific aggregation rate is low and does not depend on receptor density.

Fig. 5.2b and 5.2c show similar curves for the DNA system with 12 and 9 basepair complementarity, respectively. The measured curves, for all ligand densities, resemble the ones of the 15 bp system. To understand this result, we need to take a closer look at the OMC experiment. During the actuation phase, dimers of particles are held in close proximity for a certain interaction time. It is known from literature that the association rate k_{on} of short DNA strands in solution only very weakly depends on the number of complementary bases[17-19]. Therefore, in the OMC experiment roughly the same number of ligand-receptor bonds are expected to be formed between the particles for the 15, 12 and 9 bp system. Subsequently, the field is turned off during a waiting time of t_{wait} = 40 s, allowing the particles to redisperse in the solution. After the waiting phase the number of bound particle dimers is measured and the aggregation rate is calculated. Dimer dissociation during the waiting phase leads to a lower aggregation rate. However, in case of 15, 12 or 9 bp complementary DNA, the single-molecular dissociation time is significantly higher than the waiting time of 40 s[20-22], so dimer dissociation is not expected in the OMC experiment. Thus we attribute the similarity of the curves in Fig. 5.2b and 5.2c for the 15, 12 and 9 bp complementary DNA, to their similar association rates and slow dissociation.

The results are very different for the 8, 7 and 5 bp systems. Fig. 5.2d-f show the aggregation rate as a function of the receptor surface density. The curves have a steep dependence on receptor density, which implies a higher selectivity parameter than for the high affinity interactions (15/12/9 bp). The receptor-density onset, i.e. the threshold where aggregation occurs, increases with decreasing ligand density and with decreasing number of complementary bases. This is in qualitative agreement with the theoretical predictions of Wang et al.[18] Note that particle aggregation is observed even for the 5 bp interaction, for which the single-molecular dissociation time[20-22], about 10^{-9} s, is much shorter than the waiting time of 40 s in the OMC experiment. Still, particle aggregation is clearly observed at high receptor densities,

which therefore must be due to the presence of multivalent bonds between the particles in a dimer.

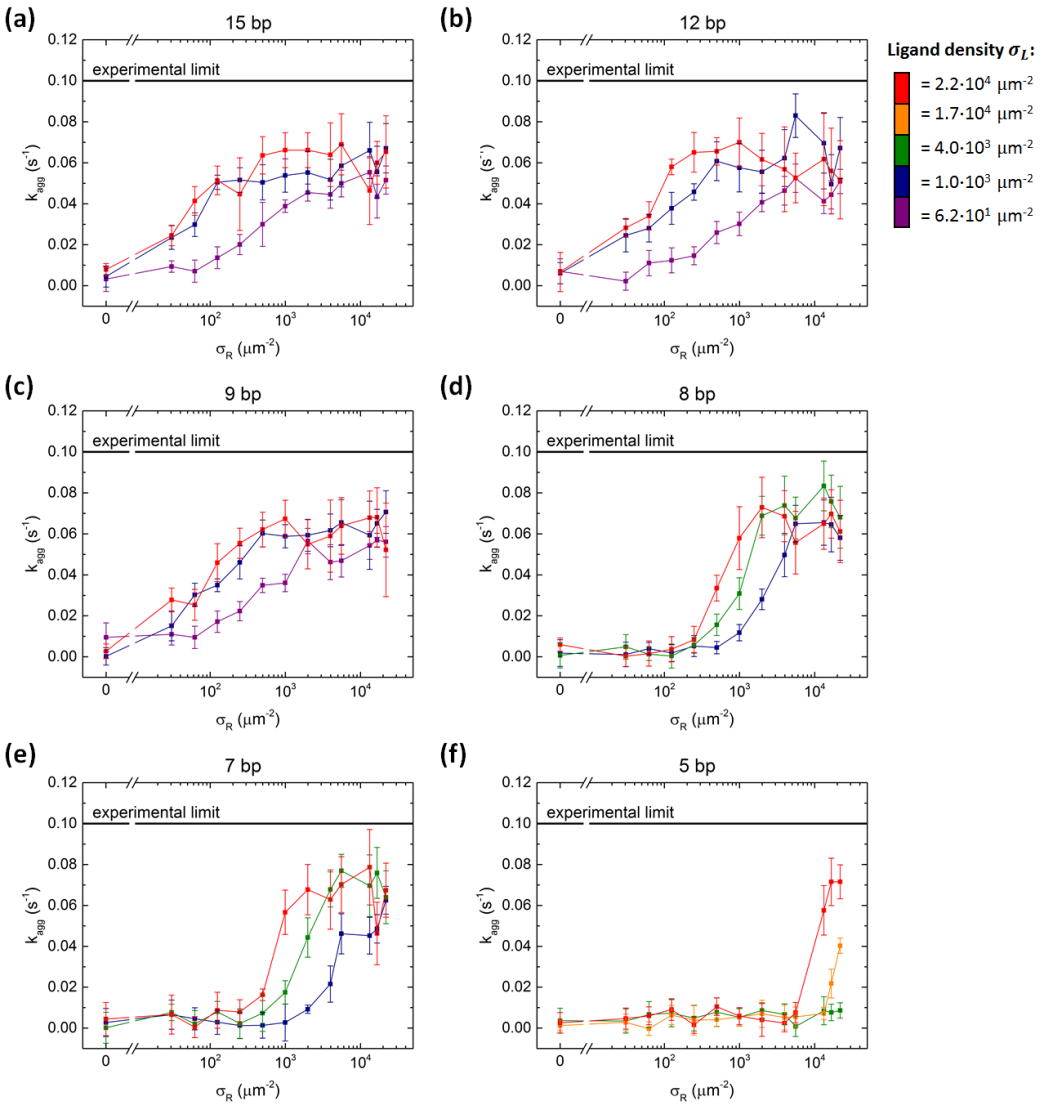

Fig. 5.2 Aggregation rate as a function of receptor density (σ_R), ligand density (σ_L) and ligand-receptor affinity (bp). (a) 15 bp **(b)** 12 bp **(c)** 9 bp **(d)** 8 bp **(e)** 7 bp and **(f)** 5 bp complementary between ligand and receptor.

5.4 Enhanced selectivity for weak multivalent interactions

To quantify and compare the selectivity of the ligand-receptor binding for different DNA lengths, the aggregation rate curves for ligand density σ_L = (2.2±0.5)·10^4 μm^{-2} for all DNA lengths are fitted and plotted in one graph, see In Fig. 5.3a. The measured curves are fitted using a sigmoid curve. More details about the fitting can be found in Section S5.5 of the Supporting Information.

In Fig. 5.3a the grey dotted line indicates the receptor density above which it is possible to from multiple bonds. This point is calculated based on the radius of the particle, the length of a ligand-receptor bond and the inter-particle distance (for the complete calculation see Section S5.6 of the Supporting Information). At receptor densities left from the dotted line, there is on average at most one receptor present in the interaction area, which is the area on the receptor particle that is at a distance from the ligand particle of at most a bond length ($L_{bond} \sim 20$ nm). For the DNA lengths for which a single bond is stable on time scales of the waiting time - 15, 12 and 9 bp - there is significant specific aggregation at receptor densities in the monovalent regime. For the weaker interaction - 8, 7 and 5 bp - higher receptor densities are necessary to allow for particle aggregation by multivalent binding.

The selectivity parameter α is defined by Martinez-Veracoechea and Frenkel[12] as the relative change in the number of bound particles N_{bound} formed in equilibrium, as a function of the number of receptors on a cell n_R, see equation 2. Here, we measured the rate of inter-particle binding k_{agg}, which represents the number of bound dimers divided by the mean interaction time, as a function of the receptor density σ_R, which is the number of receptors divided by the particle area. Since α describes a relative change in the number of bound particles with the number of receptors, we can multiply N_{bound} and n_R by any nonzero constant, without changing α. Thus, we can replace N_{bound} and n_R in equation 5.2 by k_{agg} and σ_R, respectively.

$$\alpha = \frac{d \ln N_{bound}}{d \ln n_R} = \frac{d \ln k_{agg}}{d \ln \sigma_R} \tag{5.2}$$

Making use of equation 5.2 and the fitted curves of Fig. 5.3a, the selectivity parameter is calculated as a function of the receptor density, see Fig. 5.3b. The shaded bands around the solid curves are obtained from the fit errors and represent the uncertainty interval in the selectivity parameter. The selectivity for the 15, 12 and 9 bp interactions are below 1, meaning that there is a sublinear increase with receptor density. The selectivities for the 8, 7 and 5 bp interaction almost reach the value 2. This proves that multivalent weak interactions lead to enhanced selectivity in inter-particle binding.

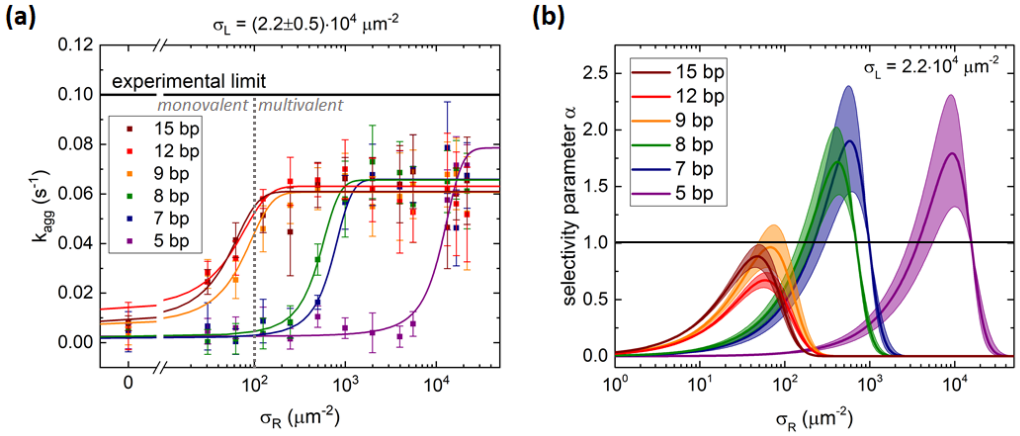

Fig. 5.3 Enhanced selectivity for weak multivalent interactions. (a) Measured aggregation rates as a function of receptor density for a constant ligand density of σ_L = (2.2±0.5)·104 μm-2, for all interaction strengths. The 15, 12 and 9 bp data is fitted with an exponential function and the 8, 7 and 5 bp data is fitted with a sigmoidal function. Details about the fitting can be found in Section S5.4 of the Supporting Information. **(b)** Calculated selectivity parameter using formula 2, with the fit parameters obtained from Fig. 5.3a. The weak ligand-receptor interactions (5/7/8 bp) yield an enhanced selectivity compared to the strong ligand-receptor interactions (9/12/15 bp).

5.5 Aggregation rate simulations

To further investigate the experimentally measured binding selectivities, a stochastic binding simulation is developed that mimics the ligand-receptor-induced particle binding. The aim of the simulation is to understand the origin of the enhanced selectivity for the weak multivalent interactions and assess the relevance of the results for conditions beyond the experimental scope.

In the simulation, particles are defined as a spheres with radius R having either a ligand density σ_L or a receptor density σ_R. During the actuation time t_{act}, particle dimers with a surface-to-surface distance Δx are formed at a constant rate k_{dim}^{mag}. Here monomer depletion and the formation of larger clusters are neglected (see SI Section S5 of ref. 16). The probability that a dimer consists of a receptor particle and a ligand particle is fifty percent. Each ligand-receptor dimer has an individual interaction time t_{int}, equal to the time between the moment that the dimer is formed and the end of the actuation time. During this interaction time the particles in a dimer can form one or more ligand-receptor bonds. The rate of bond formation depends on the ligand density σ_L, the receptor density σ_R and the intrinsic binding rate between ligand and receptor molecules k_{LR} [$\mu m^2 s^{-1}$]. The intrinsic binding rate k_{LR} is defined as the rate at which ligand-receptor bonds are formed between a particle with unit ligand

density σ_L and a particle with unit receptor density σ_R. Because the particle surfaces are curved and the ligand-receptor interaction depends on the distance, k_{LR} represents the average binding rate over all possible ligand-receptor distances. The maximum distance equals the length of the ligand-receptor bond.

The ligand-receptor bond density σ_{LR} can be calculated numerically according to equation 5.3.

$$\frac{d\sigma_{LR}}{dt} = k_{LR}\sigma_L\sigma_R - k_{off}\sigma_{LR} \tag{5.3}$$

Here k_{off} [s^{-1}] is the rate at which ligand-receptor bonds dissociate. To calculate the total number of inter-particle bonds that is formed during the interation time, first the bond density is calculated numerically and subsequently the total number of bonds is determined using equation 5.4.

$$N_{LR} = \sigma_{LR}A_{int} \tag{5.4}$$

Here A_{int} is the interaction area on the particles, which is defined as the area on the particles where the distance between the two particles is smaller than the length of the hybridized DNA construct $L_{bond} \approx 20$ nm, see Fig. S5.6. The size of the interaction area depends on the inter-particle distance Δx. Since the total DNA density on each particle is equal (ligand or receptor density completed with filler DNA), the charge induced inter-particle repulsion which balances the magnetic attraction is unchanged and Δx is assumed to be constant throughout the experiments.

When at least one ligand-receptor bond has been formed during the interaction time, the dimer is called aggregated. Subsequently, during the waiting time t_{wait}, already formed ligand-receptor bonds may dissociate, but simultaneously new bonds can be formed since the particles are still held in close proximity by the already formed bonds. During the waiting time, the bond formation process continues in a similar way. After the waiting time, the final number of ligand-receptor bonds inside a dimer is calculated using equation 5.3 and 5.4. Ultimately, a certain fraction of the dimers is aggregated by one or more ligand-receptor bonds. Also nonspecific interactions are taken into account, by including a nonspecific interaction rate k_{ns} [s^{-1}]. From the total fraction of aggregated dimers, the aggregation rate k_{agg} is calculated according to equation S5.1. A complete parameter scan of the simulation is given in section S5.7 of the Supporting Information.

The simulation can be used to interpret the experimentally measured aggregation rates. First, the experimental results for the high affinity interaction are simulated (15/12/9 bp). The experimental data is very similar and therefore this data is

averaged and represented by the orange datapoints in Fig. 5.4a. As mentioned above, molecular dissociation can be neglected, implying a dissociation rate equal to zero, so unknown simulation parameters are Δx and k_{LR}. The other simulation parameters are kept constant, see Table S5.8. Fig. 5.4b and S5.8 show that there are multiple combinations of Δx and k_{LR} for which the simulated aggregation rate matches with the measured aggregation rate. Small inter-particle distances ($\Delta x \leq 8$ nm) and high ligand-receptor binding rates ($k_{LR} \geq 10^{-5}$ μm^{2}s^{-1}) are necessary to match the simulation with the experiment. The shape of the curve is solely due to the geometrical effect that at lower receptor densities it is more likely that there is no receptor present in the interaction area.

Subsequently, the experimental data for the 8, 7 and 5 bp DNA interaction is reproduced using the simulation. For each matching combination of Δx and k_{LR} simulations are performed with a varying nonzero dissociation rate. Fig. 5.4a shows the simulated aggregation rate curves for Δx = 4 nm and k_{LR} = 10^{-4} μm^{2}s^{-1} (red dot in Fig. 5.4b), accompanied by the experimental data. The simulation can reproduce the measured data for each DNA length. This implies that the enhanced binding selectivity for weak affinities can indeed be obtained by modifying only the dissociation rate of the ligand-receptor interaction.

Table 5.1 gives an overview of the simulated dissociation rates (green columns) that lead to a match between simulation and experiment, for all matching combinations of Δx and k_{LR} (grey columns). For a certain Δx multiple k_{LR} values are possible that range over orders of magnitude. It turns out that for a ten times higher binding rate, the corresponding dissociation rate that follows from the simulation is also ten times higher. We calculate the affinity constant K_a according to equation 5.5 for each simulation in Table 5.1 (blue columns).

$$K_a = \frac{k_{LR}}{k_{off}} \tag{5.5}$$

The affinity constant does not depend on the binding rate that is used in the simulation and only slightly depends on the interparticle distance. Although the simulation cannot yield the exact ligand-receptor binding rate and dissociation rate, it does give a very narrow range for the affinity constant. For shorter DNA lengths the obtained affinity constant decreases as expected. The obtained affinity constants are defined in terms of surfaces, but can be converted to volume affinity constants and then compared with the K_a calculated from the DNA sequences (for details see Section S5.9 of the Supporting Information). Table S5.9 shows that the affinity measured here is weaker than the affinity calculated from the DNA sequence. For example for the 7 bp DNA the measured K_a = 4·10^1 M^{-1} is significantly lower than the calculated affinity constant K_a = 8·10^7 M^{-1}. Several factors can be identified that might

be responsible for this lower affinity. The DNA molecules are bound to a particle surface which significantly alters their mobility as well as accessibility while in addition the particles are electrostatically charged by the large number of DNA molecules per surface area.

The selectivity parameter can be extracted from the simulation results, see Table 5.1 (orange columns). The selectivity values increase with decreasing DNA length. This is in agreement with the experimental observation that the selectivity increases with decreasing ligand-receptor affinity. The selectivity parameters resemble the measured values shown in Fig. 5.3b, for all DNA lengths except for the 5 bp DNA. However, the discrepancy for the 5 bp DNA is likely due to the limited data points in the rising edge of the experimental curve.

In this paper we measured the aggregation rate of DNA coated microparticles to mimic cell-particle binding. In the OMC experiment, the particles are held quasi continuously in close proximity ($< t_{int} >$ = 10 s). The interaction time is long enough to form multiple weak ligand-receptor bonds, which together form a stable bond between the particles. However, when identical particles were freely dispersed in a solution, the proximity time would be much shorter. If the proximity time is shorter than the typical time to form a single ligand-receptor bond, particle aggregation is very unlikely to occur.

We calculate the interaction time for particles free in solution using the diffusivity of the particles. For particles with radius R = 0.25 μm in an aqueous solution with viscosity η = 1 mPa·s, the typical time in which a particle diffuses a distance equal to the ligand-receptor bond length L_{bond} = 0.02 μm is calculated by equation 5.6.

$$\tau_{prox} = \frac{\pi \eta R L_{bond}^2}{k_B T} \tag{5.6}$$

This gives a proximity time of τ_{prox} = 10^{-4} s. Experimentally, we cannot install such short actuation times, but we can calculate the typical time τ_{LR} in which a single ligand-receptor bond is formed, by rewriting equation 5.3 and 5.4 to equation 5.7.

$$\tau_{LR} = \frac{1}{k_{LR} \sigma_L \sigma_R A_{int}} \tag{5.7}$$

For the highest ligand and receptor densities that were experimentally assessed in this study, σ_L = σ_R = 10^4 μm^{-2}, and a typical ligand-receptor association rate in solution of 10^5 M^{-1}s^{-1} that corresponds to k_{LR} = 10^{-2} μm^{2}s^{-1}, we obtain a typical binding time of τ_{LR} = 10^{-4} s. This implies that there is a significant chance to for a single ligand-receptor bond during a single particle encounter. For the high affinity DNA interaction (15/12/9 bp) a single bond can cause particle aggregation. However, for

the low affinity DNA interaction (8/7/5 bp) it is unlikely that a stable multivalent bond will be formed during a single particle encounter, i.e. many particle encounters are necessary to obtain a significant probability for particle aggregation.

These calculations suggest that to observe selective particle binding for particles free in solution, similar to Fig. 5.3a, either the particles should be larger to enhance the proximity time and the interaction area, or the ligand and receptor densities should be higher. The results described in this paper, hold implications for the relevant field of targeted drug delivery. Particle size, ligand densities and ligand-receptor affinities need to be tailored to target the correct onset receptor density.

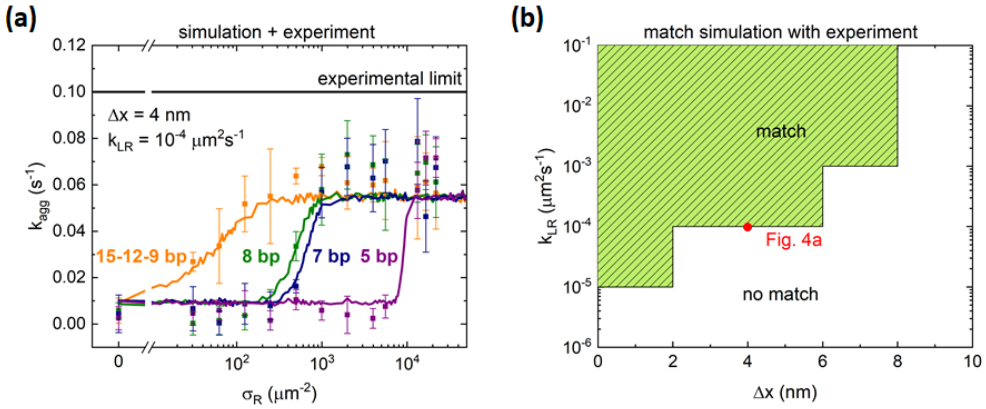

Fig. 5.4 Simulation results compared to experimental data. (a) Experimental data points accompanied by simulated aggregation rate curves for an inter-particle distance Δx = 4 nm and a ligand-receptor binding rate k_{LR} = 10^{-4} μm^{2}s^{-1}. The experimental data of the 15, 12 and 9 bp DNA is averaged as this data is very similar. Simulated aggregation rate curves for the other combinations of Δx and k_{LR} are shown in Fig. S5.8. **(b)** Heat map showing the possible combinations of Δx and k_{LR} for which the simulation reproduces the experimental data. Small inter-particle distance and high ligand receptor binding rates lead to a match between simulation and experiment. The red dot shows the specific combination of Δx and k_{LR} for the simulation curves in Fig. 5.5a.

Table. 5.1 Overview of simulation results. Simulations were performed for each consistent combination of the inter-particle distance Δx and ligand-receptor binding rate k_{LR} (grey columns). The dissociation rate k_{off} for which the simulation reproduces the experimental data of the 8, 7 and 5 bp DNA was determined for each combination of Δx and k_{LR} (green columns). The affinity constant K_a, the ratio of ligand-receptor binding rate k_{LR} and dissociation rate k_{off}, are independent of the used k_{LR} and depend only slightly on the inter-particle distance Δx (blue columns). The selectivity parameter of the simulated aggregation rate curves were extracted by fitting the curves of Fig. S5.8 (orange columns).

		k_{off} (s^{-1})			$K_a = k_{LR} / k_{off}$ (μm^2)			selectivity α			
Δx (nm)	k_{LR} ($\mu m^2 s^{-1}$)	8 bp	7 bp	5 bp	8 bp	7 bp	5 bp	9-15 bp	8 bp	7 bp	5 bp
2	10^{-5}	$3.0 \cdot 10^{0}$	$4.0 \cdot 10^{0}$	$6.0 \cdot 10^{0}$	$3.3 \cdot 10^{-6}$	$2.5 \cdot 10^{-6}$	$1.7 \cdot 10^{-7}$	0.5	1.6	1.9	7.2
	10^{-4}	$3.0 \cdot 10^{1}$	$4.0 \cdot 10^{1}$	$6.0 \cdot 10^{1}$							
	10^{-3}	$3.0 \cdot 10^{2}$	$4.0 \cdot 10^{2}$	$6.0 \cdot 10^{2}$							
4	10^{-4}	$2.5 \cdot 10^{1}$	$3.5 \cdot 10^{1}$	$4.0 \cdot 10^{1}$	$4.0 \cdot 10^{-6}$	$2.9 \cdot 10^{-6}$	$2.5 \cdot 10^{-7}$	0.5	1.5	1.9	6.1
	10^{-3}	$2.5 \cdot 10^{2}$	$3.5 \cdot 10^{2}$	$4.0 \cdot 10^{2}$							
6	10^{-4}	$2.0 \cdot 10^{1}$	$3.0 \cdot 10^{1}$	$3.5 \cdot 10^{1}$	$5.0 \cdot 10^{-6}$	$3.3 \cdot 10^{-6}$	$2.9 \cdot 10^{-7}$	0.5	1.4	1.7	5.6
	10^{-3}	$2.0 \cdot 10^{2}$	$3.0 \cdot 10^{2}$	$3.5 \cdot 10^{2}$							
8	10^{-3}	$1.7 \cdot 10^{2}$	$2.7 \cdot 10^{2}$	$3.0 \cdot 10^{2}$	$5.9 \cdot 10^{-6}$	$3.7 \cdot 10^{-6}$	$3.3 \cdot 10^{-7}$	0.5	1.3	1.7	6.1

5.6 Conclusion

In this paper, the selectivity was studied of the multivalent binding between DNA coated ligand and receptor particles, quantified by the rate of aggregation observed in an optomagnetic cluster experiment. The aggregation rate was measured for a broad range of receptor and ligand densities, showing how increasing densities lead to increasing aggregation rates. A selectivity parameter is defined as the relative increase in the number of particle dimers as a function of the receptor density on the particle, where a selective binding process is characterized by a selectivity parameter exceeding 1. For DNA receptors with different numbers of complementary base pairs, from 15 to 5 bp, the following selectivity parameters were obtained: α_{15bp} = 0.9±0.1, α_{12bp} = 0.7±0.1, α_{9bp} = 1.0±0.2, α_{8bp} = 1.7±0.3, α_{7bp} = 1.9±0.5 and α_{5bp} = 1.8±0.5. These results proof that weaker ligand-receptor affinity leads to enhanced binding selectivity.

A simulation model tailored to the optomagnetic experiment reproduces the experimentally obtained values of the selectivity parameter α. Moreover the simulation indicates that the enhanced selectivity for a weaker ligand-receptor affinity can be explained by only an increase in the dissociation rate of ligand and receptor. The simulation results show the importance of the proximity time of the particles for the possibility to form multivalent bonds. Guidelines are suggested for the design of particles for drug delivery in terms of particle size, ligand density and ligand-receptor affinity.

5.7 Supporting Information

S5.1 Optomagnetic cluster (OMC) experiment

In this paper specific particle aggregation rates will be measured using the OMC experiment described in a previous paper[22]. Fig. S5.1a sketches the optomagnetic cluster (OMC) experiment. A square glass cuvette filled with a solution of particles is situated in the centre of a quadrupole electromagnet setup, which can produce a rotating magnetic field in the y,z plane. A 660 nm laser is focussed insight the cuvette and the light scattered by the particles is measured by a photodetector at an angle of 90° w.r.t. to the incoming laser beam. In the presence of a rotating magnetic field, with a rotation frequency below the breakdown frequency, the dimers in the solution will rotate along with the magnetic field. Fig. S5.1c shows the oscillating scattering signal for the superparamagnetic particles used in this paper: polystyrene Ademtech Masterbeads (d = 528 nm, CV ≈ 25%). The amplitude of the oscillating scattering signal is a measure of the dimer concentration. The Fourier transform of this oscillating scattering signal is shown Fig. S5.1d. The peak at four times the field rotation frequency, |A4f|, is the largest contribution to the scattering signal and is used as a measure of the dimer concentration. Fig. S5.1e shows a calibration measurement of the |A4f| peak, indicating that |A4f| scales linear with dimer concentration.

To quantify the aggregation rate a four-step actuation protocol is followed, as can be seen in Fig. S5.1b. Initially the number of already present chemical dimers is measured using magnetic pulses with a short on-time, t_{on} = 0.4 s, and a long off time, t_{off} = 10 s. During the subsequent actuation phase, the rotating magnetic field is turned on continuously during a time t_{act} = 20 s to induce additional magnetic dimers, causing the |A4f| signal to increase approximately linearly over time (this is true for both types of particles, see Fig. S5.1f). Since each magnetic dimer is formed at a different point in time, each magnetic dimer has a different interaction time in which it has the possibility to form a chemical bond. The mean interaction time of all dimers, for a constant magnetic dimer formation rate, equals half the actuation time. After the actuation phase, the field is turned off during a waiting time t_{wait} = 40 s to let the non-aggregated particles redisperse in solution. Ultimately, the number of chemical dimers is measured again and compared to the initial number of dimers. The increase in the number of chemical dimers, ΔN_{chem}, depends on how reactive the particles are. To calculate the aggregation rate k_{agg}, the fraction of magnetic dimers that becomes a chemical dimer during the actuation phase, $\Delta N_{chem}/N_{mag,tot}$, is divided by the mean interaction time of all magnetic dimers.

$$k_{agg} = \frac{\Delta N_{chem} \,/\, N_{mag,tot}}{\frac{1}{2} t_{act}} \tag{S5.1}$$

In case of very reactive particles, it is possible that all magnetic dimers form a chemical bond during the interaction time. For a 20 s actuation time the maximum experimentally measurable aggregation rate is limited to $k_{agg,max}$ = 0.1 s^{-1}.

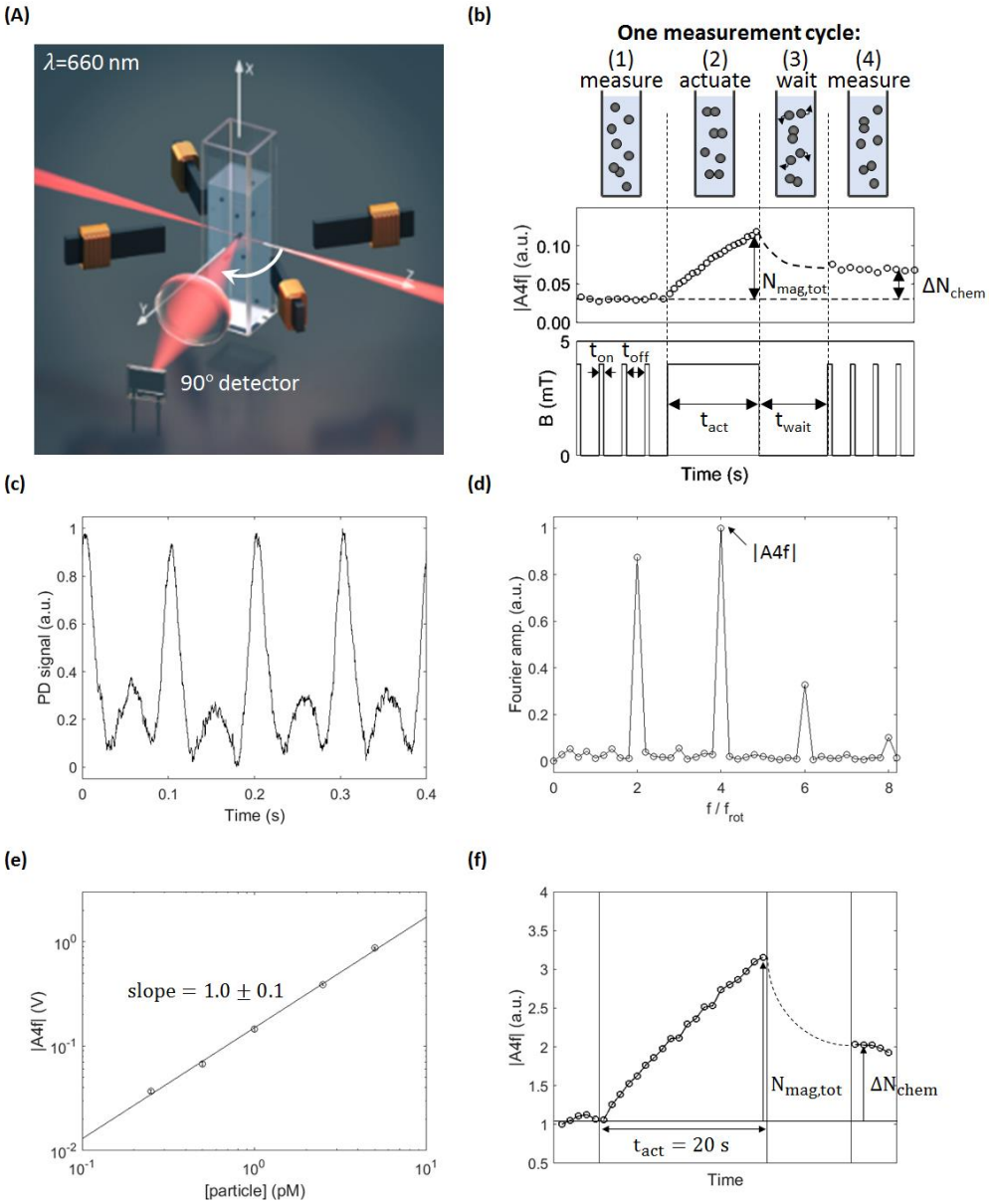

Fig. S5.1 Optomagnetic cluster experiment. (a) Optomagnetic dimer quantification: A 660 nm laser is focussed inside a cuvette filled with a particle solution. The scattering of the particles is measured at an angle of 90° w.r.t. the incoming laser beam. Four electromagnets are placed around the cuvette to apply a

rotating magnetic field. Particle dimers are rotated, which leads to an oscillating scattering signal. The amplitude of the oscillating signal is used as measure of the dimer concentration. **(b)** Four-step actuation protocol to quantify the aggregation rate. First, the initial number of chemical dimers in the solution is measured using short magnetic field pulses. Then the field is turned on continuously to induce additional magnetic dimers, during an actuation time t_{act}. The field is subsequently turned off for a waiting time t_{wait} to let the unbound particles redistribute in the solution. Finally, the new number of chemical dimers is measured. Using equation 5.2 the aggregation rate can be determined. **(c)** Oscillating scattering signal of the Ademtech Masterbeads, measured by a photodetector at an angle of 90° w.r.t. the incoming laser beam in the presence of a rotating magnetic field, f_{rot} = 5 Hz. **(d)** Fourier transform of the oscillating scattering signals of Fig. S5.1c, showing peaks at multiples of two times the field rotation frequency. **(e)** Calibration measurement of |A4f| as a function of particle concentration of a stock solution (containing a constant number of dimers), indicating that the |A4f| scales linearly with dimer concentration. **(f)** Single actuation cycle to measure the aggregation rate with the OMC experiment.

S5.2 Info DNA strands

In this paper several different DNA constructs are used: ligand DNA, receptor DNA and filler DNA. Table S5.2 gives an overview of all the ssDNA sequences that have been purchased from IDT to build these functional dsDNA constructs from. The light blue part of the ligand- or receptor sequences is complementary with the dark blue part of the biotinylated base sequence. The light green parts of the receptor strands are complementary with the dark green parts of the ligand strand. Ligand DNA strands are made by annealing the ligand strand to the base strand (L15+B). Receptor DNA strands are made by annealing a receptor strand to the base strand (Rx+B). Filler DNA strands are made by annealing the filler strand to the base strand (F+B).

Table S5.2 Info DNA sequences. Overview of the single stranded DNA sequences from which the ligand DNA, receptor DNA and filler DNA is made.

Code:	Name:	5′ mod:	Strand 5′ to 3′:
B	base strand	biotin	CCT CCC AGC CCA TCC TAA CC
F	filler strand	-	GG TTA GGA TGG GCT GGG AGG
L15	ligand strand 15	-	AAA CAA GAC GAC GAA GG TTA GGA TGG GCT GGG AGG
R15	receptor strand 15	-	TTC GTC GTC TTG TTT GG TTA GGA TGG GCT GGG AGG
R12	receptor strand 12	-	GTC GTC TTG TTT GG TTA GGA TGG GCT GGG AGG
R9	receptor strand 9	-	GTC TTG TTT GG TTA GGA TGG GCT GGG AGG
R8	receptor strand 8	-	TC TTG TTT GG TTA GGA TGG GCT GGG AGG
R7	receptor strand 7	-	C TTG TTT GG TTA GGA TGG GCT GGG AGG
R5	receptor strand 5	-	TG TTT GG TTA GGA TGG GCT GGG AGG

S5.3 Supernatant assay for DNA docking strand density quantification

To determine the maximum DNA coverage of the streptavidin coated Ademtech Masterbeads for short biotinylated DNA strands, an indirect fluorescence supernatant assay is performed. Fig. S5.3a shows in blue a calibration curve of the fluorescence intensity corresponding to concentration of biotin-atto655. The capacity of the Ademtech Masterbeads for b-atto655 is measured by incubating different b-atto655 concentrations with a constant particle concentration (2.5 pM). After 60 minutes of incubation in an incubator shaker (1200 rpm, room temperature), the fluorescence of the supernatant is measured (green line in Fig. S5.3a). The b-atto655 capacity per particle is obtained from the point in the graph where the fluorescence intensity of the supernatant starts increasing, $N_{b-atto655,SN}$ = (7.3±0.6)·10⁴. The measured capacity is slightly lower than the geometrical capacity ($N_{b-atto655,geometrical}$ = 10⁵) that can be expected based on the size of the particle (d = 500 nm), the size of a streptavidin (sphere, d ~ 5 nm) and the number of functional biotin binding pockets per streptavidin (~2.5 out of 4).

In the indirect supernatant assay the particles are first functionalized with different amounts of biotinylated DNA strands for 60 minutes in an incubator shaker (1200 rpm, room temperature). Subsequently particles are magnetically washed and another incubation step is performed with a b-atto655 concentration that is slightly higher than the b-atto655 capacity. From the fluorescence intensity of the supernatant, the DNA coverage can be calculated using equation 1. Fig. S5.3b shows that when increasing the DNA concentration the DNA coverage also increases, until a plateau is reached at $N_{DNA,max}$ = (1.7±0.4)·10⁴. The corresponding maximum DNA coverage is $\sigma_{DNA,max}$ = (2.2±0.5)·10⁴ µm⁻². The DNA capacity is about a factor four lower than the b-atto655 capacity, which can most likely be explained by the negative charge on the DNA backbone.

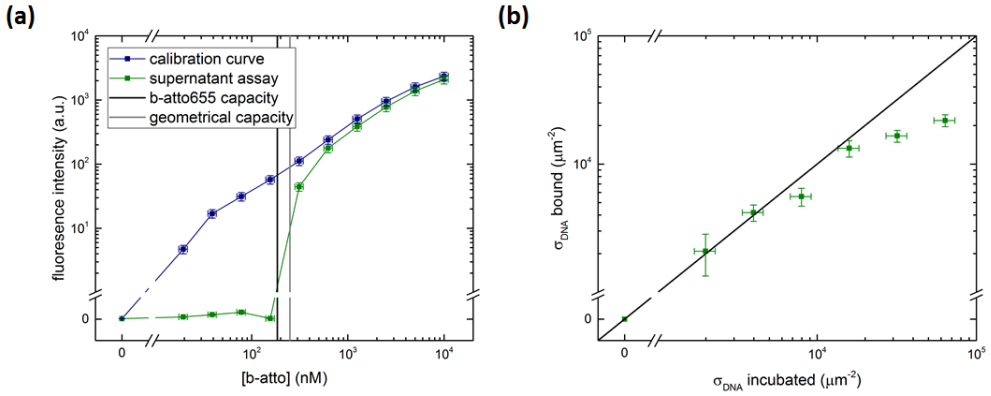

Fig. S5.3 Supernatant assay for DNA docking strand quantification. (a) Calibration curve (blue) of the fluorescence intensity as a function of the biotin-atto655 concentration. Supernatant assay (green) after b-atto655 incubation with streptavidin coated Ademtech Masterbeads to obtain the capacity of the particles for b-atto655. **(b)** DNA areal density as a function of the incubated maximum DNA areal density, measured with an indirect fluorescence supernatant assay.

S5.4 Control experiment of nonspecific aggregation rates

A control experiment is performed to investigate the nonspecific aggregation rate between ligand particles or between receptor particles. Fig. S5.4a shows that the aggregation of particles coated with the same ligand with a 15 nt single-stranded overhang is below 0.01 s^{-1} for the complete range of receptor and ligand densities. Fig. S4b shows similar aggregation rates for particles coated with ligands of shorter complementary DNA interaction, at high receptor and ligand density.

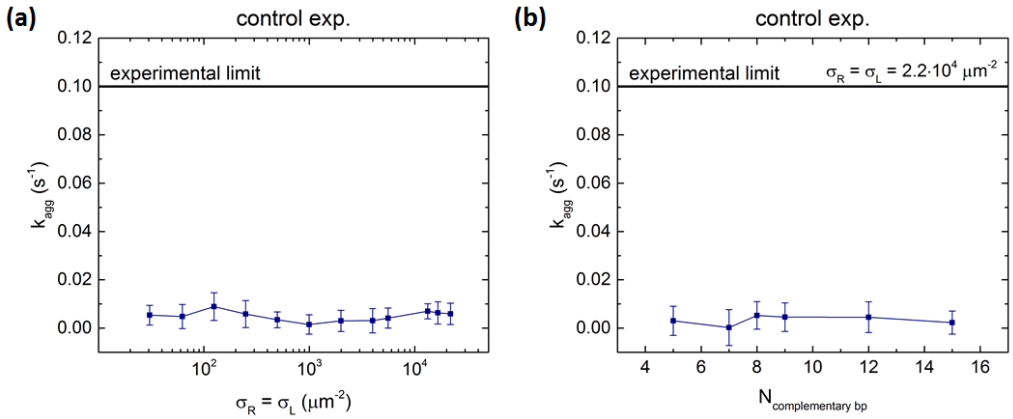

Fig. S5.4 Control experiment of nonspecific aggregation between similar particles. (a) Aggregation rate of similar particles as a function of the density of ligand or receptor DNA, showing low rates that are independent of the density. **(b)** Aggregation rate for similar particles, for different lengths of the single-stranded overhang.

S5.5 Fitting aggregation rate as a function of receptor density

To quantify the selectivity parameter α for each DNA length, the aggregation rate graphs are fitted, see Fig. S5.5. The S-shaped curves are fitted using the sigmoid function of equation S5.2.

$$y = \frac{a}{1+\exp(-k(x-x_c))} \tag{S5.2}$$

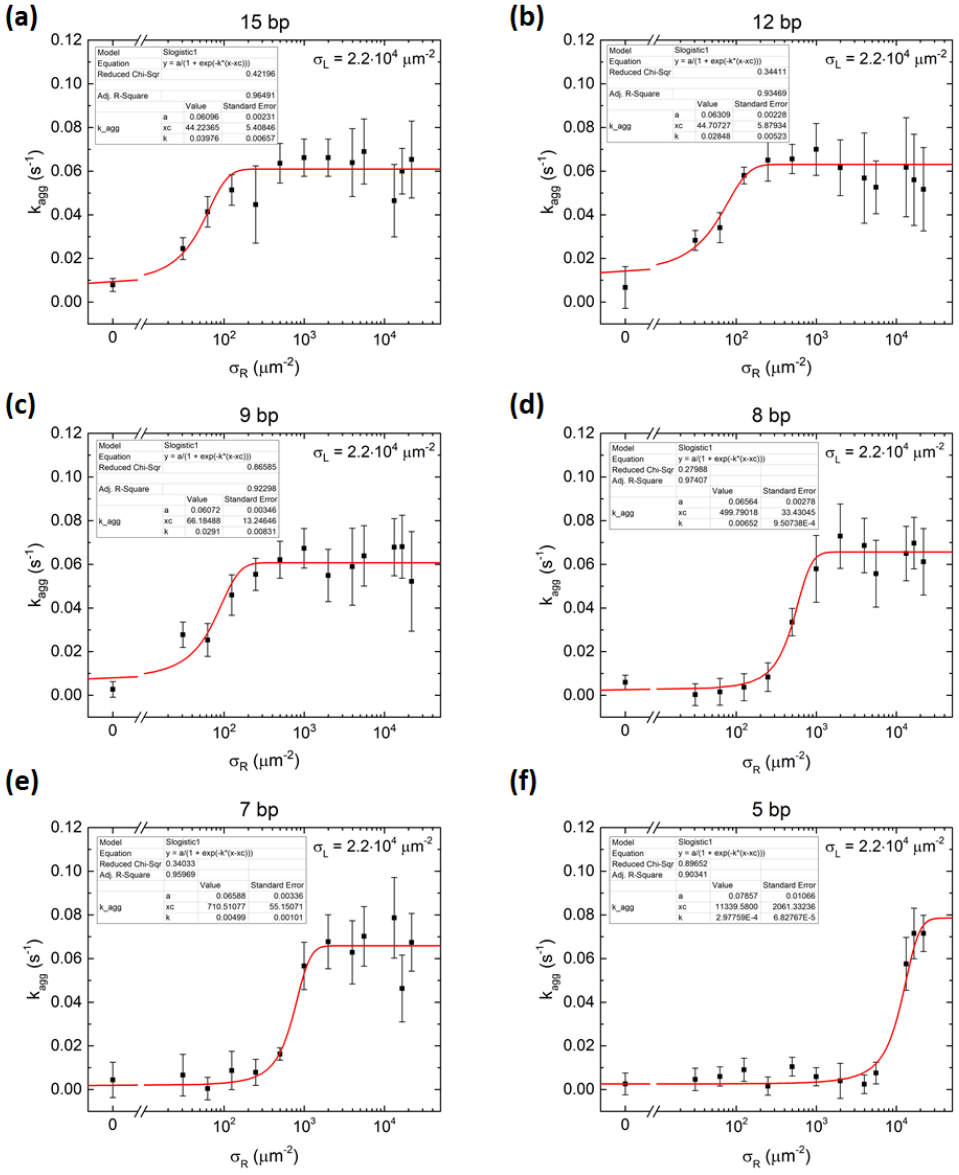

Fig. S5.5 Fitted aggregation rate curves. Aggregation rate as a function of the receptor density fitted with the sigmoid function of equation S2: **(a)** 15 bp **(b)** 12 bp **(c)** 9 bp **(d)** 8 bp **(e)** 7 bp and **(f)** 5 bp.

S5.6 Calculation of multivalent interaction point

There exists a receptor density at which there is on average exactly one receptor able to bind to the other particle in the dimer. For higher receptor densities there can on average be more than one receptor able to bind to the other particle, thus multivalent binding is possible. Fig. S5.6 shows a sketch of the particle dimer,

including the important length scales: The bond length L_{bond} ~ 20 nm, the particle radius R_p = 250 nm and the interparticle distance Δx ~ 5 nm. Using these length scales and equation S5.3, the receptor density at which on average one receptor is present in the interaction area can calculated:

$$\sigma_{R1} = \frac{1}{\pi R_p (L_b - \Delta x)} \approx 10^2 \text{ µm}^{-2} \quad \text{(S5.3)}$$

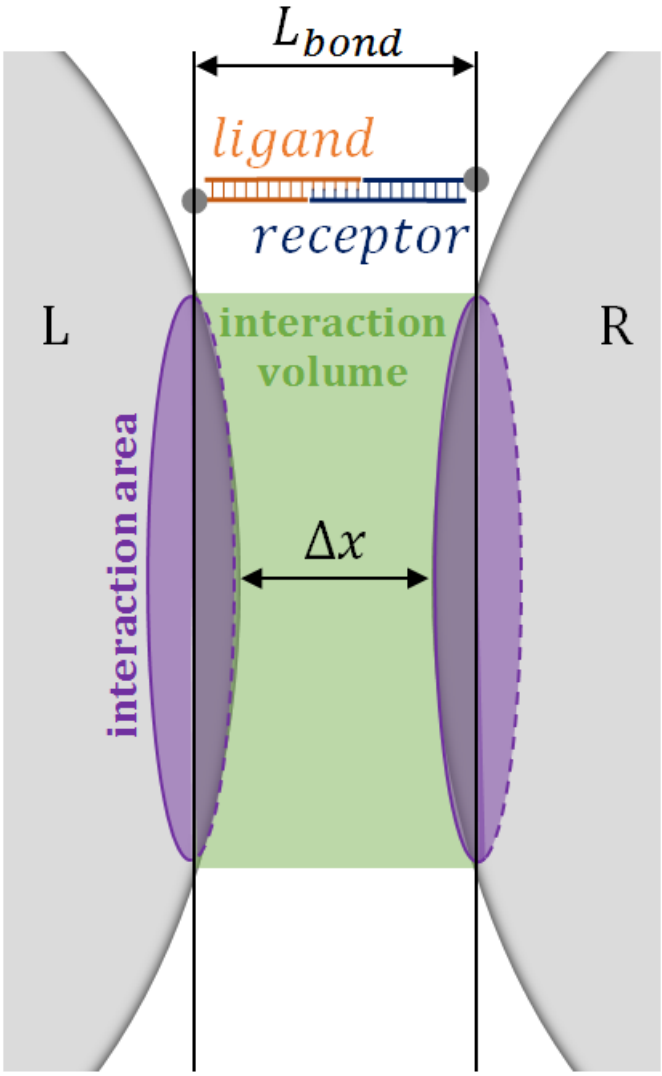

Fig. S5.6 Length scales for calculation of multivalent interaction rage. Sketch of the interface between two particles indicating the area on the particles where the ligands or receptors can bind to the other particle.

S5.7 Parameter scan of aggregation rate simulation

To get insight in the effect of different simulation parameters on the simulated aggregation rate, a parameter scan is performed. One parameter is varied in the simulation while the other parameters are kept constant to the default values shown in Table S5.7.

Table S5.7 Default input values parameter scan. Overview of the default input values in the parameter scan of the aggregation rate simulation shown in Fig. S5.6.

default input values parameter scan			
parameter	**symbol**	**value**	**unit**
particle radius	R	0.25	μm
maximum bond length	L_{bond}	0.016	μm
interparticle distance	Δx	0.006	μm
actuation time	t_{act}	20	s
waiting time	t_{wait}	40	s
simulation time step	dt	10^{-4}	s
ligand surface density	σ_L	10^3	μm^{-2}
magnetic dimer formation rate	k_{dim}^{mag}	10^2	s^{-1}
ligand receptor binding rate	k_{LR}	10^{-5}	$\mu m^2 s^{-1}$
ligand receptor dissociation rate	k_{off}	0	s^{-1}
nonspecific particle aggregation rate	k_{ns}	0.01	s^{-1}

Fig. S5.7 shows the results of a parameter scan of the simulation for the paramters: ligand density σ_L, inter-particle distance Δx, ligand-receptor binding rate k_{LR} and dissociation rate k_{off}, as a function of the receptor density σ_R. Table S5.7 shows the default input values for the parameter scan of the simulations. All simulated curves level off at an aggregation rate slightly above k_{agg} = 0.05 s^{-1}, half of the experimental limit, because only fifty percent of the dimers is a ligand-receptor dimer and the other dimers only have nonspecific interaction. Fig. S5.7a shows the simulated aggregation rate as a function of the receptor density for varying inter-particle distance Δx. The inter-particle distance Δx determines the size of the interaction area on the particles. For increasing Δx the aggregation rates decrease and the curves shift to slightly higher receptor densities and become somewhat less steep. By increasing the ligand-receptor binding rate k_{LR}, bonds are formed faster whereby the simulated curves shift to substantially lower receptor densities, see Fig. S5.7b. Increasing the ligand density σ_L has a similar but stronger effect on the simulated aggregation rate as decreasing the inter-particle distance. Higher ligand densities lead to faster aggregation, see Fig. S5.7c. For nonzero dissociation rates k_{off}, particle dimers can dissociate such that the

simulated aggregation rate decreases. Fig. S5.7d shows how the aggregation rate curves decrease and become steeper. At low receptor densities, the rate at which bonds are formed is lower than the rate at which a bonds dissociate, therefore a low aggregation rate is obtained. For high receptor densities, bonds are formed faster than they dissociate and the aggregation rate becomes equal to the aggregation rate curve with k_{agg} = 0 s^{-1}.

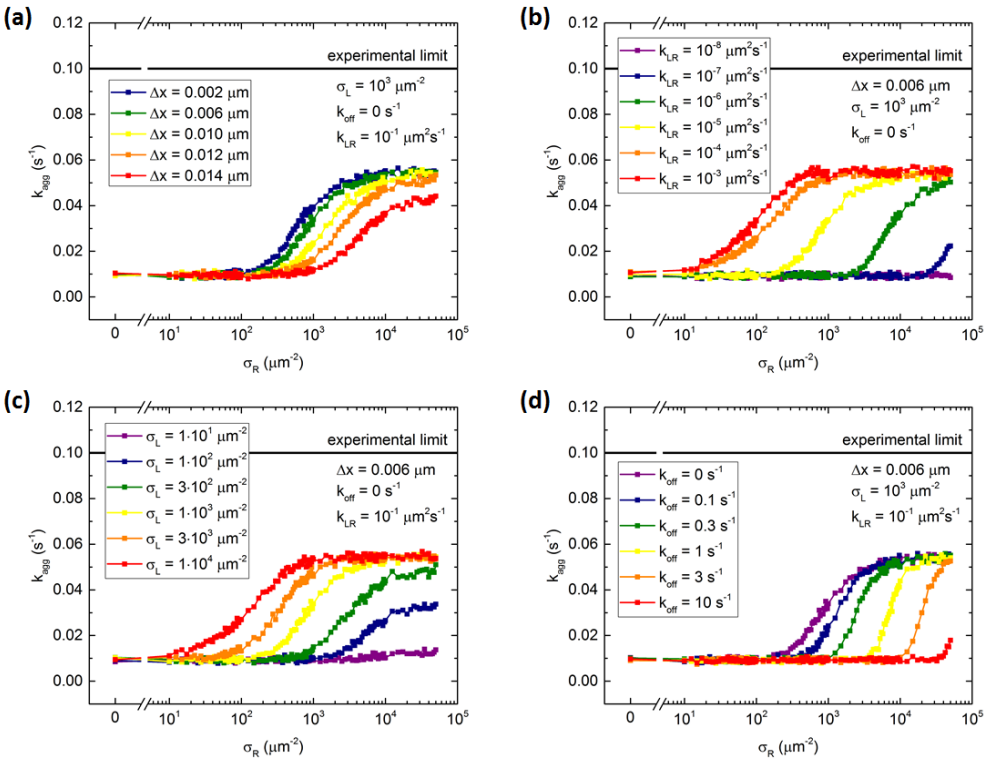

Fig. S5.7 Simulation parameter scan. Simulated aggregation rate as a function of the receptor density, for a parameter scan of **(a)** the surface-to-surface distance Δx **(b)** the ligand-receptor binding rate k_{LR} **(c)** the ligand density σ_L and **(d)** the dissociation rate k_{off}.

S5.8 Matching simulation with experimental data

Simulation are performed to reproduce the experimental data. Initially, the 9-15 bp data is reproduced using the input parameters that are shown in the second column in Table S5.58. The dissociation rate k_{off} is kept equal to zero as dissociation is not likely to occur for these DNA lengths. The interparticle distance Δx and the ligand-receptor binding rate k_{LR} are varied. Several combinations lead to agreement between simulation and experiment, as can be seen in Fig. S5.8 and Fig. 5.4b.

Subsequently the 8, 7 and 5 bp data is reproduced by performing the simulation for each correct combination of Δx and k_{LR}, while increasing the dissociation rate k_{off}. Fig. S5.8 shows that the measured data for the 8, 7 and 5 bp DNA can be reproduced with the simulation.

Table S5.8 Input values simulation. Overview of the default input values for the aggregation rate simulations shown in Fig. S5.8. For the 9-12 bp simulation, the dissociation rate is chosen equal to zero and Δx and k_{LR} are varied to match the simulation with experimental data. For the simulation of the 8, 7 and 5 bp data the Δx and k_{LR} are kept equal to the values that are found in the 9-12 bp simulation. The dissociation rate is varied to match the simulation with the experimental results of the 8, 7 and 5 bp DNA.

input values simulation					
parameter	**15 – 9 bp**	**8 bp**	**7 bp**	**5 bp**	**unit**
R	0.25	0.25	0.25	0.25	μm
L_{bond}	0.020	0.020	0.020	0.020	μm
t_{act}	20	20	20	20	s
t_{wait}	40	40	40	40	s
dt	10^{-4}	10^{-4}	10^{-4}	10^{-4}	s
σ_L	$2.2 \cdot 10^4$	$2.2 \cdot 10^4$	$2.2 \cdot 10^4$	$2.2 \cdot 10^4$	μm^{-2}
k_{dim}^{mag}	10^2	10^2	10^2	10^2	s^{-1}
k_{ns}	0.01	0.01	0.01	0.01	s^{-1}
k_{off}	0	varied	varied	varied	s^{-1}
Δx	varied	constant	constant	constant	μm
k_{LR}	varied	constant	constant	constant	$\mu m^2 s^{-1}$

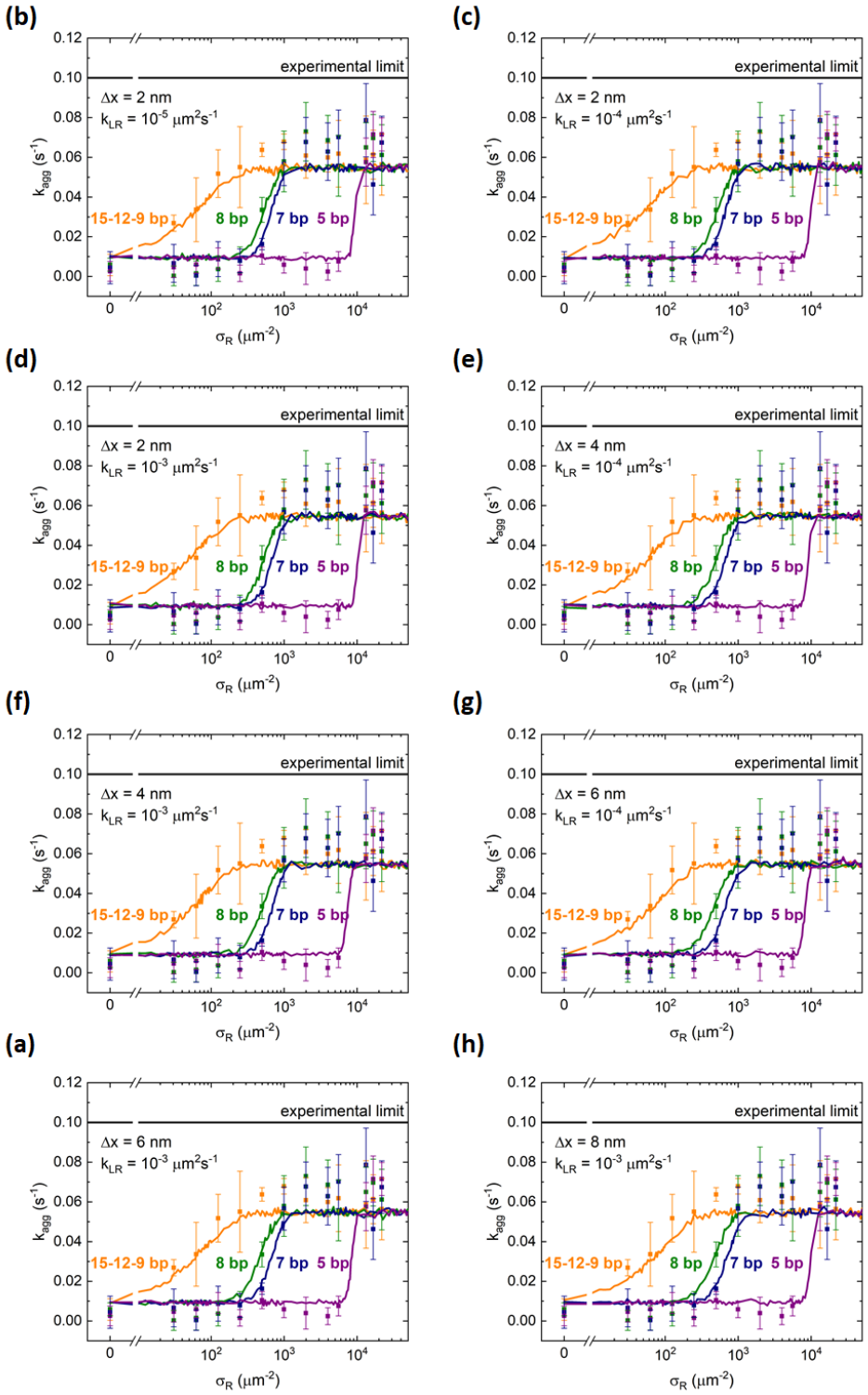
(b)
Δx = 2 nm
k_LR = 10^-5 μm^2s^-1
(c)
Δx = 2 nm
k_LR = 10^-4 μm^2s^-1
(d)
Δx = 2 nm
k_LR = 10^-3 μm^2s^-1
(e)
Δx = 4 nm
k_LR = 10^-4 μm^2s^-1
(f)
Δx = 4 nm
k_LR = 10^-3 μm^2s^-1
(g)
Δx = 6 nm
k_LR = 10^-4 μm^2s^-1
(a)
Δx = 6 nm
k_LR = 10^-3 μm^2s^-1
(h)
Δx = 8 nm
k_LR = 10^-3 μm^2s^-1
experimental limit
15-12-9 bp
8 bp
7 bp
5 bp
k_agg (s^-1)
σ_R (μm^-2)

Fig. S5.8 Match simulation with experimental data. Measured data points matched with simulated aggregation rate curves for different combinations of the interparticle distance Δx and the ligand-receptor binding rate k_{LR}: **(a)** Δx = 2 nm, k_{LR} = 10^{-5} $\mu m^2 s^{-1}$ **(b)** Δx = 2 nm, k_{LR} = 10^{-4} $\mu m^2 s^{-1}$ **(c)** Δx = 2 nm, k_{LR} = 10^{-3} $\mu m^2 s^{-1}$ **(d)** Δx = 4 nm, k_{LR} = 10^{-4} $\mu m^2 s^{-1}$ **(e)** Δx = 4 nm, k_{LR} = 10^{-3} $\mu m^2 s^{-1}$ **(f)** Δx = 6 nm, k_{LR} = 10^{-4} $\mu m^2 s^{-1}$ **(g)** Δx = 6 nm, k_{LR} = 10^{-3} $\mu m^2 s^{-1}$ **(h)** Δx = 8 nm, k_{LR} = 10^{-3} $\mu m^2 s^{-1}$.

S5.9 Converting surface affinity constants to volume affinity constants

The surface affinity constants that are obtained from the match between simulations and experimental data are compared with the calculated affinity constants for each DNA length. To compare these values, they are converted to volume affinity constants. To convert the surface affinity constant to a volume affinity constant, the K_a is divided by the interaction area and multiplied by the interaction volume, see Fig. S5.6. The interaction area is the area of the spherical cap on the particle and is calculated using equation S5.4.

$$A_{int} = \pi R(L_{bond} - \Delta x) = 1.2 \cdot 10^{-2}\ \mu m^2 \quad \text{(S5.4)}$$

Here R = 0.25 μm is the particle radius, L_{bond} = 0.02 μm is the length of the DNA bond and Δx = 0.005 μm is the interparticle distance. The interaction volume is estimated by a cylinder with length L_{bond} and a radius equal to the radius a of the base of the spherical cap, see equation S5.5.

$$V_{int} = L_{bond}\pi a^2 = L_{bond}\pi[2(L_{bond} - \Delta x)R - (L_{bond} - \Delta x)^2] = 2.3 \cdot 10^{-4}\ \mu m^3 \quad \text{(S5.5)}$$

The volume affinity constant is now calculated using equation S5.6. Table S5.9 shows the calculated affinity constants.

$$K_a^V = K_a^A \frac{V_{int}}{A_{int}} \quad \text{(S5.6)}$$

The ΔG for each used DNA sequence is also converted to an affinity constant using equation S5.7, in which k_B is the Boltzmann constant and T is the absolute temperature.

$$K_a = \exp\left(\frac{\Delta G}{k_B T}\right) \cdot 1\text{M} \quad \text{(S5.7)}$$

The affinity constants obtained from the DNA sequences are significantly higher than the ones obtained from the match between simulation and experiment. Electrostatic repulsion between the DNA coated particles in a dimer may exert a force on the DNA bond and explain why a weaker affinity is measured here.

Table S5.9 Comparison of volume affinity constants from simulation and from DNA sequence. Upper part shows an overview of surface affinity constants that are obtained from the simulation and converted

to volume affinity constants according to equation S6. Bottom part shows the volume affinity constants calculated for each DNA sequence.

simulation results			
	8 bp	**7 bp**	**5 bp**
K_a (µm^2)	$4.6 \cdot 10^{-6}$	$3.1 \cdot 10^{-6}$	$2.6 \cdot 10^{-7}$
K_a (M^{-1})	$5.3 \cdot 10^{1}$	$3.6 \cdot 10^{1}$	$3.0 \cdot 10^{0}$
calculated from DNA sequence			
	8 bp	**7 bp**	**5 bp**
sequence	TCTTGTTT	CTTGTTT	TGTTT
ΔG (kcal/mol)	-12.3	-10.7	-7.18
K_a (M^{-1})	$1.1 \cdot 10^{9}$	$7.5 \cdot 10^{7}$	$1.9 \cdot 10^{5}$

References

[1] Liyanage, P.Y.; Hettiarachchi, S.D.; Zhou, Y.; Ouhtit, A.; Seven, E.S.; Oztan, C.Y.; Celik, E.; Leblanc, R.M. Nanoparticle-mediated targeted drug delivery for breast cancer treatment. *BBA* **2019**, 1871, 2, 419-433

[2] Wang, Z.; Deng, X.; Ding, J.; Zhou, W.; Zheng, X.; Tang, G. Mechanisms of drug release in pH-sensitive micelles for tumour targeted drug delivery system: a review. *Int. J. Pharm.* **2018**, 535, 253-260

[3] He, F.; Wen, N.; Xiao, D.; Yan, J.; Xiong, H.; Cai, S.; Liu, Z.; Liu, Y. Aptamer-based targeted drug delivery systems: current potential and challenges. *Curr. Med. Chem.* **2018**, 25

[4] Linja, M.J.; Savinainen, K.J.; Saramäki, O.R.; Tammela, T.L.J.; Vessella, R.L.; Visakorpi, T. Amplification and overexpression of androgen receptor gene in hormone-refractory prostate cancer. *Cancer Research* **2001**, 61, 3550-3555

[5] Di Renzo, F.; Olivero, M.; Katsaros, D.; Crepaldi, T.; Gaglia, P.; Zola, P.; Sismondi, P.; Comoglio, P.M. Overexpression of the MET/HGF receptor in ovarian cancer. *Int. J. Canc.* **1994**, 58, 658-662

[6] Martinez-Veracoechea, F.J.; Frenkel, D. Designing super selectivity in multivalent nano-particle binding. *PNAS* **2011**, 108, 10963-10968

[7] Carlson, C.B.; Mowery, P.; Owen, R.M.; Dykhuizen, E.C.; Kiessling, L.L. Selective tumor cell targeting using low-affinity multivalent interactions. *ACS Chem. Biol.* **2007**, 2, 119-127

[8] Joshi, A.; Vance, D.; Rai, P.; Thiyagarajan, A.; Kane, R.S. The design of polyvalent therapeutics. *Chemistry - A European Journal* **2008**, 14, 7738-7747

[9] Collins, B.E.; Paulson, J.C. Cell surface biology mediated low affinity multivalent protein glycan interactions. *Curr. Opin. Chem. Biol.* **2004**, 8, 617-625

[10] Morel, N.; Simon, S.; Frobert, Y.; Volland, H.; Mourton-Gilles, C.; Negro, A.; Sorgato, M.C.; Créminon, C.; Grassi, J. Selective and efficient immunoprecipitation of the disease-associated form of the prion protein can be mediated by nonspecific interactions between monoclonal antibodies and scrapie-associated fibrils. *J. Biol. Chem.* **2004**, 279, 30143-30149

[11] Curk, T.; Dobnikar, J.; Frenkel, D. Optimal multivalent targeting of membranes with many distinct receptors. *PNAS* **2017**, 114, 7210-7215

[12] Wang, S.; Dormidontova, E.E. Selectivity of ligand-receptor interactions between nanoparticle and cell surfaces. *Phys. Rev. Lett.* **2012**, 109, 238102

[13] Mani, V.; Wasalathanthri, D.P.; Joshi, A.A.; Kumar, C.V.; Rusling, J.F. Highly efficient binding of paramagnetic beads bioconjugated with 100 000 or more antibodies to protein-coated surfaces. *Analytical chemistry* **2012**, 84, 10485-10491

[14] Albertazzi, L.; Martinez-Veracoechea, F.J.; Leenders, C.M.A.; Voets, I.K.; Frenkel, D.; Meijer, E.W. Spatiotemporal control and superselectivity in supramolecular polymers using multivalency. *PNAS* **2013**, 110, 30, 12203-12208

[15] Dubacheva, G.V.; Curk, T.; Auzély-Velty, R.; Frenkel, D.; Richter, R.P. Designing multivalent probes for tunable superselective targeting. *PNAS* **2015**, 112, 18, 5579-5584

[16] Scheepers, M.R.W.; Romijn, A.R.; van IJzendoorn, L.J.; Prins, M.W.J. Rate of dimer formation in stable colloidal solutions quantified using an attractive interparticle force. *Langmuir*, **2019**, 35, 10533-10541

[17] Wetmur, J.G. Hybridization and renaturation kinetics of nucleic acids. *Annu. Rev. Biophys. Bioeng.* **1976**, 5, 337-361

[18] Wetmur, J.G.; Davidson, N. Kinetics of renaturation of DNA. *J. Mol. Biol.* **1968**, 31, 349-370

[19] Reynaldo, L.P.; Vologodskii, A.V.; Neri, B.P.; Lyamichev, V.I. The kinetics of oligonucleotide replacements. *J. Mol. Biol.* **2000**, 297, 511-520

[20] Sugimoto, N.; Nakano, S.; Yoneyama, M.; Honda, K. Improved thermodynamic parameters and helix initiation factor to predict stability of DNA duplexes. *Nucleic Acids Res.* **1996**, 22, 4501-4505

[21] Breslauer, K.J.; Frank, R.; Blocker, H.; Marky, L.A.; Predicting DNA duplex stability from the base sequence. *PNAS* **1986**, 83, 3746-3750

[22] Strunz, T.; Oroszlan, K.; Schäfer, R.; Güntherodt, H. Dynamic force spectroscopy of single DNA molecules. *PNAS* **1999**, 96, 11277-11282

Chapter 6

Protein corona induced inter-particle binding in blood plasma: the influence of biomolecular particle coating

The protein corona that forms around particles in complex biological fluids is very important for the stability and bio-functionality of the particles. In this study we quantify the aggregation kinetics of particles in blood plasma, for various surface coatings and solution conditions. The aggregation rate is demonstrated to increase with plasma concentration for particles coated with proteins, carboxylic acids, Tris and polyethylene glycol (PEG). In some cases, the aggregation rate increases super-linearly with plasma concentration, suggesting that multivalent weak interactions are responsible for the inter-particle aggregation. The particle aggregation rate is significantly reduced in plasma that has been pre-exposed to particles with the same functionalization. This demonstrates that the aggregation inducing corona proteins are different for the different particle coatings.

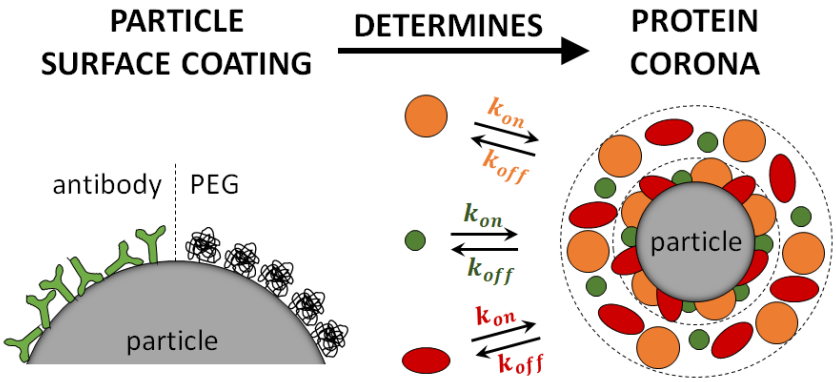

6.1 Introduction

Micro and nanoparticles are used in a wide range of medical applications, for example in biosensing[1,2] and targeted drug delivery[3,4]. Upon administration of particles in a complex biological fluid like blood plasma, a protein corona is formed around the particles which modifies the stability and functionality of the particles[5]. The presence of a protein corona typically increases nonspecific particle aggregation[6], negatively affecting drug delivery processes[7] and particle-based diagnostic assays[8].

The thousands of different plasma proteins[9] have affinities to the particle surface that vary over a wide range. Initially, the protein corona is formed by highly concentrated proteins which rapidly bind to the particle surface; this is followed by an exchange of proteins that have lower concentrations but higher affinities toward the particle surface[10,11]. The composition of the protein corona around a particle thus depends on plasma composition and many particle characteristics, e.g. particle size[12,13], shape[14], material[15], charge[16] and coating[16,17]. The protein corona is often described as consisting of a hard and a soft corona where the affinity of the proteins for the particle surface is the discriminating factor[18]. The hard corona is generally considered to consist of tightly bound proteins that do not readily desorb, whereas the soft corona contains the weakly bound proteins that are in a dynamic equilibrium with the bulk.

Finding out which plasma proteins are responsible for particle aggregation is a complex problem, not only due to the diversity of plasma proteins[9] and the dependence of corona composition on physicochemical properties of the particles[10-15,19], but also due to the difficulty to experimentally quantify the particle surface reactivity and to correlate this with protein corona composition.

Only few experimental reports exist in literature that measure particle-particle or particle-surface interaction in complex biological matrices. Gebauer et al. quantified the particle size distribution as a function of time by tracking Brownian motion trajectories of individual particles, in the presence of different concentrations of human serum albumin (HSA) in buffer[6]. The group of To Ngai made use of total internal reflection microscopy (TIRM) to quantify the potential energy landscape of protein coated particles above a protein coated surface in fetal bovine serum[20,21]. Ho et al. quantified the agglomeration of plasma protein coated gold nanoparticles using an aggregation index that is based on the spectral changes of surface plasmon resonance[22]. However, a comprehensive study that quantifies the surface reactivity of particles in diluted and undiluted blood plasma, is still lacking.

Here, we use a previously developed optomagnetic cluster (OMC) experiment[23] to study particle surface reactivity by quantifying the particle aggregation rate constant k_{agg} directly in blood plasma. The parameter k_{agg} represents the rate at which biochemical inter-particle aggregation occurs, for particles that are in a well-defined state of proximity. In the OMC experiment, the proximal state is created and controlled by an attractive magnetic inter-particle force. Briefly, a dispersion of superparamagnetic particles is exposed to an external magnetic field. The attractive inter-particle magnetic force brings particles together and the number of biochemically bonded dimers is recorded as a function of time. This allows a quantification of the inter-particle aggregation rate k_{agg}. A complete description of the OMC experiment is given in Section S6.1 of the Supporting Information.

In this chapter, we study the aggregation rate of particles in blood plasma as a function of the biomolecular surface coating (Fig. 6.1a). Measurement results as a function of plasma dilution suggest that the aggregation is caused by multivalent weak interactions between the protein coronas around the particles. The data show that particle aggregation in blood plasma is mainly caused by the hard corona proteins. Finally, the results demonstrate that aggregation inducing corona proteins are different for the different particle coating and that the aggregation rate increases on the time-scale of hours.

6.2 Materials and methods

6.2.1 Materials

Carboxylic acid coated superparamagnetic Ademtech Masterbeads were purchased from Ademtech (diameter 528 nm, coefficient of variation 25%). Phosphate buffered saline (PBS) tablets, 2-(N-morpholino)ethanesulfonic acid (MES), 1-ethyl-3-(dimethylaminopropyl) carbodiimide hydrochloride (EDC), tris (hydroxymethyl) aminomethane (tris), N-hydroxysulfosuccinimide (sulfo-NHS), bovine serum albumin (BSA, >98% pure) and Protein LoBind Eppendorf tubes were obtained from Sigma Aldrich. Monoclonal mouse IgG against cardiac troponin I (anti-cTnI 19C7) was supplied by Abcam. Amine-terminated polyethylene glycol (PEG) with a molecular weight of 5 kDa (Blockmaster CE510) was purchased from JSR Life Sciences. Amicon Ultra-0.5 mL centrifugal filters for protein purification were purchased from Merck. Mini-PROTEAN TGX precast gels (4-20%) were obtained from BIO-RAD. Borosilicate glass 3.3 cuvettes with inner dimensions of 1.00±0.05 x 1.00±0.05 mm and outer dimensions of 1.23±0.05 x 1.23±0.05 mm, and a length of 20±1 mm were obtained from Hilgenberg.

6.2.2 *Particle functionalization*

Carboxylic acid coated Ademtech Masterbeads were functionalized through an EDC-NHS reaction with one of the following four molecules: tris, BSA, 5 kDa PEG or a-cTnI 19C7. A solution of a large excess of one of these molecules will be referred to as the coating solution. All steps were performed at room temperature.

First, 4 µL of particle stock solution (50 mg/mL) was mixed with 196 µL a 100 mM MES solution (pH 5.0), 50 µL EDC in MES solution (10 mg/mL) and 50 µL NHS in MES solution (10 mg/mL). The particles were incubated for 30 minutes on a roller bench to activate the carboxyl groups on the particle surface.

After the activation step the particles were magnetically washed twice and redispersed in 200 µL MES solution. Subsequently the particle solution was sonicated (10x 0.5s) to undo the particle clustering that occurred during the magnetic washing steps. Then, 100 µL of coating solution was added to the particles and incubated for 3 hours on a roller bench, to covalently attach to the particles.

After the coating step the remaining active carboxyl groups are blocked by adding 100 µL of tris buffer (150 mM NaCl, 50 mM tris, pH 7.6) and incubating overnight on a roller bench. Finally, the particle solution is magnetically washed twice and the particle are redispersed in PBS buffer. Finally, the particle solution was sonicated (10x 0.5s) to undo the particle clustering that occurred during the functionalization process.

6.2.3 *Plasma dilution, filtration and washing*

Samples of citrate stabilized human blood plasma from healthy anonymous donors were obtained from Sanquin. Plasma was diluted using a PBS buffer, where a plasma concentration of x percent corresponds to a solution which consists of x percent of plasma and 100-x percent of PBS.

Plasma was filtered using Amicon spin filters with a molecular weight cut-off of 100 kDa. A volume of 500 µL blood plasma was inserted in the spin filter and placed in the centrifuge for 20 minutes at 13.000 rpm to separate the proteins based on molecular weight. PBS buffer was added to the filtrate to make the total volume equal to 500 µL, to keep the individual protein concentrations equal to their concentration in unfiltered plasma. The filter was taken out of the reaction tube and put upside down in another reaction tube and centrifuged again for 20 minutes at 13.000 rpm to retrieve the residue from the filter. Again PBS buffer was added to the residue to keep the individual protein concentrations equal to their concentration in unfiltered plasma.

Plasma samples were washed with (functionalized) particles to fish out the proteins that are present in the hard corona of those particular particles. For this purpose 0.2 mg of (functionalized) particles were added to 200 µL of plasma and incubated for 60 minutes on a roller bench at room temperature. Subsequently, the particle solution is magnetically washed three times and the particle are redispersed in PBS buffer. The depleted plasma solutions are used in the experiments.

6.3 The effect of particle coating on aggregation rate in (diluted) blood plasma

To study the effect of blood plasma on the surface reactivity of biofunctionalized particles, the aggregation rate was measured in various dilutions of plasma using the OMC experiment. The particles were functionalized with either carboxyl groups, the proteins IgG or BSA, or the blocking agents Tris or PEG (2 kDa). We used a large excess of coating molecules (>100x the amount of molecules that fit on the particle surface) and a long incubation time (3 hours). More details about the functionalization process can be found in the Materials and methods section.

Fig. 6.1b shows the nonspecific aggregation rate of biofunctionalized particles as a function of the plasma concentration, where a concentration of 0% corresponds to pure PBS buffer and a concentration of 100% corresponds to undiluted blood plasma. In buffer, the PEG and the carboxyl coating lead to the lowest aggregation rate compared to the other functionalizations, most likely due to steric and electrostatic stabilization of the particles, respectively. By gradually increasing the plasma concentration, the aggregation rate significantly increases independent of the functionalization. Note that the aggregation rate of the carboxyl coated particles exceeds the other coatings already at 3% plasma, whereas the aggregation rate of the PEG coated particles remains lowest at all plasma concentrations. While the steric stabilization by PEG limits the aggregation rate for buffer and plasma[24,25], the presence of reactive carboxyl groups (partially negatively charged) likely attracts protein moieties enhancing the nonspecific particle surface reactivity. The tris, BSA and anti-cardiac troponin I (a-cTnI) functionalized particles show a similar increase in aggregation rate when going from buffer to plasma.

In previous research, we studied inter-particle aggregation for DNA-functionalized particles[26]. In case of weak multivalent interactions, i.e. DNA interactions for which a single bond has a lifetime that is much shorter than the experiment ($\tau_{off} \ll 10^2$ s), the aggregation rate increased super-linearly with DNA surface density, indicative of a selectivity parameter above 1. The selectivity parameter α is defined by Martinez-Veracoechea and Frenkel[27] as the relative change

in the number of bound particles N_{bound} as a function of the number of receptors on a cell n_R, see equation 6.1.

$$\alpha = \frac{d \ln N_{bound}}{d \ln n_R} \tag{6.1}$$

In the present paper, the dependence of the aggregation rate k_{agg} on plasma concentration is measured. As the relation between protein surface coverage and protein concentration is unknown, we quantify the volume-selectivity α_V, i.e. the selectivity of the aggregation process for the protein concentration in the solution. Since the selectivity describes a relative change in the number of bound particles with the number of receptors, we can multiply N_{bound} and n_R in equation 6.1 by any nonzero constant, without changing α. Thus, we can replace N_{bound} and n_R by k_{agg} and plasma concentration, respectively.

$$\alpha_V = \frac{d \ln k_{agg}}{d \ln [plasma]} \tag{6.2}$$

Fig. 6.1c shows the volume-selectivity parameter as a function of the plasma concentration obtained from the aggregation rate curves of Fig. 1b. The volume-selectivity parameter exceeds 1 for different particle coatings. The tris, BSA and a-cTnI coated particles show a selectivity above 1 around a plasma concentration of 10% and the PEG coated particles show a selectivity above 1 for a plasma concentration of about 50%.

The obtained selectivities suggest that the inter-particle aggregation in blood plasma might be induced by multivalent weak interactions between the protein coronae of the interacting particles. However, to draw conclusions we need to know the relation between protein surface density and plasma concentration. By increasing the plasma concentration we basically increase the concentration of each individual protein in the solution. In case the protein surface density increases linearly with protein concentration in the solution, which may be expected for low protein concentration, the calculated volume-selectivity is equal to the selectivity of the aggregation process for protein surface density. At high protein concentration, the particle surface might become saturated whereby the protein surface density increase sub linearly with protein concentration. In this case the volume-selectivity parameter is an underestimation of the actual selectivity. However, cooperative binding effects between proteins on the particle surface might cause the protein surface density to increase super linearly with protein concentration. In this case the obtained volume-selectivity is an upper limit for the selectivity.

In order to investigate which corona proteins are responsible for particle aggregation we have carried out experiments with different plasma fractions

prepared using spin filters (MW cut-off 100 kDa). Unfortunately, the used spin filters were quickly saturated during the filtration process and the intended separation was not achieved, indicated by the presence of many small molecules (< 100 kDa) in the residue of the filter. A complete description of this experiment is given in Section S6.2 of the Supporting Information.

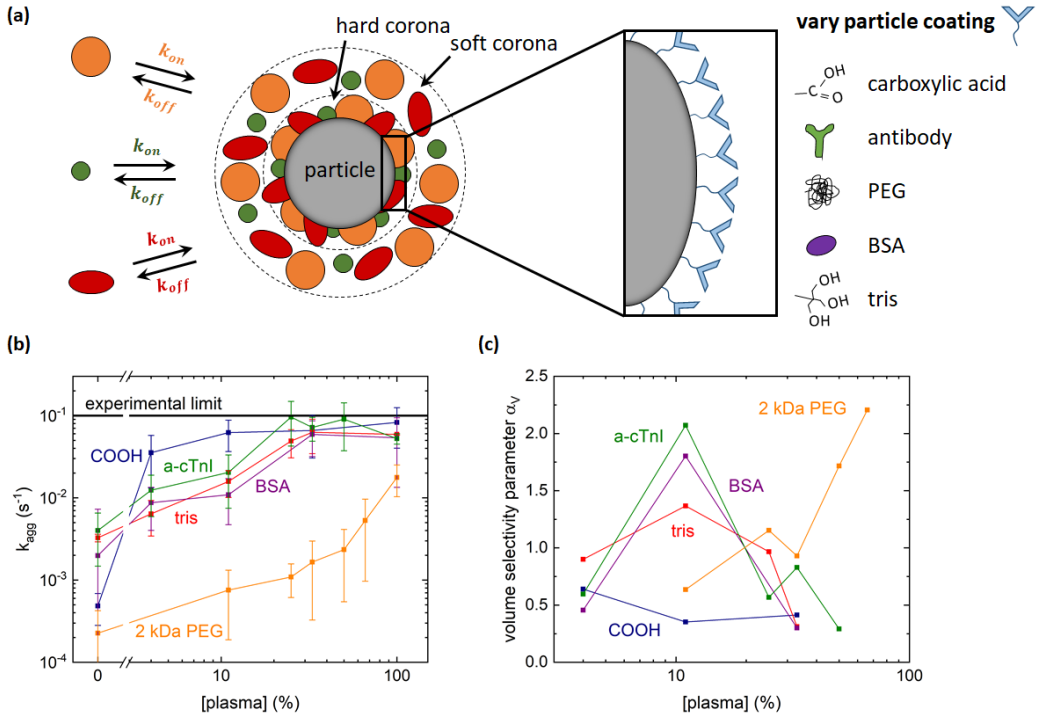

Fig. 6.1 Effect of particle coating on particle aggregation in blood plasma. (a) Interaction between plasma proteins and the particle surface causes the formation of a protein corona. The hard corona proteins are tightly bound to the particle surface, whereas the soft corona proteins are more weakly bound and in a dynamic equilibrium with the proteins in the solution. We vary the particle surface coating and investigate the effect on the rate of particle aggregation. **(b)** Particle aggregation rate as a function of the plasma concentration, for different particle functionalizations. At zero plasma concentration (pure PBS buffer) the COOH and PEG coated particles show the lowest aggregation rate. For nonzero plasma concentration the PEG coating gives the lowest aggregation rate. **(c)** Selectivity parameter α determined from the aggregation rate curves in Fig. 6.1b, as a function of the plasma concentration. A selectivity parameter above 1 corresponds to a super linear-increase in the aggregation rate curves, which suggests that multivalent weak interaction might be responsible for particle aggregation in blood plasma. The a-cTnI, BSA and tris functionalized particles have the highest selectivity parameter at a plasma concentration of 10%, whereas the PEG functionalized particles show high selectivity above 50% plasma concentration.

6.4 Effect of plasma composition on inter-particle aggregation

The optomagnetic cluster experiment also provides the opportunity to investigate whether the aggregation rate and composition of the protein corona depends on the functionalization of the particles. For this purpose, the corona proteins are depleted from a plasma sample using particles with a specific functionalization. This is achieved by incubating plasma samples with functionalized particles for one hour at room temperature, as illustrated in Fig. 6.2a. After incubation, the particles are magnetically separated and the supernatant, i.e. the depleted plasma, is preserved in another Eppendorf tube. Subsequently the particles are washed twice with PBS buffer. Ultimately we have a dispersion of particles with their hard corona in PBS buffer, and a plasma of which (part of) the hard corona proteins are washed out.

The aggregation rate of PEG or IgG functionalized particles was measured in buffer, in undiluted plasma and in plasma that has been depleted using particles with either a carboxyl coating, a PEG coating or an IgG coating, see Fig. 6.2b. The measurement in buffer yields the lowest aggregation rate and serves as a reference. The aggregation rate in plasma is highest and represents an upper limit for the aggregation rate. It is assumed that the presence of the protein corona around the particle is responsible for the increased aggregation rate in plasma compared to the aggregation rate in buffer. When measuring in the depleted plasmas the aggregation rate is lower compared to the full plasma measurement. The composition of the protein corona in the depleted plasma samples is apparently different from the protein corona in a non-depleted plasma. Moreover, when the plasma is depleted using particles with the same functionalization as the particles that are used for the aggregation rate measurements, the decrease in aggregation rate is larger than when the plasma is depleted using particles with a different functionalization. The composition of the depleted plasma samples must be different, hence the proteins that have been removed from the plasma during the depletion process are different when using particles with different particle functionalizations. This indicates that the composition of the protein corona depends on the particle functionalization. Apparently, the aggregation inducing proteins for a specific particle coating are selectively removed from the plasma, when depleting the plasma with particles having the same coating.

To investigate if particle aggregation is induced by proteins in the hard corona or in the soft corona, the aggregation rate was measured both in the presence of a hard and a soft corona, and in the presence of only a hard corona. In full plasma both the hard and the soft corona are present. To obtain only a hard corona around the particles, particles were incubated in full plasma for one hour, subsequently magnetically washed three times and finally redispersed in PBS buffer, see Fig. 6.2a.

These particles contain the hard corona, but lack the soft corona. The soft corona represents the dynamic equilibrium between association and dissociation of plasma proteins on the particle surface. However, when the bulk proteins in the solution are removed during the magnetic separation step, the dynamic equilibrium of the soft corona is distorted, whereby the soft corona proteins will dissociate from the particle surface. Fig. 6.2c shows the aggregation rate measured for PEG and IgG coated particles in either buffer (no corona), in full plasma (hard + soft corona) or in buffer after plasma incubation (only hard corona). For both functionalizations the aggregation rate for the hard corona only is about equal to the hard + soft corona, and significantly higher than the measurement without a corona. It seems that the aggregation inducing proteins are mainly present in the hard corona.

6.5 Timescale of protein corona formation

To investigate the timescale of protein corona formation, particles were incubated in plasma for different incubation times before the aggregation rate was measured, see Fig. 6.2d. The aggregation rate of PEG functionalized particles increases with incubation time and starts to reach a plateau for incubation times of more than one hour. However, because the plateau is close to the experimental limit, the particle reactivity may still be increasing with incubation time, but this is not measurable with the OMC method. Studies by Dell'Orco et al.[10] and Saneh et al.[11] also report protein corona formation times of multiple hours.

Particle-based diagnostic assays, such as the Magnotech technology[28] and cluster assays[29], suffer from the enhanced non-specific interactions in blood plasma. For point-of-care assays that typically take about 10 minutes, the nonspecific aggregation is relatively low, but the protein corona formation process is still in the kinetic regime. Small changes in the incubation time of the particles can cause variations in the outcome of the measurements. Therefore care should be taken to keep the incubation time constant in these assays. For assays with much longer assay times, up to hours, the nonspecific aggregation is larger. This might make it more difficult to measure small analyte concentrations, as the background nonspecific interactions could become more important with respect to the specific interactions.

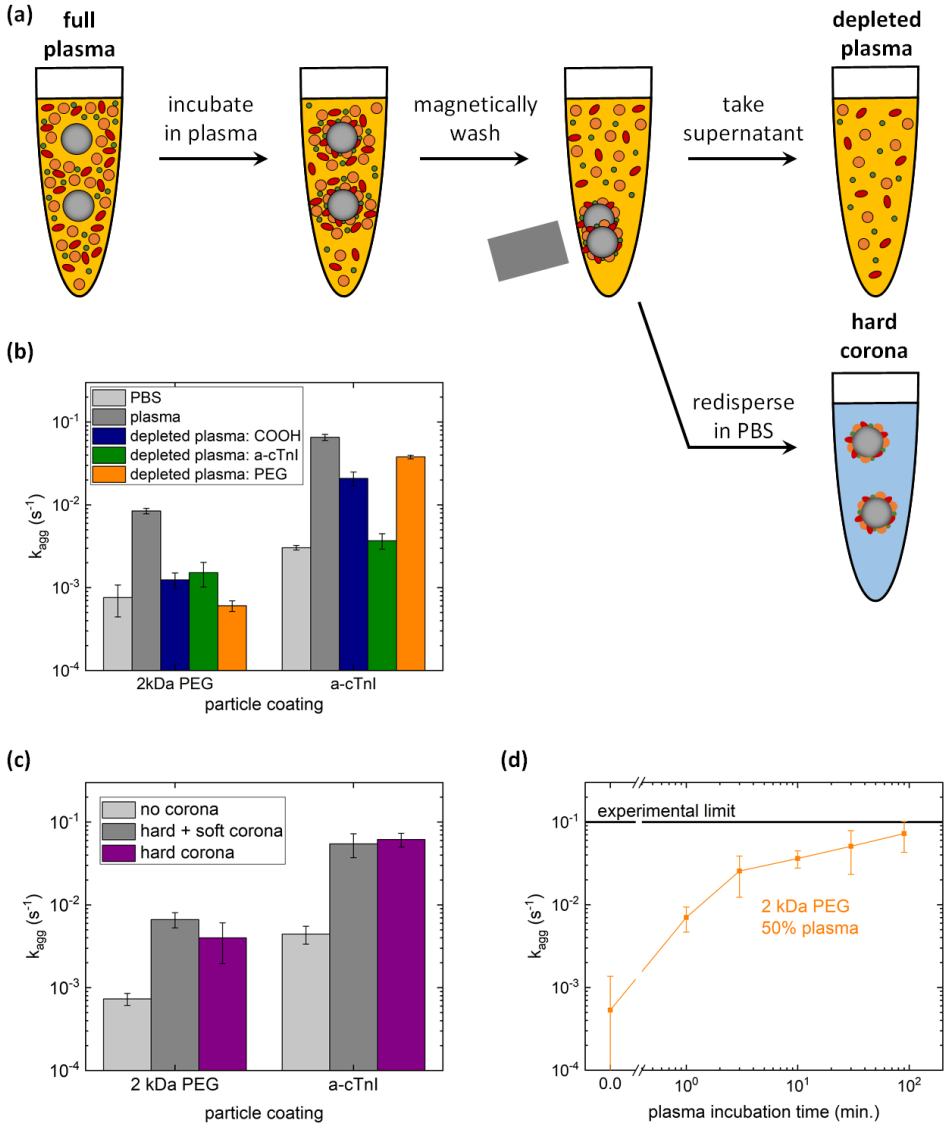

Fig. 6.2 Effect of plasma composition on the particle aggregation rate. (a) Functionalized particles were incubated in plasma for one hour at room temperature, during which a protein corona forms around the particles. The particles are magnetically washed out of the plasma and the supernatant, i.e. the depleted plasma, is stored in a different Eppendorf tube. The particles are washed magnetically two more times, and redispersed in PBS buffer. **(b)** Particle aggregation rate measured in buffer, undiluted plasma, and in plasma samples depleted by particles with either a COOH, a-cTnI or PEG coating. Depleting the plasma with particles with the same coating as the measurement particles leads to the largest reduction in aggregation rate w.r.t. the full plasma sample. **(c)** Particle aggregation rate measured in buffer (no corona), in undiluted plasma (hard + soft corona) and in buffer with particles that have been incubated in plasma (only hard corona). The aggregation inducing corona proteins seems to be dominantly positioned in the hard corona. **(d)** Particle aggregation rate measured for PEG coated particles, incubated in 50% plasma for different durations.

6.6 Conclusion

Nonspecific inter-particle aggregation rates of biofunctionalized particles were measured in blood plasma. The aggregation rate is demonstrated to increase with plasma concentration for various particle functionalizations. PEG coated particles show the lowest aggregation rate at each plasma concentration. Binding selectivities greater than 1 are obtained, which suggests that multivalent weak interactions between the protein coronae of particles are responsible for particle aggregation.

Plasma samples were depleted by incubation with functionalized particles. The particle aggregation rate measured in depleted plasmas is lower compared to the aggregation rate in full plasma. Moreover the reduction in aggregation rate is greatest when depleting the plasma with particles that have the same functionalization as the particles that are used for the aggregation rate measurement. These results proves that the composition of the protein corona depends on the biomolecular functionalization of the particles. The particles that were used to deplete the plasma, were separated from the plasma by magnetic washing. Their aggregation rate was subsequently measured in buffer, and compared to measurements of similar particles in plasma. This experiment showed that the aggregation inducing proteins are mainly present in the hard corona.

From the experiments performed in this chapter we conclude that the aggregation inducing corona proteins are specific for the biomolecular surface coating of the particles and that they are part of the hard corona. Over time the protein corona evolves and the aggregation rate increases, on the timescale of hours.

6.7 Supporting Information

S6.1 Optomagnetic cluster (OMC) experiment

In this paper specific particle aggregation rates will be measured using the OMC experiment described in a previous paper[25]. Fig. S6.1a sketches the optomagnetic cluster (OMC) experiment. A square glass cuvette filled with a solution of particles is situated in the centre of a quadrupole electromagnet setup, which can produce a rotating magnetic field in the y,z plane. A 660 nm laser is focussed insight the cuvette and the light scattered by the particles is measured by a photodetector at an angle of 90° w.r.t. to the incoming laser beam. In the presence of a rotating magnetic field, with a rotation frequency below the breakdown frequency, the dimers in the solution will rotate along with magnetic field. Fig. S6.1c shows the oscillating scattering signal for the superparamagnetic particles used in this paper: polystyrene Ademtech Masterbeads (d = 528 nm, CV ≈ 25%). The amplitude of the oscillating scattering signal is a measure of the dimer concentration. The Fourier transform of this oscillating scattering signal is shown Fig. S6.1d. The peak at four times the field rotation frequency, |A4f|, is the largest contribution to the scattering signal and is used as a measure of the dimer concentration. Fig. S6.1e shows a calibration measurement of the |A4f| peak, indicating that |A4f| scales linear with dimer concentration.

To quantify the aggregation rate a four-step actuation protocol is followed, as can be seen in Fig. S6.1b. Initially the number of already present chemical dimers is measured using magnetic pulses with a short on-time, t_{on} = 0.4 s, and a long off time, t_{off} = 10 s. During the subsequent actuation phase, the rotating magnetic field is turned on continuously during a time t_{act} = 20 s to induce additional magnetic dimers, causing the |A4f| signal to increase approximately linearly over time (this is true for both types of particles, see Fig. S6.1f). Since each magnetic dimer is formed at a different point in time, each magnetic dimer has a different interaction time in which it has the possibility to form a chemical bond. The mean interaction time of all dimers, for a constant magnetic dimer formation rate, equals half the actuation time. After the actuation phase, the field is turned off during a waiting time t_{wait} = 40 s to let the non-aggregated particles redisperse in solution. Ultimately, the number of chemical dimers is measured again and compared to the initial number of dimers. The increase in the number of chemical dimers, ΔN_{chem}, depends on how reactive the particles are. To calculate the aggregation rate k_{agg}^{mag}, the fraction of magnetic dimers that becomes a chemical dimer during the actuation phase, $\Delta N_{chem}/N_{mag,tot}$, is divided by the mean interaction time of all magnetic dimers.

$$k_{agg} = \frac{\Delta N_{chem} \,/\, N_{mag,tot}}{\frac{1}{2} t_{act}} \tag{S6.1}$$

In case of very reactive particles, it is possible that all magnetic dimers form a chemical bond during the interaction time. For a 20 s actuation time the maximum experimentally measurable aggregation rate is limited to $k_{agg,max}$ = 0.1 s^{-1}.

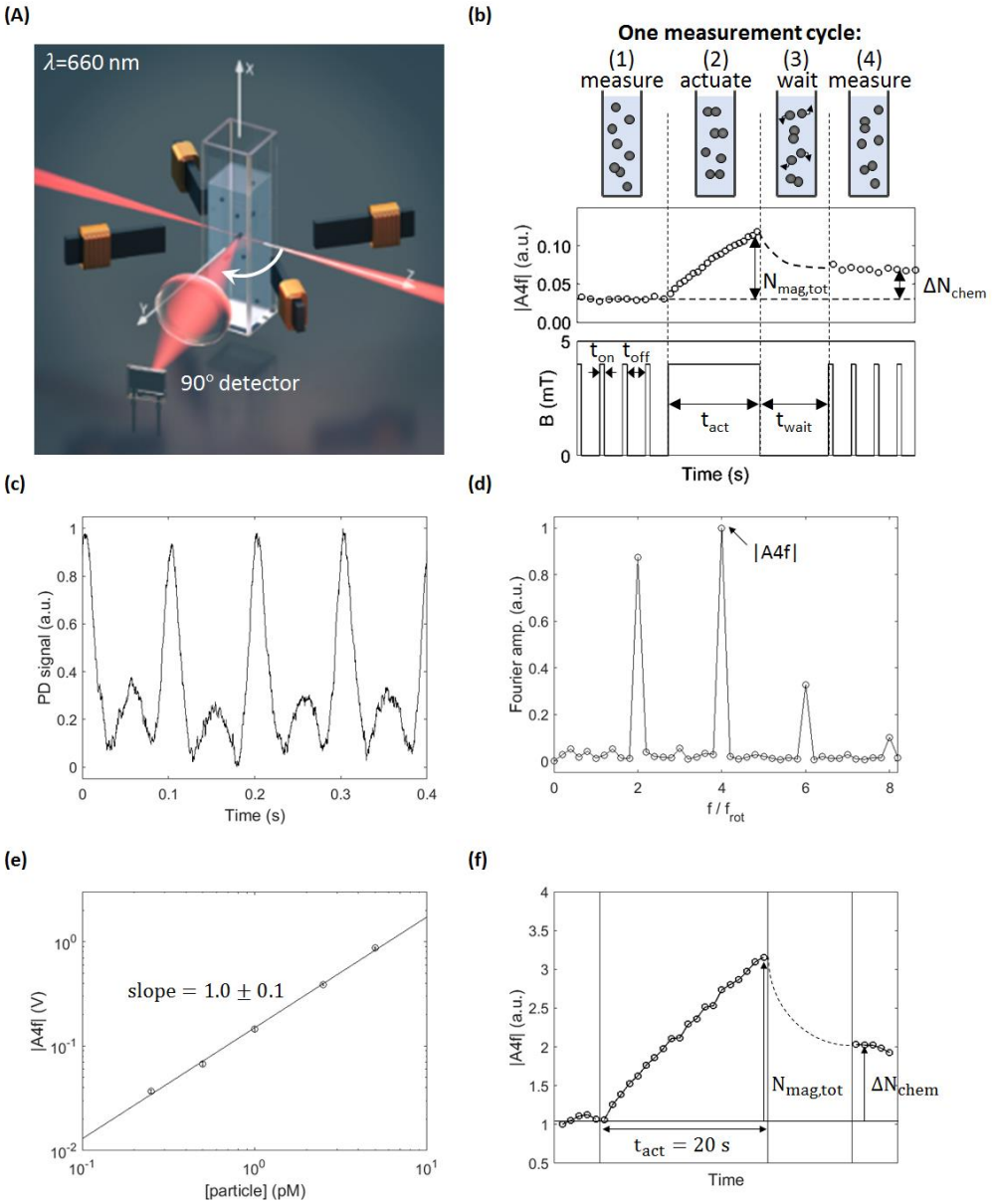

Fig. S6.1 Optomagnetic cluster experiment. (a) Optomagnetic dimer quantification: A 660 nm laser is focussed inside a cuvette filled with a particle solution. The scattering of the particles is measured at an angle of 90° w.r.t. the incoming laser beam. Four electromagnets are placed around the cuvette to apply a

rotating magnetic field. Particle dimers are rotated, which leads to an oscillating scattering signal. The amplitude of the oscillating signal is used as measure of the dimer concentration. **(b)** Four-step actuation protocol to quantify the aggregation rate. First, the initial number of chemical dimers in the solution is measured using short magnetic field pulses. Then the field is turned on continuously to induce additional magnetic dimers, during an actuation time t_{act}. The field is subsequently turned off for a waiting time t_{wait} to let the unbound particles redistribute in the solution. Finally, the new number of chemical dimers is measured. Using equation S6.1 the aggregation rate can be determined. **(c)** Oscillating scattering signal of the Ademtech Masterbeads, measured by a photodetector at an angle of 90° w.r.t. the incoming laser beam in the presence of a rotating magnetic field, f_{rot} = 5 Hz. **(d)** Fourier transform of the oscillating scattering signals of Fig. S6.1c, showing peaks at multiples of two times the field rotation frequency. **(e)** Calibration measurement of |A4f| as a function of particle concentration of a stock solution (containing a constant number of dimers), indicating that the |A4f| scales linearly with dimer concentration. **(f)** Single actuation cycle to measure the aggregation rate with the OMC experiment.

S6.2 Effect of plasma filtration on particle aggregation

To investigate which proteins are responsible for particle aggregation, plasma samples are filtrated to separate the larger proteins (MW ≥ 100 kDa) from the smaller proteins (MW < 100 kDa), see Fig. S6.2a. The plasma samples are first centrifuged for 20 minutes at 14,300 rpm in a spin filter with a molecular weight cut off of 100 kDa, after which the filtrate and the residue are separated. Ultimately, the volume of the filtrate and residue is restored to the original amount, to keep the concentrations of the individual molecules equal to those in plasma.

An SDS PAGE experiment is performed with (diluted) plasma samples before and after filtration (residue and filtrate), see Fig. S6.2b. Unfiltered plasma contains too many proteins to visualize the individual bands on the gel, but for the diluted plasma samples the bands are visible. The filtrate should contain the proteins with MW < 100 kDa and the residue the proteins with MW ≥ 100 kDa. However, the filtrate only shows some intensity around 50 kDa, which are most likely albumins. The other bands below 100 kDa that are visible in the unfiltered samples are not observed for the filtrate samples. We hypothesize that during the spin filtering process, the filter is clogged whereby almost all plasma proteins remain in the filtrate.

The inter-particle aggregation rate for PEG coated particles and a-cTnI coated particles is measured in PBS buffer, full plasma and in the residue and filtrate of filtered plasma, see Fig. S6.2c. The aggregation rate in buffer is low and represents the baseline aggregation in this experiment. The aggregation rate in full plasma is higher and represents the upper limit of the aggregation rate. For both particle functionalization, the aggregation rates of the filtrate and residue are about equal to the aggregation rate in buffer and full plasma, respectively. These results agree with our hypothesis that due to the filtration process almost all proteins remain in the residue.

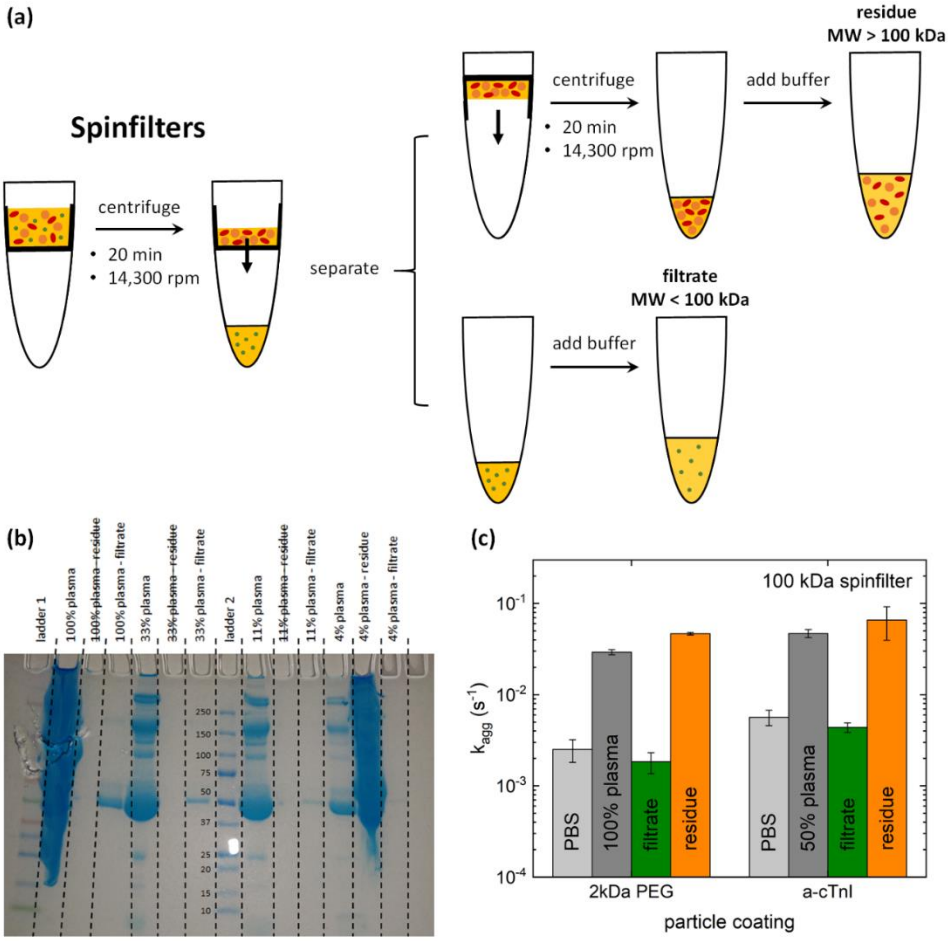

Fig. S2 Effect of plasma filtration on particle aggregation. (a) Plasma is filtered by centrifuging the sample using spin filters with a molecular weight cut off of 100 kDa. The filtrate and the residue are separated and for both the volume is restored to the original amount to keep the concentrations of the individual molecules constant. **(b)** SDS Page gel of (diluted) plasma samples before and after filtration, both residue and the filtrate. The columns of which the header is crossed out failed. **(c)** Inter-particle aggregation rate for particles dispersed in PBS buffer, plasma or in the filtrate or residue of the filtered plasma. The aggregation rate in the filtrate solution is about equal to the aggregation rate in buffer, and the aggregation rate in the residue solution is about equal to the rate in full plasma.

References

[1] Zeng, S.; Yong, K. T.; Roy, I.; Dinh, X. Q.; Yu, X.; Luan, F. A review on functionalized gold nanoparticles for biosensing applications. *Plasmonics* **2011**, 6, 491-506

[2] Howes, P. D.; Chandrawatti, R.; Stevens, M. M. Colloidal nanoparticles as advanced biological sensors. *Science* **2014**, 346 (6205)

[3] Sun, C.; Lee, J. S. H.; Zhang, M. Magnetic nanoparticles in MR imaging and drug delivery. *Adv. Drug. Del. Rev.* **2008**, 60, 1252-1265

[4] Pankhurst, Q. A.; Connoly, J.; Jones, S. K.; Dobson, J. Applications of magnetic nanoparticles in biomedicine. *J. Phys. D: Appl. Phys.* **2003**, R167-R181

[5] Caracciolo, G.; Farokhzad, O.C.; Mahmoudi, M. Biological identity of nanoparticles in vivo: clinical implications of the protein corona. *Trends in Bioltechnol.* **2017**, 35, 257-264

[6] Gebouwer, J.S.; Malissek, M.; Simon, S.; Knauer, K.S.; Maskos, M.; Stauber, R.H.; Peukert, W.; Treuel, L. Impact of the nanoparticle-protein corona on colloidal stability and protein structure. *Langmuir* **2012**, 28, 9673-9679

[7] Suk, J. S.; Xu, Q.; Kim, N.; Hanes, J.; Ensign, L. M. PEGylation as a strategy for improving nano-particle based drug and gene delivery. *Adv. Drug Del. Rev.* **2016**, 99, 28-51

[8] Ranzoni, A.; Schleipen, J. J. H. B.; van IJzendoorn, L. J.; Prins, M. W. J. Frequency-selective rotation of two-particle nanoactuators for rapid and sensitive detection of biomolecules. *Nano Lett.* **2011**, 11, 2017-2022

[9] Schwenk, J.M.; Omenn, G.S.; Sun, Z.; Cambell, D.S.; Baker, M.S.; Overall, C.M.; Aebersold, R.; Moritz, R.L.; Deutsch, E.W. The human plasma proteome draft of 2017: Building on the human plasma PeptideAtlas from mass spectrometry and complementary assays. *J. Proteome. Res.* **2017**, 16, 4299-4310

[10] Dell'Orco, D.; Lundqvist, M.; Oslakovic, C.; Cedervall, T.; Linse, S. Modeling the time evolution of the nanoparticle protein corona in a body fluid. *PLoS ONE* **2010**, 5, 6, e10949

[11] Sahneh, F.D.; Scoglio, C.; Riviere, J. Dynamics of nanoparticle-protein corona complex formation: Analytical results from population balance equations. *PLoS ONE* **2013**, 8, 5, e64690

[12] Tenzer, S.; Docter, D.; Rosfa, S.; Wlodarski, A.; Kuharev, J.; Rekik, A.; Knauer, S.K.; Bantz, C.; Nawroth, T.; Bier, C.; Sirirattanapan, J.; Mann, W.; Treuel, L.; Zellner, R.; Maskos, M.; Schild, H.; Stauber, R.H. Nanoparticle size is a critical physicochemical determinant of the human blood plasma corona: a comprehensive quantitative proteomic analysis. *ACS Nano* **2011**, 5, 9, 7155-7167

[13] Foroozandeh, P.; Aziz, A.A. Merging worlds of nanomaterials and biological environment: factors governing protein corona formation on nanoparticles and its biological consequences. *Nanoscale Res. Lett.* **2015**, 10, 221

[14] García-Álvares, R.; Hadjidemetriou, M.; Sánchez-Iglesias, A.; Liz-Marzán, L.M.; Kostarelos, K. In vivo formation of protein corona on gold nanoparticles. The effect of their size and shape. *Nanoscale* **2017**, 10, 1039

[15] Lundqvist, M.; Stigler, J.; Elia, G.; Lynch, I.; Cedervall, T.; Dawsen, K.A. Nanoparticle size and surface properties determine the protein corona with possible implications for biological impacts. *PNAS* **2008**, 105, 38, 14265-14270

[16] Sakulkhu, U.; Mahmoudi, M.; Maurizi, L.; Salaklang, J.; Hofmann, H. Protein corona composition of superparamagnetic iron oxide nanoparticles with various physico-chemical properties and coatings. *Sci. Rep.* **2014**, 4, 5020

[17] Johnston, B.D.; Kreyling, W.G.; Pfeiffer, C.; Schäffer, M.; Sarioglu, H.; Ristig, S.; Hirn, S.; Haberl, N.; Thalhammer, S.; Hauck, S.M.; Semmler-Behnke, M.; Epple, M.; Hühn, J.; Del Pino, P.; Parak,

W.J. Colloidal stability and surface chemistry are key factors for the composition of the protein corona of inorganic gold nanoparticles. *Adv. Funct. Mater.* **2017**, 27, 1701956

[18] Pederzoli, F.; Tosi, G.; Vandelli, M.A.; Belletti, D.; Forni, F.; Ruozi, B. Protein corona and nanoparticles: how can we investigate on? *WIREs Nanomed Nanobiotechnol.* **2017**, 9, 1467

[19] Treuel, L.; Nienhaus, G.U.; Toward a molecular understanding of nanoparticle-protein interactions. *Biophys. Rev.* **2012**, 4, 137-147

[20] Wang, Z.; He, C.; Gong, X.; Wang, J.; Ngai, T. Measuring the surface-surface interactions induced by serum proteins in a physiological environment. *Langmuir* **2016**, 32, 12129-12136

[21] Li, W.; Coa, F.; He, C.; Ohno, K.; Ngai, T. Measuring the interactions between protein coated microspheres and polymer brushes in aqueous solutions. *Langmuir* **2018**, 34, 8798-8806

[22] Ho, Y.T.; Azman, N.A.; Loh, F.W.Y.; Ong, G.K.T.; Engudar, G.; Kriz, S.A.; Kah, J.C.Y. Protein corona formed from different blood plasma proteins affects the colloidal stability of nanoparticles differently. *Bioconjugate Chem.* **2018**, 29, 3923-3934

[23] Scheepers, M.R.W.; Romijn, A.R.; van IJzendoorn, L.J.; Prins, M.W.J. Rate of dimer formation in stable colloidal solutions quantified using an attractive interparticle force. *Langmuir*, **2019**, 35, 10533-10541

[24] Blaszykowski, C.; Sheikh, S.; Thompson, M. A survey of state-of-the-art surfactant chemistries to minimize fouling from human and animal biofluids. *Biomater. Sci.* **2015**, 3, 1335-1370

[25] Müller, J.; Bauer, K.N.; Prozeller, D.; Simon, J.; Mailänder, V.; Wurm, F.R.; Winzen, S.; Landfester, K. Coating nanoparticles with tunable surfactants facilitates control over the protein corona. *Biomaterials* **2017**, 1-8

[26] Scheepers, M.R.W.; IJzendoorn, L.J.; Prins, M.W.J. Multivalent weak interaction enhance selectivity in inter-particle binding – experimental proof. *In preparation.*

[27] Martinez-Veracoechea, F.J.; Frenkel, D. Designing super selectivity in multivalent nano-particle binding. *PNAS* **2011**, 108, 10963-10968

[28] Jarrige, V.; Nieuwenhuis, J.H.; van Son, J.P.H.F.; Martens, M.F.W.C.; Vissers, J.L.M. A fast intraoperative PTH point-of-care assay on the Philips handheld magnotech system. *Langenbecks Arch. Surg.* **2011**, 396, 337-343.

[29] Ranzoni, A.; Sabatte, G.; van IJzendoorn, L.J.; Prins, M.W.J. One-step homogeneous magnetic nanoparticle immunoassay for biomarker detection directly in blood plasma. *ACS Nano*, **2012**, 6, 4, 3134-3141

Chapter 7

Conclusion and outlook

In this thesis, the inter-particle biomolecular reactivity of functionalized submicrometer sized particles has been investigated by experiments and simulations. Particles have been confined in dimers using magnetic fields and particle aggregation has been measured by optical techniques. To quantify particle surface reactivity, two experimental methods have been developed that measure the aggregation rate: an ensemble optomagnetic cluster (OMC) experiment and a single-dimer aggregation (SDA) experiment. Particle reactivity was studied in buffers and (diluted) blood plasma as a function of the particle surface functionalization with antibodies, DNA, PEG, and combinations thereof. An enhanced binding selectivity was proven in experiments with multivalent low-affinity biomolecular surface functionalization. In this chapter the main conclusions of this thesis will be summarized and discussed, and an outlook is presented.

7.1 Quantification of inter-particle surface reactivity

The optomagnetic cluster experiment has been introduced in chapter 2 as a method for measuring aggregation rates on an ensemble of particles. Many experimental parameters have been varied to find the optimal settings to allow for measuring the dimer formation rate instead of the formation of multiplets: magnetic field amplitude, magnetic field actuation time and waiting time, magnetic field pulse sequences and particle concentration. A simulation based on the Smoluchowski rate equations has been used to validate that under the optimal experimental settings the clusters are dominantly dimers. The sensitivity and dynamic range of the OMC experiment have been investigated using a model experiment in which the pH and ionic strength of an aqueous buffer were varied in a solution with negatively charged carboxylic acid coated 500 nm particles. An increase of over two orders of magnitude in the aggregation rate was observed when decreasing the pH of the buffer from 8 to

4. The measured aggregation rates are representative for magnetically confined particles. Using DLVO theory it has been shown that these magnetically confined aggregation rates can be converted to dimer formation rates in the absence of an attractive inter-particle force, showing that with the OMC experiment it is possible to measure rates in the range of 10^1-10^5 $M^{-1}s^{-1}$.

In chapter 3 we studied particle surface reactivity on a single-dimer level using optical microscopy. Using a single-dimer aggregation (SDA) experiment, we have been able to follow multiple aggregation and dissociation events of single-dimers. Video microscopy of the aggregation and dissociation events of individual dimers revealed discrete areas on the particle surfaces with high reactivity, indicating strong heterogeneity of the surface reactivity. The pH of the aqueous buffer was varied for two particle systems: The first consisted of two identical particles that were coated with anti-cardiac troponin I (a-cTnI) antibodies and blocked with PEG, and the second particle system consisted of one particle coated with a-cTnI and blocked with PEG and another particle with a diameter of one micron and coated with carboxylic acids. The measured average dimer formation rate increased over multiple orders of magnitude when decreasing the pH of the buffer from 8 to 4, which is in qualitative agreement with the experimental results of the OMC experiment in chapter 2. To study the influence of the particle surface functionalization on the aggregation rate, the antibody density on the surface of the secondary particle was varied. However, no significant effect on the aggregation rate has been observed. A stochastic binding simulation on the aggregation of particles with a heterogeneously reactive surface resulted in quantitative agreement between the OMC experiment and the SDA experiment, when assuming that the secondary particle makes a shoving motion over the primary particle.

7.2 How particle surface reactivity depends on molecular surface composition

In chapter 4 the OMC experiment was used to study the dependence of the inter-particle surface reactivity on the molecular composition of the surface, consisting of strong specific binders and passive surface crowders. For this purpose two experimental systems were used: A DNA based model system and a PSA antibody-based sandwich system. Specific interaction was induced by adding a specific bridging molecule to the colloidal solution, either analyte-DNA or PSA. The inter-particle surface reactivity was measured as a function of the analyte concentration for several binder areal densities. In addition, the molecular weight of the passive PEG surface crowder was varied. The experiments show that specific particle aggregation significantly exceeds nonspecific aggregation and that the particle surface reactivity

changes with the surface composition: increasing the areal binder density leads to increased particle surface reactivity. Increasing the molecular weight of the PEG, such that the PEG becomes significantly larger than the specific binder, leads to a decreased particle surface reactivity. Simulations confirmed that the decrease in surface reactivity by the high molecular weight PEG can be modelled as an effective decrease in the molecular rate of bond formation. In addition, experiments and simulations reveal that particle aggregation has a multivalent character.

In chapter 5 the selectivity of the inter-particle binding process was studied further using a DNA-based model system in which particles were either coated with ligand DNA or with receptor DNA. To quantify the particle surface reactivity, the inter-particle aggregation rate was measured using the OMC experiment. The inter-particle aggregation rate was found to increase with binder density for a broad range of receptor and ligand densities. The multivalent character of the interactions was investigated by changing the affinity of the ligand-receptor pair by changing the number of complementary base pairs of the DNA interaction. For DNA bonds as short as 5 base pairs significant inter-particle aggregation still occurred, which indicates that multivalent bonds are formed between the particles. It has been experimentally proven that multivalent weak interactions enhance the binding selectivity. A simulation model that is tailored to the OMC experiment confirmed the experimental observations and indicated that the enhanced selectivity for weaker ligand-receptor affinity is explained by an increase in the dissociation rate of ligand and receptor.

7.3 Inter-particle surface reactivity in a complex matrix

In chapter 6 the particle surface reactivity was investigated in a complex biological solution. Inter-particle aggregation rates have been measured in various dilutions of blood plasma, using particles functionalized with antibodies, PEG, tris or carboxylic acids. Experiments show that electrostatic repulsion by carboxylic acids and steric repulsion by PEG molecules both induce particle stability in aqueous buffer solutions. However, in blood plasma, the electrostatic stabilization does not occur. Nonspecific interactions increase with plasma concentration in a seemingly super linear fashion, which suggests that aggregation was caused by multivalent weak interactions e.g. between the protein coronas formed around particles.

To investigate if the aggregation inducing corona proteins were specific for the particle functionalization, corona-forming proteins were removed from the plasma samples by incubation with and removal of functionalized particles. After removal, measurements showed that inter-particle aggregation was most efficiently decreased

when corona-forming proteins had been removed using particles with the same functionalization as the measurement particles. This suggests that the aggregation-inducing corona proteins are coating specific. Moreover, we found that the aggregation-inducing corona proteins were dominantly present in the hard corona. Over time the protein corona evolves and the inter-particle surface reactivity increases, on the time-scales of hours.

7.4 Outlook

The optomagnetic cluster experiment and the single-dimer aggregation experiment make a range of very low aggregation rates experimentally accessible, both for nonspecific and specific inter-particle aggregation. The OMC experiment provides a screening method for developing anti-aggregation coatings on particles, or as a method to screen for specific protein-protein interaction, e.g. for finding combinations of antibodies that form a matched pair. The range of thermal particle aggregation rates that is accessible for the OMC experiment is 10^{1}-10^{5} $M^{-1}s^{-1}$. However, the dynamic range of the method can be extended to $4{\cdot}10^{5}$ $M^{-1}s^{-1}$ using shorter actuation times. The SDA experiment can be used to study heterogeneity in particle surface reactivity to investigate different functionalization protocols and coupling chemistries.

Nonspecific particle aggregation has been measured for particles with different surface functionalizations. The PEG coating is most efficient in suppressing the nonspecific particle aggregation both buffer and blood plasma, in agreement with literature. In order to understand the origin of the strong nonspecific aggregation in blood plasma and eventually scavenge for the aggregation-inducing corona proteins, it is important to be able to correlate the surface reactivity with the protein corona composition. Our experiments lead to the hypothesis that the protein corona composition is specific for a certain particle functionalization. By eluting the hard corona from particles and analyzing their composition using liquid chromatography-mass spectrometry (LCMS), the coating specific proteins can be identified.

For applications that employ specific particle interactions, we obtain a couple of design rules. The surface reactivity can be tuned by the density of specific binders and by passive surface crowders that are significantly larger than the specific binders. Follow up research should focus on how the PEG density influences the specific inter-particle surface reactivity, in order to tune the surface reactivity in a more continuous way. Additionally, to obtain a high binding selectivity, high densities of weak binders are needed to maximize the combinatorial entropy of the ligand-receptor binding. Flexible multivalent binders, i.e. molecules with multiple analyte binding sites, ought

to be most effective for this purpose. The experiments in this thesis show that multivalent weak interactions are very promising for targeted drug delivery, because the specificity for cell receptor density is higher using multivalent weak interactions compared to single strong interactions.

About the author

Max Rose-Marie Wilhelmus Scheepers was born as the son of John Scheepers and Resi Weijers on the 19th of November 1991 in Heerlen, the Netherlands. Together with his twin sister Eva and older sister Lisa he went to primary school at Basisschool De Wegwijzer in Heerlen. He followed his secondary education at the Bernardinus College in Heerlen combining the profiles of Nature and Technology and Nature and Health. This profile allowed him to pursue a scientific oriented education with a broad interdisciplinary interest. He concluded his secondary education in 2010.

Max performed his bachelor and master education in Applied Physics at the TU/e, where he followed the track Functional Nano Materials. He worked side jobs as a postman for PostNL and worked as a tutor for secondary school students in mathematics and physics. As part of his education he performed an internship at the Universitat de Válencia under supervision of dr. ir. Henk Bolink, where he investigated the time -and temperature stability of perovskite solar cells. In 2015, Max finished his master with a thesis project studying the binding kinetics in a tethered particle motion system.

In September 2015, he started his PhD in the group Molecular Biosensing for Medical Diagnostics under the supervision of prof. dr. ir. Menno Prins and dr. ir. Leo van IJzendoorn. During his PhD, he studied how inter-particle biomolecular reactivity are influenced by charge, surface crowders, and multivalent interactions. The main results of the work during his PhD are summarized in this thesis.

List of publications

Journal papers

- **Scheepers, M.R.W.**; van IJzendoorn, L.J.; Prins, M.W.J. Multivalent weak interactions enhance selectivity in inter-particle binding – experimental proof. *In preparation*.

- **Scheepers, M.R.W.**; Haenen, S.; Coers, J.; van IJzendoorn, L.J.; Prins, M.W.J. Inter-particle biomolecular reactivity tuned by surface crowders. *In preparation*.

- **Scheepers, M.R.W.**; van IJzendoorn, L.J.; Prins, M.W.J. Single dimer formation rate reveals heterogeneous particle surface reactivity. *Langmuir*, **2019**, 35, 44, 14272-14281.

- **Scheepers, M.R.W**.; Romijn, A.R.; van IJzendoorn, L.J.; Prins, M.W.J. Rate of dimer formation in stable colloidal solutions quantified using an attractive interparticle force. *Langmuir*, **2019**, 35, 32, 10533-10541.

- Wetzelaer, G.J.; **Scheepers, M.R.W.**; Sempere, A.; Momblona, C.; Ávila, J.; Bolink, H.J. Trap-assisted non-radiative recombination in organic-inorganic perovskite solar cells. *Adv. Mat.* **2015**, 27, 11, 1837-1841.

- Van Reenen, S.; **Scheepers, M.R.W**.; van de Ruit, K.; Bollen, D.; Kemerink, M. Explaining the effects of processing on the electrical properties of PEDOT:PSS. *Org. Electron.* **2014**, 15, 3710-3714.

- Momblona, C.; Malinkiewicz, O.; Roldan-Carmona, C.; Soriano, A.; Gil-Escrig, L.; Bandiello, E.; **Scheepers, M.R.W.**; Edri, E.; Bolink, H.J. Efficient metthylammonium lead iodide perovskite solar cells with active layers from 300 to 900 nm. *Appl. Phys. Lett. Matt.* **2014**, 2, 081504.

Patents

- Prins M.W.J.; Merkx, M.; van IJzendoorn, L.J.; Zijlstra, P.; Visser, E.W.A.; **Scheepers, M.R.W.**; Biosensor Based on a Tethered Particle, *Patent Application WO 2016096901 A1* **2015**.

Conference presentations

- Australian Colloid and Interface Symposium 2019 (oral) - Rate of single-dimer formation reveals heterogeneous particle surface reactivity.

- Dutch Biophysics 2018 (poster) - Aggregation kinetics quantified on single particle dimers reveals heterogeneity in particle surface reactivity.

- Dutch Biophysics 2017 (poster) - Quantifying nonspecific particle aggregation kinetics for improved biosensor performance.

- Chains 2016 (poster) - The (in)stability of nanoparticles in blood plasma: How to quantify at the single-particle level?

- NanoBioTech Montreux 2016 (poster*) - The (in)stability of nanoparticles in blood plasma: How to quantify at the single-particle level?

- Dutch Biophysics 2016 (poster) - The (in)stability of nanoparticles in blood plasma: How to quantify at the single-particle level?

- Nanocity Amsterdam 2016 (poster) - Quantifying aggregation of individual magnetic nanoparticle pairs in blood plasma.

- Wetenschapsavond Catharina Ziekenhuis Eindhoven (2016) - Quantifying aggregation of individual magnetic nanoparticle pairs in blood plasma.

* Poster prize winner

Acknowledgements

"*One small step for mankind, a giant leap for myself*." That pretty much describes my PhD project. Looking back at the past four years, I realize how much I have developed myself, as a scientist, but also as a person. On the first of September 2015, when I started this scientific journey, I literally never thought I would be able to finish it. And yet here I am proudly writing the final pages of my Thesis. The cover of this thesis only says my name, however, there are few people that have played a crucial role for me and without them I would never have been able to finish this journey. I would very much like to thank them.

Most important of all, my daily supervisor. Leo, you have been like a scientific father for me. We first met when I started my master's project with you and Emiel, but we really got to know each other during my PhD project. The hours lasting discussions about my experiments, our students, the SensUs team, or about non-scientific subjects like our hobbies, my handball club and your chess club, or our injuries, my knee and your back. You might sometimes be told that you should keep these meetings shorter, but please ignore those well-meant advices, because I learned so much from you during those discussions. After such a meeting, I was always full of inspiration and positive energy. You have really shaped me into the person that I am now. Thank you for everything Leo.

Menno, your sharpness in discussions, your pragmatic way of thinking and nearly-infinite knowledge of our research field, those are qualities that I am really jealous off. You have matured my way of thinking both scientifically and in my everyday live a lot. Also a big thanks to the rest of the MBx group. You have made me feel part of the group from the very first day. The fun we had during the game nights, group outings and borrels, make the working much more fun too. And although I know that I have often rejected your invitations for the birthday parties, the spring roll evenings or the knitting nights, partly because I live quite far from the TU/e and partly because I never skip a handball training, I really enjoyed the parties that I did join.

Matej and Yuyang, you started on the same day as me and throughout these years we could always discuss our experiences, our progress in the project and of course our failures in the lab. As I will leave the university I want to wish you good luck in the rest of your careers. A special word of thanks to you, Rafiq. You were part of the first Eindhoven SensUs team that Leo and I supervised and later on you started your

PhD in our group as well. During the last two years that we were office mates, we had a lot of fun. We laughed so much about stuff that I really cannot discuss openly here, but you know exactly what I mean. Good luck on finishing your PhD.

During my PhD I have had the privilege to supervise a lot of students: Max Bergkamp, Joost, Annabel, Chris, Dennis, Stijn, Ivo, Joris and Esmay. Supervising you was something I enjoyed a lot. I really hope that you have learned something from me. I sure learned something from all of you. Thank you all for your efforts and hard work, especially my master students Annabel and Stijn. When I finished my master's project with Emiel and started a PhD, I made him a promise that I would make sure that at least one my students would also stay in our group. Hereby I fulfil my promise Emiel, as Max and Stijn recently started a PhD and a PdEng, respectively. Max and Stijn, I hope you will continue the series.

Tot slot wil ich geer een aantal lui in 't biezonder bedanken. Pap en mam, bedankt dat d'r mich altied gesteund en gemotiveerd hubt. En bedankt dat d'r altied noa mien lestige verhalen euver mien onderzeuk geloesterd hubt en mit alle moeite geprobeerd hubt om een inhoudelikke vroag d'r euver te stellen. Lisa en Eva, d'r zeet neet allein mien zussen, mer v'r zeen auch goeie vrung. Ich kin mit euch alles bespreaken en bedankt dat d'r altied veur uch irritante broortje kloar sjtut.